



The University of  
**Nottingham**

School of Electrical and Electronic Engineering  
Faculty of Engineering

# **Investigation of the Electrical Properties of III-V Semiconductor Doped with Mn**

*by*

**Noorah Ahmed AlAhmadi, MSc**

GEORGE GREEN LIBRARY OF  
SCIENCE AND ENGINEERING

Thesis submitted to the University of Nottingham for  
the degree of Doctor of Philosophy

March 2011

## ABSTRACT

III–V semiconductors doped with Mn atoms have been studied recently for their potential applications in spintronic devices. These materials are referred to as diluted magnetic semiconductors (DMS) or ferromagnetic semiconductors. The lattice of these materials has Mn atoms (transition metal) and due to their half filled shell carries a spin and also donates carriers, “p-type” in case of Mn doping to the semiconductor lattice. Ferromagnetism is mediated by exchange interactions between localized d electrons and p-type carriers. A high transition temperature (in fact above room temperature) called Curie point, is necessary for these materials to have a practical value. The transition temperature  $T_C$  depends on the densities of both Mn impurity and the resultant hole concentration. A low density of defects, a high crystal quality and a high concentration of Mn atoms are desirable to achieve a high  $T_C$ .

Additionally, cubic (zinc blende) structure offers several advantages over the hexagonal structure normally obtained for III–V semiconductors e.g. a higher crystal symmetry, smaller effective masses, higher carrier mobility, and significantly a higher doping density-which is expected to give a higher value of  $T_C$ .

Both GaMnAs and GaMnN have been the materials of choice and have been studied intensely. The problems however, are related to fabricated technique, crystal quality and achieving a high doping concentration. The materials exhibit a solubility limit beyond which doping concentration are difficult to achieve.

This thesis describes the investigation of the electronic properties of the zinc blend GaMnAs and GaMnN films grown at low temperature by molecular beam epitaxy (MBE) for varies concentration of Mn doping over the temperature range 15-400 K.

Metal/c-GaAs: Mn/c-GaAs:Si p n junctions were studied by the I-V, C-V and C-F methods over the temperature range 15-400 K. It was found that I-V-T data could be interpreted on the basis of a back to back diode model. The c-GaAs:Mn made a Schottky contact with the metal and a p n junction with c-GaAs:Si. It was found that for the forward bias, where metal was biased negative with respect to the GaAs:Mn, the I-

V-T data could also be analysed on the basis of a Schottky behaviour. Here ideality factor  $n$  increased and the barrier height  $\Phi_b$  decreased with temperature. This was seen to be a consequence of TFE through the metal/GaAs barrier. This was borne out by the Richardson's plots [ $\ln (I_s/T^2)$  versus  $10^3/nT$ ] which exhibited straight lines. The slope indicated the barrier heights, which ranged between 1.1-1.4 eV. The backward diode on the other hand gave a barrier height of 1.4 eV, which was compatible with the proposed model. C-V-T measurements could also be accounted for, at least qualitatively, on the basis of the proposed back to back diode model.

The device structure of c-GaMnN was planar. Both the Ohmic and Schottky contact were in the same plane on the top surface. I-V measurements were performed over the temperature range 100-480 K. I-V-T was explained in the terms of the Schottky model. The current was limited, however, by the Poole-Frenkel type centres in the bulk which behaved as an insulator (high resistivity semiconductor). The C-V-T was satisfactorily accounted for on the basis of MIS/MOS model.

Low temperature grown films had poor material quality which made any correlation between samples difficult.

## Nomenclature

### List of abbreviations and variables

|              |   |
|--------------|---|
| $\Delta\Phi$ | The barrier lowering amount                 |
| $\Phi_b$     | The barrier height                          |
| $\beta_{PF}$ | The Poole-Frenkel constant                  |
| $\beta_S$    | The Schottky field lowering constant        |
| C-F-T        | Capacitance -frequency-temperature          |
| c-GaN        | Cubic GaN                                   |
| C-V-T        | Capacitance-voltage-temperature             |
| DMS          | Diluted magnetic semiconductors             |
| fcc          | Faces centreed cubic                        |
| FE           | Field emission                              |
| I-V-T        | Current-voltage-temperature                 |
| LEDs         | Light emitting diodes                       |
| LT           | Low-temperature                             |
| MBE          | Molecular beam epitaxy                      |
| MCD          | Magnetic circular dichroism                 |
| MOCVD        | Metal organic chemical vapor deposition     |
| n            | Ideality factor                             |
| PA-MBE       | Plasma-assisted molecular beam epitaxy      |
| P.F.         | Poole-Frenkel effect                        |
| RHEED        | Reflection high energy electron diffraction |
| SI           | Semi-insulating                             |
| SIMS         | Ion mass spectroscopy                       |
| TE           | Thermionic emission                         |
| TFE          | Thermionic field emission                   |
| TM           | Transition metal                            |
| TES          | Transmission electron microscopy            |
| UHV          | Ultra high vacuum                           |
| u.i.d.       | Unintentionally doped                       |
| ZB           | Zinc blende                                 |

**ACKNOWLEDGMENT**

I would like to express my indebtedness to Dr. Ian Harrison for all his help, guidance and patience. I owe him a special debt of gratitude for his frequent visits to Saudi Arabia (Jeddah) which contributed greatly in setting up the program for connecting computer and devices which enabled me to get the necessary measurements. His constant help and encouragement have been a major source of support and are deeply appreciated.

Special thanks are also due to Professor A.A. Ansari from King Abdulaziz University for his helpful comments and for enriching my general understanding of different theories that underlie some of the issues discussed in this thesis, and for supervising the lab aspects of my work.

I am grateful to R. Dykeman and to Laura Sun for their expeditious help and assistance. I also wish to thank Professor T. Foxon for his help in the discussion of how the samples grow. I cannot thank him enough.

Thanks are also due to King Abdulaziz University, Saudi Arabia for their financial support and for setting up a fully-integrated lab in the research facility that can be used to conduct future research studies in the field of semiconductors.

Finally, my family's assistance and support throughout this process was boundless. I would like to thank my two brothers Professor Awwad and Professor Mohammed for their moral support and constant encouragement.

## COPYRIGHT

### Note on Access to Contents

“It is a condition of use of this thesis that anyone who consults it must recognise that the copyright rests with the author and that no quotation from the thesis and no information derived from it may be published unless the source is properly acknowledged.”

## TABLE OF CONTENT

|  |     |
|--|-----|
| ABSTRACT .....   | I   |
| Nomenclature .....   | III |
| ACKNOWLEDGMENT .....   | IV  |
| COPYRIGHT .....  | V   |
| LIST OF FIGURES .....  | XI  |
| LIST OF TABLES.....  | XXI |
| CHAPTER 1 General Introduction.....                                      | 1   |
| 1.1 Introduction.....  | 1   |
| CHAPTER 2 Electrical Measurements.....                                   | 4   |
| 2.1 Introduction.....  | 4   |
| 2.2 I-V Measurements.....  | 4   |
| 2.2.1 The ideal p n junction .....                                       | 4   |
| 2.2.2 Non-ideal p n junction .....                                       | 6   |
| 2.2.3 Theory of metal-semiconductor contacts.....                        | 7   |
| 2.2.4 Deviation from Schottky theory .....                               | 9   |
| 2.2.5 Mathematical approach to the current transport processes .....     | 12  |
| 2.2.6 Thermionic field emission and field emission theory.....           | 14  |
| 2.2.7 Schottky barrier inhomogeneity model.....                          | 16  |
| 2.2.8 The temperature dependence of the ideality factor.....             | 19  |
| 2.2.9 Interpretation of “T <sub>0</sub> ” effect using Werner model..... | 20  |
| 2.3 Capacitance- Voltage measurement .....                               | 21  |
| 2.3.1 The role of traps in Capacitance-Voltage measurement .....         | 23  |
| 2.4 Admittance Spectroscopy .....  | 25  |
| 2.4.1 The principal of Admittance Spectroscopy.....                      | 26  |
| 2.4.2 The logistic equation.....   | 28  |
| 2.4.3 Analysis of the data: .....  | 28  |
| CHAPTER 3 Theoretical Background and Literature Review .....             | 30  |
| 3.1 Introduction.....  | 30  |
| 3.2 Review of Growth conditions of III-V magnetic semiconductor .....    | 32  |
| 3.3 The Ferromagnetic behaviour of the devices used in this study.....   | 34  |
| 3.4 Impact of defects on electrical properties of materials.....         | 35  |

|  |           |
|--|-----------|
| 3.5 General features of the GaN .....  | 37        |
| 3.6 Advantages of cubic structure for GaN.....   | 37        |
| 3.7 The electrical measurements on the GaN.....  | 38        |
| 3.8 The study of electrical defects in cubic GaMnN .....                                 | 41        |
| 3.8.1 The native defects of wurzite GaN .....  | 41        |
| 3.8.2 The native defects of cubic GaN .....  | 42        |
| 3.9 Studies of doped cubic GaN .....   | 43        |
| 3.10 General features of GaAs.....   | 45        |
| 3.11 General features of the (Ga, Mn)As .....  | 45        |
| 3.12 The electrical measurements on the GaAs.....  | 46        |
| 3.13 The native defects in the GaAs .....  | 47        |
| 3.14 The study of structural and electrical defects in LT-GaAs and GaMnAs .....          | 49        |
| <b>CHAPTER 4 Setup of the Equipment .....</b>  | <b>52</b> |
| 4.1 Introduction.....  | 52        |
| 4.2 The experimental setup.....  | 52        |
| 4.2.1 Sample mounting .....  | 53        |
| 4.2.2 Temperature Controller .....   | 55        |
| 4.2.3 Keithley Source measure unit (SMU) 238 .....                                       | 55        |
| 4.2.4 7200 Capacitance meter .....   | 56        |
| 4.2.5 Precision Component Analysers 6640B .....  | 56        |
| 4.2.6 LabView program.....   | 57        |
| 4.3 Verification of experimental setup.....  | 58        |
| 4.3.1 Introduction .....   | 58        |
| 4.3.2 Si diode .....   | 58        |
| 4.3.3 GaN light emitting diode.....  | 64        |
| 4.3.4 Conclusion for Si diode and LED-GaN diode.....                                     | 73        |
| <b>CHAPTER 5 Measurement Results of GaMnAs .....</b>                                     | <b>74</b> |
| 5.1 Introduction.....  | 74        |
| 5.2 Device Fabrication .....   | 75        |
| 5.3 Estimation of hole concentration .....   | 77        |
| 5.3.1 Determination of the hole concentration and Fermi level for Mn (374) Device .....  | 79        |
| 5.3.2 Determination of the hole concentration and Fermi level for Mn (375) Devices ..... | 81        |
| 5.3.3 Determination of the hole concentration and Fermi level for Mn (376) Devices ..... | 83        |
| 5.3.4 Determination of the electron concentration and Fermi level for Si-GaAs ....       | 85        |

|   |            |
|---|------------|
| 5.4 Using the Simulation program to determine the band diagram .....  | 85         |
| 5.5 Possible models to analyse the results.....                       | 87         |
| 5.6 Comparison of the samples with different Mn concentrations .....  | 94         |
| 5.7 I-V-T behaviour of Mn (374) device.....                           | 95         |
| 5.7.1 C-V-T behaviour of Mn (374) device.....                         | 107        |
| 5.7.2 C-F-T behaviour of Mn (374) .....                               | 110        |
| 5.8 (Mn375) Devices.....  | 111        |
| 5.8.1 (Mn375-1) Device .....  | 112        |
| 5.8.2 C-V measurement of Mn (375) .....                               | 118        |
| 5.8.3 C-F-T behaviour of Mn (375-1) .....                             | 119        |
| 5.9 (Mn375-2) Device .....  | 121        |
| 5.9.1 C-V measurement of Mn (375-2).....                              | 127        |
| 5.9.2 C-F-T behaviour of Mn (375-2) .....                             | 129        |
| 5.10 (Mn376-1) Device .....   | 130        |
| 5.10.1 C-V measurement of Mn (376-1).....                             | 135        |
| 5.10.2 C-F-T for Mn (376-1) .....                                     | 138        |
| 5.11 (Mn376-2) Device .....   | 139        |
| 5.11.1 C-V measurement of Mn (376-2).....                             | 144        |
| 5.11.2 C-F-T behaviour of Mn (376-2) .....                            | 145        |
| 5.12 Discussion of Results .....                                      | 146        |
| 5.12.1 I-V-T measurements on GaAs: Mn /GaAs:Si Devices .....          | 146        |
| 5.12.2 Capacitance measurements on GaAs: Mn /GaAs: Si Devices .....   | 150        |
| <b>CHAPTER 6 Measurement Results of GaMnN .....</b>                   | <b>152</b> |
| 6.1 Introduction.....   | 152        |
| 6.2 Possible models to analyse the results.....                       | 154        |
| 6.3 Comparison of the samples with different Mn concentrations .....  | 158        |
| 6.4 800 diameter device (no.2) .....                                  | 159        |
| 6.4.1 I-V Behaviour .....   | 159        |
| 6.4.2 C-V Behaviour.....  | 162        |
| 6.5 Interpretation of the I-V-T results for 800 diameter device ..... | 162        |
| 6.5.1 Forward Bias .....  | 162        |
| 6.5.1.1 Thermionic-field emission (TFE) Model.....                    | 164        |
| 6.5.1.2 Barrier Height Inhomogeneities Model.....                     | 166        |
| 6.5.2 Reverse Bias .....  | 168        |
| 6.5.2.1 Thermionic-field emission (TFE) Model.....                    | 168        |
| 6.5.2.2 Barrier Height Inhomogeneities Model:.....                    | 169        |
| 6.5.3 The Insulator GaMnN layer in both polarities: .....             | 171        |

|  |     |
|--|-----|
| 6.6 400 diameter device (no.3) .....   | 173 |
| 6.7 400 diameter device (no.4) .....   | 174 |
| 6.7.1 I-V Behaviour .....  | 174 |
| 6.7.2 C-V Behaviour.....   | 175 |
| 6.8 Interpretation of the I-V-T results for 400 diameter device (no.4) ..... | 176 |
| 6.8.1 Forward Bias .....   | 176 |
| 6.8.1.1 Barrier Height Inhomogeneities Model.....                            | 178 |
| 6.8.2 Reverse Bias .....   | 179 |
| 6.8.2.1 Barrier Height Inhomogeneities Model.....                            | 179 |
| 6.8.3 The Insulator GaMnN layer .....  | 179 |
| 6.9 200 diameter device (no.6) .....   | 181 |
| 6.9.1 I-V Behaviour .....  | 181 |
| 6.9.2 C-V Behaviour.....   | 183 |
| 6.10 Interpretation of the I-V-T results for 200 diameter device .....       | 184 |
| 6.10.1 Forward Bias .....  | 184 |
| 6.10.1.1 Barrier Height Inhomogeneities Model.....                           | 185 |
| 6.10.2 Reverse Bias: .....   | 186 |
| 6.10.3 The Insulator GaMnN layer .....                                       | 186 |
| 6.11 C-V data analysis .....   | 188 |
| 6.12 Conclusion .....  | 190 |
| 6.12.1 Model to explain I-V behaviour of GaN: Mn.....                        | 190 |
| 6.12.1.1 Forward bias .....  | 191 |
| 6.12.1.2 Reverse bias.....   | 192 |
| 6.12.2 Model to explain C-V response of GaN: Mn .....                        | 193 |
| CHAPTER 7 General Conclusions.....   | 195 |
| 7.1 Introduction.....  | 195 |
| 7.2 GaMnAs devices .....   | 195 |
| 7.3 GaMnN devices.....   | 197 |
| 7.4 General conclusion.....  | 199 |
| REFERENCES .....   | 200 |
| APPENDIX A: Equations used in Matlab Program .....                           | 209 |
| APPENDIX B: LabView flow chart for I-V measurement .....                     | 211 |
| Appendix C: LabView flow chart for C-V measurement .....                     | 212 |
| APPENDIX D: LabView flow chart for C-F measurement.....                      | 213 |

APPENDIX E: Published Paper ..... 214

## LIST OF FIGURES

|   |    |
|---|----|
| Figure 2.1 The p n Junction.....  | 5  |
| Figure 2.2 A metal-p-type semiconductor contact (a) band diagram before joining. (b) Equilibrium band diagram after joining.....  | 8  |
| Figure 2.3 Ohmic contact on an p-type semiconductor (a) Metal semiconductor contact before contact (b) metal semiconductor contact after contact at thermal equilibrium. .... | 9  |
| Figure 2.4 The potential well in the presence of an electric field [6] .....  | 10 |
| Figure 2.5 Plot of the $nkT/q$ versus $kT/q$ showing the temperature dependence of the ideality factor [24]. .....  | 19 |
| Figure 2.6 Schottky barrier on an n-type semiconductor containing deep states [35]...   | 23 |
| Figure 2.7 Schematic plot of $1/C^2$ versus $V$ for n-type material [35]. .....   | 25 |
| Figure 2.8 The curve for $C(\omega)$ as a function of logarithm of ac signal frequency .....  | 28 |
| Figure 3.1 Schematic diagram of MBE machine .....   | 32 |
| Figure 4.1 The setup of the equipment for this study .....  | 53 |
| Figure 4.2 Closed Cycle refrigerator (CCR) for the system used in this study.....   | 53 |
| Figure 4.3 Closed Cycle Refrigerator Systems from Janis manual [108].....   | 54 |
| Figure 4.4 The arrangement of the GPIB connection.....  | 57 |
| Figure 4.5 The experimental linear (a) and semi-log (b) in forward and reverse I-V characteristics of the Si diode at different temperatures in the range 420-50K .....       | 59 |
| Figure 4.6 Ideality factor versus temperatures for Si diode .....   | 60 |
| Figure 4.7 Plot of the activation energy as a function of the inverse temperature of forward bias for Si diode.....   | 61 |
| Figure 4.8 $\ln(I)$ versus $\ln(V)$ at different temperatures (a) and at R.T. (b) .....   | 61 |
| Figure 4.9 The plot of $1/C^3$ versus $V_R$ at various temperatures.....  | 63 |
| Figure 4.10 The plot between $1/C^2$ and $1/C^3$ as a function of reverse bias voltage .....  | 63 |
| Figure 4.11 Capacitance –frequency curves temperatures between 300 and 460 K for Si diode.....  | 64 |
| Figure 4.12 Arrhenius plot to get activation energy by admittance spectroscopy of Si diode.....   | 64 |

|  |    |
|--|----|
| Figure 4.13 The structure of the light emitting diode similar to the Nakamura's device [113].....  | 65 |
| Figure 4.14 The experimental semi-log forward and reverse I-V characteristics of the GaN blue LED at different temperatures in the range 100-440K in linear and logarithm scale..... | 66 |
| Figure 4.15 The ideality factor (red) and series resistance (blue) versus temperature for GaN-LED .....  | 67 |
| Figure 4.16 I-V characteristic of the GaN-LED with the series resistance $R_S$ (black dots) and the effect of series resistance removed (red dots) at room temperature .....         | 68 |
| Figure 4.17 The activation energy determination at different forward biases .....  | 69 |
| Figure 4.18 (a) The capacitance versus voltage in both forward and reverse biases at different temperatures and (b) $1/C^2$ versus $V_R$ measured for GaN-LED .....                  | 69 |
| Figure 4.19 The plot of $1/C^2$ versus $V_R$ at room temperature .....   | 70 |
| Figure 4.20 Capacitance –frequency curves temperatures between 100 and 480 K for GaN-LED .....   | 71 |
| Figure 4.21 Arrhenius plot to get activation energy by admittance spectroscopy of the GaN (LED) device .....   | 71 |
| Figure 4.22 The proposal model given in [113] .....  | 72 |
| Figure 5.1 Schematic drawing of the device geometry of the GaMnAs film .....   | 75 |
| Figure 5.2 Schematic diagram of properties of GaMnAs films in terms of substrate temperature and Mn concentration provide a rough guide [43] .....                                   | 76 |
| Figure 5.3 The calculated hole concentration as a function of temperature .....  | 79 |
| Figure 5.4 The Fermi level position as a function of temperature, presenting the degeneracy region after 200 K. Zero energy is considered to be the top of the valence band.....     | 80 |
| Figure 5.5 The hole concentration as function of the inverse temperature.....  | 80 |
| Figure 5.6 The energy band diagram at room temperature for GaMnAs Mn (374) diode .....   | 81 |
| Figure 5.7 Hole concentration versus T of Mn (375-1) device .....  | 82 |
| Figure 5.8 The Fermi level position as a function of temperature, presenting the degeneracy region after 300 K. Zero energy is considered to be the top of the valence band.....     | 82 |
| Figure 5.9 The energy band diagram at room temperature for GaMnAs Mn (375) diode .....   | 83 |

|   |    |
|---|----|
| Figure 5.10 The calculated hole concentration as a function of temperature for Mn (376-1) device .....  | 83 |
| Figure 5.11 The Fermi level position as a function of temperature, which is above the valence band .....  | 84 |
| Figure 5.12 The energy band diagram at room temperature for GaMnAs Mn (376) diode .....   | 84 |
| Figure 5.13 The Fermi level position as a function of temperature, which is inside the conduction band for the Si-GaAs. Zero energy is considered to be the bottom of the conduction band.....              | 85 |
| Figure 5.14 The band diagram given by the simulation program for Mn (374) device at RT .....  | 86 |
| Figure 5.15 The band diagram given by the simulation program for Mn (374) device at 77 K.....   | 86 |
| Figure 5.16 The depletion layer width between p and n side Mn (374) device using the simulation program [125].....  | 86 |
| Figure 5.17 Schottky diode model.....   | 88 |
| Figure 5.18 The band diagram for n-type Schottky diode .....  | 89 |
| Figure 5.19 Insulator model .....   | 89 |
| Figure 5.20 The band diagram for the insulator model which shows the $E_F$ in the middle .....  | 90 |
| Figure 5.21 Simple p n junction model.....  | 90 |
| Figure 5.22 The band diagram for simple p n junction model .....  | 91 |
| Figure 5.23 The back-to-back model.....   | 91 |
| Figure 5.24 The band diagram for back-to-back junction (degenerate GaAs: Si) .....  | 92 |
| Figure 5.25 The band diagram for back-to-back junction (non-degenerate GaAs: Si) ..   | 92 |
| Figure 5.26 Comparison of the samples with different Mn concentration at 300 K .....  | 94 |
| Figure 5.27 Current-voltage curve for GaMnAs (Mn374) device.....  | 95 |
| Figure 5.28 The applied forward bias against current (a) at room temperature and (b) at 200 K. The graph shows the fitting applied to equation (5.6) (red lines) for Mn (374) device. ....                  | 96 |
| Figure 5.29 The series resistance versus temperatures for GaMnAs sample Mn (374) device in both polarities with small errors in case of reverse bias compared to the forward bias in low temperatures ..... | 97 |

|   |     |
|---|-----|
| Figure 5.30 (a) The plot $\ln(I_S/T^3)$ versus $10^3/T$ and (b) The plot $\ln(I_S/T^3)$ versus $10^3/nT$ with correlation coefficient $R=0.98756$ for Mn (374) device in the forward bias .....   | 98  |
| Figure 5.31 Natural log of $\ln(I_S/T^2)$ versus $10^3/T$ for Mn (374) device in the forward bias .....   | 99  |
| Figure 5.32 (a) The temperature dependence of the barrier height for GaMnAs as estimated from equation (2.14) and (b) The modified Richardson plot ( $R= 0.99631$ ) for sample Mn (374).....  | 99  |
| Figure 5.33 The modified Richardson plot in case of reverse bias ( $R= 0.996624$ ).....   | 100 |
| Figure 5.34 Ideality factor versus temperatures for GaMnAs sample Mn (374) device in forward bias .....   | 101 |
| Figure 5.35 The Arrhenius plots of GaMnAs film (Mn374-1) sample in reverse bias   | 101 |
| Figure 5.36 Reverse characteristic in the form of $\ln(I) - \ln(V)$ for Mn (374) device at different temperatures (a) before $R_S$ corrections and (b) after $R_S$ corrections .....  | 102 |
| Figure 5.37 Semi-logarithmic plot of the I-V characteristic versus the applied forward bias at room temperature of the sample (374) and showing the data before the $R_S$ correction (black line) and after the $R_S$ correction (red line) ..... | 103 |
| Figure 5.38 The estimation of the slope of the $\ln(I)-\ln(V)$ plot before and after the $R_S$ correction at 320 K of the sample (374) .....  | 104 |
| Figure 5.39 Reverse I-V characteristic in the form of $\ln(I) - V^{1/2}$ for Mn (374) device at different temperatures (a) before $R_S$ corrections and (b) after $R_S$ corrections .....   | 105 |
| Figure 5.40 The proposed model for back-to-back diode in case of forward bias .....   | 106 |
| Figure 5.41 Experimental values of $E_0$ as a function of temperature for Mn (374) device .....   | 107 |
| Figure 5.42 The capacitance versus bias voltage for GaMnAs sample Mn (374) device .....   | 108 |
| Figure 5.43 Plot of the $1/C^2$ versus reverse voltage for GaMnAs sample Mn (374) device .....  | 109 |
| Figure 5.44 Plot $1/C^2$ versus reverse bias voltage for GaMnAs film Mn (374) device, showing the experimental data as well as the extrapolated line meeting the x-axis.....  | 110 |
| Figure 5.45 The capacitance versus the frequency voltage for GaMnAs sample Mn (374).....  | 111 |
| Figure 5.46 The Arrhenius plot for Mn (374) .....   | 111 |
| Figure 5.47 Current-voltage curve for GaMnAs (Mn375-1) device .....   | 112 |

|  |     |
|--|-----|
| Figure 5.48 The modified Richardson plot ( $\ln(I_S/T^3)$ ) versus $10^3/nT$ with $E_a = 0.982 \pm 0.1$ eV ( $R=0.96627$ ).....  | 113 |
| Figure 5.49 Ideality factor ( $n$ ) versus temperatures in forward bias for (Mn375-1) device .....   | 113 |
| Figure 5.50 (a) Natural log of $\ln(I_S/T^2)$ versus $10^3/T$ for Mn (375-1) device in the forward bias and (b) The modified Richardson plot ( $\ln(I_S/T^2)$ ) versus $10^3/nT$ ( $R=0.94188$ ) .....                               | 114 |
| Figure 5.51 (a) Natural log of $\ln(I_S/T^2)$ versus $10^3/T$ and (b) The modified Richardson plot ( $\ln(I_S/T^2)$ ) versus $10^3/nT$ with $E_a = 0.85 \pm 0.05$ eV ( $R=0.99056$ ) for Mn (375-1) device in the reverse bias ..... | 114 |
| Figure 5.52 The temperature dependence of the barrier height for GaMnAs (sample Mn (375-1) in the temperature range 400-15 K.....  | 115 |
| Figure 5.53 The plot of the ideality factor versus $10^3/T$ (a) in forward bias (b) reverse bias for (Mn375-1) device.....   | 115 |
| Figure 5.54 Reverse I-V characteristic in the form of $\ln(I) - V^{1/2}$ for Mn (375-1) device at different temperatures (a) before $R_S$ corrections and (b) after $R_S$ corrections .....  | 116 |
| Figure 5.55 The capacitance versus bias voltage for GaMnAs sample Mn (375-1) ....  | 118 |
| Figure 5.56 $1/C^2$ versus reverse voltage for GaMnAs sample Mn (375-1) device .....   | 118 |
| Figure 5.57 Plot $1/C^2$ versus reverse bias voltage at room temperature for GaMnAs film Mn (375-1) device .....   | 119 |
| Figure 5.58 The capacitance versus the frequency voltage for GaMnAs sample Mn (375-1).....   | 120 |
| Figure 5.59 The Arrhenius plot for Mn (375-1).....   | 120 |
| Figure 5.60 Current-voltage curve for GaMnAs (Mn375-2) device .....  | 121 |
| Figure 5.61 (a) The activation energy which gives $0.85 \pm 0.05$ eV ( $R=0.99951$ ) in the forward bias and (b) The activation energy gives $0.8 \pm 0.03$ eV ( $R=0.99548$ ) in the reverse bias .....                             | 122 |
| Figure 5.62 (a) The plot $\ln(I_S/T^2)$ versus $10^3/T$ and (b) The plot $\ln(I_S/T^2)$ versus $10^3/nT$ with $E_a = 0.93 \pm 0.01$ eV ( $R=0.99943$ ) for Mn (375-2) device in the forward bias .....                               | 122 |
| Figure 5.63 (a) The plot $\ln(I_S/T^2)$ versus $10^3/T$ and (b) The plot $\ln(I_S/T^2)$ versus $10^3/nT$ with $E_a = 1 \pm 0.02$ eV ( $R=0.99888$ ) for Mn (375-2) device in the reverse bias .....                                  | 123 |
| Figure 5.64 The temperature dependence of the barrier height in forward bias for GaMnAs sample Mn (375-2) in the temperature range 400-15 K .....  | 123 |
| Figure 5.65 Ideality factor versus temperatures for GaMnAs sample (Mn375-2) device .....   | 124 |

|  |     |
|--|-----|
| Figure 5.66 The plot of the ideality factor versus $10^3/T$ in (a) forward and (b) reverse bias from temperature range 400-100 K for (Mn375-2) device .....  | 124 |
| Figure 5.67 Reverse I-V characteristic in the form of $\ln(I) - V^{1/2}$ for Mn (375-2) device at different temperatures (a) before $R_S$ corrections and (b) after $R_S$ corrections.....   | 125 |
| Figure 5.68 The experimental values of $E_0$ as a function of temperature for Mn (375-2) device .....  | 126 |
| Figure 5.69 Theoretical temperature dependence of ideality factor obtained by the TFE model for tunnelling characteristic energy $E_{00}=0.06$ eV (red line), and the experimental determined ideality factor (black line) as a function of temperature in the reverse bias. It is found that a value of 60 meV for $E_{00}$ gives a good fit above 240 K..... | 126 |
| Figure 5.70 The capacitance versus bias voltage for GaMnAs sample Mn (375-2) ....  | 127 |
| Figure 5.71 The $1/C^2$ versus reverse voltage for GaMnAs sample Mn (375-2) device   | 127 |
| Figure 5.72 Plot of the $1/C^2$ versus reverse bias voltage for GaMnAs film Mn (375-2) device .....  | 128 |
| Figure 5.73 The capacitance versus the frequency voltage for GaMnAs sample Mn (375-2).....   | 129 |
| Figure 5.74 The Arrhenius plot for Mn (375-2).....   | 129 |
| Figure 5.75 Current-voltage curve for GaMnAs (Mn376-1) device .....  | 130 |
| Figure 5.76 The activation in the forward bias gives $1.25\pm 0.03$ eV (with $R=0.99764$ )   | 131 |
| Figure 5.77 (a) The plot $\ln(I_S/T^2)$ versus $10^3/T$ and (b) The plot $\ln(I_S/T^2)$ versus $10^3/nT$ (with $R=0.99883$ ) for Mn (376-1) device in the forward bias .....   | 132 |
| Figure 5.78 The temperature dependence of the barrier height in forward bias for GaMnAs (sample Mn (376-1) in the temperature range 400-15 K .....   | 132 |
| Figure 5.79 Ideality factor versus temperatures for sample Mn (376-1) device .....   | 133 |
| Figure 5.80 The plot of the ideality factor versus $10^3/T$ in forward bias from temperature range 400-15 K in Mn (376-1) device .....   | 133 |
| Figure 5.81 Reverse characteristic in the form of $\ln(I) - V^{1/2}$ for Mn (376-1) device at different temperatures (a) before $R_S$ corrections and (b) after $R_S$ corrections .....  | 134 |
| Figure 5.82 The capacitance versus bias voltage for GaMnAs sample Mn (376-1) ....  | 135 |
| Figure 5.83 The $1/C^2$ versus reverse voltage for GaMnAs sample Mn (376-1) device   | 136 |
| Figure 5.84 Plot $1/C^2$ versus reverse bias voltage for GaMnAs film Mn (376-1) device at 360 K.....   | 137 |

|  |     |
|--|-----|
| Figure 5.85 The capacitance versus the frequency voltage for GaMnAs sample Mn (376-1).....   | 138 |
| Figure 5.86 The Arrhenius plot for Mn (376-1).....   | 138 |
| Figure 5.87 Current-voltage curve for GaMnAs (Mn376-2) device .....  | 139 |
| Figure 5.88 (a)The activation energy estimation using $\ln(I_S/T^3)$ versus $10/T^3$ and (b) The modified activation energy plot $\ln(I_S/T^3)$ versus $10/T^3$ method for Mn (376-2) both in the forward bias ..... | 140 |
| Figure 5.89 (a) The activation energy estimation using $\ln(I_S/T^2)$ versus $10/T^3$ and (b) The modified activation energy plot method for Mn (376-2) in forward bias .....  | 140 |
| Figure 5.90 The temperature dependence of the barrier height in forward bias for GaMnAs (sample Mn (376-2) in the temperature range 400-15 K.....  | 141 |
| Figure 5.91 Ideality factor versus temperatures for Mn (376-2) device .....  | 141 |
| Figure 5.92 The plot of the ideality factor versus $10^3/T$ in forward bias from temperature range 400-15 K for Mn (376-2) device.....   | 142 |
| Figure 5.93 Reverse characteristic in the form of $\ln(I) - V^{1/2}$ for Mn (376-2) device at different temperatures (a) before $R_S$ corrections and (b) after $R_S$ corrections .....                              | 143 |
| Figure 5.94 The capacitance versus bias voltage for GaMnAs sample Mn (376-2) ....  | 144 |
| Figure 5.95 Plot $1/C^2$ versus reverse bias voltage for GaMnAs film Mn (376-2) device .....   | 145 |
| Figure 5.96 The capacitance versus the frequency voltage for GaMnAs sample Mn (376-2).....   | 145 |
| Figure 5.97 The Arrhenius plot for Mn (376-2).....   | 146 |
| Figure 5.98 The proposed model for GaMnAs devices.....   | 148 |
| Figure 6.1 Schematic drawing of the device geometry of the GAMnN film.....   | 152 |
| Figure 6.2 Bright field cross section TEM image of Pd/Au 25/160 nm annealed at 600 °C† Courtesy of Dr. Michael Fay, School of Physics and Astronomy, University of Nottingham [130].....                             | 153 |
| Figure 6.3 Schottky diode model for p-type GaMnN.....  | 154 |
| Figure 6.4 The band diagram for Schottky diode with p-type GaN: Mn.....  | 155 |
| Figure 6.5 Schottky diode model for n-type GaMnN.....  | 156 |
| Figure 6.6 The band diagram for Schottky diode with n-type GaN: Mn.....  | 156 |
| Figure 6.7 Insulator model for GaN: Mn.....  | 157 |

|   |     |
|---|-----|
| Figure 6.8 The band diagram for the insulator model, which shows the $E_F$ in the middle<br>.....   | 157 |
| Figure 6.9 I-V comparison of different areas of GaMnN sample at 300 K .....   | 158 |
| Figure 6.10 I-V characteristic of GaMnN device (2).....   | 159 |
| Figure 6.11 The applied forward bias against current at (a) 200 K and (b) at room<br>temperature. The graph shows the fitting applied to equation (2.15) (red lines) for 800<br>device .....  | 160 |
| Figure 6.12 The series resistance versus temperatures for GaMnN sample (800 $\mu$ m<br>device) in both polarities .....   | 161 |
| Figure 6.13 (a) Ideality factor as a function of temperature in case of forward and (b) In<br>reverse biases for GaMnN material (800 device) .....  | 161 |
| Figure 6.14 The capacitance versus voltage for device 800. The labels assume a MIS<br>kind of structure.....  | 162 |
| Figure 6.15 (a) The temperature dependence of the barrier height and (b) The plot of $\ln$<br>( $I_S/T^2$ ) versus $10^3/T$ in case of forward bias which gives barrier height $\Phi_b = 0.37 \pm 0.03$<br>eV. The data for both is taken in the temperature range 300 K to 480 K.....                                | 163 |
| Figure 6.16 the plot $\ln(I_S/T^2)$ versus $10^3/nT$ .....  | 164 |
| Figure 6.17 Experimental values of $E_0$ as a function of temperature for 800 $\mu$ m diameter<br>device .....  | 165 |
| Figure 6.18 The saturation current versus $1/E_0$ as given by equation (2.23).....  | 165 |
| Figure 6.19 (a) The forward barrier height and (b) Ideality factor versus $q / (2kT)$ plot of<br>the GaMnN Schottky diode according to the Gaussian distribution model of the barrier<br>heights. The modified Richardson plot as given by this model can be obtained by<br>combining equation (2.14) and (2.28)..... | 166 |
| Figure 6.20 Modified Richardson plot as given by equation (2.34) for the GaMnN<br>Schottky diode which gives barrier height $\Phi_b = 0.38 \pm 0.03$ eV in forward bias .....   | 167 |
| Figure 6.21 Theoretical temperature dependence of ideality factor obtained by the TFE<br>model for tunnelling characteristic energy $E_{00} = 0.07$ eV (red line), and the experimental<br>determined ideality factor (black line) as a function of temperature in the reverse bias<br>.....                          | 169 |
| Figure 6.22 (a) The plot of $\ln(I_S/T^2)$ versus $10^3/T$ in case of reverse bias and (b) Zero-<br>bias reverse apparent barrier height versus $q / (2kT)$ plot of the GaMnN Schottky diode<br>according to the Gaussian distribution model of the barrier heights .....   | 170 |
| Figure 6.23 The plot of $\ln[(I_S/T^2)] - q \sigma_{so}^2 / 2k^2 T^2$ versus $10^3/T$ in case of reverse bias<br>which gives barrier height $\Phi_b = 0.2 \pm 0.03$ eV. The data is taken in the temperature range<br>300 K to 480 K .....  | 170 |

|  |     |
|--|-----|
| Figure 6.24 (a) Variation of $\ln(I/V)$ versus $V^{1/2}$ and (b) $\ln(I)$ versus $V^{1/2}$ in high forward voltage range at various temperatures with good correlation coefficient. In both cases, these two plots after the $R_s$ correction. ....  | 171 |
| Figure 6.25 I-V characteristic of GaMnN device (3).....  | 173 |
| Figure 6.26 The Mn layer short circuits the two contacts.....  | 174 |
| Figure 6.27 I-V characteristic of GaMnN for 400 device (no.4).....   | 174 |
| Figure 6.28 The temperature dependence of the barrier height and ideality factor of 400 device .....   | 175 |
| Figure 6.29 The capacitance verses voltage for device 400 (no.4) .....   | 176 |
| Figure 6.30 (a) The temperature dependence of the barrier height and (b) The plot of $\ln(I_s/T^2)$ versus $10^3/T$ in case of forward bias for 400 (no.4).....  | 177 |
| Figure 6.31 The plot of $\ln(I_s/T^2)$ versus $10^3/T$ the barrier height yields a value of $1.61 \pm 0.098$ eV in case of forward bias for (400d no.4).....   | 177 |
| Figure 6.32 (a) Zero-bias forward apparent barrier height versus $q / (2kT)$ plot with a value of $1 \pm 0.03$ eV and standard deviation of $0.17 \pm 0.01$ eV and (b) Plot of $\ln[(I_s/T^2)] - q \sigma_{so}^2 / 2k^2T^2$ versus $10^3/T$ which gives barrier height $\Phi_b = 0.96 \pm 0.05$ eV in case of forward bias for 400 (no.4) device.....                          | 178 |
| Figure 6.33 (a) Zero-bias reverse apparent barrier height versus $q / (2kT)$ plot with a value of $0.93 \pm 0.035$ eV and standard deviation ( $\sigma_{so}$ ) of $0.173 \pm 0.013$ eV and (b) Plot of $\ln[(I_s/T^2)] - q \sigma_{so}^2 / 2k^2T^2$ versus $10^3/T$ in case of reverse bias which gives barrier height $\Phi_b = 0.98 \pm 0.048$ eV for 400 device (no.4)..... | 179 |
| Figure 6.34 Shows (a) plot of $\ln(I/V)$ versus $V^{1/2}$ in high reverse voltage range and (b) $\ln(I)$ versus $V^{1/2}$ at various temperatures. A straight line is an indication of Poole-Frenkel emission in (a) and the Schottky effect in (b).....   | 180 |
| Figure 6.35 I-V characteristic of GaMnN device 200 .....   | 181 |
| Figure 6.36 Variation of the ideality factor as a function of the temperature .....  | 182 |
| Figure 6.37 Energy band profile of the proposed model for the p-GaMnN; (a) schematic diagram for the depletion region (b) under applying “forward bias” on the semiconductor and (c) under applying “reverse bias” on the semiconductor .....  | 183 |
| Figure 6.38 The capacitance verses voltage for 200 device.....   | 184 |
| Figure 6.39 The activation energy plot: (a) Richardson plot $\ln(I_s/T^2)$ and (b) Modified Richardson plot $\ln(I_s/nT^2)$ in forward bias for 200 devices .....  | 184 |
| Figure 6.40 (a) Zero-bias forward apparent barrier height versus $q / (2kT)$ plot with a value of $0.75 \pm 0.016$ and standard deviation ( $\sigma_{so}$ ) of $0.16 \pm 0.0064$ eV and (b) Plot of $\ln[(I_s/T^2)] - q \sigma_{so}^2 / 2k^2T^2$ versus $10^3/T$ which gives barrier height of the value $1.06 \pm 0.067$ eV in case of the forward bias .....                 | 185 |

- Figure 6.41 (a) Zero-bias reverse apparent barrier height versus  $q / (2kT)$  plot gives a value of  $0.66 \pm 0.026$  eV and standard deviation ( $\sigma_{s0}$ ) of  $0.15 \pm 0.012$  eV and (b) The barrier height  $\Phi_b = 0.79 \pm 0.067$  eV as obtained from equation (2.34) in case of reverse bias or 200 device ..... 186
- Figure 6.42 (a) Variation of  $\ln(I/V)$  versus  $V^{1/2}$  and (b)  $\ln(I)$  versus  $V^{1/2}$  in high forward voltage range after  $R_s$  correction at various temperatures..... 187
- Figure 6.43 The explanation of the behaviour of GaMnN samples on the basis of MOS capacitor under (a) forward bias and (b) reverse bias..... 189
- Figure 6.44 The energy band diagram of the metal- semiconductor in case of existing interfaces state under (a) in accumulation, and (b) at mid- gap [7]..... 189
- Figure 6.45 The P-F centres in the compensated layer below the Schottky contact .... 193
- Figure 6.46 The lowering of the barrier height due to high field for a P-F centre ..... 193

## LIST OF TABLES

|   |     |
|---|-----|
| Table 3.1 The atomic percent, doping concentration, $T_C$ and the condition of GaMnAs samples.....  | 35  |
| Table 3.2 Type of defects and their effect on electrical properties of semiconductors ..  | 37  |
| Table 3.3 Different device parameters of Schottky contact to hexagonal GaN as presented by different workers.....   | 41  |
| Table 3.4 Native defects in GaN .....   | 41  |
| Table 3.5 Formation energies for point defects in zinc blende GaN .....   | 43  |
| Table 3.6 Results of some workers for Schottky contact to GaAs.....   | 47  |
| Table 3.7 The formation energy and the ionization energy of different defects given in [94].....  | 48  |
| Table 4.1 Some of the parameters estimated from I-V data shown in Figure 4.5.....   | 59  |
| Table 4.2 The slope between $\ln(I)$ versus $\ln(V)$ in Si diode .....  | 62  |
| Table 5.1 Doping levels of samples.....   | 76  |
| Table 5.2 The depletion width sizes and the barrier height at RT (300 K) as calculated from the simulation program for all devices [125].....                                       | 87  |
| Table 5.3 The ionized impurities atoms concentration, depletion layer on the n and p-side and the barrier height as calculated from the simulation program for sample Mn (374)..... | 87  |
| Table 5.4 Some parameters calculated for Mn (374) device when in forward bias .....   | 96  |
| Table 5.5 The slope between $\ln I$ versus $\ln V$ after $R_S$ corrections in both polarities ..  | 104 |
| Table 5.6 The slope between $\ln I$ versus $V^{1/2}$ plot after $R_S$ corrections in both polarities .....  | 105 |
| Table 5.7 The doping concentration and the corresponding $E_{00}$ value estimated from equation (2.22).....   | 106 |
| Table 5.8 The slope between $\ln I$ versus $V^{1/2}$ plot after $R_S$ corrections in both polarities .....  | 117 |
| Table 5.9 The slope between $\ln I$ versus $V^{1/2}$ plot after $R_S$ corrections in both polarities .....  | 125 |
| Table 5.10 The slope between $\ln I$ versus $V^{1/2}$ plot after $R_S$ corrections in both polarities .....   | 134 |

|   |     |
|---|-----|
| Table 5.11 The doping concentration as obtained from $1/C^2$ versus $V$ and the intercept of the x-axis of this plot .....  | 137 |
| Table 5.12 The slope between $\ln I$ versus $V^{1/2}$ plot after $R_s$ corrections in both polarities .....   | 143 |
| Table 5.13 The doping concentration as obtained from $1/C^2$ versus $V$ .....   | 144 |
| Table 5.14 The measured experimental values of the barrier height using $\ln(I_s/T^3) - 10^3/nT$ plot for pn junction analysis and $\ln(I_s/T^2) - 10^3/nT$ plot for Schottky analysis (except the last device analysed by additional method which is $\ln(I_s/T^3) - 10^3/T$ for p n junction and $\ln(I_s/T^2) - 10^3/T$ for Schottky)..... | 147 |
| Table 6.1 Some parameters obtained experimentally from the forward I-V characteristic of the GaMnN (800 device) Schottky diode at some selected temperatures .....  | 160 |
| Table 6.2 The parameters used to apply the modified Richardson plot in case of the forward bias .....   | 167 |
| Table 6.3 Coefficient of barrier lowering for 800 device .....  | 172 |
| Table 6.4 The estimated dielectric constant $\epsilon_s$ from both plots.....   | 173 |
| Table 6.5 Coefficient of barrier lowering for 400 device (no.4).....  | 180 |
| Table 6.6 The estimated dielectric constant $\epsilon_s$ from both plots.....   | 181 |
| Table 6.7 Coefficient of barrier lowering for 200 devices.....  | 187 |
| Table 6.8: The estimated dielectric constant $\epsilon_s$ from both plots.....  | 188 |
| Table 6.9 The size, barrier height and the standard deviation of the devices under study .....  | 192 |

## CHAPTER 1 General Introduction

### *1.1 Introduction*

In this thesis, the electrical characteristics of two diluted magnetic semiconductors (GaMnAs and GaMnN) are reported. Two III-V diluted magnetic semiconductor materials GaMnN and GaMnAs have been studied. Much attention has been given to the III–V diluted magnetic semiconductors (DMS) because it is a promising candidate for spintronic materials. However, above the Curie temperature ( $T_C$ ), the material no longer exhibits ferromagnetic order. All the commercial applications require the Curie temperature to be above room temperature. Therefore, further study is needed to improve the understanding of the nature of the ferromagnetism. The literature has paid particular attention to GaMnAs because of two factors: firstly, GaMnAs has high Curie temperature of up 173 K and secondly the similarity of GaMnAs to the GaAs which are used in a wide variety of semiconductor applications. Corresponding attention is currently being given to the GaMnN due to the theoretical model derived by Dietl et al. [1] which predicts a  $T_C$  higher than room temperature.

In order to have a ferromagnetic state, holes are required to couple the magnetic moment of the magnetic dopants [2]. In 1996, Ohno et al. [3] succeeded in fabricating a ferromagnetic p-type Mn doped GaAs. Later, Edmonds et al. [4] detected ferromagnetic behaviour in their p-type cubic GaMnN film fabricated by plasma assisted molecular beam epitaxy (PAMBE).

Zaja et al. [5] has studied the magnetic properties of Mn doped GaN and concluded that the magnetic properties of GaMnN are similar to those of Mn doped GaAs. Crystalline structures of Mn doped GaN films have been analysed by x-ray diffraction technique. They have found the presence of  $Mn_3N_2$  phase- which according

to them- is a common phenomenon in III–V DMS which includes GaMnAs. Electrical properties of the GaMnN and GaMnAs are yet to be studied in details.

The objectives of this thesis are to study the I-V-T, C-V-T and C-F-T behaviour of both GaMnN and GaMnAs.

The thesis is divided into three sections. The first three chapters include the theories used as the basis of the analysis for the data, the theoretical background, and the setup of the equipment used in the study, respectively. The second section deals with the results of the analyses of GaMnAs. The last part attends to the electrical properties of the GaMnN.

A review of the theoretical background is given in chapter two. Both Schottky and p-n junctions are discussed. The experimental data has shown that the samples do not follow any set pattern. Therefore, attempts have been made to explain the behaviour of each sample in light of the existing models and different explanations are used to explain the data for different samples. The response of every sample has been interpreted separately based on the data and the proposed models. It seems that not one model explains the response of all the samples and the justification has been provided for separate explanations.

Chapter three, a review of the theoretical background, is related to the diluted magnetic semiconductor (DMS) material. The growth conditions of III–V magnetic semiconductors are investigated. The electrical defects in both GaN and GaAs are discussed in detailed. Also, the recent developments in fabrication of GaMnN and GaMnAs materials and the difficulties facing many groups are discussed.

Chapter four presents the setup of the equipment. The setup was tested on a commercially available Si and GaN-LED diodes, the results obtained were consistent with those reported by other workers, and this was taken to be a proof that the measurement setup was operating properly.

The results of the temperature dependence of I-V-T, C-V-T and C-F-T measurements on the GaMnAs are presented in chapter five. This data is analysed and the various parameters are extracted in order to explain the behaviour of this material.

Chapter six, deals with the electrical characteristic of GaMnN samples for which the same measurements were made as the GaMnAs samples in the previous chapter.

In chapters 5 and 6, the electrical response of the GaMnAs and GaMnN materials has been presented and attempts have been made to explain the behaviour based on a model derived from the device structure.

Chapter seven discusses the general conclusions for both materials under study and outlines the similarities and differences.

## CHAPTER 2 Electrical Measurements

### *2.1 Introduction*

In this chapter, the theory of the p n junction and metal-semiconductor contact (Schottky) diodes are introduced. Also, the deviation of the current- voltage-temperature characteristics from ideal is given because they are used to study both diodes. The capacitance-voltage measurement will be discussed in terms of the presence of deep states inside of the depletion region. In addition, admittance spectroscopy technique has been addressed to gain information about the device parameters. These techniques are presented in this chapter in order to investigate the behaviour of deep impurities in semiconductors.

### *2.2 I-V Measurements*

#### **2.2.1 The ideal p n junction**

A p n junction is formed by connecting two different materials (p to n semiconductor) as shown in Figure 2.1. When the two materials are joined together, the excess of electrons in the n-type side diffuses into the p-type side and excess of holes in the p-type region diffuses into the n-type side. This diffusion effect produces a depletion of carriers at the interface which is known as depletion region. The resulting uncompensated charge at both sides of the junction caused by the fixed charged acceptors and donors atoms gives rise to an internal electric field. This electric field, in turn, generates a drift current opposite to the diffusion current until the Fermi energy is the same throughout the joined materials. At which point, equilibrium is achieved and the diffusion current and the drift current are equal but in opposite directions.

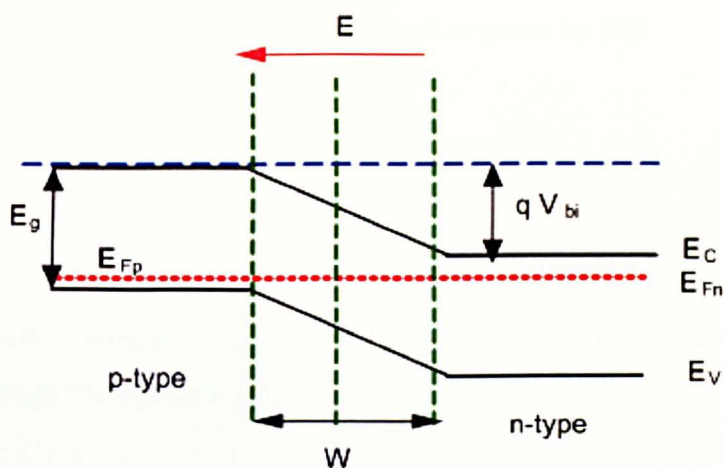


Figure 2.1 The p n Junction

The potential drop across the junction is known as built-in voltage. It is given by the difference between the Fermi levels of the p and n type material and so it will depend on doping concentration on either side of the junction. In the abrupt junction model the field outside of the depletion region is zero and so the diode current can be obtained by calculating the diffusion current of the minority carriers on either side of the junction. The concentration of the minority carriers at the depletion region edge is strongly affected by the variations in the potential barrier between the two sides of the junction.

The applied external bias adds (reverse bias) or subtracts (forward bias) from the built in field and consequently the depletion region width also changes. When the p n junction is forward biased, both the potential barrier and the depletion width decrease. The lower barrier results in an increase in the transport of majority carriers across the junction, thus enhancing the minority carrier concentration at the edge of the depletion region and the diode current. In reverse bias, the external potential bias increases both the depletion width and the barrier height. Consequently, the transport of carriers crossing the depletion width reduces. The concentration of minority carriers at the edges of the depletion region will decrease below the equilibrium value and a small reverse bias current will flow. This current will saturate when the approximate concentration of the minority carriers is equal to zero at the depletion edge.

Mathematically the ideal I-V characteristic is given by [6]:

$$I = I_S \left[ \exp\left(\frac{qV}{kT}\right) - 1 \right] \quad (2.1)$$

where the saturation current  $I_S$  is related to the acceptors and donors concentration respectively through the equation [6]:

$$I_S = qA \left[ \frac{D_n n_i^2}{L_n N_a} + \frac{D_p n_i^2}{L_p N_d} \right] \quad (2.2)$$

where  $D_n$  and  $D_p$  are the hole and electron diffusion coefficients respectively,  $n_i$  the intrinsic carrier concentration and  $L_n$  and  $L_p$  are the hole and electron diffusion length respectively. The saturation current  $I_S$  can also be expressed as:

$$I_S = AA^* T^3 \exp\left(\frac{-E_g}{kT}\right) \quad (2.3)$$

where  $A$  is the area of the p n junction,  $A^{**}$  is the Richardson constant,  $E_g$  is the band gap of the semiconductor,  $k$  is the Boltzmann constant and  $T$  is the absolute temperature.

### 2.2.2 Non-ideal p n junction

Several affects perturb the current flowing through a diode from the ideal case presented in the previous section. Thus we have recombination in the depletion region, high injection and series resistance.

Defects with the crystal structure will aid the recombination of electrons and holes throughout the diode. Outside the depletion region, these defects change the minority carrier lifetime and consequently are not taken into account by the simple theory presented in the previous section. However, the presence of these defects within the depletion region was neglected in the theory. The recombination current is taken

into account by including an additional term called the recombination current. This current is dominant at low bias levels and can be neglected at higher bias levels [7].

When the forward bias is applied to the p n junction, the barrier is reduced which permits more carriers to diffuse across the junction. The simple theory assumes the increase in minority carrier concentration does not affect the majority carrier concentration. However, as the forward bias increases the minority carrier concentration at the edge of the depletion region increases and it will eventually become comparable to the majority carrier concentration. Space charge neutrality means the majority carrier concentration will now increase and add an additional diffusion current term but in the opposite direction to the normal minority carrier diffusion current, thereby reducing in the diode current from that predicted by equation (2.1). In this region the current takes the form,  $I \sim \exp(qV/2kT)$  [8].

The effect of the series resistance  $R_s$  is observable in the forward bias. When a forward bias is applied, the current becomes almost linear with applied bias. The simple theory assumes that the whole voltage is dropped across the junction. However, the effect of the semiconductor outside the depletion region can be taken into account by defining a series resistance. The voltage drop across the undepleted semiconductor depends on the diode current and is given by  $IR_s$  and the junction voltage is now given by  $V_j = V_{app} - IR_s$ .

### 2.2.3 Theory of metal-semiconductor contacts

The schematic energy diagram of the Schottky contact between the metal and p-type semiconductor is shown in Figure 2.2. In Figure 2.2 (a), the two materials are physically separated from each other. The work functions of the metal and semiconductor are  $\Phi_m$  and  $\Phi_s$  respectively. (The work function is defined as the energy required for removing an electron from the Fermi level into vacuum.) Also shown in Figure 2.2 (a) is the electron affinity  $\chi$ , which is defined as the difference between the vacuum level and the lower edge of the conduction band  $E_C$ .

Assuming that the metal work function is less than the semiconductor work function ( $\Phi_m < \Phi_s$ ), on contact, carriers will move across the junction until the Fermi level of the metal and the Fermi level in the bulk of the semiconductor have the same energy. The resulting band diagram is shown in Figure 2.2 (b). The valence band bends downwards towards the interface. There is a potential barrier preventing the flow of holes from the metal into the semiconductor. The size of this barrier is given by:

$$\Phi_b = \Phi_m - \chi \quad (2.4)$$

Holes in the semiconductor also experience a potential barrier preventing them from reaching the metal contact and the barrier is given by:

$$qV_{bi} = q[\Phi_s - \Phi_m] \quad (2.5)$$

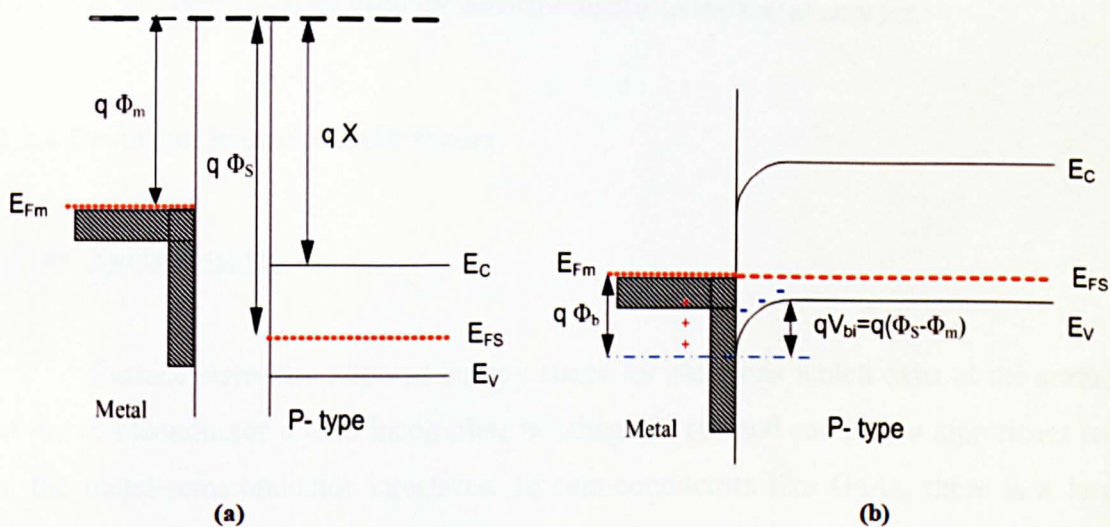


Figure 2.2 A metal-p-type semiconductor contact (a) band diagram before joining. (b) equilibrium band diagram after joining.

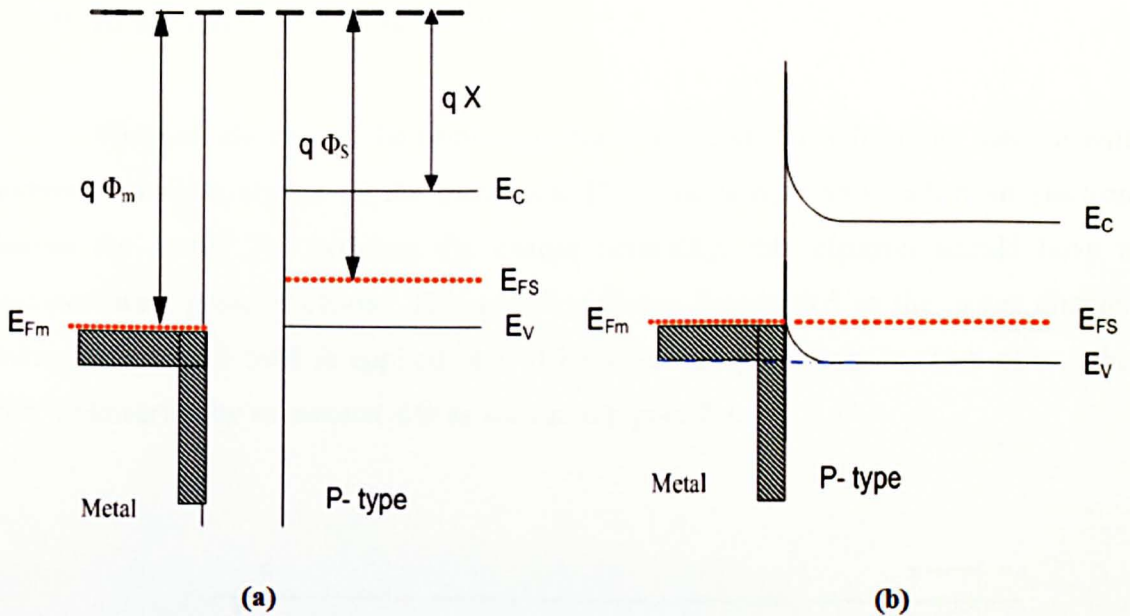


Figure 2.3 Ohmic contact on an p-type semiconductor (a) metal semiconductor contact before contact (b) metal semiconductor contact after contact at thermal equilibrium.

The situation where the metal work function is greater than the work function of the semiconductor ( $\Phi_m > \Phi_s$ ) is shown in Figure 2.3 (a) and the equilibrium state is shown in Figure 2.3 (b). The contact is called Ohmic or injecting because it offers no barrier to the flow of holes from the semiconductor to the metal contact.

#### 2.2.4 Deviation from Schottky theory

##### a) Surface states

Surface states are allowed energy states for electrons which exist at the surface of the semiconductor due to incomplete bonding [9, 10] and can play a significant role in the metal-semiconductor interfaces. In semiconductors like GaAs, there is a large density of states of surface states which have an energy inside the band gap, resulting in the Fermi-level being pinned at the surface. Consequently, the measured barrier height of a metal semiconductor contact is independent of the metal work function.

### b) Image Force Lowering of Barrier

When an electron in the semiconductor is at a distance  $x$  from the metal it will induce a positive charge on the metal side [7]. This is only valid when an electron leaves the metal. To maintain the charge neutrality, this electron should have a compensating positive charge. This positive charge is regarded as the image charge. When an external field is applied, it will be affected by both fields. This causes the barrier lowering by an amount  $\Delta\Phi$  as shown in Figure 2.4.

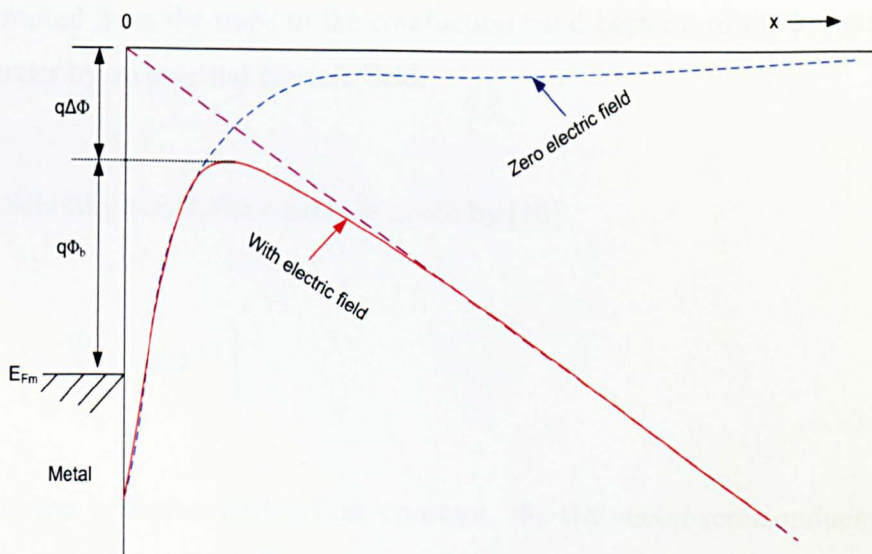


Figure 2.4 The potential well in the presence of an electric field [6]

At high field the Schottky barrier is lowered by an amount which is given by [6]:

$$\Delta\Phi = \sqrt{\frac{qE}{4\pi\epsilon_s}} \quad (2.6)$$

and in terms of built-in potential and the doping concentration it is given by:

$$\Delta\Phi = \sqrt{\frac{q}{4\pi\epsilon_s}} \left[ \frac{2qN_D(V + V_{bi} - kT/q)}{\epsilon_s} \right]^{\frac{1}{4}} \quad (2.7)$$

If lowering effect is taken into account, the barrier seen by holes in the metal becomes:

$$\Phi_b = (\Phi_s - \Phi_m) - \Delta\Phi \quad (2.8)$$

### c) Schottky effect and Poole-Frenkel effect

In Schottky effect, electrons are transported by thermionic emission across the metal-semiconductor junction. While in the Poole-Frenkel effect, electrons are thermally emitted from the traps to the conduction band because of the lowering of the potential barrier by an external electric field.

For Schottky effect, the current is given by [10]:

$$I = AA^* \exp\left[\left(\frac{-\Phi_b}{kT}\right) - \beta_s V^{1/2}\right] \quad (2.9)$$

where  $A^*$  is the effective Richardson constant,  $\Phi_b$  the metal-semiconductor barrier height and  $\beta_s$  is the Schottky field lowering constant has the form:

$$\beta_s = \left[q^3 / 4\pi\epsilon_s\epsilon_0\right]^{1/2} \quad (2.10)$$

where  $q$  is the electronic charge,  $\epsilon_s$  the relative dielectric constant of the material and  $\epsilon_0$  the primitively of free space.

In case of Poole-Frenkel effect, the current is given as [10]:

$$I \propto V \exp\left[-\Phi_{PF} + \beta_{PF} V^{1/2}\right] \quad (2.11)$$

where  $\beta_{PF}$  is the Poole-Frenkel constant, which is given by:

$$\beta_{PF} = [q^3 / \pi \epsilon_s \epsilon_0]^{1/2} \quad (2.12)$$

therefore  $\beta_{PF} = 2 \beta_S$ .

### 2.2.5 Mathematical approach to the current transport processes

For a p-n junction, the current transport is due mainly to minority carriers while for Schottky it is governed by majority carriers. The equation which governs the current-voltage characteristic for both Schottky and p n junction is identical and is given in equation (2.1), while the saturation current is different. The saturation current for p n junction is given by equation (2.2) and equation (2.3), while for Schottky diode it is given by equation (2.14). The diode current-voltage relationship is written in terms of ideality factor  $n$  and series resistance  $R_S$  as [6]:

$$I = I_S \left[ \exp \left( \frac{q(V_a - IR_S)}{nkT} \right) \right] \quad (2.13)$$

with  $I_S$  for Schottky diode:

$$I_S = AA^{**} T^2 \exp \left[ -\frac{q\Phi_b}{kT} \right] \quad (2.14)$$

re-arranged equation (2.13) gives:

$$V = \frac{nkT}{q} \left[ \ln \left( \frac{I}{I_S} \right) + 1 \right] + IR_S \quad (2.15)$$

where  $I_S$  is the saturation current,  $V_a$  is the applied voltage,  $k$  is the Boltzmann constant,  $T$  is the absolute temperature,  $A$  is the contact area,  $A^{**}$  is the Richardson constant, and  $\Phi_b$  is the barrier height at zero bias voltage.

A comparison of equation (2.3) and (2.14) reveals a linear relationship between a plot of  $\ln(I_S/T^3)$  versus  $10^3/T$  for the p n junction, whereas a plot between  $\ln(I_S/T^2)$  versus  $10^3/T$  will be a straight line for the Schottky contact. The slope in the former will yield the band gap of the semiconductor and the latter the Schottky barrier height.

For the Schottky contact,  $n$  is the ideality factor which identifies the non-ideal thermionic emission behaviour defined as:

$$n = \frac{q}{kT} \left[ \frac{dV_F}{d(\ln I_F)} \right] \quad (2.16)$$

The ideality factor is very close to unity at low doping and high temperatures. It can be determined from the forward characteristic by plotting  $\ln I_F$  versus  $V_F$ . The slope of the linear part of plots extrapolated to cut the  $\ln I$  axis at  $V = 0$  gives the saturation current density  $J_s$ . The slope of this line is used to calculate the ideality factor  $n$ . The theoretical value of the ideality factor is equal to one. But, there are many factors which make ideality factor larger than unity like the barrier height dependence on the applied voltage, tunnelling across the potential barrier, and the carrier recombination in the space charge region [11]. Also, carrier trapping by interface states and the oxide layer at the metal – semiconductors interface can affect the ideality factor [12].

From equation (2.14), we can get the Schottky barrier height  $\Phi_b$ :

$$\Phi_b = -\frac{kT}{q} \ln \left[ \frac{AA^{**}T^2}{I_s} \right] \quad (2.17)$$

Arrhenius plot of the forward current can be obtained by plotting  $\ln I_F$  against  $1/T$  for several fixed biases. The slope of the plot gives the activation energy according to the following equation:

$$I = I_s \exp\left[\frac{-E_a}{kT}\right] \quad (2.18)$$

and the activation energy is given by:

$$E_a = k \left[ \frac{\ln I_F}{1/T} \right] \quad (2.19)$$

### 2.2.6 Thermionic field emission and field emission theory

The current transport in metal-semiconductor contacts is mainly due to majority carriers. It is known that the width of the depletion region is proportional to the inverse of square root of the doping concentration ( $N_D^{-1/2}$ ) [6], so for low-doped semiconductors the space charge region can be wide and current arises from the carrier which can jump over the barrier as a result of thermionic emission. There are two other transport forms; field emission and thermionic field emission. The description below is given for an n-type Schottky contact but similar processes are expected to occur in p-type Schottky contact.

In highly doped semiconductors, as a result of increasing the carrier concentration, the width of the depletion layer decreases and the barrier becomes thin enough for the electrons to tunnel through the potential barrier into the metal. This takes place close to the Fermi level in the semiconductor. This mechanism is known as field emission and only occurs in degenerate semiconductors at low temperature.

In intermediate doped semiconductors, the potential barrier is thin enough for tunnelling but at energies above the Fermi level. At low temperatures there will be insufficient electrons with the appropriate energy to tunnel through the potential barrier. As the temperature increases, the concentration of electrons with the appropriate energy increases and the current rises. This mechanism is called thermionic-field emission [13]

If the current transport is dominated by thermionic field emission (TFE), the current is related to the voltage by [6]:

$$I = I_s \exp\left[\frac{qV}{E_0}\right] \quad (2.20)$$

where  $E_0$  represents the efficiency of the tunnelling process as stated by Rodrigues [14]. Mathematical analysis of Padovani and Stratton [15] led to useful expressions in order to explain the TFE/FE theory. Their analysis is based on the Taylor expansion of the tunnelling probability ( $E_{00}$ ). The tunnelling ideality factor ( $n_{\text{tun}}$ ) is given by [15]:

$$n_{\text{tun}} = \frac{qE_0}{kT} = \frac{qE_{00}}{kT} \coth\left[\frac{qE_{00}}{kT}\right] \quad (2.21)$$

where  $E_{00}$  is the characteristic tunnelling energy which is related to doping concentration by [8]:

$$E_{00} \equiv \frac{q\hbar}{2} \sqrt{\frac{N_D}{\epsilon_0 \epsilon_s m^*}} \quad (2.22)$$

where  $q$  is the electronic charge,  $\hbar$  is the Planck constant divided by  $2\pi$ ,  $N_D$  is the doping impurity density,  $\epsilon_s$  is the dielectric constant,  $\epsilon_0$  is the permittivity of free space and  $m^*$  is the effective mass. This equation indicates that the tunnelling current will increase exponentially with the square root of donor impurity density [6]. Note that according to equation (2.20), the logarithmic plot of the current, as a function of the applied bias  $V$ , gives a straight line of slope  $q/E_0$ , and thus the impurity concentration  $N_D$  can be calculated using equation (2.22).

As a rough guide, field emission occurs if  $q E_{00} \gg k T$ , thermionic -field emission if  $q E_{00} \approx k T$  and thermionic emission if  $q E_{00} \ll k T$  [16].

The saturation current on the basis of TFE theory given by Padovani and Stratton [15] in terms of  $E_{00}$  is represented by:

$$I_s = \frac{A^* \pi^{1/2} E_{00}^{1/2} (\Phi_b - E)^{1/2}}{kT \cosh(E_{00}/kT)} x \exp\left[-\frac{\Phi_b}{E_0}\right] \quad (2.23)$$

where  $A^*$  is the classical Richardson constant for the semiconductor under study,  $E$  is the potential energy associated with the applied bias  $V$  between the metal and semiconductor and  $\Phi_b$  is the barrier height.

### 2.2.7 Schottky barrier inhomogeneity model

The behaviour of the barrier at the interface between the metal-semiconductor (MS) contact was discussed by Tung [17] and Werner and Guttler [18]. They explain the large variations in Schottky barrier height (SBH) with temperature. This model referred this to the spatially inhomogeneous barrier height at the MS interface, which consists of low and high barrier height or as called patches. They assume that the barrier height variations are represented by a Gaussian distribution [18]:

$$P(\Phi_b) = \frac{1}{\sigma_s \sqrt{2\pi}} \exp\left[-\frac{[\Phi_b - \Phi_{b(mean)}]^2}{2\sigma_{s0}^2}\right] \quad (2.24)$$

where the pre-exponential term is the normalization constant of the Gaussian barrier height distribution. The total current  $I(V)$  across a Schottky diode containing a barrier inhomogeneities can be expressed as:

$$I(V) = \int I(\Phi_b, V) P(\Phi_b) d\Phi_b \quad (2.25)$$

integration of equation (2.25) yields [18]:

$$I(V) = I_s \exp\left[\frac{qV}{n_{ap}kT}\right] \left[1 - \exp\left[-\frac{qV}{kT}\right]\right] \quad (2.26)$$

with

$$I_s = AA^{**}T^2 \exp\left[-\frac{q\Phi_{bo}}{kT}\right] \quad (2.27)$$

where  $\Phi_{b0}$  and  $n_{ap}$  are the apparent barrier height and the apparent ideality factor respectively, given by [18] (equation 2.28 and equation 2.29):

$$\Phi_{bo} = \Phi_{b0(\text{mean})} - \frac{q\sigma_{s0}^2}{2kT} \quad (2.28)$$

the mean barrier height at zero bias ( $\Phi_{b0(\text{mean})}$ ) and the standard deviation ( $\sigma_{s0}$ ) are the distribution parameters. The lower the value of  $\sigma_{s0}^2$ , the more homogeneous the barrier height is. Equation (2.28) gives a straight line with  $\Phi_{b0(\text{mean})}$  and  $\sigma_{s0}$  as the intercept and the slope respectively.

$$\left[\frac{1}{n_{ap}} - 1\right] = \rho_2 - \frac{q\rho_3}{2kT} \quad (2.29)$$

the plot of  $(n^{-1}-1)$  against  $q/(2kT)$  should give a straight line with  $\rho_2$  and  $\rho_3$  as the y-intercept and the slope respectively, where  $\rho_2$  (dimensionless) and  $\rho_3$  are the voltage coefficients. Both of these parameters depend on temperature and quantify the voltage deformation of the barrier height distribution.

It is known that the barrier height depends on the electric field and therefore on the applied bias (V). The barrier height  $\Phi_b$  is related to the bias coefficient  $\beta$  by [19]:

$$\Phi_b = \Phi_{b0} + \beta V \quad (2.30)$$

where  $\Phi_{b0 \text{ (mean)}}$  is the mean barrier height at zero bias. Extending the linear bias dependence to the mean barrier height of the distribution parameters gives:

$$\Phi_{b(\text{mean})} = \Phi_{b0(\text{mean})} + \beta V \quad (2.31)$$

The standard deviation for the barrier height is given by:

$$\sigma_s = \sigma_{s0} + \rho_3 V \quad (2.32)$$

Comparing equation (2.31) and equation (2.32) and using equation (2.27) and equation (2.28) a modified Richardson's equation is obtained. This is given below as equation (2.33) [20]:

$$I_s = AA^{**} T^2 \exp \left[ -\frac{q\Phi_{ap}}{kT} + \frac{q^2 \sigma_{s0}^2}{2k^2 T^2} \right] \quad (2.33)$$

which leads to the following equation:

$$\ln \left[ \frac{I_s}{T^2} \right] - \left[ \frac{q^2 \sigma_{s0}^2}{2k^2 T^2} \right] = \ln [AA^{**}] - \frac{q\Phi_{ap}}{kT} \quad (2.34)$$

The plot between  $\ln (I_s/T^2) - (q^2 \sigma_{s0}^2 / 2k^2 T^2)$  versus  $10^3/T$  yields a straight line with the slope giving the mean barrier height and the intercept is equal to the  $(\ln AA^{**})$ . Again this theory was developed for n-type Schottky diodes but the analysis will also hold for p-type Schottky barriers.

### 2.2.8 The temperature dependence of the ideality factor

Brillson [21] attempts to predict the current conduction based on Saxena's work using the plot between  $(nkT/q)$  versus  $kT/q$  as shown in Figure 2.5. An ideal case when the straight line goes through the origin with a slope equal to the ideality factor  $n$  which is represented by line (1) as predicted by thermionic emission (TE) theory. Pure TE gives an ideality factor of one. Slight deviations from TE give a value greater than unity. Recombination in the depletion layer gives a value of  $n=2$  [22]. Higher value of a (9-12) has also been reported [23] and corresponded to either TFE or FE mechanisms. Line (2) corresponds to a straight line that passes through the origin; but with a value of  $n$  greater than 1. The " $T_0$ " abnormality arises when the line does not extrapolate through the origin. This is line (3) in Figure 2.5 and  $n$  has abnormally high values due to TFE or FE. The case when the line approaches a constant value at low temperature is indicative of thermionic field emission (TFE) and is shown by line (4). The final case, the plot represented by a horizontal straight line as shown by line (5), indicates that the field emission conduction process (FE) dominates the current transport mechanism.

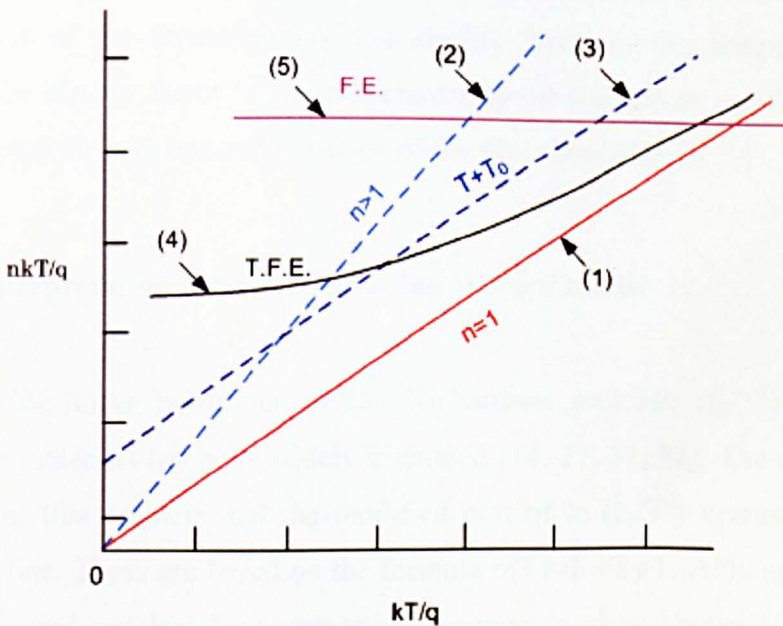


Figure 2.5 Plot of the  $nkT/q$  versus  $kT/q$  showing the temperature dependence of the ideality factor [24].

According to Padovani and Stratton [15] the forward current is assumed to fit to  $\exp[qV/k(T+T_0)]$  where  $T_0$  is a parameter independent of the temperature and voltage. Maeda [25] states that the expression  $\exp[qV/k(T+T_0)]$  is equivalent to writing the ideality factor in the form of  $n= 1+T_0/T$ . At high temperature,  $n$  should go through one. Brillson [21] suggests that the only valid explanation of the  $T_0$  anomaly is the inhomogeneities of the Schottky barrier height (SBH). The function is in the form  $nT = T+T_0$  where " $T_0$ " is a measure of the temperature dependence of the ideality factor [24]. Then equation (2.14) becomes [26]:

$$I_s = AA^{**}T^2 \exp\left[-\frac{q\Phi_b}{nkT}\right] \quad (2.35)$$

which is called the modified Richardson equation [14, 27].

Several authors [28-30] have explained the increase of the ideality factor with decreasing temperature on the basis of what is called the " $T_0$  effect". This behaviour has been reported in various materials like Cr/n-GaAs and Au/n-GaAs.  $T_0$  parameter is the evaluation of the dependence of the ideality factor on the temperature. This theory relates the ideality factor " $n$ " to temperature by the relation  $n= n_0+T_0/T$ . Ideally, the plot should pass through one and the slope of the plot should be  $T_0$ .

### 2.2.9 Interpretation of " $T_0$ " effect using Werner model

Non-linear behaviour of the Richardson plot ( $\ln(I_s/T^2)$  versus  $10^3/T$ ) for different materials has been widely discussed [14, 27, 31, 32]. The replacement of  $T$  by  $nT$  solves this problem and the modified plot of  $\ln(I_s/T^2)$  versus  $10^3/nT$  produces a straight line. These are based on the formula  $n(T)=1 +T_0/T$ . Although it is an empirical approach and not based on theoretical arguments, they obtained a good result. The values of the parameter  $T_0$  behave randomly for a set of Au/n-GaAs Schottky contacts which are fabricated on the same slice of GaAs and where the temperature can vary from 10-100 K [13]. Werner and Guttler [18] state that there is no general validity to predict the values of the parameter  $T_0$  and they invoke the concept of a distribution of surface states, already mentioned in the previous section, to explain the dependence of

the ideality factor on temperature ( $n(T)$ ) which is presented by  $n(T)=1 +T_0/T$  by the following approximation of equation (2.29) :

$$n = \frac{1}{1 - \rho_2 + \rho_3 / (2kT/q)} \quad (2.36)$$

for the validity of  $-\rho_2 + \rho_3 / (2kT/q) \ll 1$ , equation (2.36) is approximated to [18]:

$$n \approx 1 - \frac{\rho_3}{2kT/q} \equiv 1 + \frac{T_0}{T} \quad (2.37)$$

which implies that  $T_0 \approx -\frac{\rho_3}{2k/q}$

The ideality factor “n” is related to the temperature by the relation  $n= n_0+T_0/T$ . The values of  $n_0$  and  $T_0$  are determined from the intercept and the slope respectively [33].

### ***2.3 Capacitance- Voltage measurement***

In general, the diode capacitance arises either from the depletion region itself or is caused by the injection of minority carriers. The first type of capacitance is called depletion layer capacitance where there is a dipole of fixed positive and negative charge. It dominates the diode capacitance at reverse biased conditions. The second one is called the diffusion capacitance where minority carriers injection has introduced charges. It is dominant under forward bias conditions [34].

The capacitance of the diode can be determined by considering the depletion region as a dielectric of width  $W$ . The total space charge width  $W$  is given in terms of the built-in potential and the applied bias for a uniformly doped material by [6]:

$$W = \sqrt{\frac{2\epsilon_s\epsilon_0}{qN_D} [V_{bi} - V_a - kT/q]} \quad (2.38)$$

where  $\epsilon_0$  is the permittivity of free space and  $\epsilon_s$  is the dielectric constant of the material.

When the applied reverse bias is increased by a small increment  $dV$ , the depletion width increases causing a small increase in the charge by  $dQ$ :

$$dV = \frac{qN_D}{\epsilon_s\epsilon_0} dW \quad (2.39)$$

$$dQ = qN_D dW \quad (2.40)$$

From equation (2.39) and equation (2.40), the capacitance per unit area is given by:

$$C = -\frac{dQ}{dV} = \frac{\epsilon_s\epsilon_0}{W} \quad (2.41)$$

The depletion layer capacitance  $C$  per unit area in terms of the space charge  $Q_{sc}$  per unit area is given by [6]:

$$C \equiv \frac{|\partial Q_{sc}|}{\partial V} = A \sqrt{\frac{q\epsilon_s\epsilon_0 N_D}{2[V_{bi} - V_a - kT/q]}} \quad (2.42)$$

$$\frac{1}{C^2} = \frac{2}{q\epsilon_s\epsilon_0 A^2 N_D} [V_{bi} - V_a - kT/q] \quad (2.43)$$

We should therefore obtain a straight line by plotting  $1/C^2$  versus the reverse bias voltage. From the slope of this line doping concentration  $N_d$ , can be found and from the x-axis intercept the built in potential can be determined.

### 2.3.1 The role of traps in Capacitance-Voltage measurement

The effect of deep traps on the junction capacitance of a Schottky barrier will be discussed in detailed. The energy band diagram of Schottky barrier with depletion width  $x_D$ , is given in Figure 2.6. The shallow donors with density  $N_D$ , located close to the bottom of conduction band, will all be ionized at room temperature.

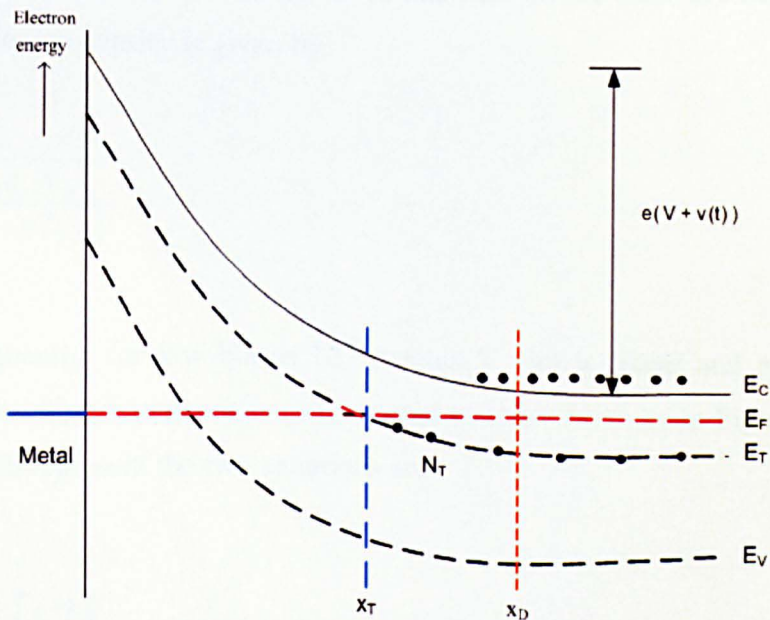


Figure 2.6 Schottky barrier on an n-type semiconductor containing deep states [35]

The deep traps, of density  $N_T$ , are located at an energy  $E_T$  below the bottom of conduction band. These traps are assumed to be neutral if filled by an electron, and positive if empty i.e. they are donor like centres [10]. For a distance greater than  $x_T$ , the traps are filled by electrons and so are neutral. On the other hand, if this distance is less than  $x_T$  the deep traps as well as the donors will be ionized. The space charge density is given by [35]:

$$\begin{array}{ll} \rho(x) = q(N_D + N_T) & x < x_T \\ \text{and } \rho(x) = q(N_D) & x < x_T < x_D \end{array}$$

At high biases,  $qV_a > E_F - E_T$ , in this case all the traps are ionized in the depletion region and  $x_T \approx x_D$ . The net space charge density  $N_D$  in equation (2.42) is replaced by  $(N_D + N_T)$ . So the capacitance becomes:

$$C = A \sqrt{\frac{q\epsilon_0\epsilon_s(N_D + N_T)}{2V_a}} \quad (2.44)$$

With the assumption  $V_a \gg kT/q$ , the applied voltage is higher than the built-in potential. At low biases,  $qV_a < E_F - E_T$ , so in this case all the traps are below the Fermi level and the charge density is given by:

$$C = A \sqrt{\frac{q\epsilon_0\epsilon_s N_D}{2[V_a - kT/q]}} \quad (2.45)$$

Consequently, for low biases  $1/C^2$  versus  $V$  plot is linear and proportional to  $(N_D)^{-1}$  while, for higher biases it is proportional to  $(N_D + N_T)^{-1}$  as in Figure 2.7. So the equations which represent the two situations are:

$$N_D = \frac{-2}{q\epsilon_0\epsilon_s A^2} \left[ \frac{C^{-2}}{V_r} \right]^{-1} \quad (2.46)$$

$$N_D + N_T = \frac{-2}{q\epsilon_0\epsilon_s A^2} \left[ \frac{C^{-2}}{V_r} \right]^{-1} \quad (2.47)$$

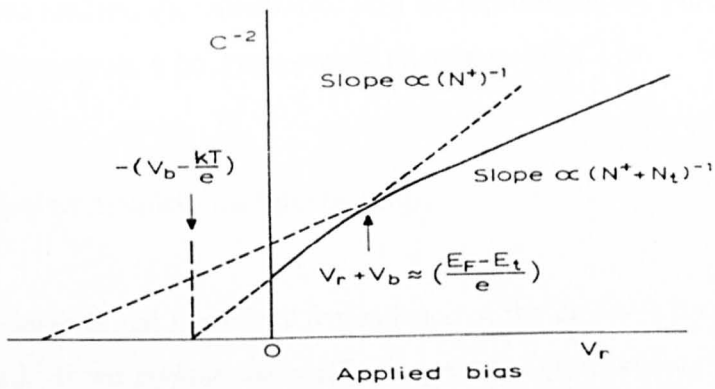


Figure 2.7 Schematic plot of  $1/C^2$  versus  $V$  for n-type material [35].

## 2.4 Admittance Spectroscopy

Admittance spectroscopy technique has been used to investigate the behaviour of deep impurities in semiconductors. This technique allows important information about the deep levels such as activation energy and capture cross section to be acquired [35, 36]. The admittance  $Y$  is given by:

$$Y = \frac{i(\omega)}{v(\omega)} = G(\omega) + j\omega C(\omega) \quad (2.48)$$

where  $C$  is the capacitance,  $G$  is the conductance and  $\omega$  is the angular frequency of the small signal. The conductance gives the real part of the  $Y$ :

$$G(\omega) = \text{Re } a|Y| = \cos \theta |Y| \quad (2.49)$$

while the imaginary part of  $Y$  is:

$$C(\omega) = \frac{\text{Im}|Y|}{\omega} = \frac{\sin \theta |Y|}{\omega} \quad (2.50)$$

At low frequencies, the admittance will be represented by purely the real part whereas at high frequencies it becomes purely imaginary [37].

### 2.4.1 The principal of Admittance Spectroscopy

In this technique, the frequency dependence of the device's response to a small signal is measured.<sup>1</sup> If we assume the small ac signal is  $v(t)$  as shown from Figure 3.6, then the total potential applied across the device is given by [35]:

$$eV_{\text{total}} = q[V_a + v(t)] \quad (2.51)$$

In the absence of the trap levels, this will cause an alternating shift of the Fermi level  $E_F$ . Thus, this motion will result in continuous change of the charges. This charge fluctuation leads to a decrease and increase in depletion width. In this case the charge responds in phase with ac voltage, and the resulting current which is the time derivative of the charges is  $\pi/2$  in advance of  $v(t)$  and therefore the device acts as a lossless capacitance [35].

In this case the admittance will be given by the capacitive contribution:

$$Y(\omega) = j\omega C \quad (2.52)$$

At low frequencies and high temperatures the trap charges which are located where the Fermi level crosses the trap energy are able to follow the ac signal because they behave like free carriers. As a consequence, they can contribute to the measured conductance and not to the capacitance. However, at high frequencies the traps cannot respond and the trapped charges lag behind  $v(t)$ . Therefore, phase angle of the current will be less than  $\pi/2$  and so there will be an imaginary component to the admittance,  $C(\omega)$ .

---

<sup>1</sup> Small ac signal means that the amplitude of the ac signal is so small and that the depletion layer width does not change sufficiently.

At high frequencies, the traps are not able to respond to the applied field and so the junction capacitance is given by the depletion layer capacitance:

$$C_{dep} = \frac{\epsilon A}{x_D} = \left[ \frac{q\epsilon N_D}{2V_{bi}} \right]^{\frac{1}{2}} \quad (2.53)$$

where  $\epsilon$  is the dielectric constant of the semiconductor,  $A$  is the junction area [38]. When the deep traps contribute to capacitance, they modify the parameters in equation (2.53) e.g. the built-in voltage  $V_{bi}$ , doping concentration  $N_D$  and the depletion layer width. At low temperature the electron emission rate is much smaller than the ac signal frequency and again the junction capacitance is just  $C_{dep}$ . [39].

Mathematically, the capacitance  $C(\omega)$  and conductance  $G(\omega)$  of the Schottky diode, as a function of the ac signal frequency are given [35]:

$$C(\omega) = C_{dep} + \frac{\Delta C}{1 + [\omega / \omega_T]^2} \quad (2.54)$$

$$G(\omega) = \frac{\Delta C \omega_T}{1 + [\omega_T / \omega]^2} \quad (2.55)$$

where  $\Delta C$  is the capacitance change due to the trap charges response, which is also represented by the height of the capacitance step as shown in Figure 2.8 and  $\omega_T$  is the angular characteristic frequency of the trap. The trap concentration and the trap emission time are related to  $\Delta C$  and  $\omega_T$  respectively. At  $\omega = \omega_T$ , the point of inflection in the  $C$ - $\omega$  curve is shown as a red dotted line in Figure 2.8, equation (2.54) and equation (2.55) become:

$$G(\omega) \Big|_{\omega=\omega_T} = \frac{\Delta C}{2} \omega_T \quad (2.56)$$

$$C(\omega)\Big|_{\omega=\omega_T} = C_{dep.} + \frac{\Delta C}{2} \quad (2.57)$$

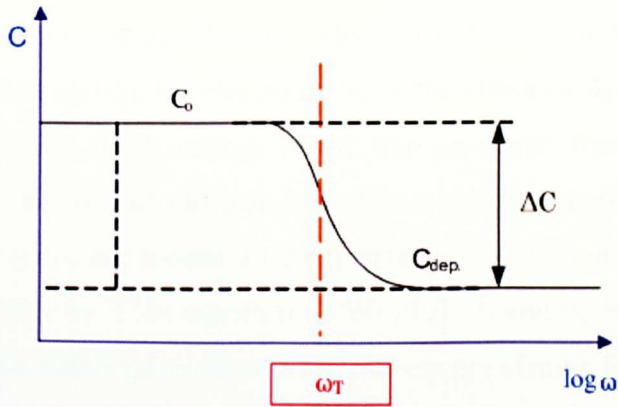


Figure 2.8 The curve for  $C(\omega)$  as a function of logarithm of ac signal frequency

### 2.4.2 The logistic equation

The value of the inflection frequency  $\omega_T$  is obtained from  $C_0$  and  $C_{dep.}$ ; these represent the high and low frequency capacitance values respectively (Figure 2.8). The equation for the capacitance is represented by:

$$C(\omega) = C_{dep.} + \frac{C_0 - C_{dep.}}{1 + [\omega / \omega_0]^2} \quad (2.58)$$

This equation is similar to the logistic equation which is used to determine the inflection frequency. The mathematical formula is given by  $y = A_2 + [A_1 - A_2 / (1 + (x/x_0)^p)]$  where  $A_1$  and  $A_2$  are constants which can be estimated from the lower and upper asymptote line of the S-shaped curve.

### 2.4.3 Analysis of the data:

The admittance spectroscopy analysis is carried out to estimate the activation energy and capture cross section from the data. The angular characteristic frequency of the electron trap is related to the emission rate of the traps  $\omega_T$  given by the following equation [35]:

$$\omega_T = e_n = \sigma_n \langle v_n \rangle N_C \exp\left[\frac{(E_C - E_T)}{kT}\right] \quad (2.59)$$

where  $\langle v_n \rangle$  is the average thermal velocity of electrons in the conduction band,  $\sigma_n$  is the capture cross section for electrons,  $N_C$  is the effective density of states in the conduction band, and  $E_T$  is the energy of the trap measured from the bottom of the conduction band in the case of electron trap. Since both the thermal velocity and the effective density of states are temperature dependent ( $v_n \propto T^{1/2}$  and  $N_C \propto T^{3/2}$ ), we can replace these two terms by  $T^2$  in equation (2.59) [40]. It can be written as  $\ln(e_n/T^2) \propto (\Delta E/kT)$ . Thus we can obtain  $\Delta E_T$  which is the free energy change for ionization or  $(E_c - E_T)$ , from the slope in the plot of  $\ln(e_n/T^2)$  versus  $1/T$  when a temperature independent  $\sigma_n$  is assumed.

## CHAPTER 3 Theoretical Background and Literature Review

### *3.1 Introduction*

Improvement in electronic and magnetic properties of semiconductors is of considerable commercial importance. It is possible to change radically the electronic properties of the semiconductor by the addition of impurities which control the nature and the transport properties of the carriers. In a similar way, the doping of semiconductors with magnetic impurities result in changed magnetic properties. Little is known about the electronic defects induced by these magnetic dopants and this thesis attempts to address this issue. The "magnetization" of conventional semiconductors in their regular structure leads to the use of electron spin which along with charge enables processing and data storage as well as the emission of polarised light [41, 42]. The electron spin is already used for the purpose of recording information in case of magnetic materials [43]. Spin polarized current injection into the semiconductors used to control the spin state of carriers. Therefore, spin polarized carriers in a ferromagnetic material will contribute to the net current of magnetization [44].

Non-magnetic III-V semiconductors can be made ferromagnetic by doping with transition metal (TM) atoms. These are known as diluted magnetic semiconductors (DMS) [43]. The most widely studied materials of the III-V magnetic semiconductor are (Ga, Mn)As and (Ga, Mn)N.

Looking closely at the electronic configuration of Mn, which is [Ar]  $4s^23d^5$ , it has a half-filled 3d electronic shell. There are five 3d electrons in this shell which provide a total spin moment of 5 Bohr magnetons ( $\mu_B$ ) [45].

When Mn atoms are added to a III-V semiconductor they act as acceptors. The spins of the Mn atoms are anti-aligned and this leads to anti-ferromagnetic behaviour.

However, the interaction of the Mn atoms with the spin polarized holes results in ferromagnetic behaviour. Consequently, the existence of the ferromagnetic behaviour in III-V semiconductors is related to the presence of the free holes [2].

One of the requirements for ferromagnetism to occur is a high concentration of Mn atoms in III-V semiconductor materials [46]. A major hurdle facing researchers achieving these high concentrations is the low solubility limit of Mn in III-V semiconductors. For GaAs, the Mn solubility limit is  $10^{19} \text{ cm}^{-3}$  [3]. This problem is resolved by using the low-temperature molecular beam epitaxy (LT-MBE) which will be discussed in the next section. This method permits the doping of the III-V semiconductor with Mn above its solubility limit [3]. In contrast, the concentration of holes created by Mn ions is restricted by the presence of donor defects that compensate the holes [47]. Once the Mn atoms have been placed into the lattice, residual donors and the large activation energy of the Mn acceptors limit the hole concentration.

The ferromagnetic order is affected by the temperature; above certain temperature called the Curie temperature  $T_C$ , the material no longer exhibits ferromagnetic behaviour. The high concentration of both Mn atoms and free hole help achieve high  $T_C$ , According to the formula [1, 48]:

$$T_C = Cxp^{1/3} \tag{3.1}$$

where C is a constant specific to the host material, x is the mole fraction of Mn ions and p is the hole concentration [48]. Therefore, it is important to have high density of both Mn atoms and free holes in order to use this material in any applications.

During the fabrication of DMS III-V materials, there are many defects which are formed during growth by the LT-MBE method [49-51].

### 3.2 Review of Growth conditions of III-V magnetic semiconductor

There are many methods of growing high quality III-V semiconductors. The two most common are molecular beam epitaxy (MBE) [52] and MOCVD (metal organic chemical vapour deposition [53]). Both techniques have been used to grow DMS. All samples used in this thesis were grown by plasma assisted molecular beam epitaxy. Figure 3.1 shows a simplified scheme of an MBE machine used to grow the Mn doped III-V semiconductors.

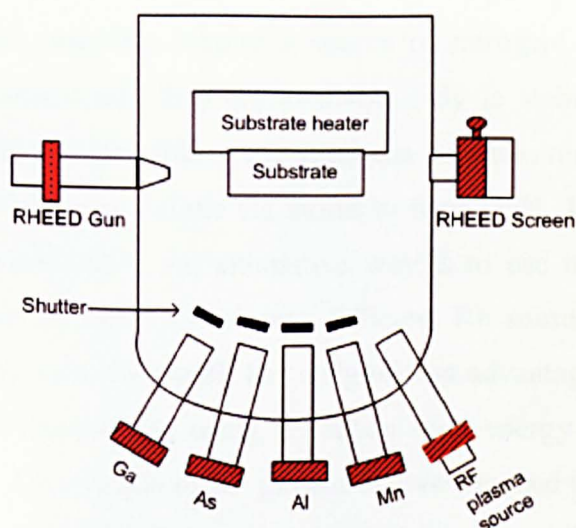


Figure 3.1 Schematic diagram of MBE machine

Fluxes of atoms are produced by heating solid sources that are placed in evaporation cells also called effusion cells. To maintain a constant flux (flow) of atoms the temperature of these cells is controlled up to  $\pm 1$  K. Since the cells are placed in an ultra high vacuum, the atoms in the beam travel until they hit the hot substrate surface. In MBE, the growth of the film requires the constant arrival on to the surface of the constituent atoms. The composition of the deposited film can be controlled by changing the arrival rate of the different atomic species. The atoms diffuse along the surface of the substrate and react with the other species to form a film of the correct stoichiometric ratio. By this method, an extremely small and highly controlled amount of Mn atoms can be added to the GaN or GaAs films to produce DMS layers.

The use of an ultra high vacuum (UHV) environment facilitates a high degree of control over the background impurities. The mean free path of the atoms in the chamber is long compared to the space between the sources and the wafer and consequently the name molecular beams. The molecular beam does not interact with itself or other beams until it reaches the substrate.

Growth rates are controlled by the temperature of the effusion cells which produces a stream of atoms depending on their temperature. It is essential that they provide flux stability, uniformity and material purity [54].

GaN and related materials require a source of nitrogen. Nitrogen atoms are highly reactive and consequently they are available only in stable molecular species such as  $N_2$  and ammonia. It is possible to use ammonia because ammonia absorbed onto a hot surface will react with the mobile Ga atoms to form GaN. This process requires very high substrate temperatures. An alternative way is to use nitrogen directly and dissociate the  $N_2$  molecules using RF plasma. Efficient RF sources are available and high growth rates can be achieved. MBE has a significant advantage over other growth techniques since in-situ monitoring using reflection high energy electron diffraction (RHEED) is available. An example of RF plasma source attached to effusion cell ports for GaN growth is given in [52]. A computer operated mechanical shutter triggers the flux. The shutters need to work much faster than the growth rate [55].

RHEED monitors the growth in situ, allowing the thickness of the layers to be precisely controlled [54]. The diffraction pattern, displayed on a phosphor screen in the growth chamber, provides information about the surface structure during growth and can differentiate (planar) 2D growth and unwanted 3D growth (columns).

The use of MBE to grow GaN has many advantages over MOCVD (metal organic chemical vapour deposition). The low growth temperature of MBE is of particular use because it reduces thermally induced strain and phase separation [56]. In addition to this, at low temperatures the choice of substrate is more flexible and there is a reduction in thermal effects like diffusion. MBE allows precise control of thickness

and composition as well as high p-type doping concentration [57]. Furthermore, there is no post-growth annealing for p-type conductivity.

The electrical characteristics of both GaMnN and GaMnAs are investigated in this study. Different aspects of these two materials like the preparation environment or different estimated parameters are discussed which gives better understanding of the devices. At the time this work started, there were no concerted attempts to study the electrical characteristics of these two materials.

### ***3.3 The Ferromagnetic behaviour of the devices used in this study***

#### **a) GaMnAs: Ferromagnetic behaviour**

For GaMnAs devices used in this study, the Mn concentrations range between  $1 \times 10^{19} \text{ cm}^{-3}$  and  $1 \times 10^{21} \text{ cm}^{-3}$  at different growth temperatures. According to Jungwirth et al. [58] samples with doping concentration between  $1 \times 10^{19}$  and  $1 \times 10^{20} \text{ cm}^{-3}$  show metallic behaviour. While a doping concentration  $\sim 10^{20} - 10^{21} \text{ cm}^{-3}$  is close to the metal-insulator transition [58].

In general it can be concluded that samples studied in this thesis covered the full range of Mn concentration which has been studied. However, the experiments performed for this thesis can not be used to clarify these materials as ferromagnetic in behaviour or otherwise. It should be noted that many factors such as solubility affect the Curie temperature  $T_C$  and that those shown in the Table (3.1) may not be strictly applicable in other conditions e.g. samples studied here may not have a  $T_C$  as reported by other workers for similar concentration. These results of various workers are summarised in Table (3.1).

**Table 3.1** The atomic percent, doping concentration,  $T_C$  and the condition of GaMnAs samples.

| X   | $N_A$ ( $\text{cm}^{-3}$ ) | Condition of samples | $T_C$ (K)            | Reference             |
|---|----------------------------|----------------------|----------------------|-----------------------|
| $0.015 < x < 0.08$                                | -                          | metallic             | 110                  | Edmonds et al. [59]   |
| $x < 0.03$ or $x > 0.06$                          | -                          | Insulator            | -                    |                       |
|   | $1 \times 10^{27}$         | -                    | 125                  |                       |
| 0.06 %  | $1 \times 10^{19}$         | -                    | -                    | Jungwirth et al. [58] |
| 0.3 %   | $6 \times 10^{19}$         | Insulator            | -                    |                       |
| 1 %   | $2.2 \times 10^{20}$       | metallic             | -                    |                       |
| 1.5 % to 8 %                                      | -                          | Metallic             | 140                  | Campion et al. [60]   |
| 2.2 %   | $5.1 \times 10^{19}$       | metallic             | 65                   | Yoon et al. [61]      |
| 4.4 %   | $4.6 \times 10^{19}$       | Insulator            | 83                   |                       |
| $x < 0.03$ , $x > 0.06$                           | $3.5 \times 10^{20}$       | insulator            | 128 (for $x=0.053$ ) | Matsukura et al. [62] |
| $0.03 \leq x \leq 0.06$                           | -                          | metallic             | 120 (for $x=0.05$ )  |                       |
| Small $x < 3\%$ and large $x > 7\%$ values of $x$ | -                          | insulator            | -                    | Das Sarma et al. [63] |
| Intermediate range of $x$ ~5%                     | -                          | metallic             | -                    |                       |

### **b) GaMnN: Ferromagnetic behaviour**

The doping concentration of Mn in GaMnN devices used in this study is in the range  $7-8 \times 10^{17} \text{ cm}^{-3}$ . Han et al. [64] detect ferromagnetic behaviour at 400 K for p-type zinc-blende GaMnN layers with carrier concentrations exceeding  $10^{18} \text{ cm}^{-3}$ . In another work Novikov et al. [65] predict in a theoretical study for room temperature carrier-mediated ferromagnetism in p-type GaMnN with hole concentration of  $3.5 \times 10^{20} \text{ cm}^{-3}$ . It is therefore highly probable that GaMnN films studied are not ferromagnetic in character.

### ***3.4 Impact of defects on electrical properties of materials***

Defects play a crucial role in determining the electrical properties (practically conduction) of semiconductors. An ideal lattice structure is difficult to achieve, in fact an ideal crystal does not exist. In a practical crystal there is a range of potential defects

which can be defined on the basis of their geometry as 0D,1D,2D,3D defects [D=Dimensional].

Zero dimensional defects (0D) are also called point defects and may be present in crystal either "unintentionally" or may be introduced in a controlled manner as dopants. Shallow defects-situated close to the band edge- enhance conductivity. On the other hand deep point defects-defects which can communicate with both bands-tend to act as recombination centres or traps and are responsible for reducing conductivity [66].

In wide band gap semiconductors (like GaN or even GaAs) a large number of point defects are liable to be present. In GaN these have been associated with N-ion vacancy which gives it a strong n-type unintentional doping [66].

Some examples of point defects are interstitial, substitutional, vacancy and voids. 1D defects-like dislocations or line defects are also common and act as non radiative recombination centres in material like GaN [66]. 2D dimensional defects are called "stacking faults". Both point defects and line defects reduce mobility by scattering carriers. Stacking faults in GaN have a small "energy of formation" and are present in large quantities [67]. Other examples of 2D defects are screw dislocation and edge dislocation. An interface between two different materials will also constitute a defect. Grain boundaries between crystallite within the same material are also 2D defects. 3D-[three-dimensional] defects are cavities inside a solid like "bubble". Conversely, a different phase may also be present such as "complex" embedded inside the bulk of the material.

All these defects affect the physical properties of solids- we are interested in the electrical behaviour of GaN and GaAs doped with Mn atoms. These are discussed separately later in this chapter. The type of defects in semiconductors and their affect on electrical properties are summerised in Table (3.1).

**Table 3.2 Type of defects and their effect on electrical properties of semiconductors**

| Reference | Defect symbol | Defect kind   | The conductivity  |
|-----------|---------------|---|---|
| [68]      | 0D            | point defects: voids, substitutional, interstitial, antisites                     | Shallow defect: (dopants): increase conductivity. Deep defects (recombination centres, trap): reduce conductivity. Both cause scattering and reduce mobility. |
| [66]      | 1D            | Line defects: dislocation   | reduce mobility and conductivity  |
| [67]      | 2D            | Surface defects: screw dislocation, stacking faults, interface, grain boundaries. | reduce mobility and conductivity  |
| [68]      | 3D            | Volume defects: voids, cavities, localized complexes.                             | reduce mobility and conductivity  |

### 3.5 General features of the GaN

The electronic structure of semiconductor surfaces and interfaces is of fundamental importance in modern technology. Gallium nitride semiconductors are currently the best materials for blue laser diodes and LEDs for their desirable properties like its large direct band gap (3.39 eV); high saturation velocity ( $2 \times 10^7$  cm<sup>2</sup>/s); high thermal stability, with a large breakdown field of 2 MV/cm [53].

The structure of both hexagonal (wurtzite) and cubic (zinc blende) was discussed by Harima [69]. The primitive unit cell of hexagonal structure consists of two Ga–N atom pairs, whereas it consists of one such pair in case of cubic structure. Both have the same surrounding neighbours due to tetrahedral structure in which an atom of one species is surrounded by atoms of the other species. The only difference between the two structures is the stacking order which is denoted by A, B and C and represent the allowed sites of the Ga–N pair. It is ABCABC... in case of cubic structure, while it is ABAB...in case of hexagonal.

### 3.6 Advantages of cubic structure for GaN

Since the material under study is cubic (c-GaN), this survey will be concerned more with c-GaN and c-GaN although only a few studies have been reported on these materials. The growth of high quality GaN with a cubic structure

remains of interest both commercially and academically because of unique properties including vertical device structure and integration of GaN based devices [70]. Cubic GaN (c-GaN) has many advantages with respect to the hexagonal structure such as higher crystallographic symmetry [71] as well as a smaller effective masses, higher carrier mobility and higher doping efficiency [72].

The main difficulty in the growth of cubic GaN arises from polytypism which leads to the formation of wurtzite subdomains within the cubic lattice [73]. Other problems result from a high density of threading dislocations and stacking faults which occur because of the large crystal lattice mismatch between GaN and GaAs. Also, etching of GaAs by the  $N^+$  ion during growth also causes surface roughness [73]. GaAs is the most frequently used substrate for cubic GaN because of its commercial availability and the well known preparation procedures [74].

### ***3.7 The electrical measurements on the GaN***

This study measures I-V-T, C-V-T and C-F-T for c-GaMnN. Most of the reported studies concentrate on the hexagonal (h-GaN). For instance, Kribes et al. [16] investigate the I-V and C-V characteristics of gold Schottky diode film of n-GaN grown by MBE method on sapphire substrates. The growth temperature was 750 °C with a carrier concentration of  $7 \times 10^{17} \text{ cm}^{-3}$  and a Hall mobility 220  $\text{cm}^2/\text{Vs}$ . The estimated barrier height and the ideality factor of Au/n-GaN were obtained from room temperature I-V measurements to be 0.98 eV and 1.4 respectively. From the C-V measurements, a barrier height of 1.16 eV and a doping concentration  $4.3 \times 10^{17} \text{ cm}^{-3}$  was found. The current transport mechanism through the Schottky diode was governed by thermionic field emission (TFE) and recombination. In the present work, the doping concentration is approximately the same but the barrier height is smaller due to inhomogeneous barrier height at the MS interface.

Another study has been reported by Benamara et al. [75] of Au/n-GaN Schottky contact over the temperature range 80-300 K. The films were grown by MOCVD method on sapphire substrates with a carrier concentration of  $10^{17} \text{ cm}^{-3}$  and a mobility 250  $\text{cm}^2/\text{Vs}$ . The ideality factor was found to be 1.18 at room temperature. The barrier

height value as computed from the I-V result at room temperature was equal to 0.84 eV. The reported conduction mechanism was thermionic field emission (TFE) and thermionic emission (TE) at lower temperature and higher temperature respectively. The estimated barrier height in this study is close to the one obtained by Kribes et al. [16] and they report the same reason for the conduction mechanism.

In another study, Osvald et al. [76] reported I-V characteristic of GaN Schottky diodes films grown by MOCVD and MBE on sapphire substrates. Films grown by MOCVD were Ga faced and those grown by MBE were N faced. The barrier heights for Ga and N faces-GaN were found to be 1.17 V and 0.89 V respectively. The ideality factor was 1.72 at 320 K for N-polarity. The authors pointed out that thermionic transport mechanism at room temperature was the possible conduction mechanism.

The barrier height as well as the activation energy had been studied by Miller et al. [77]. MBE GaN layer was grown at 600 °C on sapphire substrate. The barrier height was extracted from I-V measurement and yielded a value of 0.798 V. The activation energy was estimated by the Arrhenius plot to be 180±20 meV. A trap assisted tunnelling process was the current transport mechanism process.

To the best of our knowledge there is no complete study about the electrical properties of the c-GaN:Mn material. But, many were reported on wurtzite GaN:Mg which will be outlined below.

Both growth techniques; MOCVD and MBE had been used for p-type GaN studied by D.J.Kim et al. [78]. The substrate temperature was kept between 750-790 °C in case of MBE and 1030 °C for GaN: Mg layer grown by MOCVD. The hole concentrations of Mg doped samples grown by MBE and MOCVD were measured using Hall effect. These gave values of  $3-6 \times 10^{17} \text{ cm}^{-3}$  and  $2 \times 10^{17} \text{ cm}^{-3}$  at room temperature respectively. They obtained activation energy of Mg doped GaN using I-V and admittance spectroscopy in the range 110-120 meV.

In a later study, J.W.Kim et al. [79] investigated Mg-doped GaN grown by MOCVD where the wafer was annealed at 750 °C. The carrier concentrations estimated from Hall and C-V measurements were found to be of  $5.5 \times 10^{16} \text{ cm}^{-3}$  and  $8 \times 10^{18} \text{ cm}^{-3}$  respectively. It was found that the barrier height estimated from I-V data ranged from 0.29 to 1.21 eV. The room temperature value measured from C-V measurements was 1.43 eV. The activation energy determined from the Arrhenius plots obtained by admittance spectroscopy was 0.12 eV. Simulation program led the authors to consider the field-assisted emission phenomenon as current mechanism.

Huang et al. [80] used the admittance spectroscopy technique to estimate the activation energy for GaN:Mg samples grown by metal organic vapour phase epitaxy (MOVPE). The activation energy was found to be 136 meV. The reported impurity concentration was  $5 \times 10^{17} \text{ cm}^{-3}$  as measured by C-V at 1MHz while it was calculated from the charge neutrality equation to be  $6.67 \times 10^{18} \text{ cm}^{-3}$ . The studies discussed above reported similar activation energy of Mg doped GaN which ranged between 110-150 meV. Albeit, they grew their material using different growth methods, for instance, MBE, MOCVD and MOVPE methods.

These studies were concerned with wurtzite GaN doped material which gave p-type GaN, while the material used in this study is c-GaN doped with Mn which also gives p-type GaN. Although the properties of these two materials differ significantly.

Summary of all the results of various workers is listed in Table (3.2).

**Table 3.3 Different device parameters of Schottky contact to hexagonal GaN as presented by different workers.**

| Source               | The doping density $N_D$ ( $\text{cm}^{-3}$ )                 | Ideality factor $n$ | The barrier height $\Phi_b$ (V)       | The activation energy (meV) | Current mechanism        |
|----------------------|---|---------------------|---------------------------------------|-----------------------------|--------------------------|
| Kribes et al. [16]   | $7 \times 10^{17}$  | 1.4                 | 0.98 (I-V)<br>1.16 (C-V)              | -                           | TFE and recombination    |
| Benamara et al. [75] | $1 \times 10^{17}$  | 1.18                | 0.84                                  | -                           | TFE and TE               |
| Osvald et al. [76]   | -   | 1.72                | 1.17 (Ga faced)<br>0.89 (N faced GaN) | -                           | TE                       |
| Miller et al. [77]   | -   | -                   | 0.798                                 | $180 \pm 20$                | Trap assisted tunnelling |
| D.J.Kim et al. [78]  | $3-6 \times 10^{17}$ (MBE)<br>$2 \times 10^{17}$ (MOCVD)      | -                   | -                                     | 110-120                     | -                        |
| J.W.Kim et al. [79]  | $5.5 \times 10^{16}$ (Hall meas.)<br>$8 \times 10^{18}$ (C-V) | -                   | 0.29-1.21                             | 120                         | Field-assisted emission  |
| Huang et al. [80]    | $6.67 \times 10^{18}$ (C-V)                                   | -                   | -                                     | 136                         | -                        |

### 3.8 The study of electrical defects in cubic GaMnN

GaN can crystallize in the wurzite (hexagonal) or in the zinc blende (cubic) structure. Most studies have relevance to the wurzite structure rather than cubic. As a result, few papers concentrate on cubic structure.

#### 3.8.1 The native defects of wurzite GaN

In a recent paper Reshchikov and Morkoç [81] discussed the native defects in the GaN. On the basis of the information given in this paper, Table 3.4 was constructed.

**Table 3.4 Native defects in GaN**

|                   | Vacancy                      |                    | Interstitials     |                    | Antisite               |                        |              |
|-------------------|------------------------------|--------------------|-------------------|--------------------|------------------------|------------------------|--------------|
|                   | $V_{\text{Ga}}$              | $V_{\text{N}}$     | $\text{Ga}_i$     | $\text{N}_i$       | $\text{Ga}_{\text{N}}$ | $\text{N}_{\text{Ga}}$ |              |
| The material type | n-type                       | p-type             |                   |                    |                        | n-type                 | p-type       |
| Growth condition  | N-rich conditions            | Ga-rich conditions | N-rich conditions | Ga-rich conditions | Ga-rich conditions     |                        |              |
| Type of impurity  | Acceptor like defect centre) | donor              | donor             | Acceptor           | compensating           | Acceptor               | Double donor |

The main causes of point defects are non-stoichiometric growth and annealing [81]. They become a source of compensation in the doped material. According to Reshchikov and Morkoç [81] in n-type GaN, the Ga vacancy ( $V_G$ ) is the dominant native defect, while the Nitrogen vacancy ( $V_N$ ) is obtained in p-type GaN. The Ga vacancy ( $V_G$ ) and the N vacancy ( $V_N$ ) behave as acceptor and donor type defects respectively. When both types of defects are nearest neighbours, the resulting defect is called a divacancy ( $V_{Ga-V_N}$ ) and creates two deep levels in the energy gap. The type of defect depends on the material type. In n-type, it is a double acceptor while in p-type it is a double donor. The other types of native defects, which occur at lower concentrations, are interstitials and antisite defects. Both the Ga interstitial ( $Ga_i$ ) and the N interstitial ( $N_i$ ) can be introduced in the form of a donor or an acceptor respectively. The existence of a particular interstitial atom ( $Ga_i, N_i$ ) is determined by the small lattice constant of GaN as well as large “size mismatch” between Ga and N atoms, e.g. Ga atom, and due to its large size can be accommodated as a stable interstitial only at an octahedral site in the lattice. In P-type GaN, the Ga antisite ( $Ga_N$ ) defects are the native defects which cause compensation under the Ga-rich conditions while the N antisite ( $N_{Ga}$ ) acts as compensating double donor or an acceptor in p-type and n-type GaN respectively.

The unintentional defects like hydrogen act as acceptor in p-type GaN while oxygen also introduced unintentionally during growth process acts as a shallow donor in GaN.

### 3.8.2 The native defects of cubic GaN

Jian-jun et al. [82] have discussed the structure of the zinc blende (ZB). They identified the nitrogen vacancy as the main defect in the intrinsic cubic GaN. A large concentration of nitrogen vacancies gives rise to a large concentration of electrons which results in an enhanced conductivity. They believe that there are eight point defects in GaN. Table 3.4 shows the calculated formation energies for point defects in zinc blende GaN. These point defects are as follows; nitrogen vacancy ( $V_N$ ), gallium vacancy ( $V_{Ga}$ ),  $Ga_N$  antisite, ( $N_{Ga}$ ) antisite, a tetrahedral interstitial gallium surrounded by four N atoms ( $Ga_{iN}$ ), a tetrahedral interstitial gallium surrounded by four Ga atoms

(Ga<sub>I</sub>Ga), a tetrahedral interstitial nitrogen surrounded by four Ga atoms (N<sub>I</sub>Ga) and a tetrahedral interstitial nitrogen surrounded by four N atoms (N<sub>I</sub>N).

**Table 3.5 Formation energies for point defects in zinc blende GaN**

|       | V <sub>Ga</sub> | V <sub>N</sub> | Ga <sub>N</sub> | N <sub>Ga</sub> | Ga <sub>IN</sub> | Ga <sub>IN</sub> | N <sub>I</sub> Ga | N <sub>I</sub> N |
|-------|-----------------|----------------|-----------------|-----------------|------------------|------------------|-------------------|------------------|
| E(eV) | 7.57            | 0.89           | 16.56           | 2.30            | 15.69            | 12.70            | 1.85              | 2.53             |

In another study Lisker et al. [83] investigated the deep defects in cubic GaN. The samples were grown on SI-GaAs substrates by rf-plasma-assisted molecular beam epitaxy (MBE) at a substrate temperature of 720°C. Deep levels in MBE samples have been studied using thermal admittance spectroscopy (TAS) to obtain information about the defects. Three different kinds of layers of GaN were studied. All were nominally undoped. The first group was nominally undoped p-type GaN-layers with carrier concentrations of  $(1-5) \times 10^{16} \text{ cm}^{-3}$ , (2) nominally undoped, p-type GaN- layer on top at a p-type GaAs buffer layer and (3) n-type GaN layers slightly Si-doped with carrier concentrations below  $10^{14} \text{ cm}^{-3}$ . Thermal admittance spectroscopy (TAS) detects a defect with energy level  $(530 \pm 30) \text{ meV}$  located in the GaAs substrate. Using the same technique another defect with thermal activation energy of  $(105 \pm 15) \text{ meV}$  was detected which was located within the GaN layer.

### ***3.9 Studies of doped cubic GaN***

The electrical properties of cubic GaN doped with different impurities have been discussed by many authors. For instance As et al. [84] investigated Si doping of cubic GaN grown by (RF) plasma assisted molecular beam epitaxy on semi-insulating GaAs (001) substrates at 720°C. The films exhibit n-type conductivity with concentrations reaching  $5 \times 10^{19} \text{ cm}^{-3}$ . They found high density of the dislocation in c-GaN:Si. By measuring the electron mobility against carrier concentration, they concluded that the dislocations act as acceptors.

In another study As et al. [85] discussed both p- and n- type doping under the same growth details. Acceptor activation energy ( $E_A$ ) of 0.230 eV was estimated for Mg by low temperature photoluminescence (PL) measurement. At concentrations above

$10^{18} \text{ cm}^{-3}$  the PL spectra contained more lines and they attributed these to complexes that act as compensating donors.

Cubic (zinc-blende) GaMnN films grown under N-rich conditions by plasma-assisted molecular beam epitaxy (PA-MBE) on GaAs (001) substrate have been discussed in a comprehensive study by Novikov et al.[65] and Edmonds et al.[4]. This data is important for this study since their samples were also grown at Nottingham University. Growth temperatures were in the range 450 to 680 °C. RHEED and X-ray studies showed that GaMnAs films had cubic symmetry and there was no evidence of the  $\text{Mn}_4\text{N}$  phase for Mn concentration of  $x < 0.1$ , while Auger measurements and secondary ion mass spectroscopy (SIMS) studies indicated that concentration of Mn atoms in the film increased with the Mn/Ga flux ratio. SIMS studies showed that the Mn concentration was  $4.5 \times 10^{20} \text{ cm}^{-3}$  with  $x \sim 0.01$ . Also, there was no indication of diffusion of Mn into the buffer layer. The hole concentration varied from  $3 \times 10^{16}$  to  $5 \times 10^{18} \text{ cm}^{-3}$ .and the ionization energy was 54 meV. These measurements were obtained from the Hall effect. The group confirmed p-type conductivity in these  $\text{Ga}_{1-x}\text{Mn}_x\text{N}$  films with  $x > 0.05$  by checking for the existence of other potential dopants like Mg and C.

Lazarov et al. [72] studied cubic and hexagonal GaMnN and the role of Mn and H in these films. Films were grown by electron-cyclotron resonance (ECR) plasma-assisted MBE on 6H-SiC and MgO substrates and then annealed at 800 °C. Two different growth schemes: (i) multilayer deposition of Mn/GaN (two samples), both samples were capped with 30 nm GaN, (ii) deposition with 5% Mn-doped GaN in the presence of hydrogen (one sample). The GaN buffer and capping layers were grown at 550 °C. There is no indication for  $\text{Ga}_x\text{Mn}_y$  or  $\text{Mn}_x\text{N}_y$  phases in the multilayer films although, they confusingly reported that  $\text{Mn}_x\text{N}_y$  phase could be the source of ferromagnetism in hexagonal GaMnN. The examination of the film structure and surface morphology showed that Mn atoms diffuse to the surface. The surface protrusion of the cubic GaMnN was formed due to either the diffusion of Mn atoms through the capping layer or threading defects. They concluded that when Ga was substituted by Mn, the cubic phase became more stable and threading dislocations assisted in the diffusion of the Mn to the surface.

### 3.10 General features of GaAs

The zinc blende structure comprises two interpenetrating face centered cubic (fcc) sublattices where one sublattice is offset from the other by one quarter of the body-diagonal. In cubic GaAs (zinc blende structure) every Ga atom has 4 nearest neighbour As atoms which form a tetrahedron around the Ga atom. The energy band gap at room temperature is 1.42 eV.

### 3.11 General features of the (Ga, Mn)As

(Ga, Mn)As had been widely studied because of its relatively high Curie temperature  $T_C$  currently recorded at 173 K [86]. As previously discussed, nonmagnetic III-V semiconductors such as GaAs could be made ferromagnetic via doping with Mn [43]. Haisy and Cronin (1964) [87] found a 0.1eV acceptor level of Mn in GaAs as a result of impurities while Ohno et al. (1996) reported ferromagnetism in epitaxial films of GaMnAs grown by MBE [3]. GaMnAs had been successfully grown using MBE at low substrate temperatures [60].

The formation of As anti-sites ( $As_{Ga}$ ) and Mn interstitial ( $Mn_I$ ) defects occur which compensate substitutional Mn acceptors ( $Mn_{Ga}$ ). These defects can be removed by low temperature annealing at 175 °C which leads to an increase in uncompensated ( $Mn_{Ga}$ ) and enhancement of hole concentration [88]. The effect of the annealing is observed by the resistivity measurement. Annealing is a two step process involving; removal of the Mn interstitial ( $Mn_I$ ) and Mn from the Ga sites which leads to low activation energy in the former case and higher activation energy in the latter [88]. The low temperature annealing affects the lattice constant due to evaporation of excess As atoms that form complexes with Mn acceptors [89]. By substituting Mn for Ga in the GaAs lattice, Mn acts as an acceptor, mediating ferromagnetism [90].

### 3.12 The electrical measurements on the GaAs

There has been considerable interest in the measurement and understanding of Schottky contacts on GaAs and related compounds. This is clearly shown by using ISI index. Over 1250 papers were found with both Schottky and GaAs in their titles. Rather than giving an in depth discussion of Schottky contacts to GaAs a very brief review of papers relating to the measurements have been presented below. In many papers [13, 28, 30, 91-93], the temperature dependence of the ideality factors ( $n$ ) has been explained by the “ $T_0$ ” effect and the value of “ $T_0$ ” determined by plotting  $n$  versus  $10^3/T$ . In the following studies the ideality factor and “ $T_0$ ” effect have been estimated in the GaAs grown by different methods.

Bengi et al. [91] discussed the electrical characteristic of Au/n-GaAs structure. It was grown by solid source molecular beam epitaxy (MBE) on Zn-doped (100) GaAs substrate and undoped GaAs as a buffer layer. On the top of the buffer layer there was layer of Si doped n-type GaAs. The ideality factor ranged between 3.97 and 1.04 at 79 K and 400 K respectively. “ $T_0$ ” effect, which represents a measure of the variation of the ideality factor with temperature [30], was observed with a value of “ $T_0$ ” as 323.42 K for Au/n-GaAs structure. The temperature dependent behaviour of the ideality factor indicates that the thermionic field emission (TFE) is the likely conduction mechanism. The high value of the ideality factor at low temperatures suggests that there is a recombination of the carriers through the interface states and a potential drop in the interfacial layer and a significant difference between the apparent barrier heights obtained from forward bias I–V (0.36 eV) and reverse bias C–V characteristics (1.198 eV) at room temperature. They conclude that the mechanism that dominates the forward current is the trap-assisted multistep tunnelling in the GaAs space charge region.

The current–voltage characteristics of Au/ n-GaAs Schottky diodes grown by MOCVD method were discussed by Hardikar et al. [92]. I-V characteristics were determined at various temperatures in the range of 77–300 K. The barrier height estimated from I-V data was 0.89 eV and C-V measurements yielded 1.012 eV for the barrier height. While the ideality factor exhibited a  $T_0$  effect with  $T_0 = 17.1 \pm 1.2$  K, TE and TFE were considered possible conduction mechanism.

Karatas and Turut [93] determined the barrier heights for n-type GaAs wafer from I-V and C-V measurements as 0.88 eV and 1.14 eV respectively. Not much information was given about the method of growth except for the surface treatment of the samples. In another work Karatas and Altindal [28] reported a value of  $473 \pm 1.2\text{K}$  for  $T_0$  factor. They considered the TFE as the mechanism controlling the current conduction.

There appears to be a considerable variation in the values of  $T_0$  as reported by different workers in previous references. The reported values of  $T_0$  given by Rhoderick [13] varied from 10K up to 100K and one of the explanations of the variation of  $T_0$  value was a non-uniformly doped surface layer. This may be considered as a possible reason in the materials under study; one of the results reported in this work is close to the value reported by Karatas and Turut [93]. The results of measurements reported by some workers are summarised in Table (3.5).

**Table 3.6 Results of some workers for Schottky contact to GaAs.**

| Source                 | $T_0$ effect (K)       | Ideality factor n | The barrier height $\Phi_b$ (V) | The activation energy (meV)                |
|------------------------|------------------------|-------------------|---------------------------------|--|
| Bengi et al. [91]      | 323.42                 | 3.79-1.04         | 0.36 (I-V)<br>1.198 (C-V)       | TFE and trap-assisted multistep tunnelling |
| Hardikar et al. [92]   | $17.1 \pm 1.2\text{K}$ | -                 | 1.012 (C-V)                     | TFE and FE                                 |
| Karatas and Turut [93] | $473 \pm 1.2\text{K}$  | -                 | 0.88 (I-V)<br>1.14(C-V)         | TFE  |

### 3.13 The native defects in the GaAs

The growth temperature varies from  $230\text{ }^{\circ}\text{C}$  to  $580\text{ }^{\circ}\text{C}$  for the GaMnAs samples used in this study and so the native defects in LT-GaAs need to be reviewed.

Deepak and Lakshminarayana [94] believe that the defects in GaAs are native to the material. Their model consists of eight types of point defects, the vacancy of Ga and As, their antisites and interstitials of Ga and As on both sub-lattices of GaAs. The concentrations of the defects are easily affected by to the crystal stoichiometry. It is found that in the case of semi-insulating (SI) GaAs, grown under As-rich condition, the

concentrations of the defects are very high and pin the Fermi level in the centre of the band gap. The electronic structure of GaAs point defects are listed in Table 3.6 according to the categories listed above where the subscripts represents the site and the interstitial I1 (I2) has 4 As (Ga) neighbours.

**Table 3.7 The formation energy and the ionization energy of different defects given in [94]**

| Defect                | $V_{Ga}$ | $V_{As}$ | $Ga_{I1}$ | $Ga_{I2}$ | $As_{I1}$ | $As_{I2}$ | $As_{Ga}$ | $Ga_{As}$ |
|-----------------------|----------|----------|-----------|-----------|-----------|-----------|-----------|-----------|
| Formation energy (eV) | 4.55     | 2.97     | 2.14      | 2         | 6.14      | 6.14      | 2.5       | 2.74      |

In another study Nabet et al. [95] discuss the formation of deep traps in GaAs grown at low (200 °C) and intermediate (400 °C) temperatures by molecular beam epitaxy (MBE). They conclude that the current transport in low temperature/intermediate temperature grown GaAs is dominated by defects and hopping conduction. They also postulate that since GaAs is grown from an As-rich melt, it will incorporate an excess of As antisites and interstitials defects. These defects are primarily responsible for tunnelling conduction. Such defects are located 0.5 eV below the conduction band.

Their conclusions are also supported by the findings of other workers. Rubinger et al. [96] report hopping conduction among arsenic antisites defect ( $As_{Ga}$ ) in LT-MBE GaAs samples grown between 265 °C and 345 °C. Krambrock et al. [97] and Look et al. [98] suggest the carrier hopping is between  $As_{Ga}$  defects. They relate  $As_{Ga}$  defects to the EL2 defects using magneto-optical and Hall-effect investigation. Hopping conduction is also reported by Weber [99] as possible mechanism in LT-MBE GaAs due to the existence of high concentration of  $As_{Ga}$  defects using magnetic circular dichroism (MCD). According to Thomas et al. [100], Arrhenius plot for current-temperature measurements for as-grown LT-GaAs show small activation energies of 0.07 eV and 0.17 eV for samples grown at 200 °C and 250 °C respectively compared to 0.63 eV to that of SI-GaAs. They relate the conduction mechanism to hopping.

### 3.14 *The study of structural and electrical defects in LT-GaAs and GaMnAs*

Several authors have studied defects formed in low temperature (LT) grown GaAs films [101-103]. Low temperature (LT) GaAs is grown between 200-400 °C [101]. During LT- growth of GaAs defects such as arsenic antisites ( $As_{Ga}$ ) are created with densities around  $10^{20} \text{ cm}^{-3}$  [101]. Despite the high concentration of defects, the material behaves in a semi-insulating manner (SI-GaA). So a great majority of these defects are arsenic antisites ( $As_{Ga}$ ) and are neutral [102]. It has been reported that some of the  $As_{Ga}$  sites are positively charged. The existence of positively charged  $As_{Ga}$  sites is an indication that the “donor electrons” have been “accepted” at some location in the structure. Since Ga vacancies act as triple acceptors ( $V_{Ga}$ ), these are the most likely cause of compensation of  $As_{Ga}$  sites [104]. It is believed that compensation results in the “pinning” of the Fermi level in the midband region and leads to a semi-insulating (SI) material which is often used as a buffer layer in devices [102]. Salamov et al. [105] explain the semi-insulating behaviour of GaAs due to the presence of deep donors which results in shifting the Fermi level to the middle of the energy gap causing high resistivity properties.

Gebauer et al. [104] studied vacancy defects in GaAs grown at low temperature LT-GaAs by positron annihilation. They found the Gallium vacancies ( $V_{Ga}$ ) concentration to be about  $2 \times 10^{18} \text{ cm}^{-3}$  for samples grown at 200 °C. This density of Ga vacancies ( $V_{Ga}$ ) was sufficient to compensate the  $As_{Ga}^+$ , which was found in the LT-GaAs samples. Annealing at 600 °C removed  $V_{Ga}$  which was replaced by As – agglomerates.

Tanaka [103] reported arsenic antisites ( $As_{Ga}$ ) in both GaAs and GaMnAs materials grown by LT-MBE at 250 °C using Hall measurement. While interstitial Mn ( $Mn_i$ ) defects with Mn content up to  $x \sim 10\%$  had been found in GaMnAs. Both  $As_{Ga}$  and  $Mn_i$  acted as donors in GaAs and compensate holes.

S.Lee and D.Kim [106] reported metallic behaviour for  $\text{Ga}_{0.974}\text{Mn}_{0.026}\text{As}/\text{LT-As}$  epilayer grown on semi-insulating GaAs (0 0 1) substrates by MBE method. They measured the resistivity as a function of temperature to prove the metallic conductivity.

Tuomisto et al. [107] identified the native defects in their GaMnAs samples grown by LT-GaAs at temperature 210-240 °C. The Mn concentration extended between 0.5-5 %, while the hole concentrations were around 30% of the Mn concentration as determined from Hall measurements. These defects were arsenic antisites ( $\text{As}_{\text{Ga}}$ ) (donor-type) observed by positron annihilation with  $10^{20} \text{ cm}^{-3}$  concentration and Ga vacancy ( $\text{V}_{\text{Ga}}$ ) (acceptors-type) investigated with infrared absorption spectroscopy. The Ga vacancy concentration decreased while  $\text{As}_{\text{Ga}}$  concentration increased with the Mn content.

In another study, Tuomisto et al. reported Ga vacancies in LT-MBE GaMnAs layers with Mn concentration between 0.5-5 %. These Ga vacancies had been found in p-type material with As antisites. When the Mn contents increased these Ga vacancies decreased [51].

Different studies indicated that GaMnAs films had high conductivity at high Mn concentration while it ranged between metallic and insulating at lower Mn concentration. Annealing played an important role in removing defects in these samples.

The electrical properties of the GaMnAs grown by MBE with Mn contents varying between 0.5-8% was discussed by Campion et al. [60]. The structural properties of these films were studied by x-ray diffraction, while the Hall measurement was used to obtain the carrier density. Their films showed high conductivity due to the reduction in both arsenic antisites ( $\text{As}_{\text{Ga}}$ ) and interstitial Mn ( $\text{Mn}_{\text{I}}$ ) defects. The latter effect was due to annealing process and was determined by observing the hole density which was reduced due to compensation of donors by Mn. They concluded that GaMnAs film with Mn concentration ranged from 1.5-8 % show metallic conduction. The removal of the Mn interstitial ( $\text{Mn}_{\text{I}}$ ) was related to an increase in Curie temperature after annealing.

In another study Campion et al. [49], discussed the procedures of removing the defects in GaMnAs film grown at low growth temperature. Among these procedures were to grow the films grown near the stoichiometric ratio (As:Ga) to remove  $As_{Ga}$  defects as well as using  $As_2$ -dimers for its shorter lifetime compared to  $As_4$ - tetramers. Annealing at low temperature was used to remove interstitial Mn ( $Mn_I$ ) and Mn at Ga site which acted as a double donor in GaMnAs. The annealing process caused the  $Mn_I$  atom to diffuse to the surface where they were oxidized.

Annealing the LT-MBE GaMnAs grown below 300 °C, with Mn content more than 1 at.% had been discussed by Sadowski [50]. The structural defects ( $As_{Ga}$ ) were observed with concentration around 0.5 at.%. While 20% of the Mn content was in the form of the interstitial Mn ( $Mn_I$ ) which acted as a double donor and partially compensated  $Mn_{Ga}$  acceptor. Unwanted phase like zinc-blende MnAs phase was formed as a result of annealing. On the other hand, this increased the ferromagnetic to paramagnetic phase transition temperature in the GaMnAs.

## CHAPTER 4 Setup of the Equipment

### *4.1 Introduction*

There are many electrical techniques used for detecting and characterising electrical defects in semiconductors. Invariably, these techniques require the temperature of the sample to be scanned. This requires the samples to be placed in a suitable cryostat. In this thesis, the samples were mounted in a closed cycle Janis CCS-450 cryostat which allowed the temperature of the device to be varied between 5K and 475K with the actual temperature being controlled by a Lake Shore temperature controller. The temperature controller and the measurement electronics, Keithley 238 source measurement unit, Boonton model 7200 capacitance meter and Wayne Kerr 6640B LCR analyser were all computer-controlled using the general Purpose Interface Bus (GPIB) for communication.

### *4.2 The experimental setup*

All experiments were performed at King Fahd research centre in Jeddah Saudi Arabia. The apparatus used for measurements was setup, tested and calibrated during the course of the PhD work. The experimental setup used for measuring the I-V-T, C-V-T and F-C-T characteristic is shown schematically in Figure 4.1. Each individual block is described in the subsequent sections.

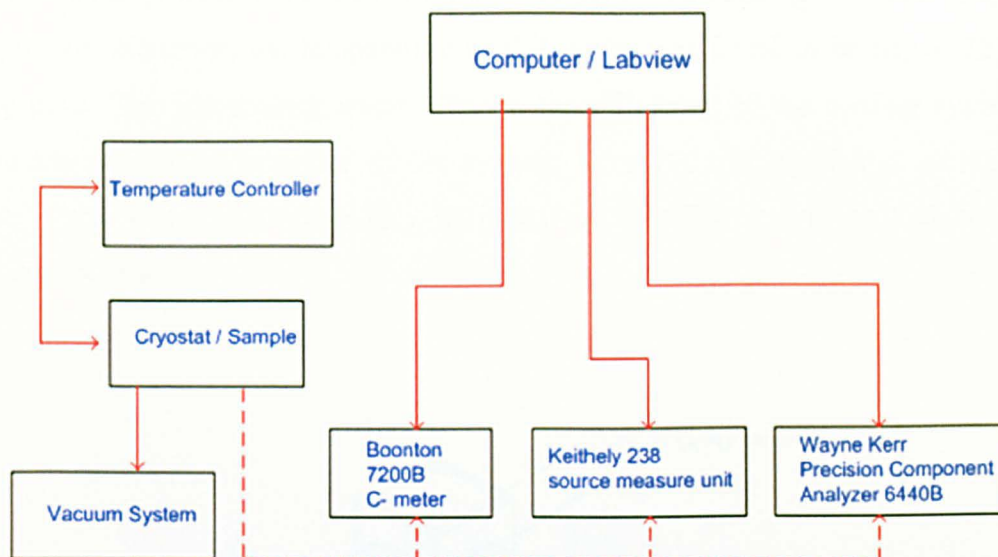


Figure 4.1 The setup of the equipment for this study

#### 4.2.1 Sample mounting

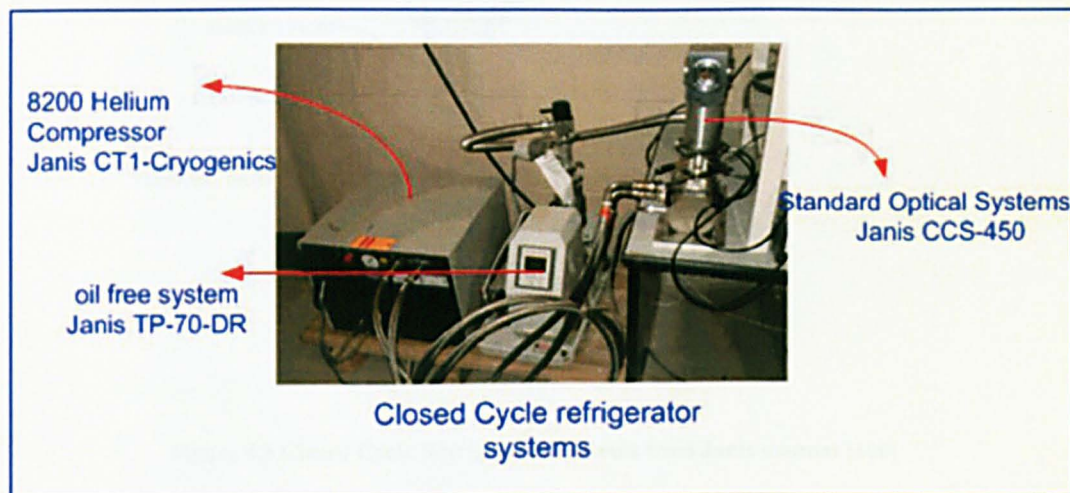


Figure 4.2 Closed Cycle refrigerator (CCR) for the system used in this study

The schematic arrangement of the cryostat, where the samples were mounted, and the associated vacuum system are shown in Figure 4.2. A Janis CCS-450 cryostat was used and the details are shown in the exploded view in Figure 4.3. The samples were mounted on a block inside the cryostat that could be maintained at any temperature from 5 K to 475 K on the basis of a heater / refrigerator principle. Cooling was provided by an 8200 Helium Compressor Janis CT1-Cryogenics system which required water

cooling. Initially, water from the main water supply of the building was used to cool the compressor. However, the temperature of this water was found to be above 32 °C on many days. The hot cooling water affected the efficiency of the cooling system and hence the overall performance of the system. To solve this problem a closed cycle chilled-water system was especially designed and installed which resulted in a more efficient cooling.

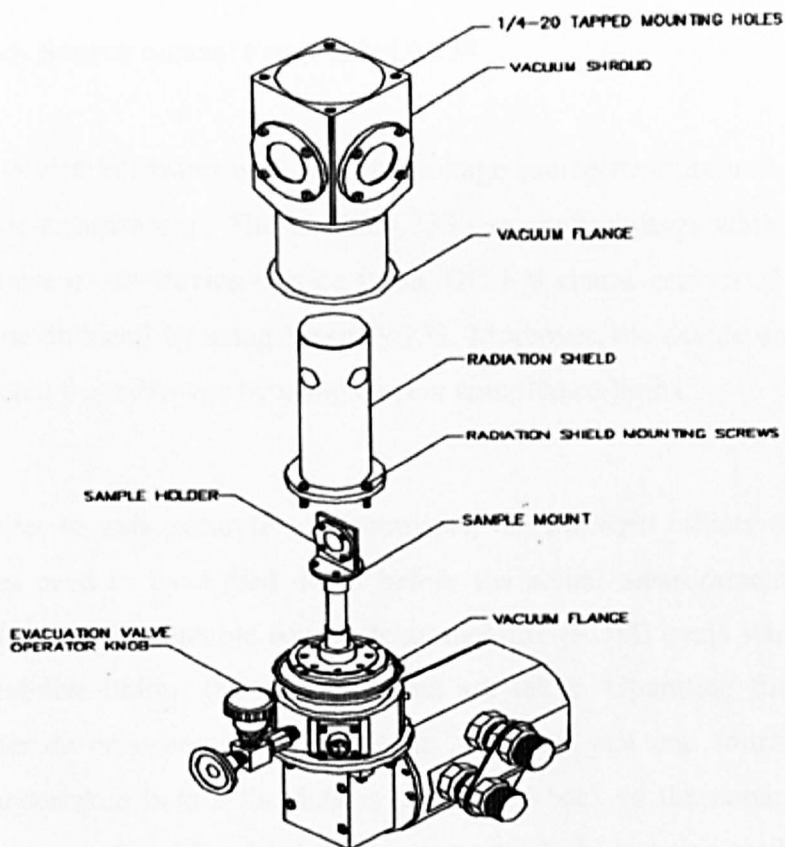


Figure 4.3 Closed Cycle Refrigerator Systems from Janis manual [108]

Since the lowest temperatures attained were close to liquid Helium, IR-radiation from the body of the cryostat tended to heat the sample. To circumvent this problem the sample holder was surrounded by a jacket that acted as a radiation shield. This jacket was also actively cooled to prevent the sample from heating. The vacuum system consisted of a turbomolecular pump which was backed by a rotary pump. The ultimate vacuum attainable was better than  $10^{-6}$  Torr.

### 4.2.2 Temperature Controller

A Lake Shore 331S automatic temperature controller was used to control the temperature of the sample holder block. The equipment was able to stabilize temperatures between 5 K and 475 K with an accuracy of about  $\pm 0.25$  K. This controller used a silicon diode as a detector and a  $25 \Omega$  heater. The heater powers are 250 mW, 2.5 W and 25 W for low, medium and high heater range respectively.

### 4.2.3 Keithley Source measure unit (SMU) 238

This device integrates both the high voltage source-measure unit (SMU) and the current source-measure unit. The Keithley 238 can apply voltage while measuring the current response of the device or vice versa. DC I-V characteristics of semiconductor devices can be obtained by using Keithley 238. Moreover, the device under test (DUT) can be protected from damage by using current compliance limits.

In order to gain accurate measurements, the transient effects of changing the source values need to have died down before the actual measurement is taken. The SMU provides a programmable source-delay measure (SDM) cycle which enables the source to stabilise before the measurements are taken. Operating functions can be selected either dc or sweep operation. In dc operation, just one source measurement cycles are undertaken before the data is transferred back to the computer. Since the GPIB bus data speed and handshaking is not particularly fast this method is slow. In sweep mode, multiple source measurement cycles are performed with the source changing after each measurement and the readings are stored internally in the SMU. After finishing the sweep, the whole data is transferred back to the computer. The SMU can store up to 1000 data points.

One of the reoccurring problems in the measurement of I-V characteristics is the inclusion of the resistance of the connecting leads. The classic way to overcome this problem is the use of 4 wires. The current is applied across the sample using two of the wires and the voltage across the device is measured using the other two wires. These wires are called the sense. The 'remote sense facility of the SMU implements this

measurement topology and allows the voltage to be measured across the DUT thus eliminating the voltage drop across the test leads or connections between SMU and the DUT.

#### 4.2.4 7200 Capacitance meter

A Boonton model 7200, a microprocessor based capacitance meter was used in this study. Measurements of fixed capacitors showed that this instrument was very susceptible to mains board interference and/or supply voltage fluctuations. Consequently, an AC voltage stabilizer was required to clean the mains signal and to ensure that the reading is accurate and stable. The equipment measures capacitance using a 1 MHz signal with amplitude of down to 5mV. The device calculates and displays the series and parallel resistances, series and parallel capacitances, dissipation factor and the quality factor. This instrument is also capable of providing a voltage (internal bias) for biasing a DUT over a voltage range of  $\pm 100$  V. The accuracy of the measured capacitance is better than 0.5% of the measured value. Moreover, it has the facility for providing external biases. Stray capacitances can be eliminated from the measurements by an automatic zeroing facility.

#### 4.2.5 Precision Component Analysers 6640B

For any passive component, reactance (serial model) or admittance (parallel model) can be automatically measured as a function of frequency using the precision component Wayne Kerr 6640B analyser. It has an operating frequency range from 20 Hz to 3MHz. The signal level can be chosen from 1 mV<sub>rms</sub> to 10 V<sub>rms</sub>. This is important because the measured reactance of a non linear device, like a Schottky diode will be averaged over the peak to peak value of the measurement signal. It also has a facility of trimming to cancel the stray capacitance or series impedance effects. The purpose of the trims and high frequency (HF) calibration is to remove the parasitic inductance, resistance and capacitance of the measurement cables from the measured result. Without trims and calibration, the measured result will be for the DUT plus the measurement leads. For open circuit trim the leads may be arranged so that they are in the same position as when they were connected to the device, but with the device removed. To

perform short circuit trim, the wires leading to the sample (DUT) are shorted by a wire. HF compensation is similar to short circuit trim, but the short is replaced by a 150 pF capacitor supplied with the 6440B.

#### 4.2.6 LabView program

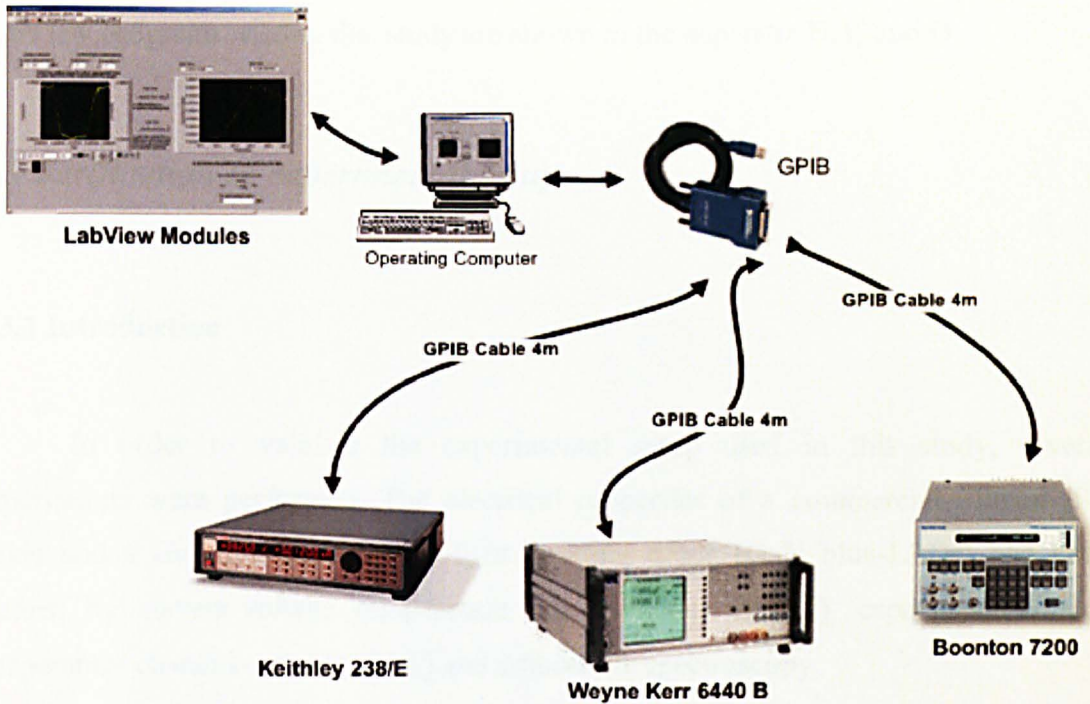


Figure 4.4 The arrangement of the GPIB connection

The general purpose-interface bus (GPIB) is used to send information between two devices usually the instrument and the PC. All the devices are connected to GPIB cables. Each device has an address, which is a number from 0 to 30. The important messages that the GPIB control carries are programming commands and measurement results. The arrangement of the GPIB connection for the devices used in this study is shown in Figure 4.4.

The important step in GPIB control is to initialize the instrument to prepare the interface to be ready for operation. The next step is to send the different commands to a device. Immediately after an instrument has taken the measurements, these data are saved to a file where they can be transferred to a spreadsheet. All these commands are carried by the PC through LabView programs.

LabView programs are called virtual instruments (VIs). The VIs contain the front panel which represents the user interface that allows the user to set appropriate device parameters. The other important aspect of the VIs is the block diagram. The block diagram contains the objects which can represent either front panel objects, mathematical operations, or other VIs and computer interface VIs. By wiring these components together a program can be written that performs the necessary tasks to control the measurement equipment, retrieve and save the data. The flow charts of the LabView programs used in this study are shown in the appendix B, C and D.

### ***4.3 Verification of experimental setup***

#### **4.3.1 Introduction**

In order to validate the experimental setup used in this study, several experiments were performed. The electrical properties of a commercial Silicon (Si) diode and a Gallium Nitride blue light emitting diode (GaN blue-LEDs) had been studied by current-voltage temperature characteristics (I-V-T), capacitance-voltage temperature characteristics (C-V-T) and admittance spectroscopy.

#### **4.3.2 Si diode**

A set of measurements were undertaken to identify the electrical properties of a Si commercial diode (1N4001). Figure 4.5 (a) and (b) show the measured IV characteristics of the diode under both forward and reverse biases. Figure 4.5 (a) shows the current plotted linearly and in (b) on a log scale. Since the reverse bias current is negative, the modulus has been taken so that it can be plotted on the figure. The measurements were carried out at different temperatures in the range 50 to 420 K.

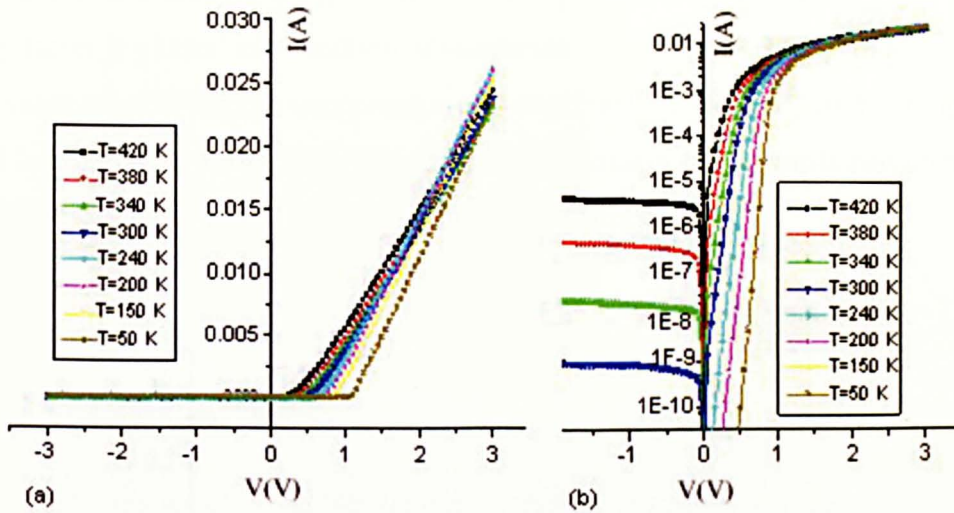


Figure 4.5 The experimental linear (a) and semi-log (b) in forward and reverse I-V characteristics of the Si diode at different temperatures in the range 420-50K

The reverse current was in the order of 1 nA at -2 V and 1.3 nA at -3 V at room temperature. From simple theory, the reverse bias current should be constant at this voltage range. Plotting the I-V-T data on log I-V scale as shown in Figure 4.5 (b) gives a straight line relationship at lower forward biases where this region is governed by thermionic emission mechanism.

Table 4.1 Some of the parameters estimated from I-V data shown in Figure 4.5.

| T   | $I_s$ (A)      | $R_s$ ( $\Omega$ ) | n           |
|-----|----------------|--------------------|-------------|
| 420 | 4.6E-06±2E-05  | 101.7±0.1          | 1.69±0.0005 |
| 400 | 1.3E-06±8E-07  | 103±0.2            | 1.6±0.0006  |
| 380 | 3E-07±2E-07    | 104±0.2            | 1.56±0.0005 |
| 360 | 7.5E-08±6E-08  | 103±0.2            | 1.54±0.0005 |
| 340 | 1.85E-08±1E-08 | 102.4±0.2          | 1.57±0.0004 |
| 320 | 2.5E-09±2E-09  | 102±0.2            | 1.5±0.0003  |
| 300 | 7.3E-10±5E-10  | 98.5±0.2           | 1.54±0.0003 |
| 280 | 1E-10±1E-10    | 92±0.2             | 1.55±0.0003 |
| 260 | 7.3E-12±6E-05  | 87±0.2             | 1.55±0.0002 |
| 240 | 1.2E-12±2E-12  | 85±0.2             | 1.6±0.0002  |
| 220 | 1 E-13±1E-11   | 82.8±0.3           | 1.67±0.0002 |
| 200 | 1.3E-14±3E-14  | 81±0.4             | 1.8±0.0005  |
| 150 | 2E-16±2E-14    | 76±0.3             | 2.4±0.0001  |

Out of the forward characteristic, the saturation current ( $I_s$ ), the series resistance ( $R_s$ ) and the ideality factor (n) can be found using least squares fit in Origin program.

The details of this method are given later. These parameters are listed in Table 4.1. The ideality factor is plotted as a function of temperature in Figure 4.6. This diode exhibits a lower value of  $n$  at higher temperature  $n=1.5\pm 0.0003$  of around 320 K compared to around  $2.4\pm 0.0001$  at 150 K where the current mechanism can be explained on the basis of thermionic emission (TE) and thermionic field emission (TFE).

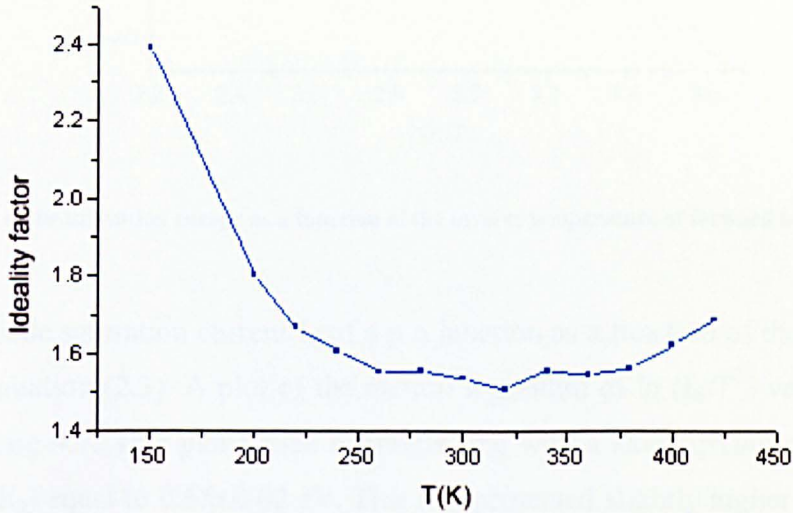


Figure 4.6 Ideality factor versus temperatures for Si diode

Figure 4.6 shows that the ideality factor  $n$  decreases when the temperature is increased to 320 K. Above this temperature, it tends to increase again leading to an increase in the generation current of the depletion region. This indicates that the generation current becomes important at this temperature range.

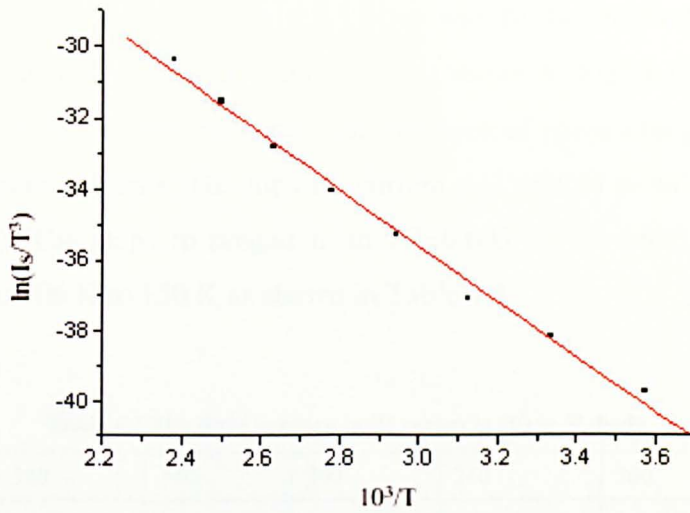


Figure 4.7 Plot of the activation energy as a function of the inverse temperature of forward bias for Si diode

The diode saturation current  $I_S$  of a p n junction as a function of the temperature is given by equation (2.3). A plot of the natural logarithm of  $\ln(I_S/T^3)$  versus  $10^3/T$  is shown in Figure 4.7. This plot yields a straight line with a slope giving the activation energy  $E_a$  ( $\sim E_g$ ) equal to  $0.65 \pm 0.02$  eV. This is represented slightly higher than the half energy gap of the Si diode ( $\sim 0.56$  eV).

The estimated energy position of the gold-acceptor level in silicon given by Engstrom and Grimmesis [109] is 641 meV. This value compares favourably with the calculated value 654 meV. Thus, gold create strong recombination centres [110].

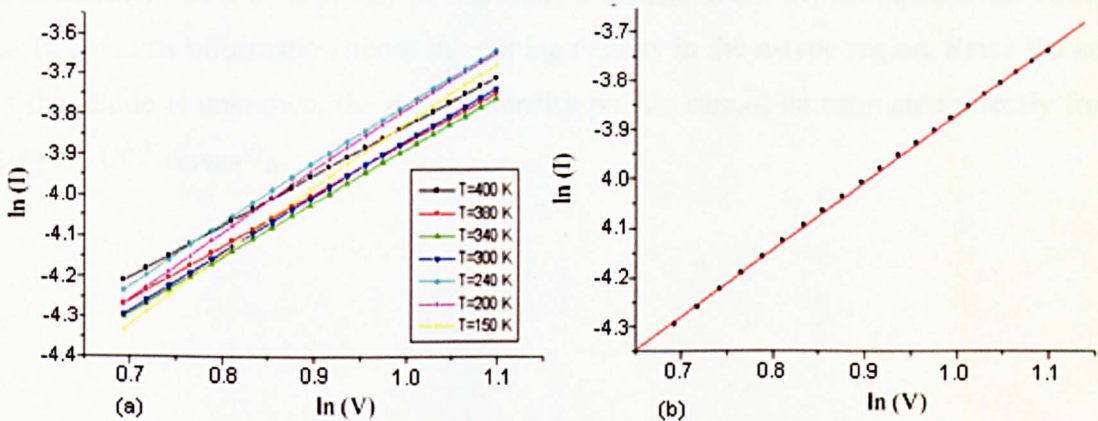


Figure 4.8  $\ln(I)$  versus  $\ln(V)$  at different temperatures (a) and at R.T. (b)

The conduction mechanism in this device was further studied by plotting both current and the voltage on the logarithmic scale as shown in Figure (4.8). The linearity of the  $\ln(I)$  versus  $\ln(V)$  plot indicated the presence of space charge limited current mechanism at higher voltages. The forward current was related to voltage and took the form of  $(I \propto V^m)$ . The slope  $m$  ranged from  $1.2 \pm 0.003$  eV to  $1.6 \pm 0.001$  eV over the temperature range 400 K to 150 K as shown in Table 4.2.

**Table 4.2 The slope between  $\ln(I)$  versus  $\ln(V)$  in Si diode**

|   |                 |                 |                  |                 |                  |                 |                 |
|---|-----------------|-----------------|------------------|-----------------|------------------|-----------------|-----------------|
| T | 400             | 380             | 340              | 300             | 240              | 200             | 150             |
| m | $1.2 \pm 0.003$ | $1.3 \pm 0.004$ | $1.36 \pm 0.005$ | $1.4 \pm 0.005$ | $1.45 \pm 0.007$ | $1.5 \pm 0.009$ | $1.6 \pm 0.001$ |

The C-V characteristics of the Si diode have been studied at different temperatures. It has been observed that the plot of  $1/C^3$  versus the reverse bias voltage is a straight line as in Figure 4.9 while, the plot of  $1/C^2$  versus the reverse bias ( $V_R$ ) does not fit to a straight line. Therefore, the junction of the Si diode is considered to be linearly graded rather than abrupt. The same result is obtained by Lucia et al. [111], using Si commercial diode (1N4001). In addition, C-V plots show that the capacitance is strongly dependent on temperature as well as the bias voltage.

At room temperature, the estimated built in voltage is 0.52 eV as shown in Figure 4.10. Close value was obtained by Lucia et al. [111] with a value of 0.59 V; also similar value for the built in voltage obtained by Sze [6] for Si diode. The silicon diode is assumed to be a  $p^+n$  diode. In this case, a measurement of the capacitance-voltage curve contains information about the doping density in the n-type region. Since the area of this diode is unknown, the doping density profile cannot be estimated directly from the plot  $1/C^3$  versus  $V_R$ .

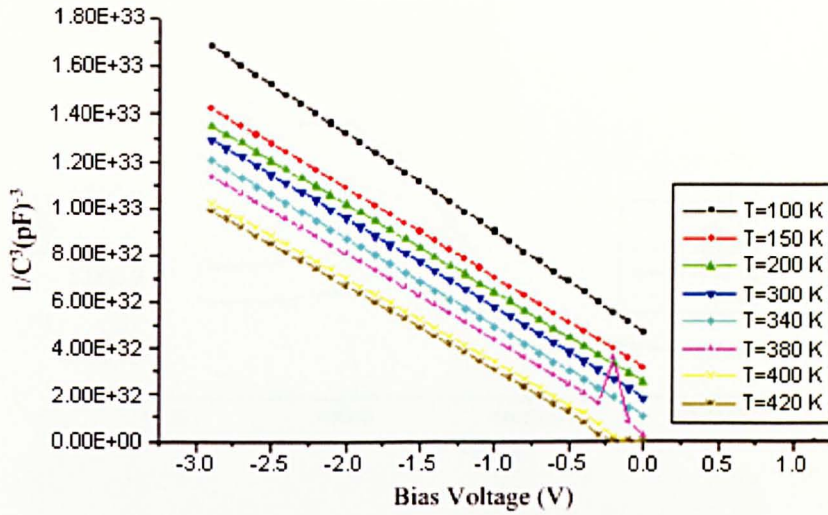


Figure 4.9 The plot of  $1/C^3$  versus  $V_R$  at various temperatures

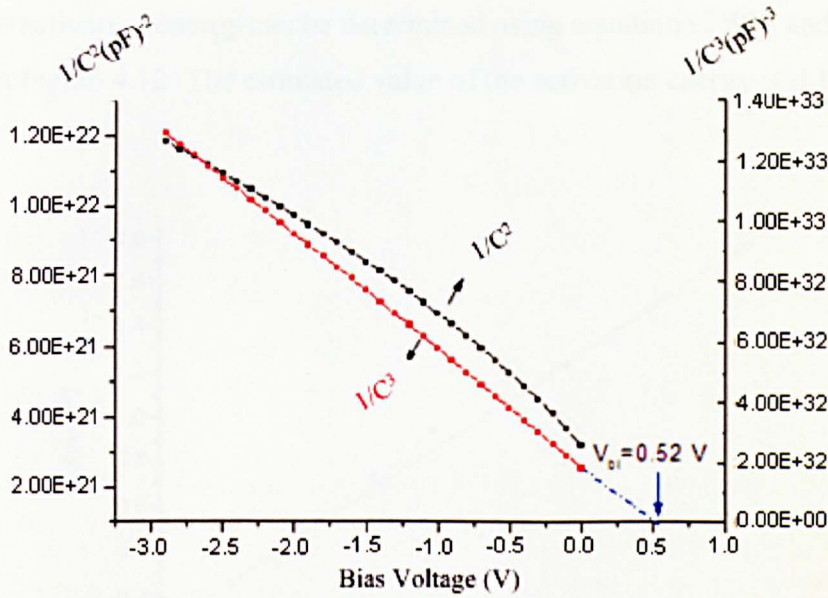


Figure 4.10 The plot between  $1/C^2$  and  $1/C^3$  as a function of reverse bias voltage

In order to obtain information about the traps in the energy gap of Si, admittance spectroscopy measurements was performed. The C-F characteristics of the Si diode had been investigated at different temperatures Figure 4.11. As discussed in chapter 2 section (2.4.1), the inflection frequency of these curves could be easily estimated using logistic equation (2.58).

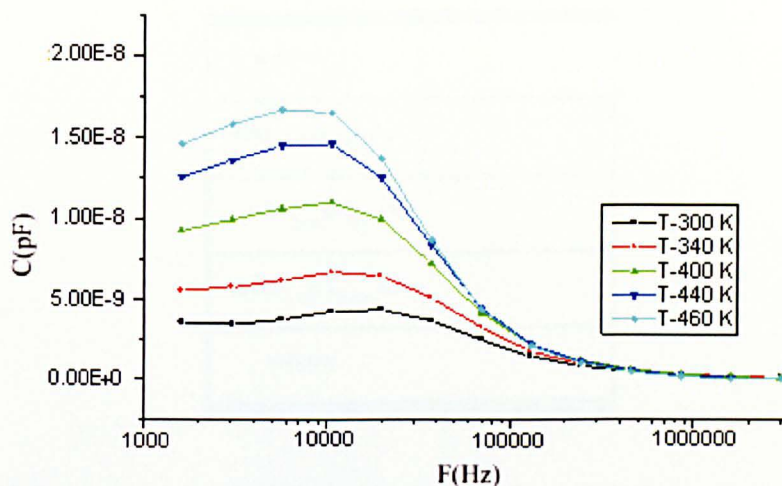


Figure 4.11 Capacitance –frequency curves temperatures between 300 and 460 K for Si diode

The activation energy can be determined using equation (2.59), and the final plot is shown in Figure 4.12. The estimated value of the activation energy is  $0.11 \pm 0.03$  eV.

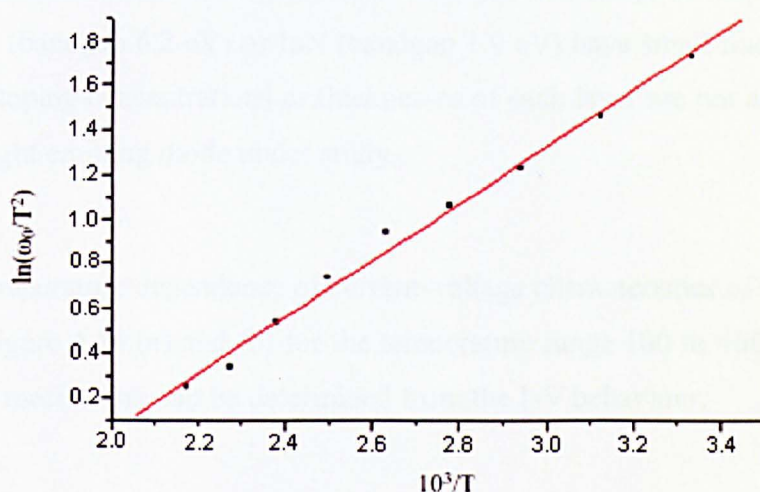


Figure 4.12 Arrhenius plot to get activation energy by admittance spectroscopy of Si diode

### 4.3.3 GaN light emitting diode

GaN as a direct band gap semiconductor is well suited for light emission. There are many applications for GaN blue light emitting diode LEDs. Lighting, displays and remote controls are examples of these applications. A light emitting diode (LED) is essentially a p-n junction diode [112].

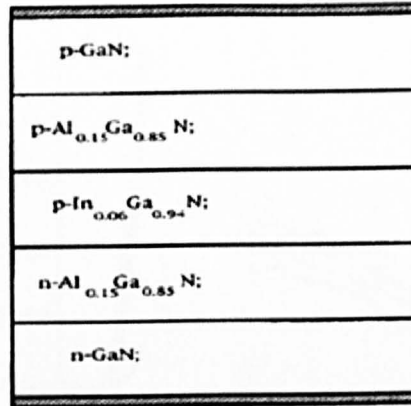


Figure 4.13 The structure of the light emitting diode similar to the Nakamura's device [113]

The famous light emitting diode fabricated by Nakamura's group is shown in Figure 4.13, further description is given in [113]. Two AlGaN layers and one InGaN layer sandwiched between p n GaN form the light emitting diode similar to Nakamura's device. Most of the light comes from InGaN layer which represents the active region in the system, the diode emits blue light with  $\lambda = 450$  nm. The alloys of GaN (bandgap 3.42 eV) with AlN (bandgap 6.2 eV) or InN (bandgap 1.9 eV) have small fraction compared to GaN. The doping concentrations or thicknesses of each layer are not available for the commercial light emitting diode under study.

The temperature dependence of current-voltage characteristics of GaN blue LED is shown in Figure 4.14 (a) and (b) for the temperature range 100 to 460 K. The nature of conduction mechanism can be determined from the I-V behaviour.

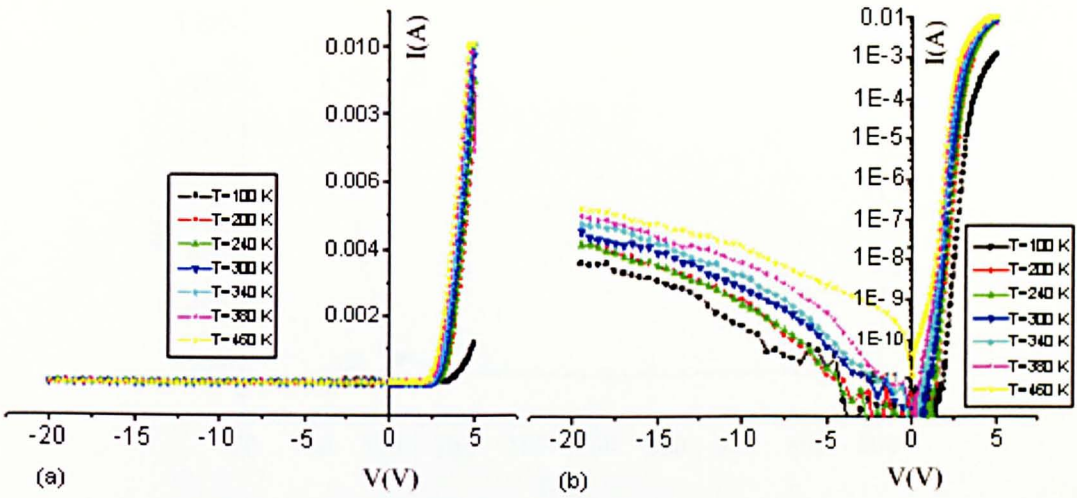


Figure 4.14 The experimental semi-log forward and reverse I-V characteristics of the GaN blue LED at different temperatures in the range 100-440K in linear and logarithm scale

As expected, the current has a higher value in the case of forward direction and increases exponentially with applied voltage until it is limited by the series resistance, as shown in Figure 4.14 (a). In both the forward and reverse bias cases, the IV characteristics are temperature dependent. In the reverse bias case, there is little sign of the diode breaking down. For example, at room temperature the leakage current is 67.9 nA at -20 V, which does not show an abnormal increase up to this voltage.

The forward I-V characteristics of GaN blue LEDs were analysed to determine the ideality factor and the saturation current. These were obtained from fitting a straight line to the linear regions of the log (I)-V curves at each temperature in Figure 4.14 (b) by the least square method using the origin program. The slope gives the ideality factor and the intercept on the current axis the saturation current.

The ideality factor  $n$  was found to vary between  $12 \pm 0.001$  and  $3.4 \pm 0.002$  between 100 K and 440 K. Therefore, this diode shows non-ideal behaviour because  $n$  is much higher than unity. The variation of the ideality factor  $n$  with temperature is shown in Figure 4.15. The curve shows that the ideality factor  $n$  is temperature dependent over the measured range of temperature.

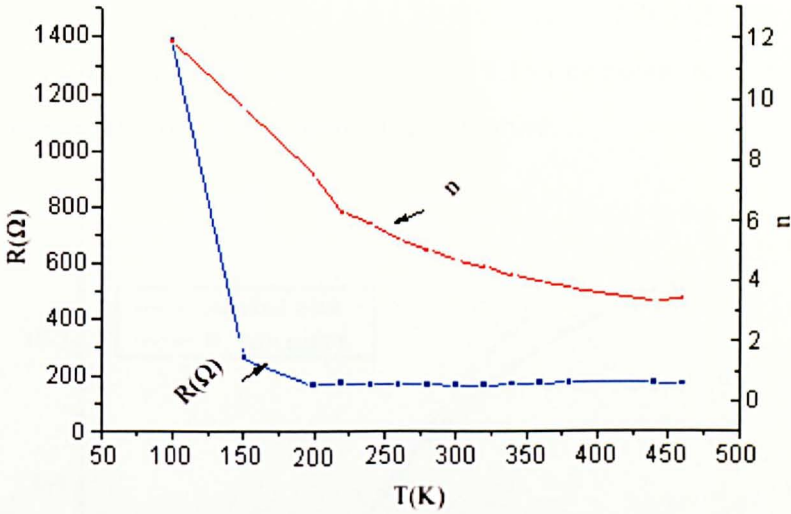


Figure 4.15 The ideality factor (red) and series resistance (blue) versus temperature for GaN-LED

Shah et al. [114] measured the ideality factors for three commercial GaN- based blue LEDs. They found that the ideality factors for these diodes were 3.2, 4.7 and 7.4. These values are close to the ideality factor measured for the device under study with a value of  $4.7 \pm 0.002$  at R.T. The high ideality factor is attributed to the sum of the ideality factors of the individual rectifying junctions with  $n = \sum_i n_i$  [114]. The ideality factor of the rectifying junctions for GaN-LED device consists of the p-n junction, the heterojunctions and the metal-semiconductor junctions represented by  $n_i$ .

One of the quantitative attempts to explain the abnormally high ideality factor was given by Di Zhu et al. [115]. They attributed high  $n$  ( $n > 2$ ) in GaN-LED to both trap assisted tunnelling and carrier leakage mechanisms.

In another study, Yang et al. [116] represent the total current injected into InGaN active region with radiative recombination current  $I_R$ , and nonradiative recombination current  $I_{NR}$ . The threading dislocation density of  $10^8 - 10^{11} \text{ cm}^{-2}$  is present in commercial III-nitride LEDs which tends to act as nonradiative recombination centres in the device [117].

The series resistance was obtained from the linear part of forward bias I-V plot which occurred at higher voltages where the current through the diode is limited by the series resistance  $R_S$ . The variation of the series resistance  $R_S$  with temperature is also

shown in Figure 4.15. Its value ranges over  $1380 \pm 37 \Omega$  to  $167 \pm 5 \Omega$  over a temperature range 100-400 K. In view of the results of Figure 4.15 one notes that the ideality factor and series resistance are strong functions of temperature.

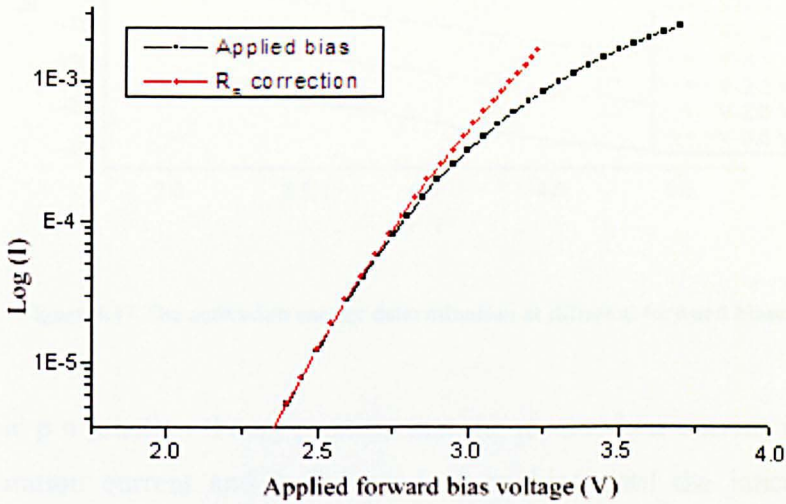


**Figure 4.16** I-V characteristic of the GaN-LED with the series resistance  $R_s$  (black dots) and the effect of series resistance removed (red dots) at room temperature

The plot of the forward I-V characteristics of GaN blue LEDs corrected for the series resistance at room temperature is shown in Figure 4.16. It is observed that the I-V characteristics are linear over several order of magnitude of the current. Since the ideality factor was found at low bias currents, the effect of the series resistance should be very small. This was verified by fitting the I-V curves after removal of the effect of the series resistance.

The temperature effect on the saturation current was discussed by Sze [6]. The equation which relates the  $I_s/T^3$  versus  $1/T$  should give a straight line with slope giving the band gap. For the device under study this relation is not valid due to the complicated structure which involves several heterojunctions. The plot  $\log(I)$  versus  $1/T$  is straight line at high temperature range at several fixed biases. The activation energy has been determined for forward biases from 1.4 V to 2.5 V using Arrhenius plot as shown in Figure 4.17. The activation energy is determined from the slopes of these curves; its values range from  $0.28 \pm 0.01$  eV at low forward voltages to  $0.2 \pm 0.0003$  eV at high forward voltages. These values compare favourably with the calculated value 0.27 eV from C-F measurement as will be seen later.

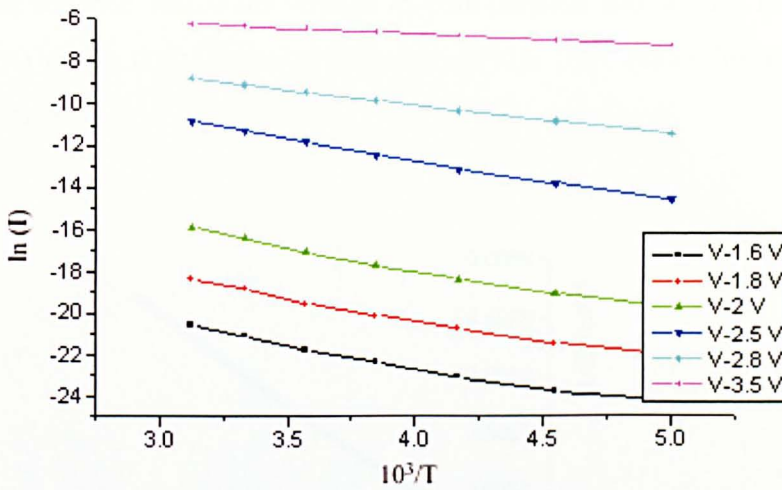


Figure 4.17 The activation energy determination at different forward biases

Simple p n junction theory predicts that the reverse bias current is given by the junction saturation current and is independent on bias until the junction begins to breakdown. However, the structure of GaN LEDs is complex. In the active layer, there are multiple InGaN recombination layers and probably an AlGaN barrier layers which aid the capture of carriers into the InGaN recombination layer [113]. These layers may also play an important role in the reverse characteristics of the diode. Barriers in both the conduction and valance band associated with the InGaN layer and the AlGaN could be the limiting factors to the reverse bias current. This is very similar to the Schottky diode.

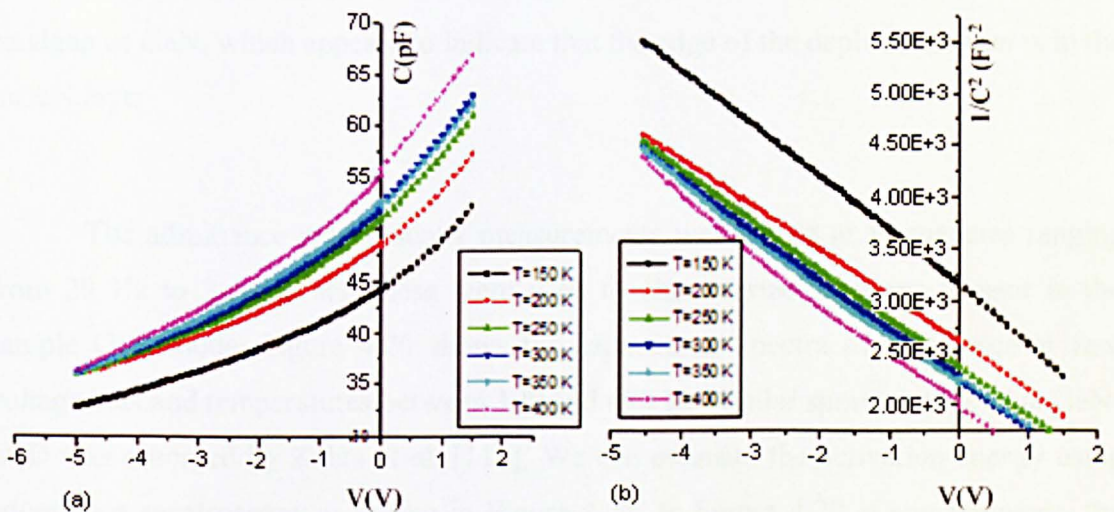


Figure 4.18 (a) The capacitance versus voltage in both forward and reverse biases at different temperatures and (b)  $1/C^2$  versus  $V_R$  measured for GaN-LED

The capacitance versus the voltage in both forward and reverse bias is shown in Figure 4.18 (a) which does not show linearity. While  $1/C^2$  varies linearly with  $V_R$  as shown in Figure 4.18 (b).

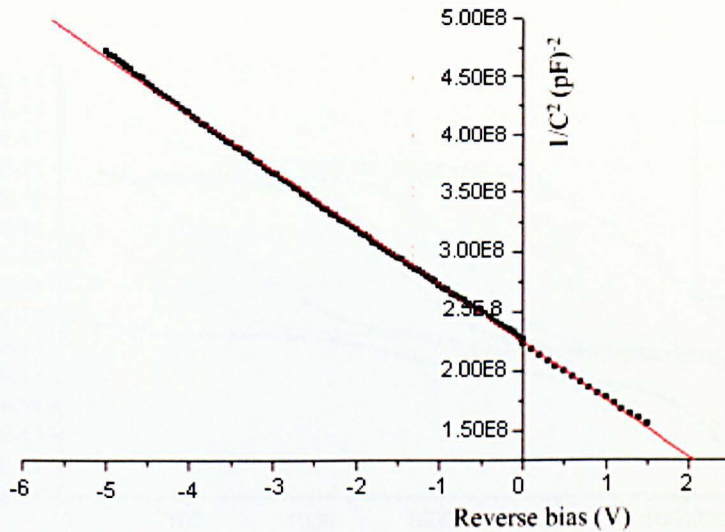


Figure 4.19 The plot of  $1/C^2$  versus  $V_R$  at room temperature

The plot of  $1/C^2$  versus  $V_R$  at room temperature is shown in Figure 4.19. There is a linear behaviour between  $1/C^2$  and  $V_R$ . By using equation (2.43) one can obtain the doping concentration  $N_D$ . The area of this device is not known. Therefore, it is difficult to estimate the doping concentration for the device under study. The intercept on the x-axis at a voltage  $V_0 = V_d - kT/q$  gives diffusion potential at around 2 eV. The diffusion potential ranges from 2.3 eV at 100 K to 1.8 eV at 420 K. This is low compared to the bandgap of GaN, which appears to indicate that the edge of the depletion region is in the InGaN layer.

The admittance spectroscopy measurements were made at frequencies ranging from 20 Hz to 3 MHz and these were used to characterize the traps present in the sample GaN diode. Figure 4.20 shows the capacitance spectra of the device at zero voltage bias and temperatures between 100 and 480 K. Similar spectra of the blue GaN-LED was observed by Zohta et al. [118]. We can estimate the activation energy using admittance spectroscopy as shown in Figure 4.21. In Figure 4.20 at any frequency the capacitance increases with temperature increase, and at any temperature, the capacitance decreases with frequency increase. At lower temperature range, the capacitance at low

frequency range seems to be constant, and at high frequency range, the capacitance decreases with increasing frequency. Conversely at higher temperature range, the capacitance at lower frequencies decreases with frequency increase while it approaches a constant value at higher frequencies.

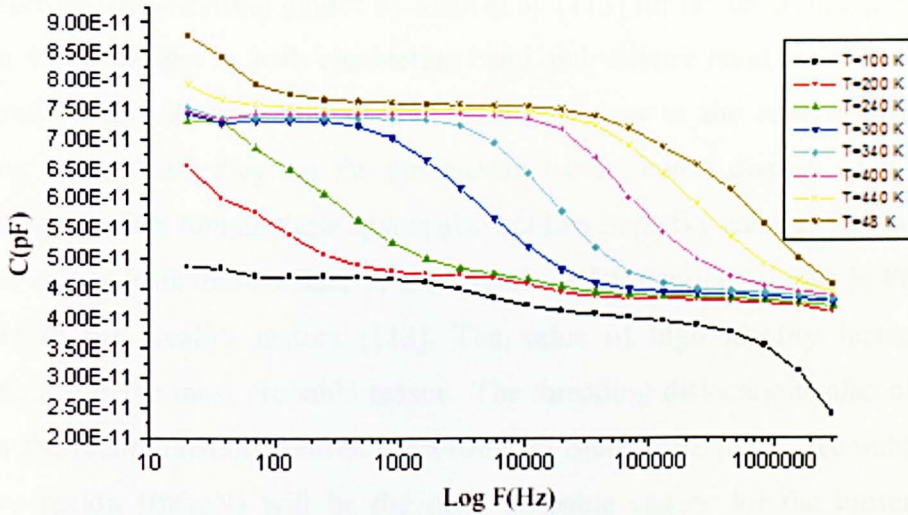


Figure 4.20 Capacitance –frequency curves temperatures between 100 and 480 K for GaN-LED

The inflection frequency  $\omega_0$  of Figure 4.20 can be determined by using the logistic equation at temperature 100-480 K. The inflection frequency is related to the emission rate of carriers from the traps ( $e_n$ ) by equation (2.59). Activation energy can be determined from the slope of  $\ln \omega_0/T^2$  as a function of  $1/T$ ; it has a calculated value of  $0.27 \pm 0.01$  eV. The depth of the Mg in GaN is between 120 and 300 meV [119].

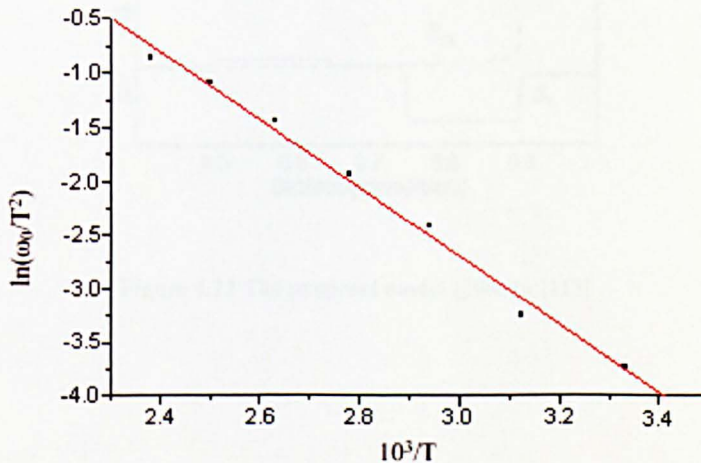


Figure 4.21 Arrhenius plot to get activation energy by admittance spectroscopy of the GaN (LED) device

Zohta et al. [118] have given a value of 70 meV which they consider to be low. According to them the value should be around 150 meV for the activation energy of holes from Mg acceptors.

The numerical simulations of AlGaIn/InGaIn performed on double-heterostructure light-emitting diodes by Shah et al. [113] for the band diagram are given in Figure 4.22. Barriers in both conduction band and valence band associated with the InGaIn and AlGaIn layers could be the limiting factors to the reverse bias current. According to the band diagram the conduction bands' edges display spikes through which charge carriers tunnel, these spikes also act like Schottky barrier. The capacitance behaviour comes from these spikes. A total number of 4 junctions shown in Figure 4.22 contribute to the ideality factors [113]. The value of high ideality factors due to recombination is the most probable reason. The threading dislocations also play a role acting as the recombination centres. According to Shah et al. [113], recombination in the active region (InGaIn) will be the most probable causes for the current at low voltages, while at high voltages the current mechanism is due to both the recombination in the active region as well as thermionic emission outside the active region.

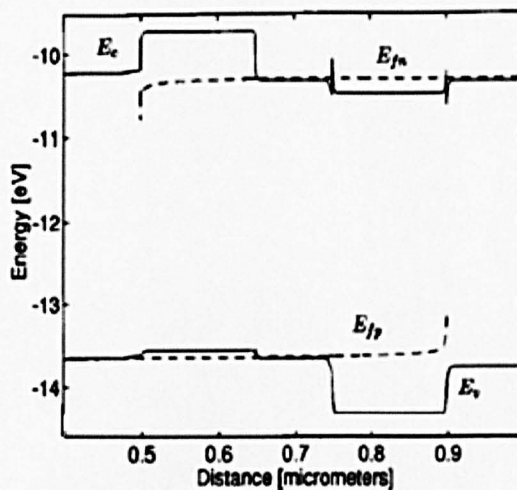


Figure 4.22 The proposal model given in [113]

#### 4.3.4 Conclusion for Si diode and LED-GaN diode

The I-V-T studies on Si diode (1N4001) give an activation energy of  $0.65 \pm 0.02$  eV. C-V-T measurements give a built-in potential 0.52 eV. This compares favourably with 0.52 eV reported by Lucia et al. [111] for similar diodes. Also the  $1/C^3 - V_R$  plots give straight line indicating a linearly graded junction also in argument with Lucia's result. Admittance spectroscopy measurements indicate the presence of a trap level at  $0.11 \pm 0.03$  eV.

From the I-V characteristic of the blue LED the ideality factors and series resistances have been determined over a wide temperature range. Both exhibit a decrease over the temperature range of 100 K to 380 K. Their values vary from 10.98 to 3 for the ideality factor, and  $1000 \Omega$  to  $200 \Omega$  for series resistance, respectively. The conduction mechanism varies from thermionic field emission to thermionic emission. I-V characteristic have been used to determine the activation energy which varies from  $0.28 \pm 0.01$  eV at 1.6 V to  $0.2 \pm 0.0003$  eV at 3.5 V. The activation energy determined from admittance spectroscopy is  $0.27 \pm 0.01$  eV. This compares favourably with the activation energy obtained from the I-V characteristic.

## CHAPTER 5 Measurement Results of GaMnAs

### *5.1 Introduction*

This chapter presents the results of a study into the electrical properties of GaAs p n diodes that were fabricated using Mn as the p-type dopant. These epitaxial thin films were grown in the Physics Department of the University of Nottingham. To achieve the necessary Mn doping the p-type layers were grown by MBE at low temperature. More details of the growth are discussed in reference [60] and they have also been presented in the literature review chapter.

GaAs and related alloys are well known to suffer from defects which cause persistent conductivity especially at low temperatures [120]. These defects are usually referred to as DX centres. One result of these defects is the variability of characterization results. To overcome this problem, the DX traps need to be thermally emptied before the experiment begins by elevating the temperature of the sample so that any trapped charge is thermally released. Consequently, the I-V-T, C-V-T and F-C-T measurement were performed from 400 K down to 15 K in predetermined steps, the samples were then heated back to 400 K while the I-V, C-V and F-C measurements were repeated.

One additional complication, which needs to be considered, is the ionization energy of the Mn acceptors. The reports in literature suggest an activation energy of 112 meV [121]. This is a large activation energy compared to other acceptors in GaAs. For example the activation energy of Be, a common p-type dopant, has an activation energy of 20 meV [122]. The Mn acceptors will begin to freeze out at significantly higher temperatures than the Si n-type dopant and so the nature of the junction may change as the temperature is reduced.

In this chapter, the electrical characteristics of GaMnAs are reported. The I-V, C-V and C-F data are then analysed using different “models” in order to obtain information about the different effects occurring in the sample, which may have caused the observed non-ideal behaviour of these devices.

## 5.2 Device Fabrication

Figure 5.1 shows a schematic diagram of the device geometry. The growth sequence consisted of  $n^+$ -GaAs substrate onto which was deposited a 100 nm thick GaAs buffer layer doped with  $2 \times 10^{18} \text{ cm}^{-3}$  Si and grown at  $580^\circ\text{C}$ . This was followed by a 700 nm thick  $n^-$  layer, doped with  $2 \times 10^{17} \text{ cm}^{-3}$  Si, grown at  $580^\circ\text{C}$ . Finally, a 500 nm GaAs Mn doped layer was grown at 3 different temperatures and concentrations which resulted in p-type conductivity. The doping levels of the GaMnAs film are shown at 300 K in Table 5.1, along with the growth temperature as well as the hole concentration estimated from the theoretical calculations, (see section (5.3)). The doping levels shown in the Table 5.1 are the atomic doping levels estimated from the atom beam flux.

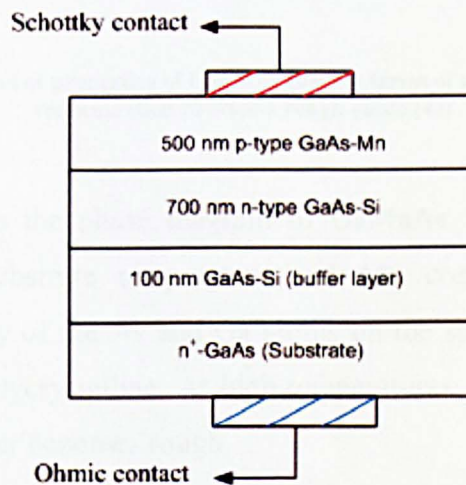


Figure 5.1 Schematic drawing of the device geometry of the GaMnAs film

The doping levels of the GaMnAs film are shown at 300 K in Table 5.1, along with the growth temperature as well as the hole concentration estimated from the

theoretical calculations,(see section 5.3). The doping levels shown in the Table 5.1 are the atomic doping levels estimated from the atom beam flux.

**Table 5.1 Doping levels of samples**

| Sample number | Physical doping ( $\text{cm}^{-3}$ ) | Growth temperature ( $^{\circ}\text{C}$ ) | Hole concentration at R.T. ( $\text{cm}^{-3}$ ) (the theoretical calculations in section (5.3)) |
|---------------|--------------------------------------|---|---|
| 374           | $10^{21}$                            | 230                                       | $2.4 \times 10^{19}$  |
| 375           | $10^{20}$                            | 380                                       | $7.4 \times 10^{18}$  |
| 376           | $10^{19}$                            | 550                                       | $2 \times 10^{18}$  |

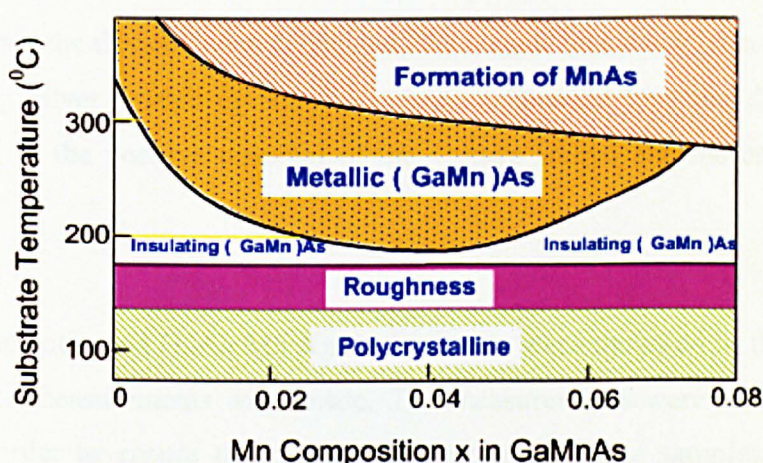


**Figure 5.2 Schematic diagram of properties of GaMnAs films in terms of substrate temperature and Mn concentration provide a rough guide [43]**

Figure 5.2 shows the phase diagram of GaMnAs films grown by LT-MBE method in terms of substrate temperature and Mn concentration. At very low temperatures the mobility of the As and Ga atoms on the surface of the GaAs is very poor and the GaAs is polycrystalline. At high temperatures, the size of the crystallites increase and the final layer becomes rough.

Three different Mn concentrations were used to dope GaAs films,  $10^{19}$ ,  $10^{20}$  and  $10^{21} \text{ cm}^{-3}$  which corresponded to an atomic percentage (x) in the range 0.02 to  $< 0.08$  [58]. Zhao et al. [123], study the structural properties of their GaMnAs films using high-resolution x-ray diffraction. According to them, results show a high crystalline

quality of the structure with x value range between 0.02 and 0.08. Although the samples under study have a similar range of atomic percentage, there is no experimental evidence of the structure quality of these films.

The top circular metallisation was 1mm in diameter and was deposited in a thermal evaporator and the pattern was defined using a shadow mask. To achieve isolation between the samples, the top metallization was used as an etch mask. The etch depth was approximately 1  $\mu\text{m}$ . The N-type metallisation was placed on the backside of the heavily doped substrate. This made a device nominally in the form of a p n junction between the n-type Si doped layer and a p-type Mn doped layer.

Once the devices were fabricated, the sample was stuck onto a TO5 header with conducting silver loaded epoxy. Therefore, to forward bias the device the pin was connected to the positive terminal of the voltage source and the case to the negative terminal.

The packaged GaAs-Mn /GaAs-Si diodes were mounted in the cryostat and the appropriate measurements were made. The measurements were repeated at least three times in order to ensure the results were repeatable. The samples were biased with Keithley 238 source measure unit. The maximum applied voltage was 3V in case of forward direction whereas it was -5V for reverse direction. The characteristics were observed over a temperature range (15-400K).

Assuming full activation of the dopants, the p-type is more heavily doped than the n-type ( $N_A > N_D$ ). Therefore, the charge concentration in the depletion region is higher in the p-side of the junction than in the n-side. Consequently, the depletion region extends mainly into the low doped n-type side.

### ***5.3 Estimation of hole concentration***

Theoretical analysis of the position of the Fermi level and the hole concentrations used in this study is presented in this section and is based on the basic

semiconductor equations given in [6]. The following charge neutrality relationship can be determined by considering a uniformly doped semiconductor

$$p - n + N_D^+ - N_A^- = 0 \quad (5.1)$$

$n$  and  $p$  are the electron and hole densities in the conduction and valence band respectively given by:

$$n = N_C \exp\left(-\frac{E_C - E_F}{kT}\right) \quad (5.2)$$

$$p = N_V \exp\left(-\frac{E_F - E_V}{kT}\right) \quad (5.3)$$

The concentration of ionized donors ( $N_D^+$ ) and the ionized acceptor ( $N_A^-$ ) are given by:

$$N_D^+ = N_D \left[ 1 - \frac{1}{1 + \frac{1}{g} \exp\left(\frac{E_D - E_F}{kT}\right)} \right] \quad (5.4)$$

$$N_A^- = \frac{N_A}{1 + g \exp\left(\frac{E_A - E_F}{kT}\right)} \quad (5.5)$$

In these equations  $E_C$ ,  $E_V$ ,  $E_A$  and  $E_D$  are the energies of the bottom of the conduction band, the top of the valence band and the energy of the acceptors and donors levels respectively. State “ $g$ ” is the degeneracy factor which is 4 for the acceptor atom and 2 for donors [6].

Rewriting the neutrality condition of equation (5.1) we can get the exact position of the Fermi level on the energy band diagram by numerical iteration. Equation (5.1) can be solved for the Fermi level  $E_F$  by substituting the following parameters [6]; the effective density of state in conduction band  $N_C = 4.7 \times 10^{17} \text{ cm}^{-3}$  and the effective density of state in valence band  $N_V = 7 \times 10^{18} \text{ cm}^{-3}$  and the activation energy  $E_a = 0.1 \text{ eV}$ .

It should be noted that these equations ignore any impurity band formation that may occur in heavily doped semiconductors. Therefore, the results should be viewed with some caution. In addition, in this analysis we are assuming that all the atoms are involved in doping i.e. all atoms are substitutional.

### 5.3.1 Determination of the hole concentration and Fermi level for Mn (374) Device

Figure 5.3 and Figure 5.4 show the variation of the hole concentrations  $p$  and the Fermi level  $E_F$  with the temperature respectively for sample Mn374. As expected, the hole concentration  $p$  increases with increasing temperature. It can be seen from Figure 5.4 that the Fermi level is located above the valence band until 200 K. For temperatures greater than 200 K, the Fermi level moves inside valence band making the material *degenerate*. Assuming all atoms are substitutional i.e. all the atoms are involved in doping.

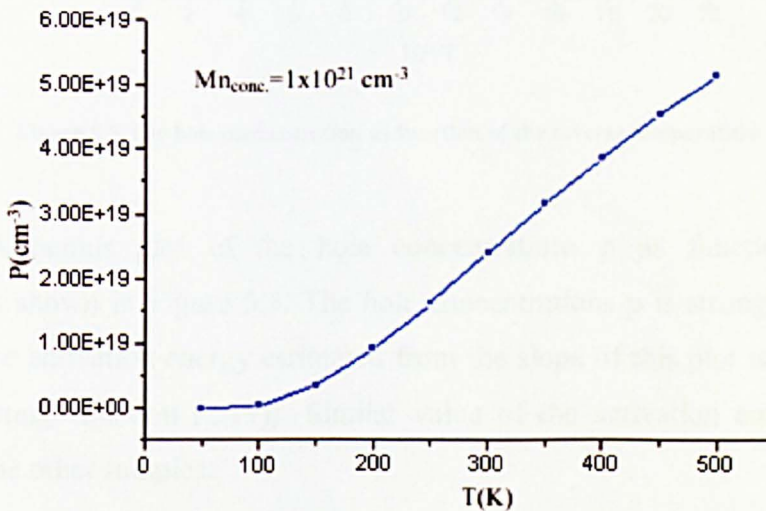
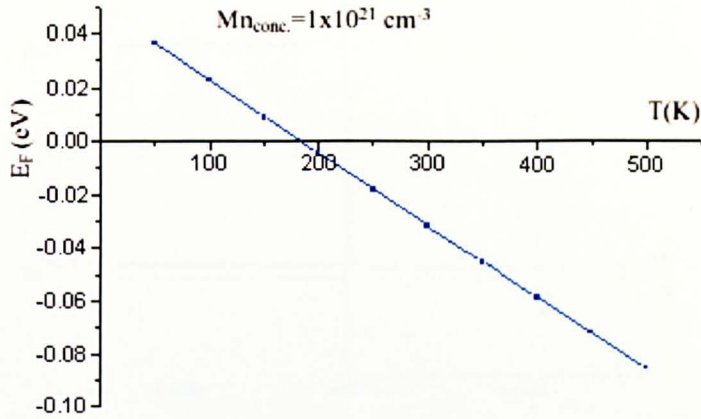
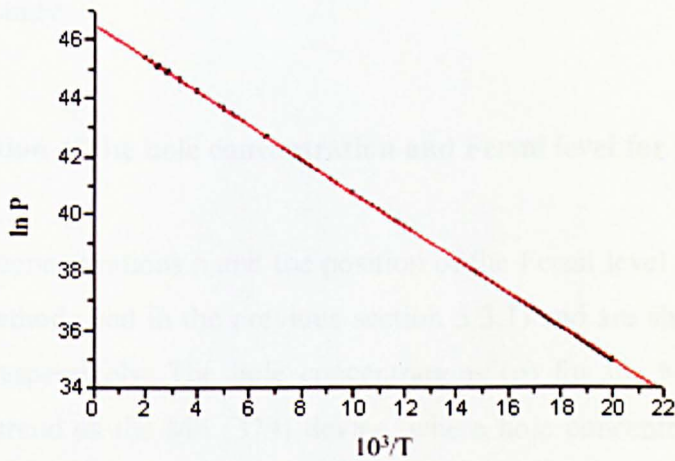


Figure 5.3 The calculated hole concentration as a function of temperature



**Figure 5.4** The Fermi level position as a function of temperature, presenting the degeneracy region after 200 K. Zero energy is considered to be the top of the valence band

At room temperature, the hole concentration  $p$  is equal to  $2.4 \times 10^{19} \text{ cm}^{-3}$  which corresponds to about 2% of ionized impurities of Mn atoms of a total doping concentration of  $1 \times 10^{21} \text{ cm}^{-3}$  (see Table 5.1).



**Figure 5.5** The hole concentration as function of the inverse temperature

The Arrhenius plot of the hole concentrations  $p$  as function of inverse temperature is shown in Figure 5.5. The hole concentrations  $p$  is strongly temperature dependent. The activation energy estimated from the slope of this plot is found to be  $\sim 50 \text{ meV}$  (plotting equation (2.19)). Similar value of the activation energy has been obtained for the other samples.

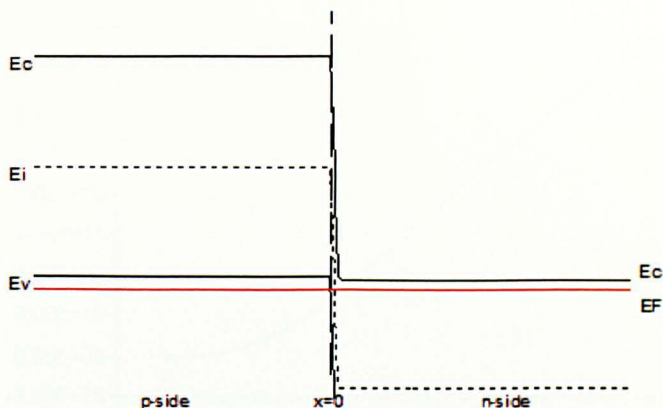


Figure 5.6 The energy band diagram at room temperature for GaMnAs Mn (374) diode

The energy band diagram for Mn (374) device is drawn by using the Matlab program as shown in Figure 5.6, which shows the material degeneracy. The full details of the program and the equations related to the Matlab program is given in appendix A. This program displays data graphically and is used to draw the energy band diagram produced in this study.

### 5.3.2 Determination of the hole concentration and Fermi level for Mn (375) Devices

The hole concentrations  $p$  and the position of the Fermi level  $E_F$  are determined with the same method used in the previous section 5.3.1) and are shown in Figure 5.7 and Figure 5.8 respectively. The hole concentrations ( $p$ ) for the Mn (375-1) device shows the same trend as the Mn (374) device, where hole concentrations  $p$  increases with increasing temperature as shown in Figure 5.7. The Mn (375) device also presents degeneracy condition as Mn (374) device but the Fermi level  $E_F$  location is above the valence band  $E_V$  until 300 K as shown in Figure (5.8). Above this temperature, the Fermi level will be lower than  $E_V$ . However, this will be evidence of the degeneracy state.

The hole concentrations  $p$  at room temperature is shown in Figure 5.7 which is equal to  $7.4 \times 10^{18} \text{ cm}^{-3}$  and corresponds to about 7% of ionized impurities of Mn atoms of a total doping concentration of  $10^{20} \text{ cm}^{-3}$ .

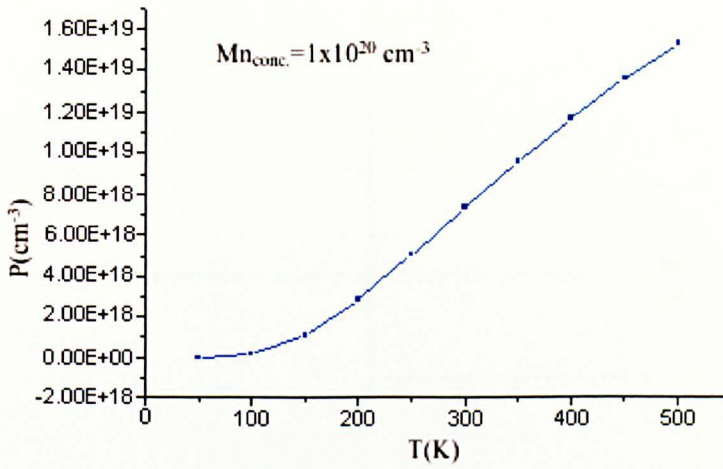


Figure 5.7 Hole concentration versus T of Mn (375-1) device

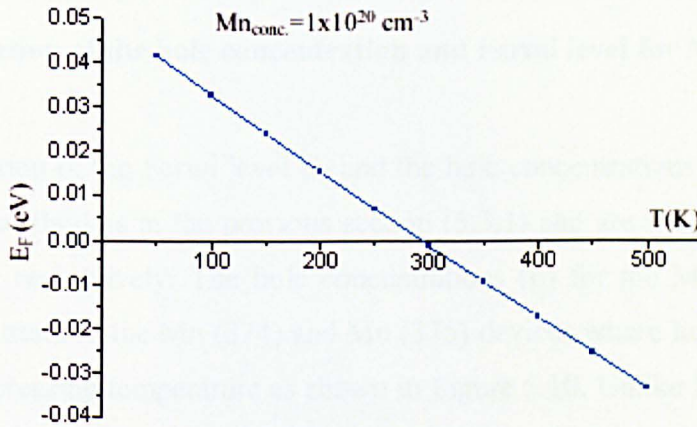


Figure 5.8 The Fermi level position as a function of temperature, presenting the degeneracy region after 300 K. Zero energy is considered to be the top of the valence band

The energy band diagram for Mn (375) device is drawn at room temperature by using the Matlab program as shown in Figure 5.9, which shows the material degeneracy.

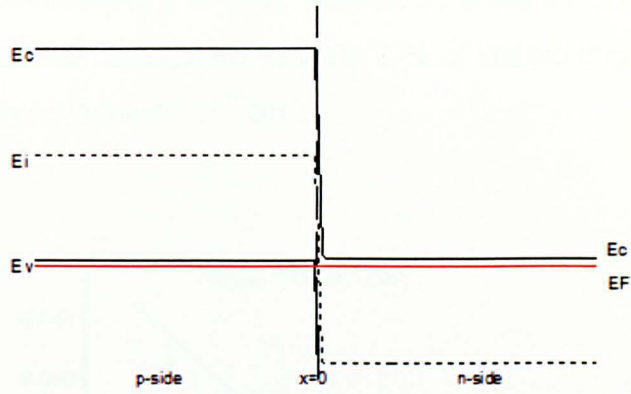


Figure 5.9 The energy band diagram at room temperature for GaMnAs Mn (375) diode

### 5.3.3 Determination of the hole concentration and Fermi level for Mn (376) Devices

The position of the Fermi level  $E_F$  and the hole concentrations  $p$  are determined using the same method as in the previous section (5.3.1) and are shown in Figure 5.10 and Figure 5.11 respectively. The hole concentrations ( $p$ ) for the Mn (376-1) device shows the same trend as the Mn (374) and Mn (375) devices where hole concentrations increase with increasing temperature as shown in Figure 5.10. Unlike Mn (374) and Mn (375), Mn (376) does not present degeneracy condition, as the position of the Fermi level  $E_F$  is above the valence band  $E_V$  for all temperatures studied as shown in Figure 5.11.

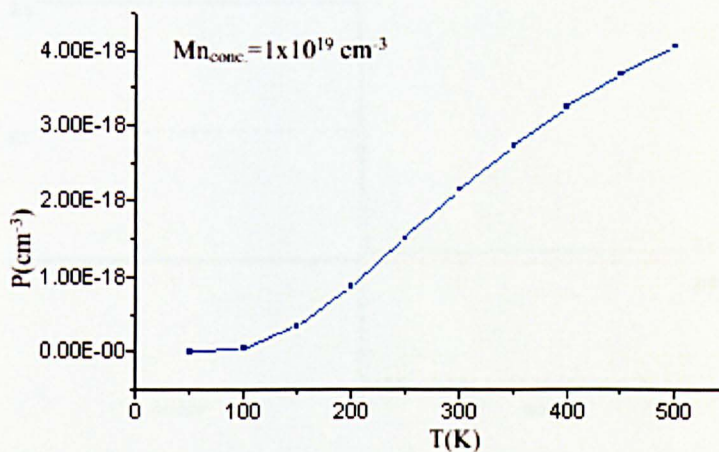


Figure 5.10 The calculated hole concentration as a function of temperature for Mn (376-1) device

The hole concentrations  $p$  at room temperature is shown in Figure 5.10 which is equal to  $2 \times 10^{18} \text{ cm}^{-3}$  and corresponds to about 20% of ionized impurities of Mn atoms of a total doping concentration of  $10^{19} \text{ cm}^{-3}$ .

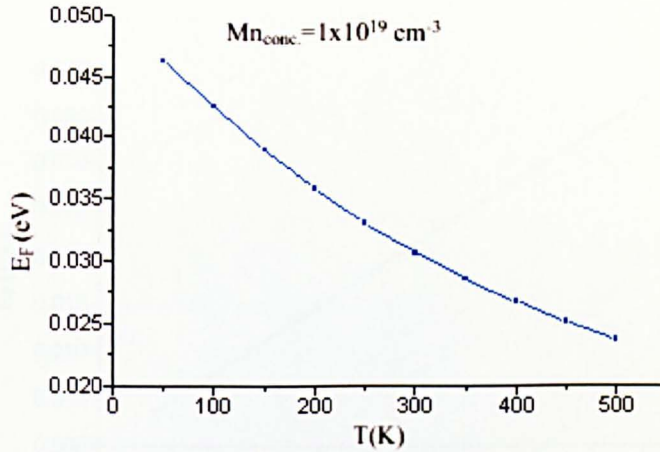


Figure 5.11 The Fermi level position as a function of temperature, which is above the valence band

The energy band diagram for Mn (375) device is drawn by using the Matlab program as shown in Figure 5.12. It was found that the position of the Fermi energy was just in contact with the top of the valence band which demonstrated that the material was not degenerate.

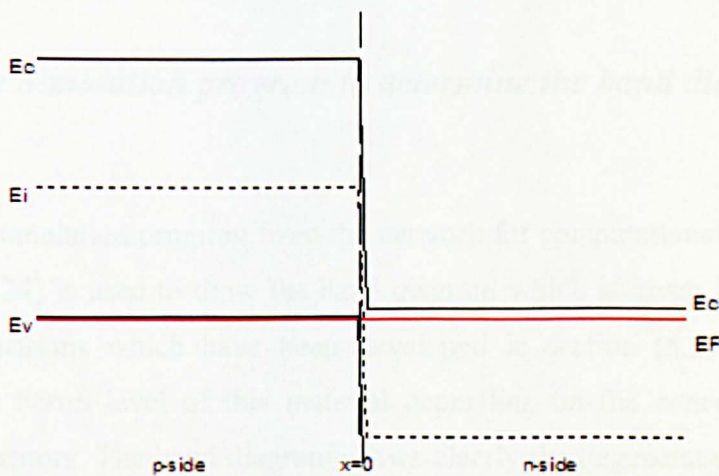
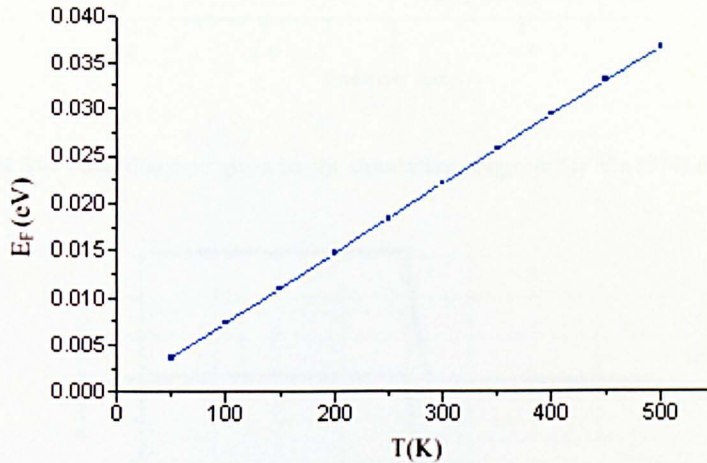


Figure 5.12 The energy band diagram at room temperature for GaMnAs Mn (376) diode

### 5.3.4 Determination of the electron concentration and Fermi level for Si-GaAs

The position of the Fermi level  $E_F$  as a function of the temperature is determined using the same method as in the previous section 5.3.1) and is shown in Figure 5.13.



**Figure 5.13** The Fermi level position as a function of temperature, which is inside the conduction band for the Si-GaAs. Zero energy is considered to be the bottom of the conduction band

According to the theoretical calculation, the electron concentration  $n$  equal  $2 \times 10^{17} \text{ cm}^{-3}$  at all the temperatures. The calculated value is equal to the doping concentration of Si in GaAs ( $2 \times 10^{17} \text{ cm}^{-3}$ ). This indicates that the Si atoms begin to ionize around 70 K due to their small activation energy  $\sim 5.8 \text{ meV}$  [6].

### 5.4 Using the Simulation program to determine the band diagram

Online simulation program from the network for computational nanotechnology (NCN) team [124] is used to draw the band diagram which is given in Figure 5.14. It utilizes the equations which have been developed in section (5.3) to estimate the position of the Fermi level of this material depending on the concentrations of the donors and acceptors. The band diagram shows clearly the degeneracy of the material. This result compares favourably with the Matlab program presented earlier in section (5.3.1). In addition, the band diagram at 77 K can be determined. This is shown in Figure 5.15.

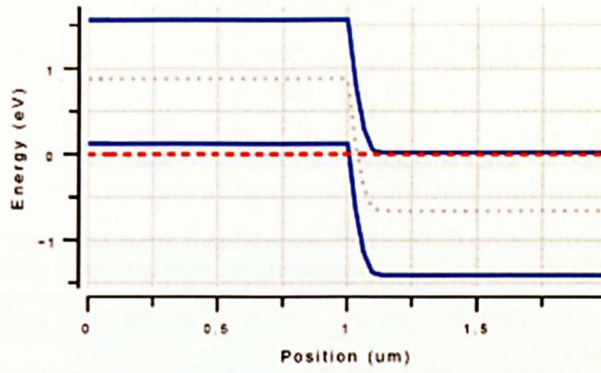


Figure 5.14 The band diagram given by the simulation program for Mn (374) device at RT

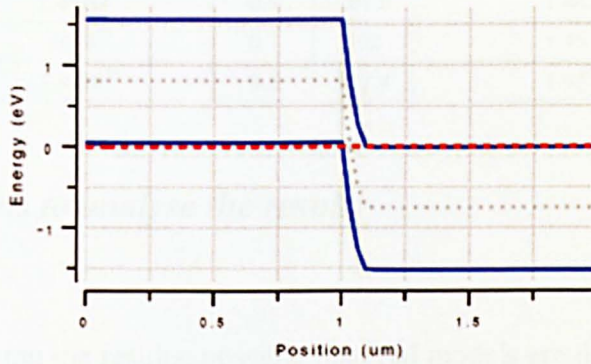


Figure 5.15 The band diagram given by the simulation program for Mn (374) device at 77 K

In addition, the simulation program gives the depletion layer width. As expected the depletion layer on the p-side is only 0.02 nm compared to 106 nm on the n-side. The hole concentration and depletion width sizes at RT (300 K) are given in Table 5.2. Table 5.3 shows how these parameters vary with temperature for Mn (374).

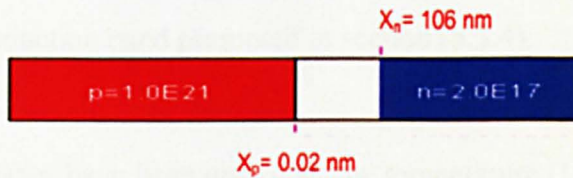


Figure 5.16 The depletion layer width between p and n side Mn (374) device using the simulation program [125]

**Table 5.2 The depletion width sizes and the barrier height at RT (300 K) as calculated from the simulation program for all devices [125]**

| Sample number | Mn con. ( $\text{cm}^{-3}$ ) | $X_p$ (nm) | $X_n$ (nm) | $\Phi_b$ (eV) at R.T.(simulation) |
|---------------|------------------------------|------------|------------|-----------------------------------|
| 374           | $10^{21}$                    | 0.02       | 106        | 1.54                              |
| 375           | $10^{20}$                    | 0.21       | 103.4      | 1.48                              |
| 376           | $10^{19}$                    | 2          | 100.4      | 1.42                              |

**Table 5.3 The ionized impurities atoms concentration, depletion layer on the n and p-side and the barrier height as calculated from the simulation program for sample Mn (374)**

| T   | ionized impurities ( $\text{cm}^{-3}$ ) | $X_p$ (nm) | $X_n$ (nm) | $\Phi_b$ (eV) at R.T. (simulation) |
|-----|---|------------|------------|------------------------------------|
| 100 | $5 \times 10^{17}$                      | 33         | 83         | 1.34                               |
| 150 | $3.5 \times 10^{18}$                    | 5.6        | 97.7       | 1.4                                |
| 200 | $9 \times 10^{18}$                      | 2          | 100        | 1.4                                |
| 250 | $1.6 \times 10^{19}$                    | 1.4        | 101        | 1.43                               |
| 300 | $2.4 \times 10^{19}$                    | 0.9        | 101.8      | 1.44                               |
| 350 | $3 \times 10^{19}$                      | 0.7        | 102        | 1.45                               |
| 400 | $3.8 \times 10^{19}$                    | 0.5        | 102.4      | 1.45                               |

### 5.5 Possible models to analyse the results

Before analysing the results, possible material models are discussed. This allows different models to be applied to the measurements and conclusions drawn.

The I-V characteristic would be determined by the nature of the contact on either side of the GaAs: Mn active layer. The activation energy of Si in GaAs is extremely low  $\sim 0.0058$  eV [6]. It is expected that all Si-donors would be ionized from around  $\sim 70$  K and above and the Si doped GaAs will behave like a metal. The base layer of GaAs is doped with silicon having concentration of  $2 \times 10^{17} \text{ cm}^{-3}$ . At this concentration, the calculations show that GaAs is an n-type degenerate material with the Fermi level 0.02 eV deep inside the conduction band presented in section (5.3.4).

The GaMnAs layer have been grown at low temperature (LT) which results in a high concentration of defects [95, 101, 104] and exhibits a donor type character [63, 126]. Mn form deep acceptors in GaAs with an activation energy (112 meV [121]) and, the electrical character of the GaAs:Mn layer will be determined by the relative population of ionized unintentionally doped (u.i.d.) donors  $N_D$  and intentionally doped Mn ( $N_A$ ).

Three possible scenarios can be identified;

1. For  $N_D > N_A$  then the material will be n-type.
2. For  $N_D \approx N_A$  then the material will be an insulator.
3. For  $N_D < N_A$  then the material will be p-type.

An energy band model based on each of these conditions has been constructed and attempts have been made to analyse the results on this basis.

### **Model one: Schottky model.**

If  $N_D > N_A$ , the structure will then look like n-GaAs: Si / (u.i.d.) n-GaAs / Schottky contact as shown in Figure 5.17.

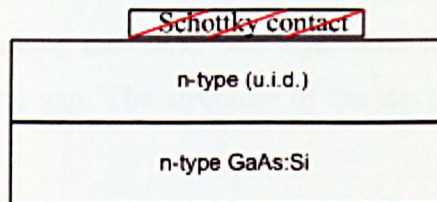


Figure 5.17 Schottky diode model

The suggested energy band diagram is given in Figure 5.18 (a), which shows the formation of the Schottky contact between the metal and the GaAs: Mn layer on one side and an (n- n<sup>+</sup>) junction with GaAs: Si on the other. The I-V characteristic obtained would be like the one in Figure 5.18 (b).

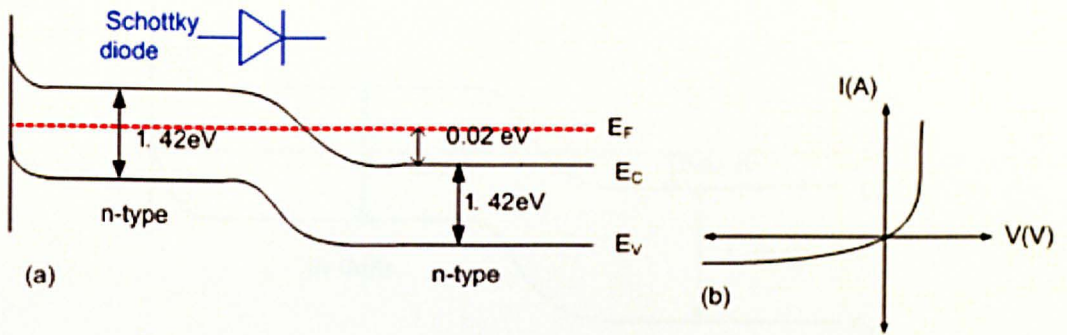


Figure 5.18 The band diagram for n-type Schottky diode

The C-V characteristics will be very similar to the CV of a p n diode and Schottky diode. Starting from the reverse bias condition, the capacitance should increase as the voltage across the diode approaches zero. As the bias becomes forward bias, the capacitance should continue to rise.

### Model Two: Insulator model.

As the concentration of donor  $N_D$  approaches  $N_A$ , the material approaches a near complete compensation making the GaAs: Mn layer semi-insulating (SI) with the Fermi level in the middle of band gap. The structure of the device will look more like that shown in Figure 5.19.

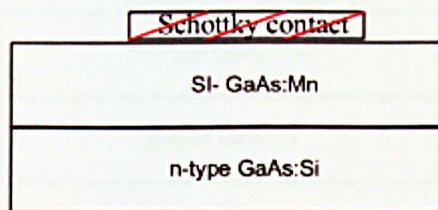


Figure 5.19 Insulator model

The electrical characteristic may be analysed in terms of Poole- Frenkel (P.F.) and space charge limited current (SCLC) mechanisms. The possible energy band diagram is given in Figure 5.20. The Fermi level ( $E_F$ ) is located in the middle of the energy gap.

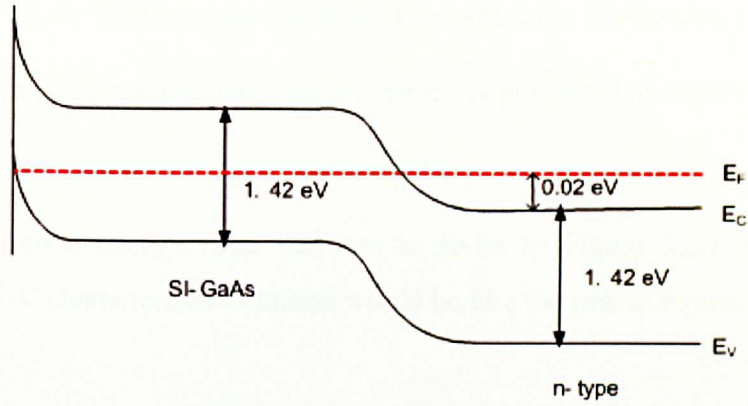


Figure 5.20 The band diagram for the insulator model which shows the  $E_F$  in the middle

In such a situation SI-GaAs: Mn layer makes a Schottky contact with the top metal electrode and a  $n^+$  intrinsic GaAs contact on the back side. When a voltage is applied across the diode most of the voltage will be dropped across the insulating Mn doped GaAs. The capacitance will be approximately constant.

### Model Three: The Standard pn junction

Should the concentration of acceptors  $N_A$  exceed  $N_D$ , the GaAs:Mn layer will become p-type making the device structure as shown in Figure 5.21. In this case, p-type and n-type layer would form p n junction.

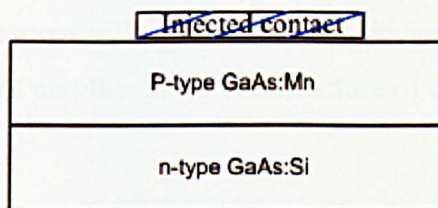


Figure 5.21 Simple p n junction model

This leads to two possibilities:

1. If the top contact behaves as an Ohmic contact, the device is simply a  $p n^+$  junction.

2. However if the contact is a Schottky contact the device structure would be more like a back to back contact which is presented as model (4).

The possible energy band diagram is given in Figure 5.22 (a) for the  $p^+n$  junction. The I-V characteristic obtained would be like the one in Figure 5.22 (b).

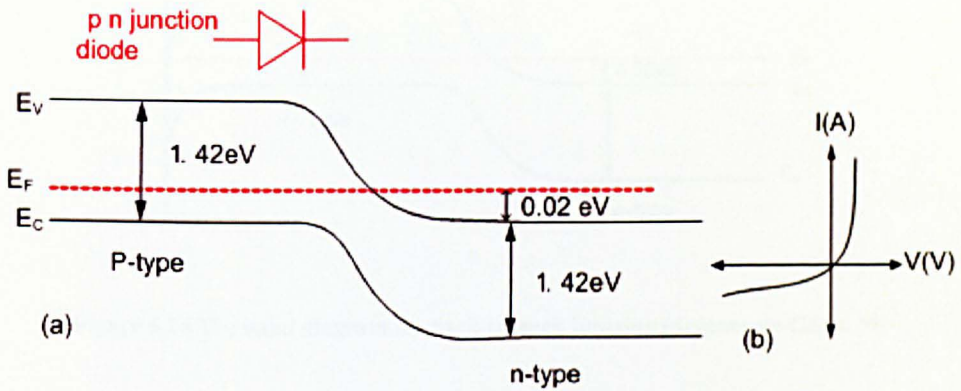


Figure 5.22 The band diagram for simple p n junction model

The CV characteristic will be the standard one associated with p n diodes. A general increase in capacitance as the applied potential is increased.

#### Model Four: The back-to-back model

There also exists a possibility of achieving a device with a p n junction on one side and a Schottky contact on other side. The structure of the device is shown in Figure 5.23.

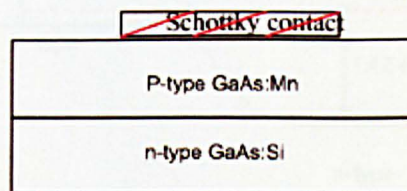


Figure 5.23 The back-to-back model

The only way the observed I-V characteristic can be obtained is if  $\Phi_m < \Phi_S$  in which case the band diagram will be as shown in Figure 5.24. The metallic contact to p-type GaAs:Mn would be a Schottky contact for holes.

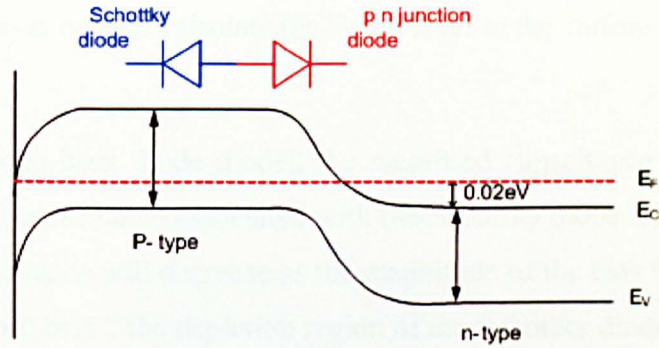


Figure 5.24 The band diagram for back-to-back junction (degenerate GaAs: Si)

Such a contact would exhibit rectifying properties. The metallic electrode is Schottky, while GaAs:Mn and GaAs:Si is the bottom electrode. Defining the forward bias condition to be when the top electrode is positive. In this model, in the forward bias the current is limited by reverse Schottky while in reverse bias the current is limited by reverse p n junction. In the highly unlikely case of GaAs:Si layer behaving as a non-degenerate material the two corresponding band diagram changes, and is shown in Figure 5.25.

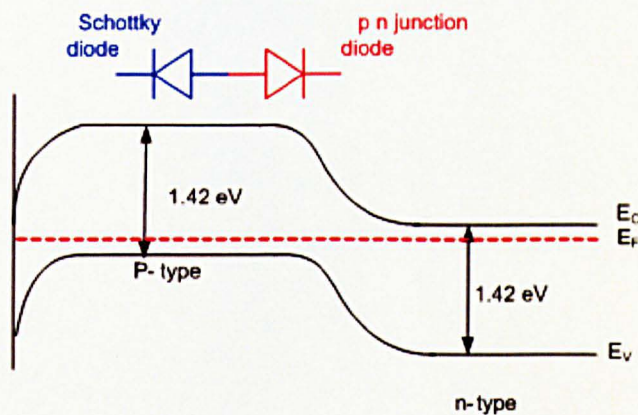


Figure 5.25 The band diagram for back-to-back junction (non-degenerate GaAs: Si)

The devices studied have three different concentrations of Mn doping. They vary from  $10^{19}$  to  $10^{21}$   $\text{cm}^{-3}$  and the growth temperature varies from 230 °C to 580 °C as shown in Table 5.1.

The I-V responses of the three devices have been analysed using these models. Theoretical analysis is used to calculate the Fermi level in the various samples.

In the back-to-back diode model, the measured capacitance will be the series combination of the capacitance associated with the Schottky diode and the p n junction. The resulting capacitance will decrease as the magnitude of the bias is increased. When the diode is “forward bias”, the depletion region of the Schottky diode will increase and so the measured capacitance will reduce. Similarly, when “reverse bias” the depletion region associated with the p n junction will increase and the overall measured capacitance should again decrease.

When analysing the results from devices made from the different wafers, the difference in growth temperature may play a pivotal role in determining the I-V-T and CV characteristics of these devices. As the concentration of Mn decreases, the growth temperature increases. The growth temperature plays a significant role in the type and concentration of the grown in crystal defects. This will make a simple comparison difficult.

### 5.6 Comparison of the samples with different Mn concentrations

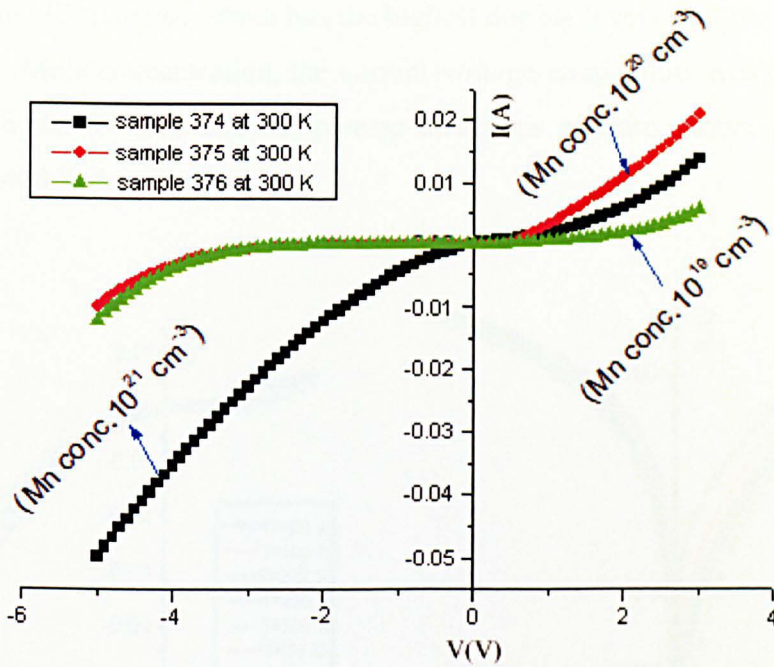


Figure 5.26 Comparison of the samples with different Mn concentration at 300 K

Figure 5.26 compares the room temperature I-V characteristic of the GaMnAs samples to different doping levels. Current through these devices does not follow a pattern. For example, Mn (374) device which has the highest doping level of the GaMnAs film exhibits the highest current in reverse bias, while sample Mn (376) displays the lowest current with the lowest doping level. The forward current is dependent upon the doping concentration through the saturation current  $I_S$  which in turn depends upon the barrier height  $\Phi_b$  and the Fermi level  $E_F$ , which is a function of the doping concentration.

The saturation current  $I_S$  is related to the acceptors and donors concentration respectively, through the equation (2.2). Such a correlation is not observed from experimental data.

### 5.7 I-V-T behaviour of Mn (374) device

For Mn (374) device which has the highest doping level of all the diodes studied with  $10^{21} \text{ cm}^{-3}$  Mn's concentration, the current-voltage-temperature measurements were made for both the forward and the reverse directions and are shown in Figure 5.27 ranging from 400 K down to 15 K.

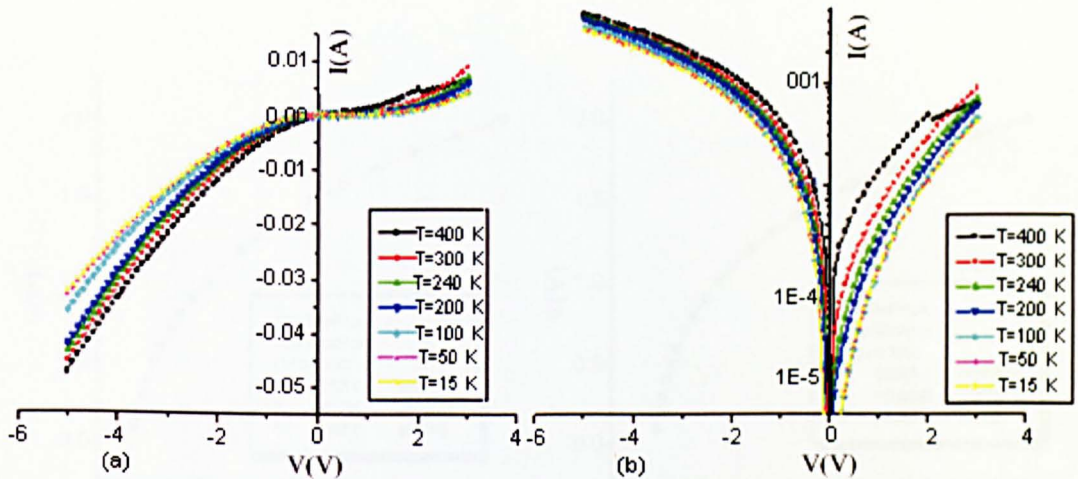


Figure 5.27 Current-voltage curve for GaMnAs (Mn374) device

Figure 5.27 presents the typical I-V behaviour of the GaMnAs p n junction with soft forward and reverse bias characteristic. The general shape of the I-V characteristic for sample Mn (374) is not symmetric. Interestingly the higher values of current occur for negative voltages. In reverse direction, the current increases considerably with the applied bias, while in the forward direction the current variation with the applied bias is remarkably less. Specifically, at 3 volts the current was near 5 mA meanwhile, it reaches 15 mA at -3 volts. This indicates that the mechanism determining the current for both polarities is not the same.

The I-V-T characteristics were processed further by plotting the  $\log I$  against  $V$  as shown in Figure 5.27 (b) to extract different parameters for the device under study in the temperatures range 15-400 K. The ideality factor ( $n$ ), the saturation current ( $I_S$ ) and the series resistance ( $R_S$ ) were found by fitting the equation as developed in chapter 2 as equation (2.15).

Nonlinear least squares fitting (NLSF) method using the Origin program was performed to extract these different parameters. This program is a software application that provides data analysis as well as graphing capability [127]. The plot has been checked manually by plotting equation (2.13) and was found to give identical results. The values of  $n$ ,  $I_S$  and  $R_S$  are consistent with temperature variation and similar to values reported by other workers. The fitting at room temperature (a) and 200 K (b) is shown in Figure 5.28. The same method is used to determine these parameters for all devices under study.

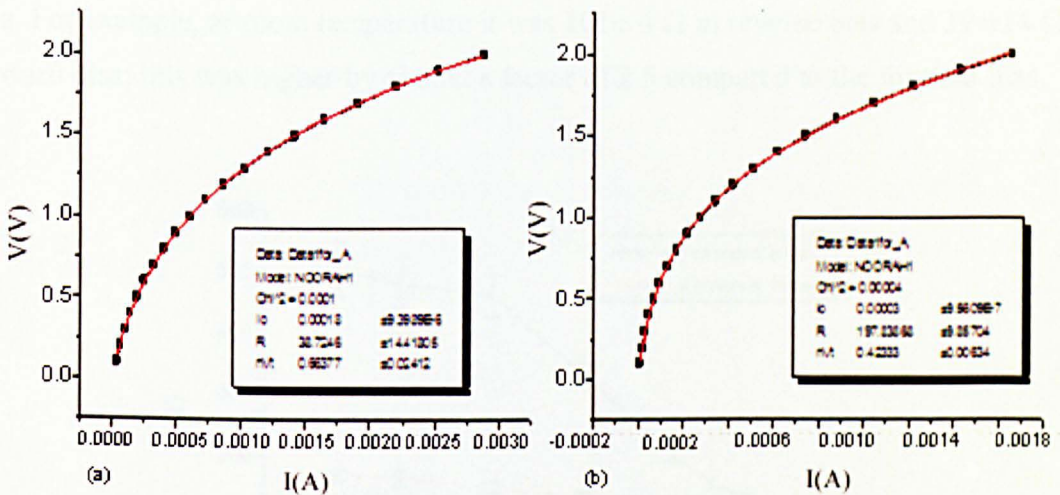


Figure 5.28 The applied forward bias against current (a) at room temperature and (b) at 200 K. The graph shows the fitting applied to equation (5.6) (red lines) for Mn (374) device.

Table 5.4 Some parameters calculated for Mn (374) device when in forward bias

| T   | KT/q  | n                | $E_o=nkT/q$ | $I_S$ (A)            | R ( $\Omega$ )  |
|-----|-------|------------------|-------------|----------------------|-----------------|
| 300 | 0.026 | 25.7 $\pm$ 0.02  | 0.66        | 0.0009 $\pm$ 1E-5    | 39 $\pm$ 14     |
| 280 | 0.024 | 24.2 $\pm$ 0.01  | 0.59        | 0.0001 $\pm$ 5E-5    | 70.9 $\pm$ 11.5 |
| 260 | 0.022 | 23.8 $\pm$ 0.01  | 0.53        | 0.00008 $\pm$ 3E-5   | 97 $\pm$ 9.7    |
| 240 | 0.021 | 23.7 $\pm$ 0.008 | 0.49        | 0.00006 $\pm$ 2E-5   | 126.5 $\pm$ 8.7 |
| 220 | 0.019 | 24.3 $\pm$ 0.007 | 0.46        | 0.00005 $\pm$ 1E-5   | 154.7 $\pm$ 8.8 |
| 200 | 0.017 | 24.6 $\pm$ 0.006 | 0.42        | 0.00003 $\pm$ 1E-5   | 197.8 $\pm$ 10  |
| 150 | 0.013 | 26 $\pm$ 0.009   | 0.34        | 0.00001 $\pm$ 8E-6   | 329.3 $\pm$ 20  |
| 100 | 0.009 | 31.5 $\pm$ 0.01  | 0.27        | 4.6 x10-6 $\pm$ 5E-6 | 459 $\pm$ 32.8  |
| 50  | 0.004 | 65.5 $\pm$ 0.01  | 0.28        | 5.2x10-6 $\pm$ 6E-6  | 478.9 $\pm$ 39  |
| 15  | 0.001 | 218 $\pm$ 0.01   | 0.28        | 49 x10-6 $\pm$ 7E-6  | 500 $\pm$ 44    |

The ideality factor, the tunnelling parameter [15], saturation current and the series resistance at different temperatures as determined from I-V-T measurements are summarised in Table 5.4.

The series resistance of the device has been determined from the I-V-T measurements using equation (2.15) for both polarities as shown in Figure 5.29. In general, it was found that the series resistance was much higher in forward compared to the reverse direction, but there was a deviation in this rule at temperature around 250 K. After 250 K the series resistance in the reverse bias began to be higher than forward bias. For example, at room temperature it was  $101 \pm 4 \Omega$  in reverse bias and  $39 \pm 14 \Omega$  in forward bias; this was higher by almost a factor of 2.5 compared to the forward bias.

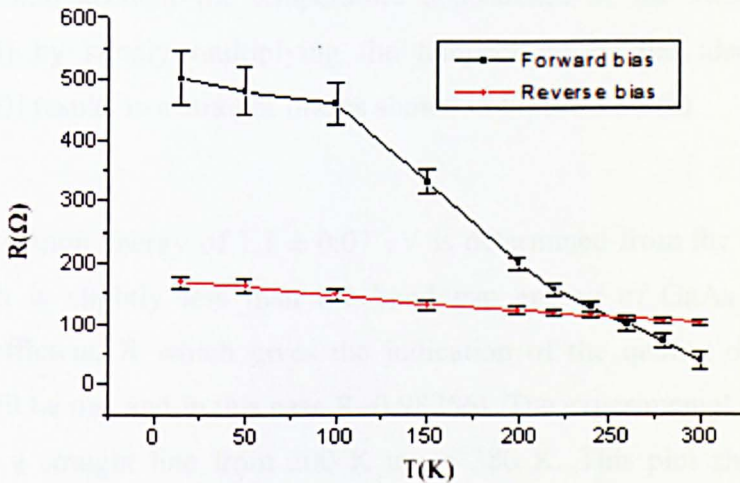


Figure 5.29 The series resistance versus temperatures for GaMnAs sample Mn (374) device in both polarities with small errors in case of reverse bias compared to the forward bias in low temperatures

### **a) Analysis of I-V using pn junction model**

The device is fabricated to be a p n junction, so the result may be analysed on the basis of p n junction. Using equation (2.3) a plot  $\ln(I_S/T^3)$  versus  $10^3/T$  should give the energy gap ( $E_g$ ) of the GaAs. The corresponding plot is shown in Figure 5.30 (a) and the resulting plot is non-linear. This seems to suggest that the standard p n junction model does not apply. Similar behaviour has been observed for all diodes under test.

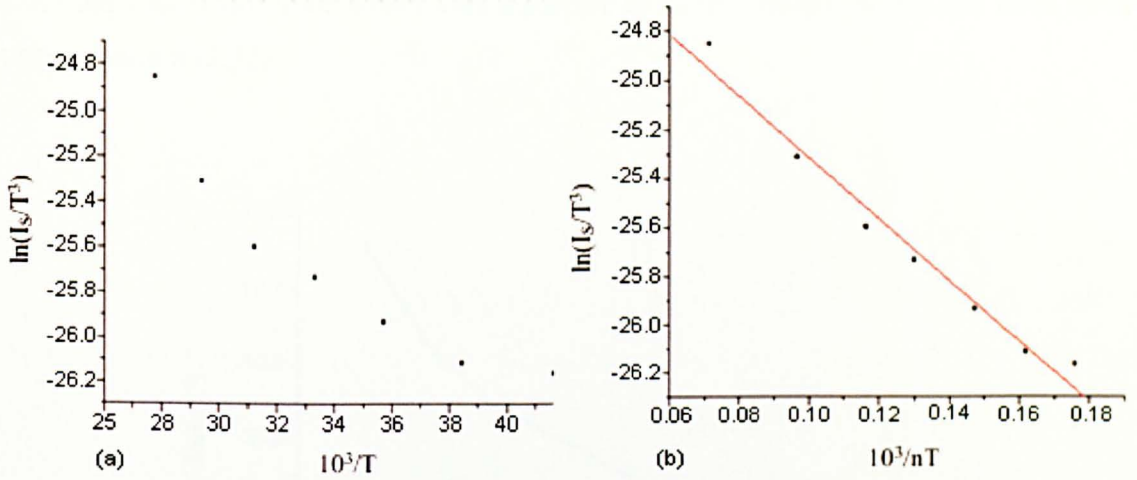


Figure 5.30 (a) The plot  $\ln(I_s/T^3)$  versus  $10^3/T$  and (b) The plot  $\ln(I_s/T^3)$  versus  $10^3/nT$  with correlation coefficient  $R=0.98756$  for Mn (374) device in the forward bias

Taking into account the temperature dependence of the ideality factor into equation (2.14) by simply multiplying the temperature by the ideality factor ( $n$ ) [equation (2.35)] results in a straight line as shown in Figure 5.30 (b).

The activation energy of  $1.1 \pm 0.07$  eV is determined from the slope of Figure 5.30 (b) which is slightly less than the band gap energy of GaAs. Moreover the correlation coefficient,  $R$  which gives the indication of the quality of the fit (for a perfect fit  $R$  will be one and in this case  $R=0.98756$ ). The experimental data are seen to begin to fit to a straight line from 200 K up to 380 K. This plot shows significant deviation from linearity below 200 K although at first sight this seems to indicate the p n junction model fits the data. The temperature dependent values of  $n$  and their magnitude indicate that mechanisms like generation/recombination in the depletion region may also be operative.

### **b) Analysis of I-V using Schottky model**

The saturation current for the Schottky contact represented by the equation (2.14) can be used to estimate the barrier height. A plot, in the form of  $\ln(I_s/T^2)$  versus  $10^3/T$  is shown in Figure 5.31 for higher temperature range from 200-380 K in case of forward bias for (Mn374) device. This plot does not fit to a straight line. Another attempt is made to estimate the barrier height theoretically and experimentally, using the

modified Richardson plot which uses a plot of  $\ln(I_S/T^2)$  versus  $10^3/nT$  has been made using equation (2.35).

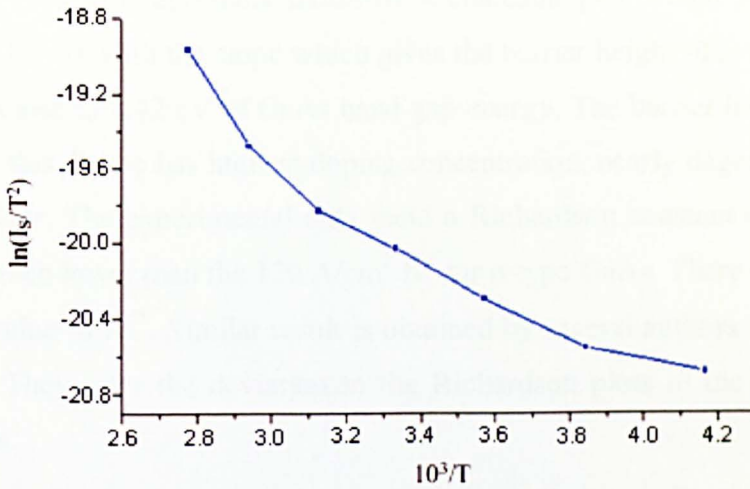


Figure 5.31 Natural log of  $\ln(I_S/T^2)$  versus  $10^3/T$  for Mn (374) device in the forward bias

The barrier height ( $\Phi_b$ ) estimated theoretically from forward bias I-V data, for different temperatures using equation (2.17) is shown plotted in Figure 5.32 (a).

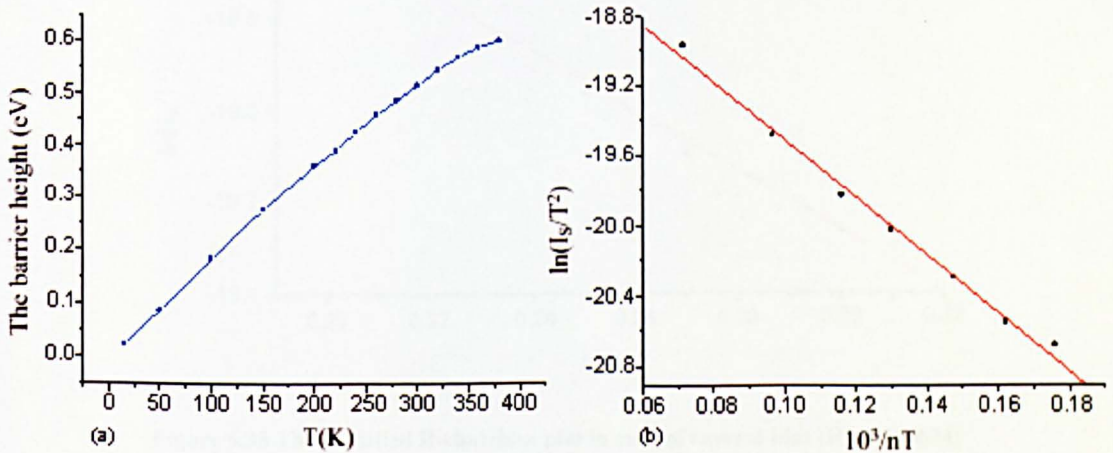


Figure 5.32 (a) The temperature dependence of the barrier height for GaMnAs as estimated from equation (2.14) and (b) The modified Richardson plot ( $R= 0.99631$ ) for sample Mn (374)

Substitution of the saturation current  $I_S$  as estimated from equation (2.15) and the effective Richardson constant  $A^{**}$  with a value of  $120 \text{ A/cm}^2 \text{ K}^2$  for p-type GaAs in equation (2.14) is required in order to calculate the barrier height at different

temperatures. This is shown in Figure 5.32 (a). The calculated values of  $\Phi_b$  were found to be strongly temperature dependent.

Figure 5.32 (b) represents modified Richardson plot which is the plot of  $\ln(I_s/T^2)$  versus  $10^3/nT$  with the slope which gives the barrier height ( $\Phi_b$ ) of  $1.4 \pm 0.05$  eV. This value is close to 1.42 eV of GaAs band gap energy. The barrier height of 1.4eV is realistic since this device has highest doping concentration, nearly degenerate and it has p-type behaviour. The experimental data yield a Richardson constant of  $2 \times 10^{-6}$  A/cm<sup>2</sup> K<sup>2</sup> which is much lower than the 120 A/cm<sup>2</sup> K<sup>2</sup> for p-type GaAs. There is uncertainty in the reported value of  $A^{**}$ . Similar result is obtained by several authors for n-type GaAs [27, 28, 92]. They refer the deviation in the Richardson plots to the inhomogeneous barrier heights.

In case of the reverse bias, the barrier height from the modified Richardson plot between  $(I_s/T^2)$  and  $10^3/nT$  is shown in Figure 5.33 which gives  $0.56 \pm 0.02$  eV.

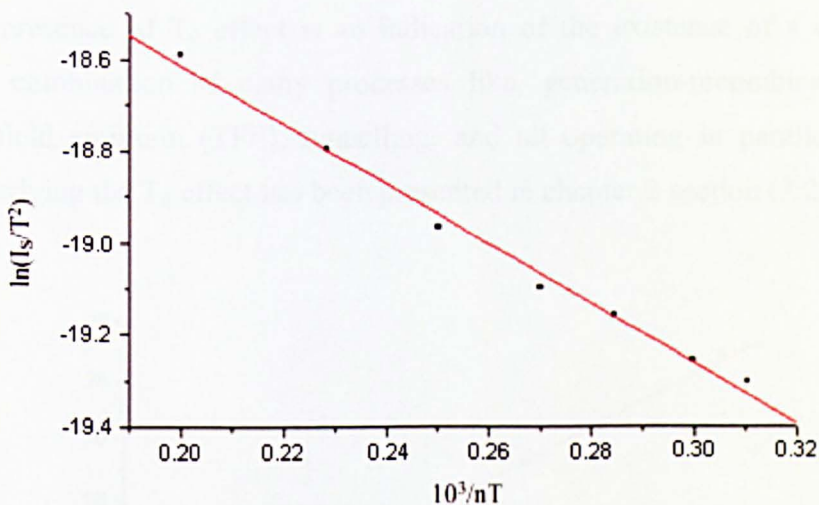


Figure 5.33 The modified Richardson plot in case of reverse bias ( $R= 0.996624$ )

The ideality factor was calculated from the fitting of equation (2.15). This is shown in Figure 5.34 as a function of temperature for forward bias.

It was found that the ideality factor ( $n$ ) increases with decreasing temperature. Also, for temperature below 100 K ideality factor increases rapidly indicating that a

mechanism other than thermionic emission has become dominant. The possibility of tunnelling cannot be ruled out. Carrier generation and recombination in the depletion region and/ or thermionic field emission can cause the ideality factor to increase rapidly with temperature [8].

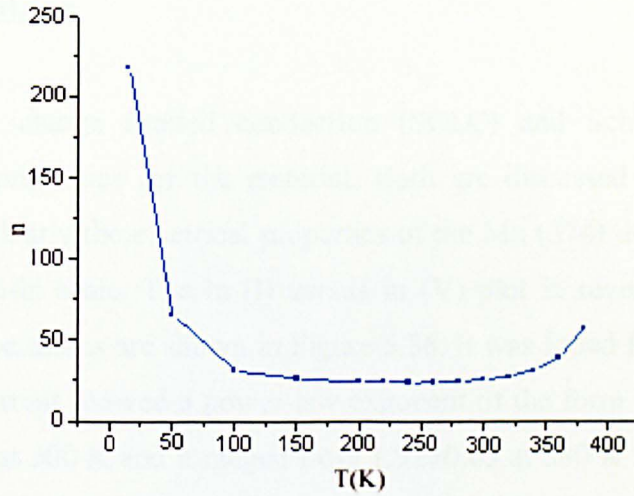


Figure 5.34 Ideality factor versus temperatures for GaMnAs sample Mn (374) device in forward bias

The presence of  $T_0$  effect is an indication of the existence of a current flow which is a combination of many processes like, generation-recombination (G-R), thermionic field emission (TFE), tunnelling, and all operating in parallel [13]. The physics underlying the  $T_0$  effect has been presented in chapter 2 section (2.2.8).

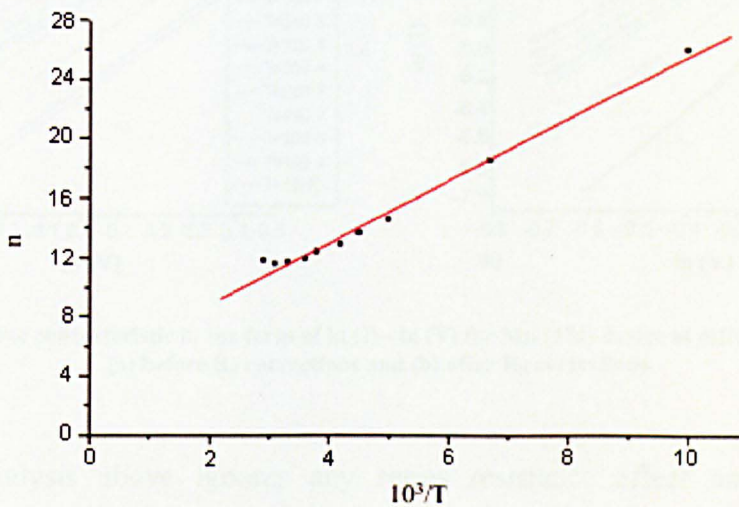


Figure 5.35 The Arrhenius plots of GaMnAs film (Mn374-1) sample in reverse bias

Figure 5.35 shows the ideality factor plotted against  $10^3/T$ . A linear relationship can be clearly seen. The values of  $n_0$  and  $T_0$  determined from the intercept and the slope are  $2 \pm 0.08$  and  $4.7 \times 10^3 \pm 0.4$  K respectively. Following the argument forwarded by Kribes et al. [16] the possible mechanism is thermionic field emission (TFE).

### c) GaAs: Mn-Insulator

The space charge limited conduction (SCLC) and Schottky emission are electrode related properties for the material. Both are discussed in this section. To understand more clearly the electrical properties of the Mn (374) device, their I-V data were plotted on ln-ln scale. The  $\ln(I)$  versus  $\ln(V)$  plot in reverse bias at different measurement temperatures are shown in Figure 5.36. It was found for sample Mn (374) that the reverse current showed a power-law exponent of the form  $I \sim V^m$  where  $m$  was equal  $2.33 \pm 0.05$  at 300 K and it ranged from  $1.92 \pm 0.03$  at 380 K to  $3.05 \pm 0.1$  at 15 K. The plot  $\ln(I)$  versus  $\ln(V)$  is linear, indicating that the device Mn (374) I-V characteristics seem to follow the space charge limited conduction (SCLC) mechanism [128]. The slopes of  $\ln(I) - \ln(V)$  plots are similar for both polarities except at 280 K as shown in Table 5.5.

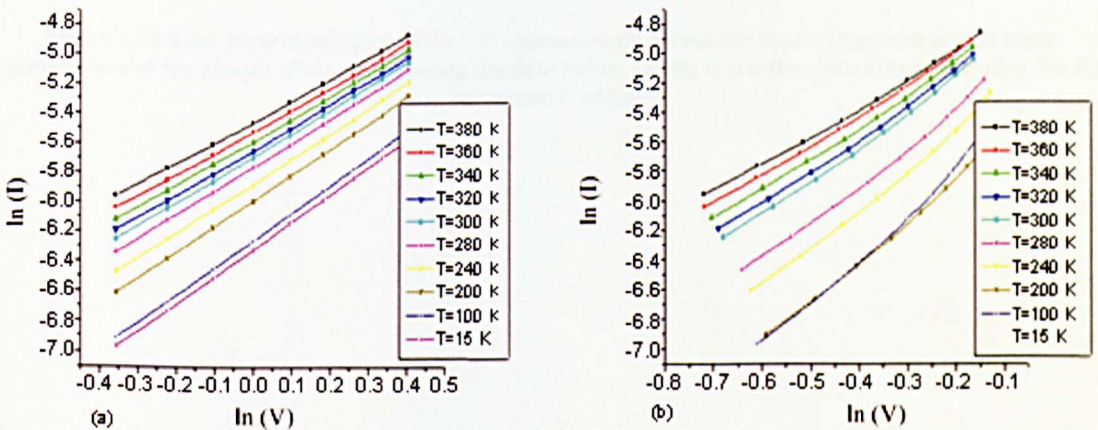


Figure 5.36 Reverse characteristic in the form of  $\ln(I) - \ln(V)$  for Mn (374) device at different temperatures (a) before  $R_s$  corrections and (b) after  $R_s$  corrections

The analysis above ignores any series resistance effect and needs to be investigated further. Both bias polarities are discussed in order to present the effect of the series resistance correction when plotting these curves using this equation ( $V_{\text{junction}} = V_{\text{applied}} - IR_s$ ). To demonstrate the procedure, the forward I-V characteristic at

room temperature is plotted in Figure 5.37. A fit of the data is shown as the solid line going through the data points. The red line is the derived I-V characteristics with the effect  $R_S$  removed.

A plot of  $\ln(I)$  versus  $\ln(V)$  at 320 K is presented in Figure 5.38 and it compares the effect of series resistance removal. It appears that this curve shows linear behaviour over several order of current magnitude. This indicates that the result may be explained in terms of the space charge limited conduction (SCLC) for Mn (374) device.

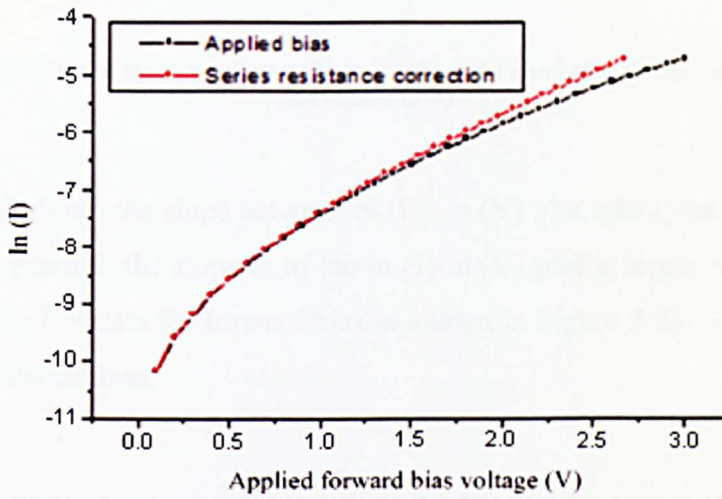


Figure 5.37 Semi-logarithmic plot of the I-V characteristic versus the applied forward bias at room temperature of the sample (374) and showing the data before the  $R_S$  correction (black line) and after the  $R_S$  correction (red line)

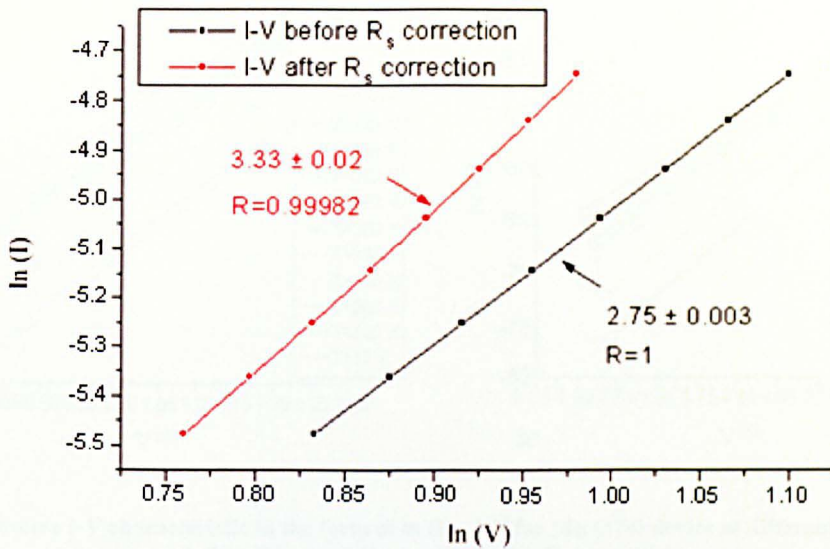


Figure 5.38 The estimation of the slope of the  $\ln(I)$ - $\ln(V)$  plot before and after the  $R_s$  correction at 320 K of the sample (374)

Table 5.5 shows the slope between  $\ln(I)$  -  $\ln(V)$  plot taking the series resistance into account. In general, the slope  $m$  of the  $\ln(I)$ - $\ln(V)$  plot is larger when  $R_s$  effect is removed from the I-V data for forward bias as shown in Figure 5.38. Similar behaviour is observed for reverse bias.

Table 5.5 The slope between  $\ln I$  versus  $\ln V$  after  $R_s$  corrections in both polarities

| T   | slope (Forward bias) | slope (Reverse bias) |
|-----|----------------------|----------------------|
| 380 | 1.18±0.009           | 1.92±0.03            |
| 360 | 2.4±0.02             | 2.05±0.04            |
| 340 | 2.87±0.03            | 2.15±0.04            |
| 320 | 3.33±0.02            | 2.24±0.05            |
| 300 | 4.25±0.07            | 2.33±0.05            |
| 280 | 7.02±0.4             | 2.43±0.06            |
| 240 | 4 ±0.1               | 2.56±0.07            |
| 200 | 1.92±0.1             | 2.69±0.07            |
| 100 | 2±0.2                | 2.89±0.09            |
| 15  | 2.2±0.2              | 3.05±0.1             |

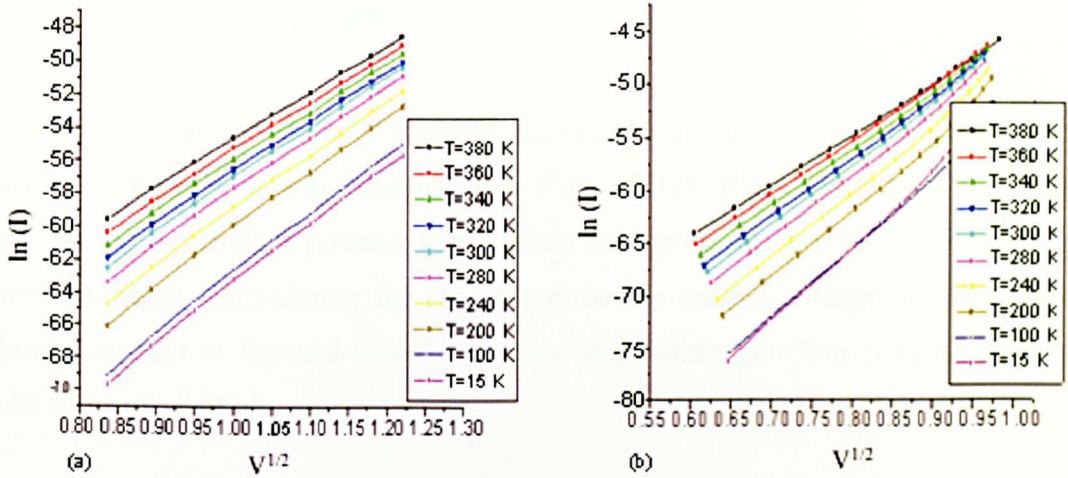


Figure 5.39 Reverse I-V characteristic in the form of  $\ln(I) - V^{1/2}$  for Mn (374) device at different temperatures (a) before  $R_s$  corrections and (b) after  $R_s$  corrections

There is also the possibility that the exponential behaviour of the I-V characteristic of GaMnAs is due to the Schottky emission. This can be explored by plotting  $\ln(I)$  versus  $V^{1/2}$ . A straight line is indicative that Schottky emission is operational. This data from this sample do show a straight line in forward and reverse bias at voltages  $V > 0.5$  V up to 2 volts. Table 5.6 shows the slope between  $\ln(I) - V^{1/2}$  plots for both polarities.

Table 5.6 The slope between  $\ln I$  versus  $V^{1/2}$  plot after  $R_s$  corrections in both polarities

| T   | $\beta_s (10^{-5} \text{ eV.m}^{1/2}.\text{V}^{-1/2})$ (Forward bias)<br>voltage range =0.7-1.5V | $\beta_s (10^{-5} \text{ eV.m}^{1/2}.\text{V}^{-1/2})$ (reverse bias)<br>voltage range =0.7-1.5V |
|-----|--|--|
| 380 | 3.8±0.08   | 4.8±0.02   |
| 360 | 3±0.01   | 5.1±0.03   |
| 340 | 3.4±0.01   | 5.4±0.04   |
| 320 | 3.8±0.01   | 5.6±0.05   |
| 300 | 4 ±0.01  | 5.8±0.06   |
| 280 | 4.3±0.01   | 6±0.08   |
| 240 | 4.7±0.02   | 6.3±0.09   |
| 200 | 5.2±0.04   | 6.2±0.05   |
| 100 | 6.8±0.08   | 6.6±0.06   |
| 15  | 6.7±0.08   | 7±0.08   |

We may conclude this section; by either suggesting that the space charge limited (SCL) or Schottky emission is the possible conduction mechanism in the Mn (374) device.

**d) Back -to -back diode model**

GaAs: Mn and GaAs:Si (bottom electrode) formed p n junction while the top metallic electrode is Schottky contact, (see Figure 5.40). The forward condition applies when the top electrode is positive while, when the top electrode is negative the sample is reverse-biased. Considering the case when the top contact is negative, then the top Schottky contact is forward-biased, whereas, the bottom junction n-Si: GaAs/p-Mn: GaAs is reverse biased.

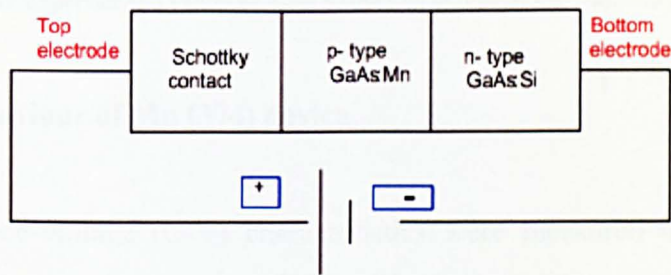


**Figure 5.40** The proposed model for back-to-back diode in case of forward bias

The estimated  $E_{00}$  using equation (2.22) was found to be 236 meV with  $N_D=1 \times 10^{21} \text{ cm}^{-3}$  which was much higher than  $kT$ . This indicates that the tunnelling mechanism plays an important role. Table 5.7 shows the doping concentrations for different devices used in this study and the value of  $E_{00}$  calculated using equation (2.22).

**Table 5.7** The doping concentration and the corresponding  $E_{00}$  value estimated from equation (2.22).

| Sample number | Physical doping ( $\text{cm}^{-3}$ ) | $E_{00}$ (meV) (equation (2.22)) |
|---------------|--------------------------------------|----------------------------------|
| 374           | $10^{21}$                            | 236                              |
| 375           | $10^{20}$                            | 74.64                            |
| 376           | $10^{19}$                            | 23.6                             |

The ideality factor is further analysed by plotting  $E_0$  ( $E_0=nkT/q$ ) versus  $kT/q$  in the case of forward bias as shown in Figure 5.41. The experimentally observed  $E_{00}$  value of 300 meV for forward bias is slightly higher than the theoretically calculated value of 236 meV. Hasegawa and Oyama [129] attributed this to the effect of defects.

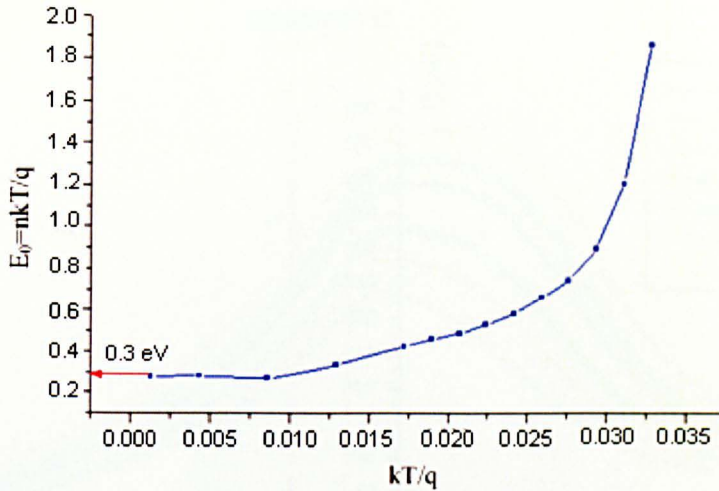


Figure 5.41 Experimental values of  $E_0$  as a function of temperature for Mn (374) device

### 5.7.1 C-V-T behaviour of Mn (374) device

Capacitance-voltage (C-V) characteristics were measured using the Boonton (model 7200) meter at a frequency of 1MHz. The instrument was controlled by written program using LabView. Capacitance was measured from 0 to -4 V in reverse bias and 0.1 to 3 V in forward bias. Each voltage sweep was delayed in time in order to make allowances for the capacitance to stabilize to equilibrium. The sample was mounted inside the cryostat where the temperatures were varied so C-V characteristic could be measured at different temperatures from 400 K to 15 K.

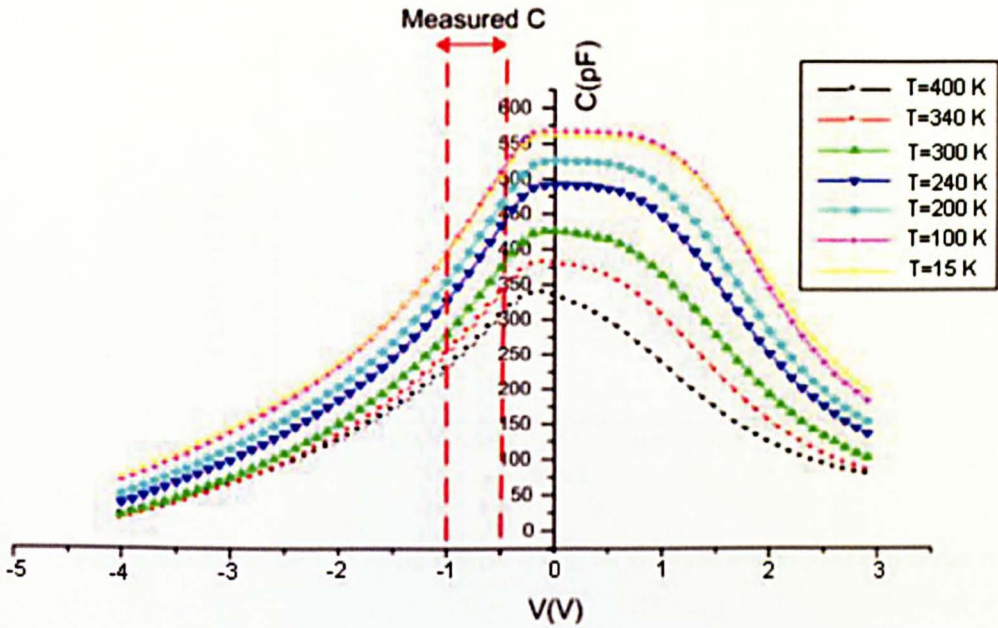


Figure 5.42 The capacitance versus bias voltage for GaMnAs sample Mn (374) device

The C-V characteristic for Mn (374) device over the temperature range 400 K to 15 K was investigated. The C-V characteristics in Figure 5.42 show that the capacitance is voltage dependent. It has been observed that the capacitance as a function of applied bias increases until it reaches a high value and stays constant over a small range of bias, and then drops with increasing bias. The validity of the measured capacitance is denoted by the two red lines shown in Figure 5.42. Outside these lines, the capacitance value is unreliable because of the high conductance of the sample. They are unreliable because the conductance increases at these voltages ranges but the general behaviour is what is expected of the back-to-back diode.

Figure 5.42 shows that there are three distinct regions. For instance, at zero bias the capacitance at room temperature is around 425.4 pF which is the highest value, and then is observed to decrease with the increasing bias in both polarities. The flat region with very small changes of capacitance extends in both forward and reverse directions. It ranges from -0.2 V to +0.3 V with a peak value of capacitance at zero bias. There is a progressive gradual decrease of capacitance in both directions. This flat region becomes sharper when the temperature increases to 400 K and it takes a wider shape at low temperature (15 K). In reverse bias condition, the flat region shows that the junction is fully depleted while the flat region in forward bias indicates that there is a charge accumulation near the  $p^+ - n$  junction in Mn (374) device.

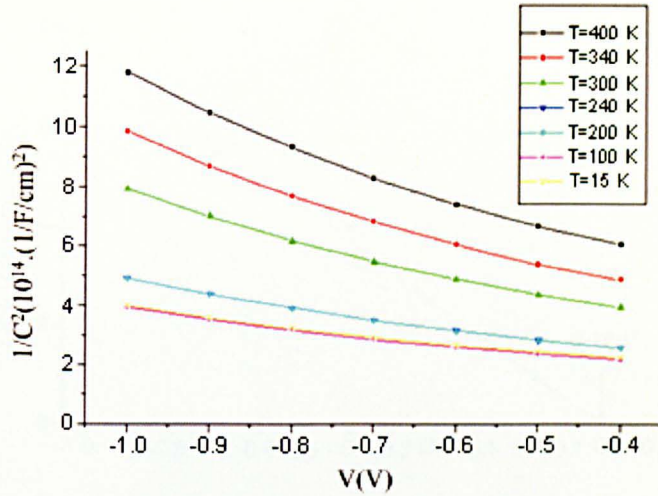


Figure 5.43 Plot of the  $1/C^2$  versus reverse voltage for GaMnAs sample Mn (374) device

The  $1/C^2$  versus voltage plot at different temperatures is shown in Figure 5.43. The doping concentration can be obtained from the plot  $1/C^2$  versus applied reverse voltage. The room temperature plotting is shown in Figure 5.44 which shows linearity behaviour in range 0.4 V up to 1 V. After this range the capacitance can not be measured due to high current. The intercept to the x-axis of this plot is extremely small at all temperatures and it is difficult to give an explanation for this behaviour.

As mentioned previously, the samples are grown at low temperature which may compensate the Mn doping. In this case, the junction may be of  $p^+-n$  junction and the depletion region will then extend into the lightly doped Mn epi-layer. If the depletion region is sufficiently large it may touch the Ohmic contact when a reverse bias is applied and an affect called “punch through” [6] occurs. This may explain the high reverse current in this device. This will be exacerbated by the uneven thickness of the layer.

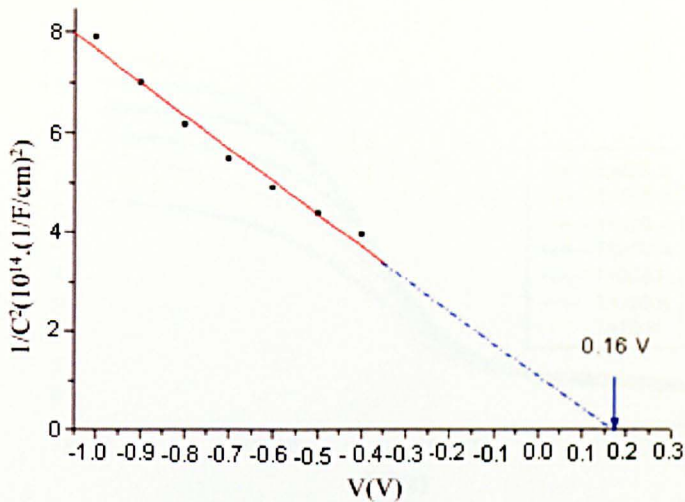


Figure 5.44 Plot  $1/C^2$  versus reverse bias voltage for GaMnAs film Mn (374) device, showing the experimental data as well as the extrapolated line meeting the x-axis

The calculated carrier concentration at 300 K has been determined to be  $5.6 \times 10^{16} \text{ cm}^{-3}$  in Mn (374) device and this value remains constant until 200 K then it begins to reach  $1 \times 10^{17} \text{ cm}^{-3}$  in the range 150 K to 15 K.

### 5.7.2 C-F-T behaviour of Mn (374)

The admittance measurements were made at frequencies ranging from 20 Hz to 3 MHz. Admittance spectroscopy was used to characterize the traps present in the Mn (374) device. Figure 5.45 shows the capacitance spectra of the device at zero voltage bias and temperatures between 400 and 15 K and the corresponding Arrhenius plot is shown in Figure 5.46.

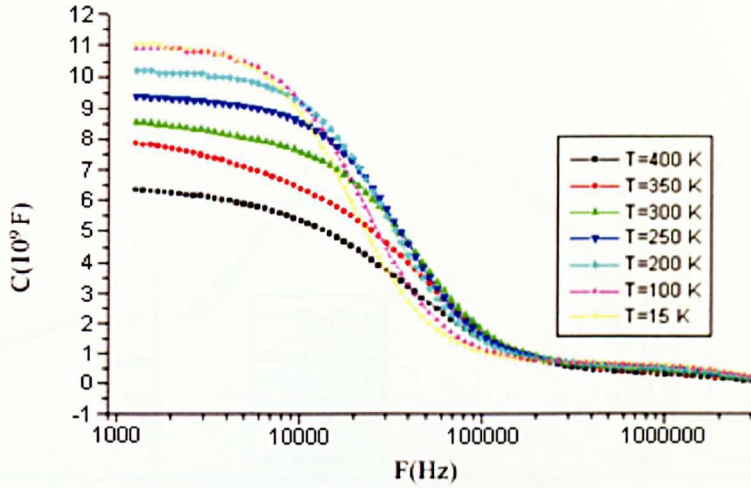


Figure 5.45 The capacitance versus the frequency voltage for GaMnAs sample Mn (374)

We can estimate the activation energy to be  $0.117 \pm 0.005$  eV which compares favourably with the activation energy of Mn in GaAs.

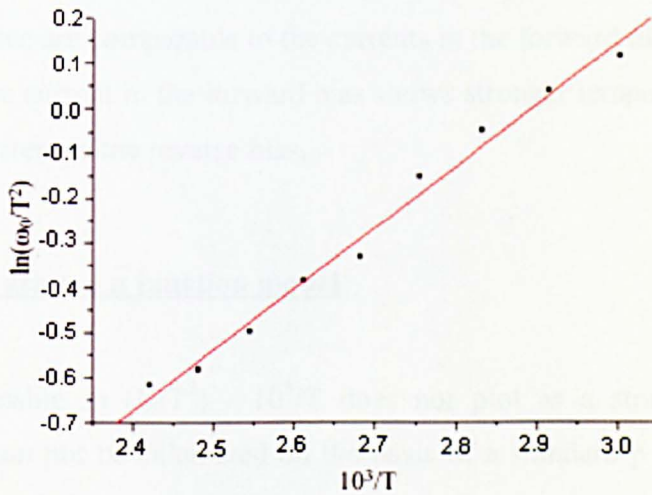


Figure 5.46 The Arrhenius plot for Mn (374)

## 5.8 (Mn375) Devices

The (Mn375) device has a Mn doping level of  $10^{20} \text{ cm}^{-3}$ . Two different samples, with the same doping concentration, were investigated and are labelled Mn (375-1) and Mn (375-2).

## 5.8.1 (Mn375-1) Device

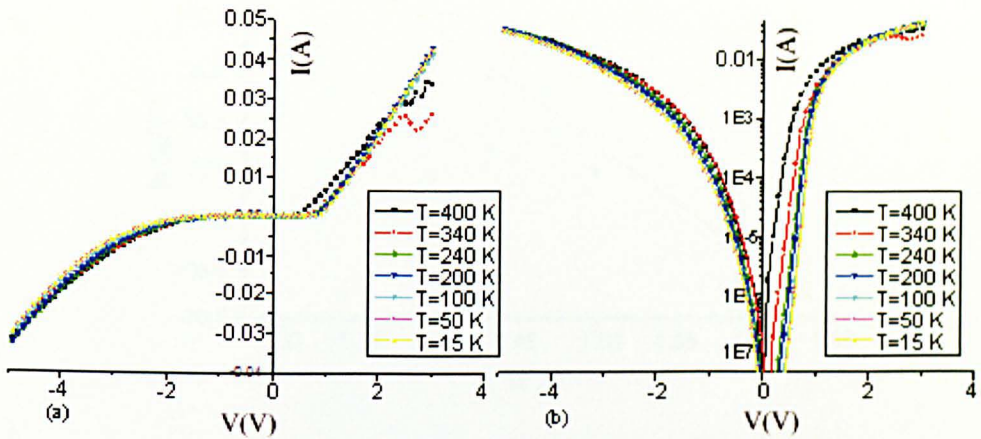


Figure 5.47 Current-voltage curve for GaMnAs (Mn375-1) device

The current-voltage-temperature measurements for device Mn (375-1), were carried out for both forward and the reverse directions as shown in Figure 5.47 (a) and (b). At all temperatures, the diodes exhibit soft characteristics. The reverse currents flowing in this device are comparable to the currents in the forward direction. It can also be observed that the current in the forward bias shows stronger temperature dependence compared to the current in the reverse bias.

#### a) Analysis of I-V using p n junction model

The relationship  $\ln(I_S/T^3) - 10^3/T$  does not plot as a straight line and the activation energy can not be calculated on the basis of a standard p n junction model. This has been earlier mentioned in section (5.7) (a). The modified Richardson plot ( $\ln(I_S/T^3)$ ) versus  $10^3/nT$  (Figure 5.48) gives an activation energy  $0.982 \pm 0.1$  eV.

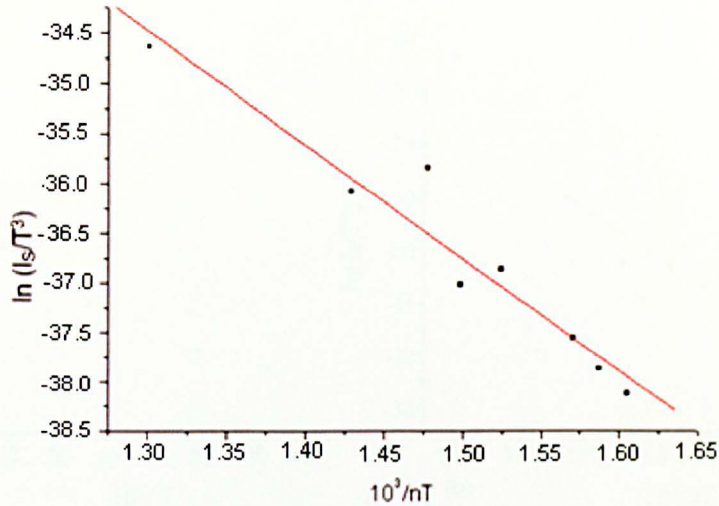


Figure 5.48 The modified Richardson plot ( $\ln(I_s/T^3)$ ) versus  $10^3/nT$  with  $E_a = 0.982 \pm 0.1$  eV ( $R=0.96627$ )

### b) Analysis of I-V using Schottky model

The values of ideality factor  $n$  at different temperatures are shown in Figure 5.49 which is a support TE and TFE theory. Value of  $n$  approaches unity as the temperature increases while at lower temperatures  $n$  increases due to TFE.

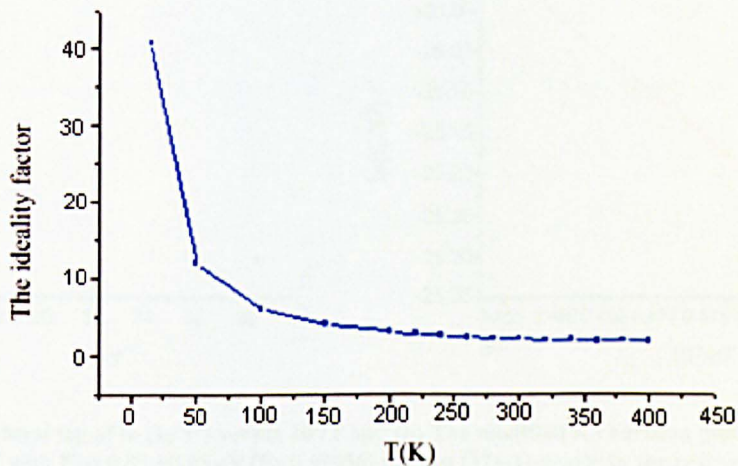


Figure 5.49 Ideality factor ( $n$ ) versus temperatures in forward bias for (Mn375-1) device

Using the values of  $n$  at different temperatures modified Richardson plot between  $(I_s/T^2)$  versus  $10^3/nT$  for forward bias is drawn and shown in Figure 5.50 (b) which gives the activation energy of  $1.4 \pm 0.2$  eV. This is in good agreement with the bandgap of GaAs.

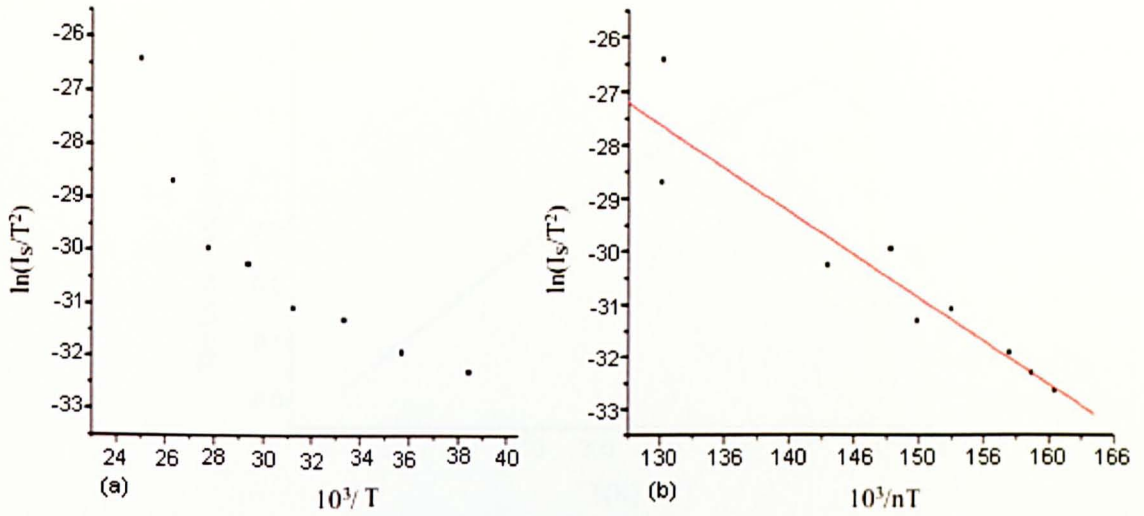


Figure 5.50 (a) Natural log of  $\ln(I_s/T^2)$  versus  $10^3/T$  for Mn (375-1) device in the forward bias and (b) The modified Richardson plot ( $\ln(I_s/T^2)$  versus  $10^3/nT$  ( $R=0.94188$ ))

For the reverse bias case the barrier height from the modified Richardson plot between  $(I_s/T^2)$  versus  $10^3/nT$  shown in Figure 5.51 (b) gives  $0.85 \pm 0.05$  eV which is slightly higher than half the bandgap of GaAs while Figure 5.51 (a) shows a curve.

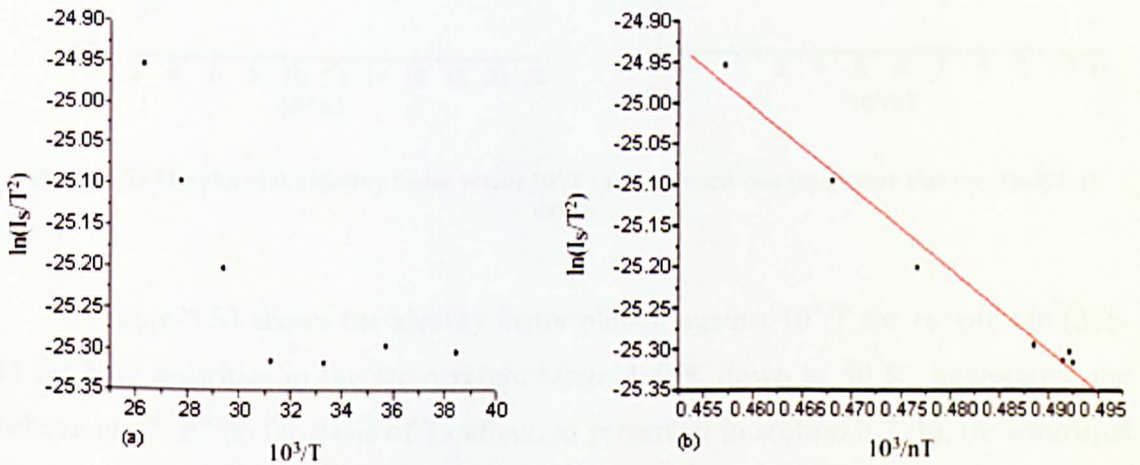


Figure 5.51 (a) Natural log of  $\ln(I_s/T^2)$  versus  $10^3/T$  and (b) The modified Richardson plot ( $\ln(I_s/T^2)$  versus  $10^3/nT$  with  $E_a = 0.85 \pm 0.05$  eV ( $R=0.99056$ )) for Mn (375-1) device in the reverse bias

A calculation of the barrier height  $\Phi_b$  for Mn (375-1) device using equation (2.17) is shown in Figure 5.52. It was found that the barrier height in the forward bias was higher than the reverse bias. In addition, the barrier height  $\Phi_b$  was strongly dependent on temperature.

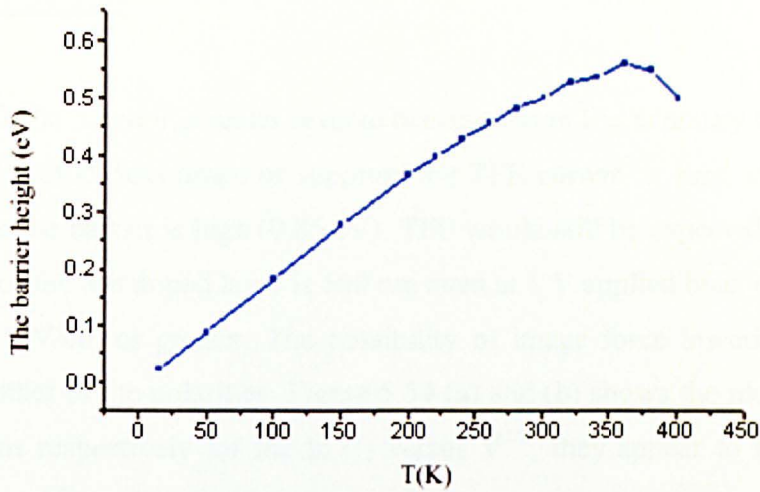


Figure 5.52 The temperature dependence of the barrier height for GaMnAs (sample Mn (375-1) in the temperature range 400-15 K

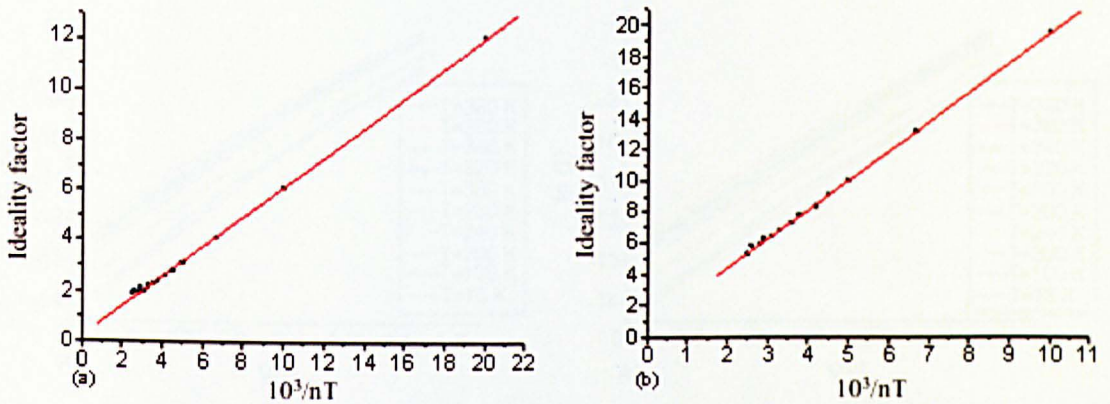


Figure 5.53 The plot of the ideality factor versus  $10^3/T$  (a) in forward bias (b) reverse bias for (Mn375-1) device

Figure 5.53 shows the ideality factor plotted against  $10^3/T$  for sample Mn (375-1) for both polarities in the temperature range 400 K down to 50 K. Interpreting the behaviour of “n” on the basis of  $T_0$  effect, as presented in section 5.7 (b), the estimated  $T_0$  is  $600 \text{ K} \pm 0.0007$  and  $1900 \text{ K} \pm 0.001$  for forward and reverse bias respectively. While the value of  $0.24 \pm 0.05$  and  $0.65 \pm 0.07$  was found for the  $n_0$  intercept for forward and reverse bias respectively; this is very close value to the origin. Following the argument put forward by Kribes et al. [16] the possible mechanism is thermionic field emission (TFE).

### c) GaAs: Mn-Insulator

It should be noted that under reverse bias condition the Schottky barrier actually broadens. This would discourage or suppress the TFE current at least at lower biases. However, since the barrier is high (0.85 eV), TFE would still be expected to play a role. The thickness of the Mn doped layer is 500 nm even at 1 V applied bias, the field across the layer is 1 MV/cm or greater. The possibility of image force lowering can not be ruled out for either of the polarities. Figure 5.54 (a) and (b) shows the plots for forward and reverse bias respectively for the  $\ln(I)$  versus  $V^{1/2}$ , they appear to follow a linear relationship suggesting a barrier lowering mechanism.

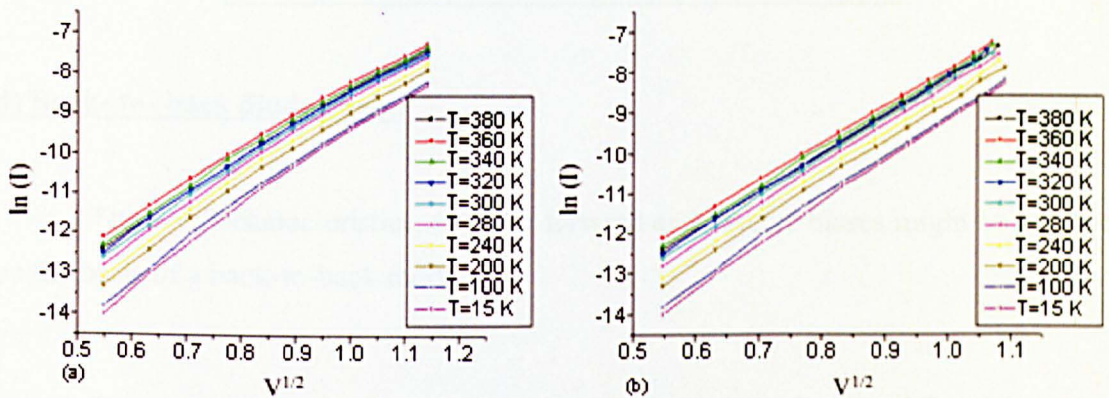


Figure 5.54 Reverse I-V characteristic in the form of  $\ln(I) - V^{1/2}$  for Mn (375-1) device at different temperatures (a) before  $R_s$  corrections and (b) after  $R_s$  corrections

The conduction mechanism is determined on the basis of Schottky barrier lowering mechanism if the plot of  $\ln(I)$  versus  $V^{1/2}$  yields a straight line. The linearity of these plots indicates that the Schottky emission is operative in the voltage range  $1.2 < V < 2.1$  V for forward bias and  $1.3 < V < 2$  V for reverse bias as shown in Figure 5.54 (a) and (b) respectively. The slopes of the  $\ln(I)$  versus  $V^{1/2}$  characteristic in both polarities are shown in Table 5.8. However, it appears more probable that it is the lowering of the Schottky barriers through which TFE is also taking place.

**Table 5.8** The slope between  $\ln I$  versus  $V^{1/2}$  plot after  $R_s$  corrections in both polarities

| T   | $\beta_s$ ( $10^{-5}$ eV.m <sup>1/2</sup> .V <sup>-1/2</sup> )<br>(Forward bias)<br>voltage range =1.2-2.1 V | $\beta_s$ ( $10^{-5}$ eV.m <sup>1/2</sup> .V <sup>-1/2</sup> )<br>(Reverse bias)<br>voltage range =1.3-2 V |
|-----|--|--|
| 380 | 1.2±0.01   | 9.44±0.02  |
| 360 | 1.13±0.01  | 9.22±0.04  |
| 340 | 1.06±0.02  | 9.46±0.06  |
| 320 | 1.03±0.02  | 9.69±0.06  |
| 300 | 1.06±0.04  | 9.72±0.06  |
| 280 | 0.99±0.02  | 9.81±0.07  |
| 240 | 0.95±0.02  | 9.96±0.1   |
| 200 | 0.91±0.02  | 9.93±0.1   |
| 100 | 0.86±0.02  | 10.07±0.1  |
| 15  | 0.83±0.02  | 10.47±0.1  |

**d) Back- to- back diode model**

The I-V-T characteristics, for both forward and reverse biases might be analysed on the basis of a back-to-back model.

The complete energy band structure is given in Figure 5.24. This gives essentially two contacts. One is the top Schottky contact with the p-type GaAs:Mn and the other between GaAs:Mn and GaAs:Si is p n junction. According to calculation of the energy band diagram using Matlab program (Figure 5.9), the p n junction above 300 K is between two degenerate semiconductors, while below 300 K, p-region becomes non-degenerate.

## 5.8.2 C-V measurement of Mn (375)

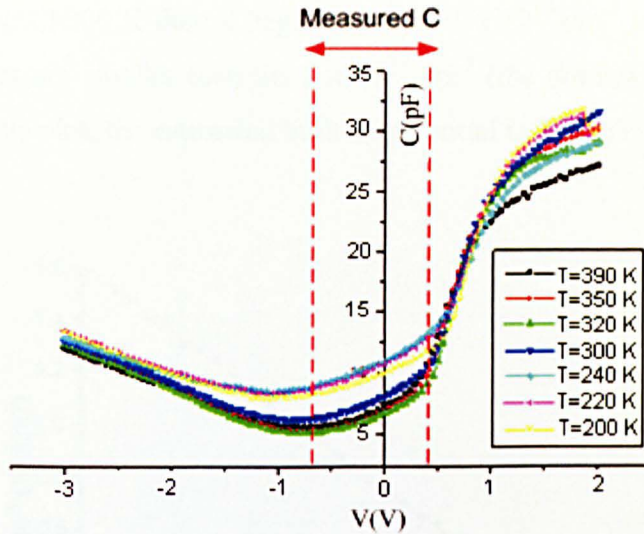


Figure 5.55 The capacitance versus bias voltage for GaMnAs sample Mn (375-1)

Figure 5.55 shows the C-V response at 1MHz for Mn (375-1) device. This device shows a similar behaviour as MOS/MIS structure. The capacitance decreases with increasing temperature beyond +1 V bias. In the reverse bias, on the other hand the sample exhibits an increase in capacitance with increasing temperature. The plot in Figure 5.56 shows  $1/C^2$  versus V at different temperatures.

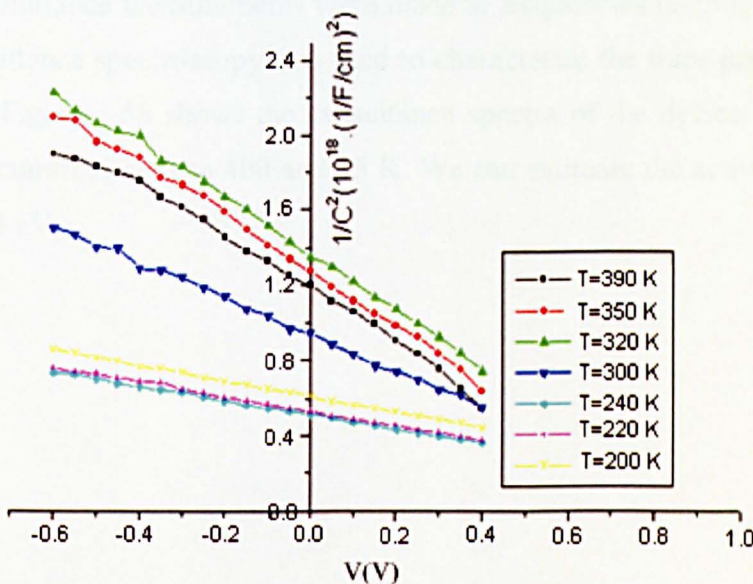


Figure 5.56  $1/C^2$  versus reverse voltage for GaMnAs sample Mn (375-1) device

The calculated carrier concentration at 300 K for Mn (375-1) is shown in Figure 5.57. It has been determined to be  $5.6 \times 10^{14} \text{ cm}^{-3}$  in Mn (375-1) device and this value remains constant until 200 K then it begins to reach  $1 \times 10^{13} \text{ cm}^{-3}$  in the range 150 K to 15 K. These values are smaller than the  $2 \times 10^{17} \text{ cm}^{-3}$  (the doping concentration of the Si-GaAs). From this plot, the estimated built-in potential is 0.96 eV.

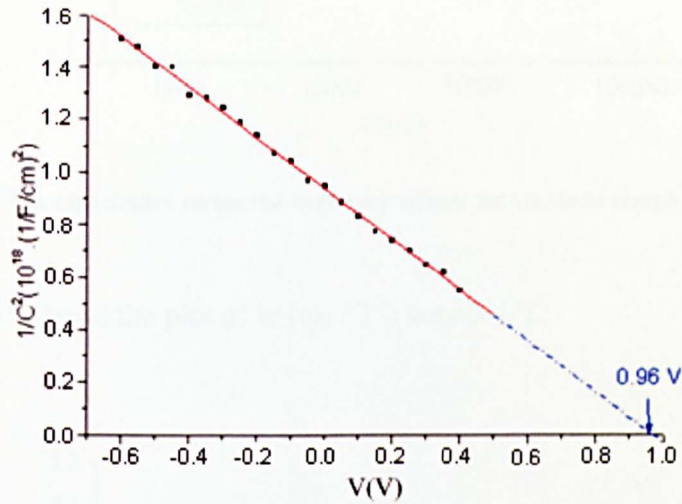


Figure 5.57 Plot  $1/C^2$  versus reverse bias voltage at room temperature for GaMnAs film Mn (375-1) device

### 5.8.3 C-F-T behaviour of Mn (375-1)

The admittance measurements were made at frequencies ranging from 20 Hz to 3 MHz. Admittance spectroscopy was used to characterize the traps present in the Mn (374) device. Figure 5.58 shows the capacitance spectra of the device at zero voltage bias and temperatures between 400 and 15 K. We can estimate the activation energy to be  $0.06 \pm 0.004 \text{ eV}$ .

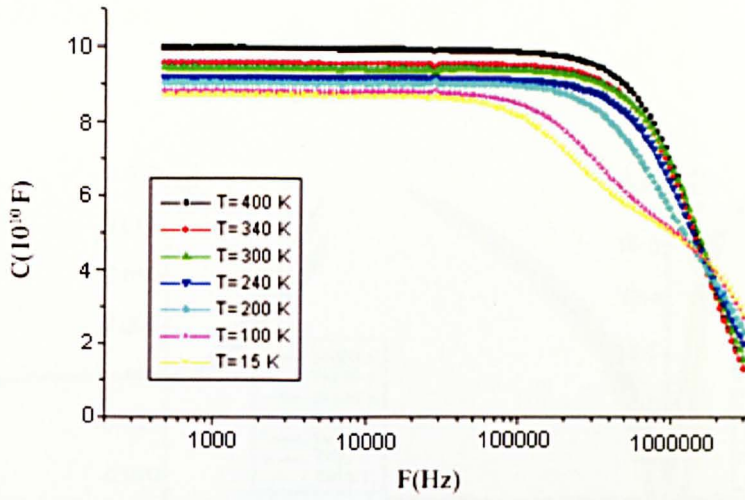


Figure 5.58 The capacitance versus the frequency voltage for GaMnAs sample Mn (375-1)

Figure 5.59 shows the plot of  $\ln(\omega_0 / T^2)$  versus  $1/T$ .

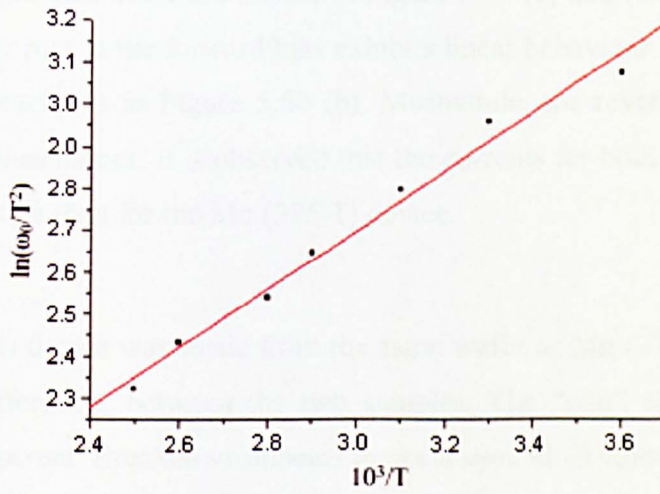


Figure 5.59 The Arrhenius plot for Mn (375-1)

### 5.9 (Mn375-2) Device

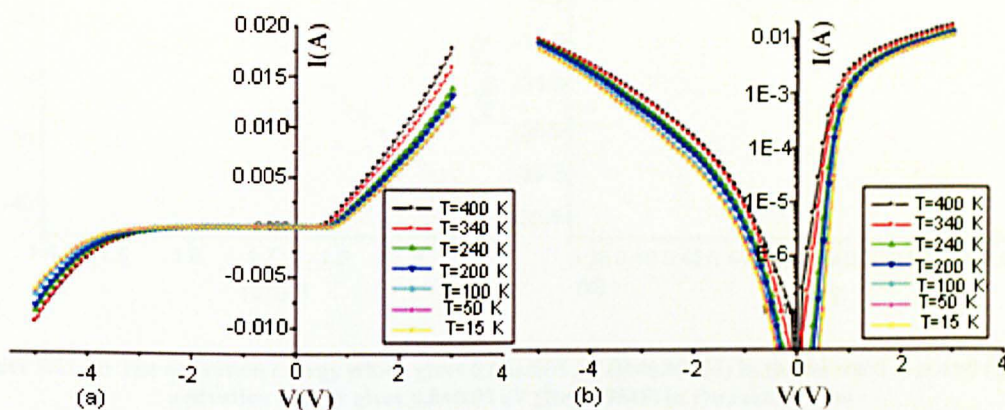


Figure 5.60 Current-voltage curve for GaMnAs (Mn375-2) device

The I-V-T plots of Mn (375-2) device in the temperature range 400-15 K on linear and semilogarithmic scale are shown in Figure 5.60 (a) and (b). As can be seen in Figure 5.60 (b) the plot in the forward bias exhibits linear behaviour up to 1 volt, then it deviates from linearity as in Figure 5.60 (b). Meanwhile, the reverse currents show a curve for all voltages ranges. It is observed that the currents for both polarities are more temperature sensitive than for the Mn (375-1) device.

Mn (375-2) device was made from the same wafer as Mn (375-1) device. There are noticeable differences between the two samples. The “soft” characteristic of the diode is not so apparent. Breakdown appears to occur around -3 volts.

#### a) Analysis of I-V using p n junction model

In order to explain the result in terms of p n junction model the plot in the form of  $\ln(I_S/T^3)$  versus  $10^3/T$  has been plotted in both polarities. The experimental data are seen to fit a straight line in the plot for (Mn375-2) device for both polarities as shown in Figure 5.61 (a) in the case of forward bias and Figure 5.61 (b) in reverse bias. The estimated activation energy in the case of forward and reverse bias condition is  $0.85 \pm 0.05$  eV and  $0.8 \pm 0.03$  eV respectively.

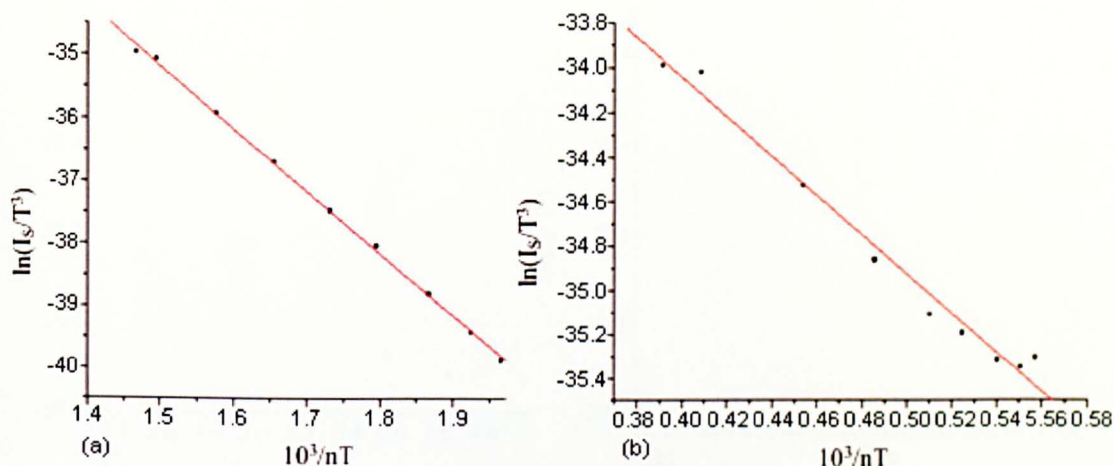


Figure 5.61 (a) The activation energy which gives  $0.85 \pm 0.05$  eV ( $R=0.99951$ ) in the forward bias and (b) The activation energy gives  $0.8 \pm 0.03$  eV ( $R=0.99548$ ) in the reverse bias

### b) Analysis of I-V using Schottky model

In order to explain the result in terms of Schottky model the plot in the form of  $\ln(I_s/T^2)$  versus  $10^3/T$  has been plotted. To determine the activation energy  $\ln(I_s/T^2)$  was plotted against  $10^3/T$  as shown in Figure 5.62 (a) for Mn (375-2) device by using equation (2.14), while the modified Richardson plot is shown in Figure 5.62 (b). The experimental data are seen to fit a straight line in the plot for Mn (375-2) device for both polarities as shown in Figure 5.62 (b) and Figure 5.63 (b). The estimated activation energy in case of forward and reverse bias condition is  $0.93 \pm 0.01$  eV and  $1 \pm 0.02$  eV respectively.

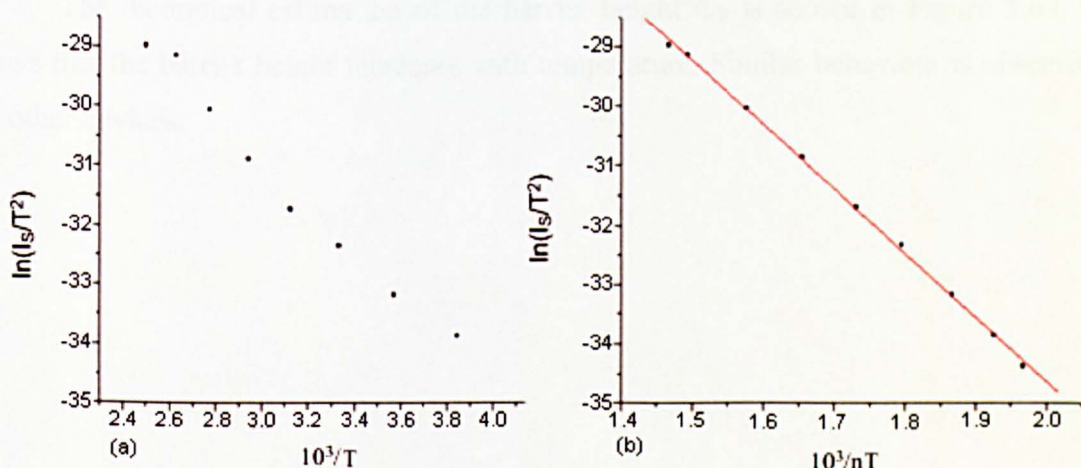


Figure 5.62 (a) The plot  $\ln(I_s/T^2)$  versus  $10^3/T$  and (b) The plot  $\ln(I_s/T^2)$  versus  $10^3/nT$  with  $E_a = 0.93 \pm 0.01$  eV ( $R=0.99943$ ) for Mn (375-2) device in the forward bias

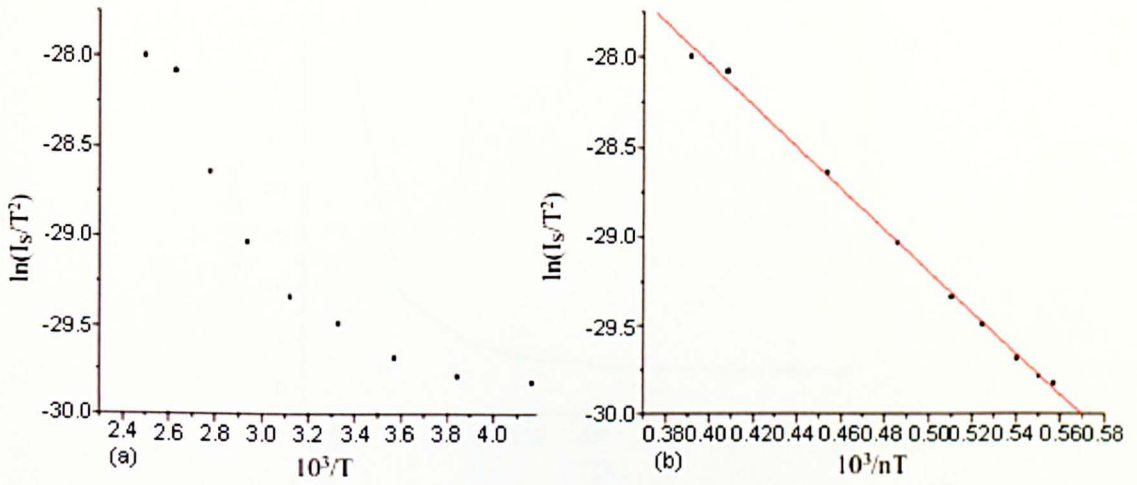


Figure 5.63 (a) The plot  $\ln(I_s/T^2)$  versus  $10^3/T$  and (b) The plot  $\ln(I_s/T^2)$  versus  $10^3/nT$  with  $E_a = 1 \pm 0.02$  eV ( $R=0.99888$ ) for Mn (375-2) device in the reverse bias

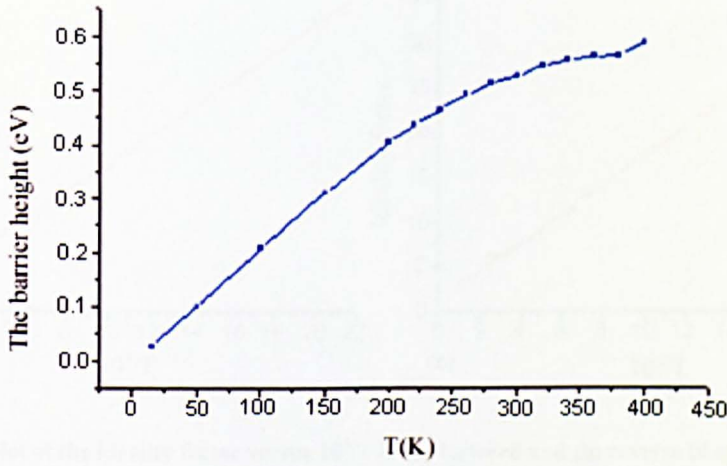


Figure 5.64 The temperature dependence of the barrier height in forward bias for GaMnAs sample Mn (375-2) in the temperature range 400-15 K

The theoretical estimation of the barrier height  $\Phi_b$  is shown in Figure 5.64. It shows that the barrier height increases with temperature. Similar behaviour is observed for other devices.

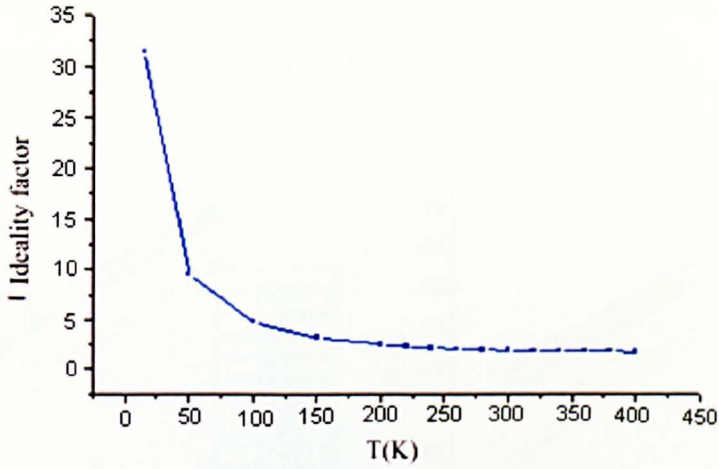


Figure 5.65 Ideality factor versus temperatures for GaMnAs sample (Mn375-2) device

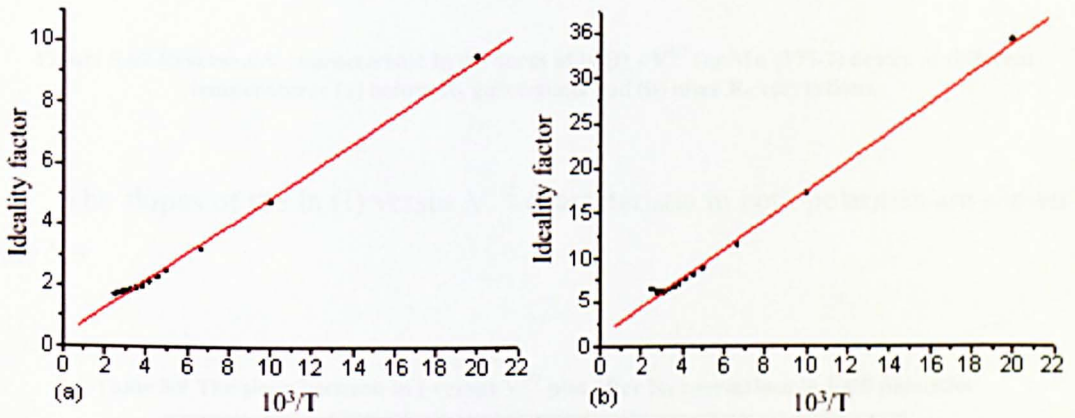


Figure 5.66 The plot of the ideality factor versus  $10^3/T$  in (a) forward and (b) reverse bias from temperature range 400-100 K for (Mn375-2) device

Figure (5.65) shows the ideality factor versus the temperature Mn (375-2) device. The ideality factor varies almost linearly with the inverse temperature for both polarities as in Figure 5.66 from 400 K up to 100 K. The estimated  $T_0$  is  $450 \pm 0.008$  K and  $1630 \pm 0.03$  K for forward and reverse bias respectively, while the value of the  $n_0$  intercept for forward and reverse bias is  $0.4 \pm 0.06$  and  $1 \pm 0.2$  respectively. Furthermore,  $T_0$  and  $n_0$  values are lower for Mn (375-2) device than for Mn (375-1) device. Karates and Altinda [28] reported a value  $T_0$  of  $473 \pm 2$  K for Au/n-type GaAs structures.

### c) GaAs: Mn-Insulator

The Schottky emission possibility is discussed by plotting  $\ln(I)$  versus  $V^{1/2}$ . This is shown in Figure 5.67. At voltage range  $-0.5 < V < -1.5$  V, the conduction mechanism

is dominated by Schottky emission in reverse bias range for Mn (375-2) device, while in forward bias the voltage range  $-0.5 < V < -1$  V.

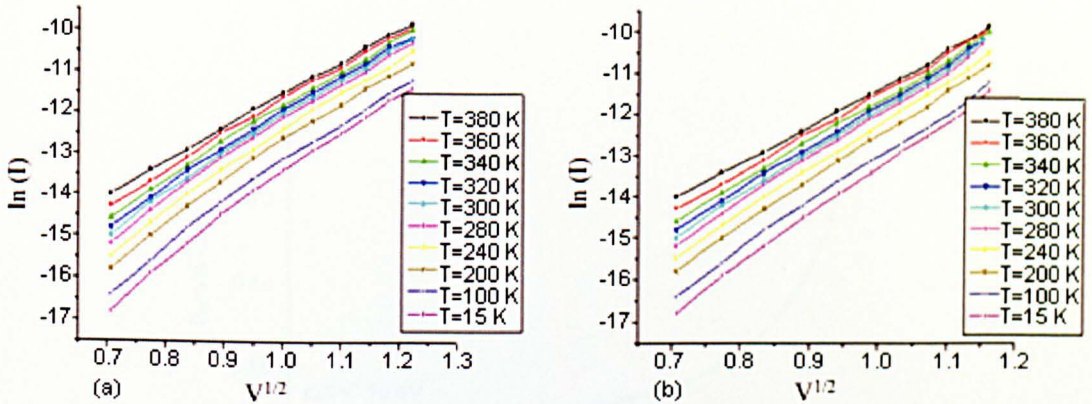


Figure 5.67 Reverse I-V characteristic in the form of  $\ln(I) - V^{1/2}$  for Mn (375-2) device at different temperatures (a) before  $R_s$  corrections and (b) after  $R_s$  corrections.

The slopes of the  $\ln(I)$  versus  $V^{1/2}$  characteristic in both polarities are shown in Table 5.9.

Table 5.9 The slope between  $\ln I$  versus  $V^{1/2}$  plot after  $R_s$  corrections in both polarities

| T   | $\beta_s$ ( $10^{-5}$ eV.m <sup>1/2</sup> .V <sup>-1/2</sup> )<br>(Forward bias)<br>voltage range =0.5-1.5 V | $\beta_s$ ( $10^{-5}$ eV.m <sup>1/2</sup> .V <sup>-1/2</sup> )<br>(reverse bias)<br>voltage range =0.5-1 V |
|-----|--|--|
| 380 | 22 ±0.8  | 9.1±0.08   |
| 360 | 27.28±0.9  | 9.6±0.08   |
| 340 | 28±0.6   | 9.95±0.1   |
| 320 | 29±0.9   | 10±0.09  |
| 300 | 30±0.7   | 10.5±0.1   |
| 280 | 32.8±0.6   | 10.7±0.1   |
| 240 | 35.8 ±0.4  | 10.8±0.08  |
| 200 | 36.2±0.3   | 10.9±0.09  |
| 100 | 34.3±0.5   | 11±0.1   |
| 15  | 34.8±0.4   | 11.6±0.1   |

#### d) Back- to-back diode model

GaAs:Mn and GaAs:Si (bottom electrode) formed p n junction while the top metallic electrode is Schottky contact.

The ideality factor is further analysed by plotting  $nkT/q$  against  $kT/q$ . The plot of  $E_0 = nkT/q$  versus  $kT/q$  in the case of forward bias is shown in Figure 5.68. The value of  $E_0$  is determined by extrapolating the plot to  $E_0$  axis which gives a value of 0.15 eV.

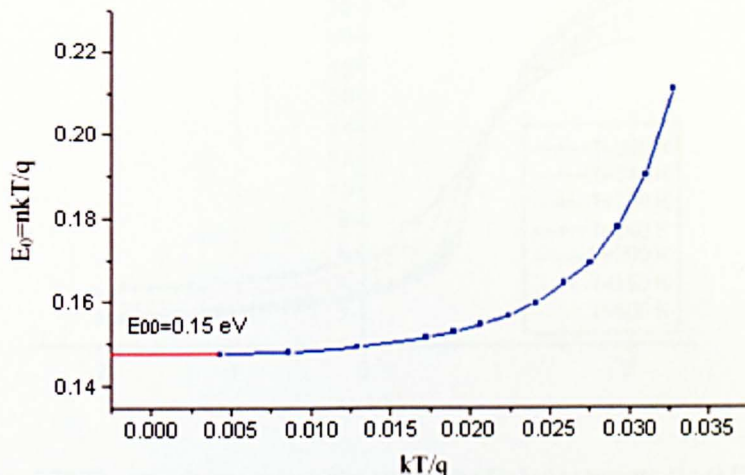


Figure 5.68 The experimental values of  $E_0$  as a function of temperature for Mn (375-2) device

Using the method of iteration, it is found that a value of 60 meV for  $E_{00}$  gives a good fit above 240 K as shown in Figure 5.69. The theoretical value of  $E_{00}$  is determined using equation (2.21). The estimated  $E_{00}$  was found to be 74.6 meV. This value is close to the value obtained from the iteration method but there is a considerable difference between this value and the experimental value obtained from Figure 5.68.

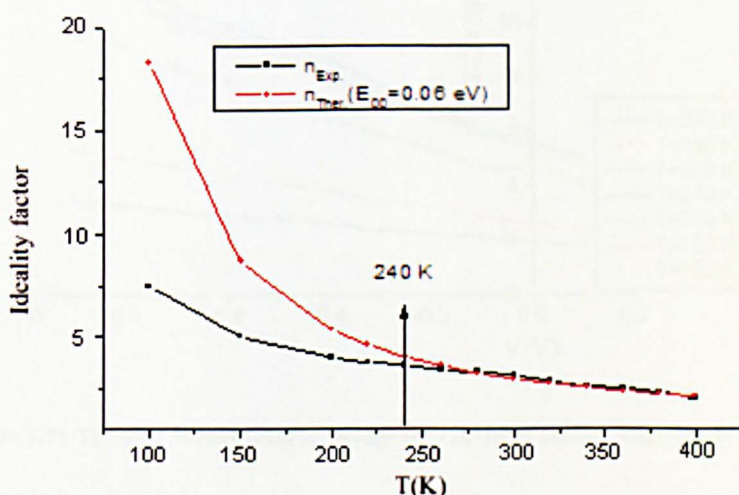


Figure 5.69 Theoretical temperature dependence of ideality factor obtained by the TFE model for tunnelling characteristic energy  $E_{00} = 0.06$  eV (red line), and the experimental determined ideality factor (black line) as a function of temperature in the reverse bias. It is found that a value of 60 meV for  $E_{00}$  gives a good fit above 240

K

## 5.9.1 C-V measurement of Mn (375-2)

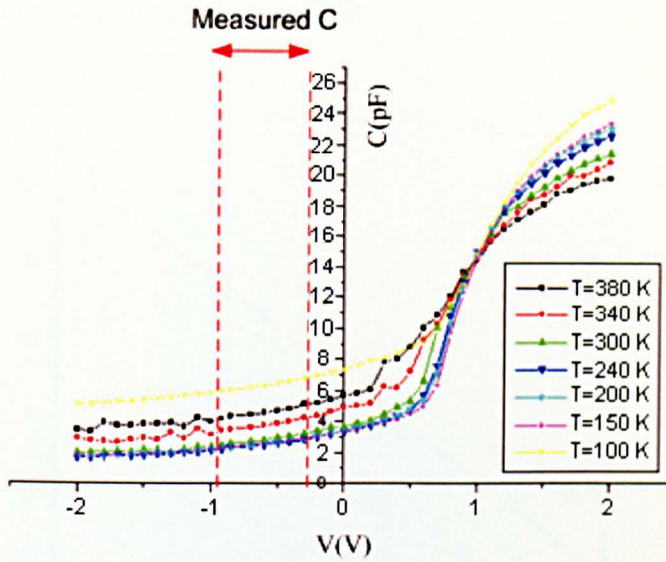


Figure 5.70 The capacitance versus bias voltage for GaMnAs sample Mn (375-2)

Figure 5.70 shows the C-V response measured at 1MHz for Mn (375-2) device. Device Mn (375-2) shows a trend where capacitance decreases with increasing temperature. The measured capacitance is denoted by the two red lines as shown in Figure 5.71 due to the high measured conductance in the remaining part.

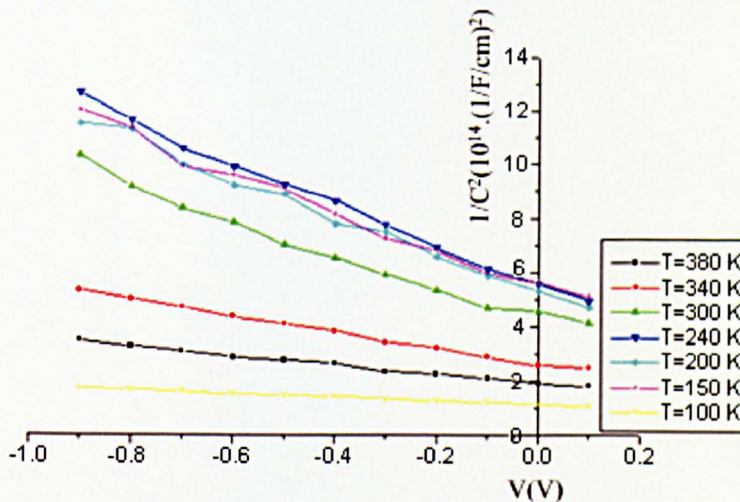


Figure 5.71 The  $1/C^2$  versus reverse voltage for GaMnAs sample Mn (375-2) device

The conductance of the device is so large that the measured capacitance is constricted between the two red lines for Mn (375-2). The plotting of  $1/C^2$  versus  $V$  at various temperatures is shown in Figure 5.72.

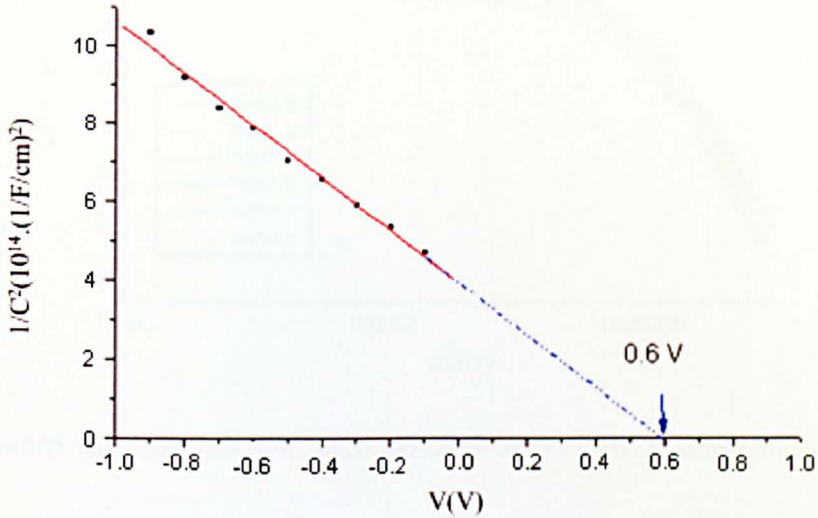


Figure 5.72 Plot of the  $1/C^2$  versus reverse bias voltage for GaMnAs film Mn (375-2) device

The doping concentration is calculated at 300 K for Mn (375-2) device as shown in Figure 5.72. It has been determined as  $5.5 \times 10^{13} \text{ cm}^{-3}$  and it remains constant until 340 K after which it approaches  $5.8 \times 10^{12} \text{ cm}^{-3}$  in the range 300 K to 200 K. These values are smaller than  $1 \times 10^{17} \text{ cm}^{-3}$  (the doping concentration of GaAs:Si).

## 5.9.2 C-F-T behaviour of Mn (375-2)

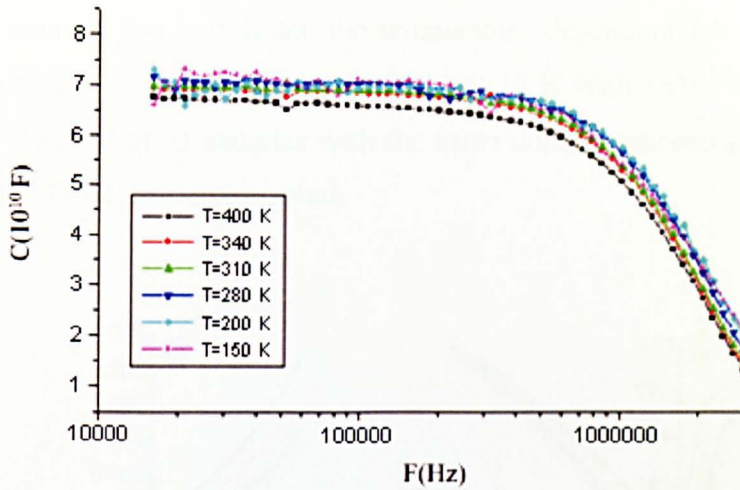


Figure 5.73 The capacitance versus the frequency voltage for GaMnAs sample Mn (375-2)

Figure 5.73 shows the capacitance spectra of the device at zero voltage bias with the temperatures range between 400 K and 150 K. The activation energy with a value of  $0.065 \pm 0.0007$  eV is estimated from Figure 5.74.

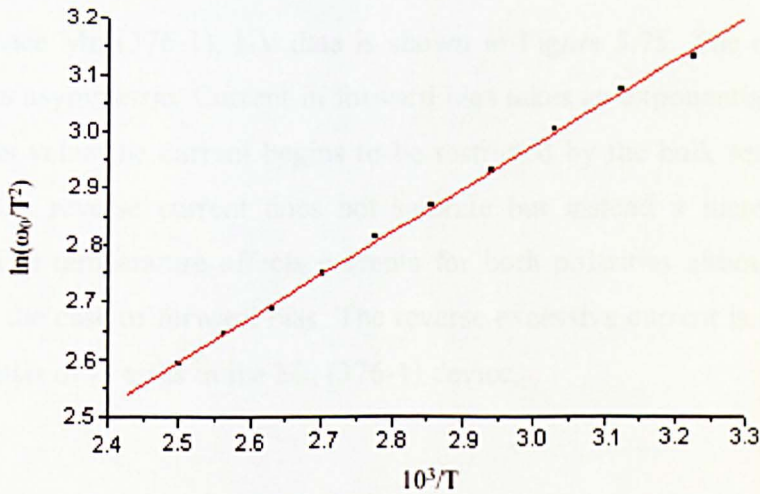


Figure 5.74 The Arrhenius plot for Mn (375-2)

### 5.10 (Mn376-1) Device

In this section, we investigate the temperature dependent I-V measurement of the Mn (376) device in the temperature range 400-15 K with  $1 \times 10^{19} \text{ cm}^{-3}$  Mn doping concentration. Two different samples with the same doping concentration labelled Mn (376-1) and Mn (376-2) are investigated.

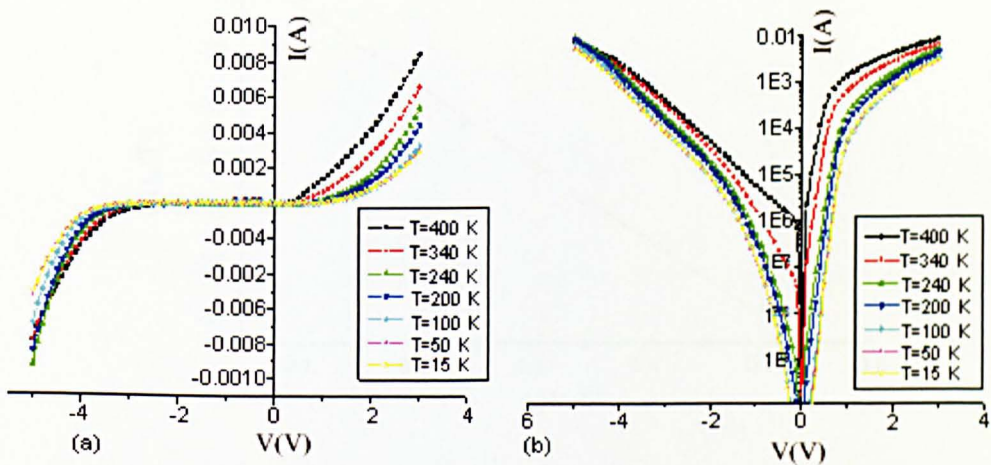


Figure 5.75 Current-voltage curve for GaMnAs (Mn376-1) device

For device Mn (376-1), I-V data is shown in Figure 5.75. The current-voltage characteristic is asymmetric. Current in forward bias takes an exponential form up to 1 volt; above this value the current begins to be restricted by the bulk series resistance. Furthermore, the reverse current does not saturate but instead it increases with the applied bias. The temperature affects currents for both polarities although it is much pronounced in the case of forward bias. The reverse excessive current is in the order of  $0.265 \mu\text{A}$  at a bias of -3 volts in the Mn (376-1) device.

The position of Fermi level ( $E_F$ ) in the Mn (376) devices with doping concentration of  $10^{19} \text{ cm}^{-3}$  is presented in section (5.3.3) using numerical iteration. Figure 5.11 shows that Mn (376) devices are not degenerate. Figure 5.11 shows that the position of the  $E_F$  lies between 0.045 eV and 0.027 eV above the valence band respectively in the temperature range between 50 K and 400 K.

**a) Analysis of I-V using pn junction model**

The activation energy from the plot  $\ln(I_s/T^3)$  versus  $10^3/nT$  for (Mn376-1) device at higher temperature range is shown in Figure 5.76. The activation energy in the forward bias is equal to  $1.25 \pm 0.03$  eV.

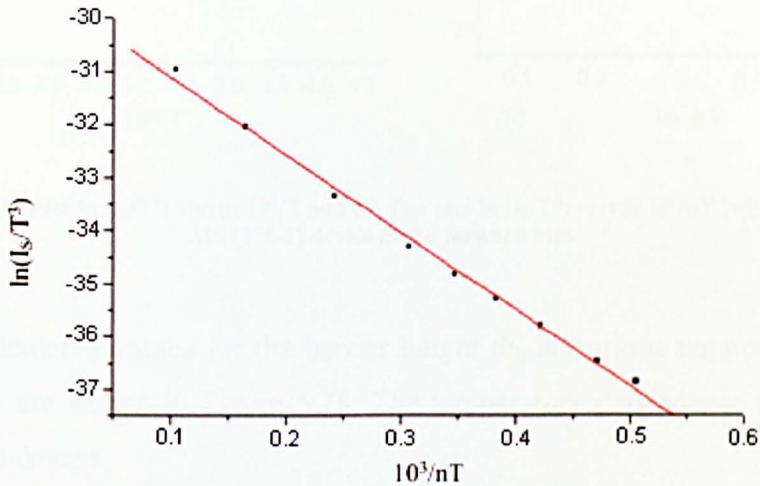


Figure 5.76 The activation in the forward bias gives  $1.25 \pm 0.03$  eV (with  $R=0.99764$ )

**b) Analysis of I-V using Schottky model**

The result is investigated further by plotting  $\ln(I_s/T^2)$  versus  $10^3/T$  for the forward bias. Under this condition, the p n junction is forward biased and the top Schottky contact is reversed biased. Since the n-type side is degenerate, the behaviour can be similar to a Schottky contact. The plot does not fit a straight line for (Mn376-1) device as shown in Figure 5.77 (a). The plot however, becomes linear if  $\ln(I_s/T^2)$  is plotted against  $10^3/nT$  as shown in Figure 5.77 (b). This again, is a familiar behaviour exhibited by all devices studied. The estimated activation energy in the case of forward bias is  $1.36 \pm 0.03$  eV which is slightly smaller than the energy gap of the GaAs.

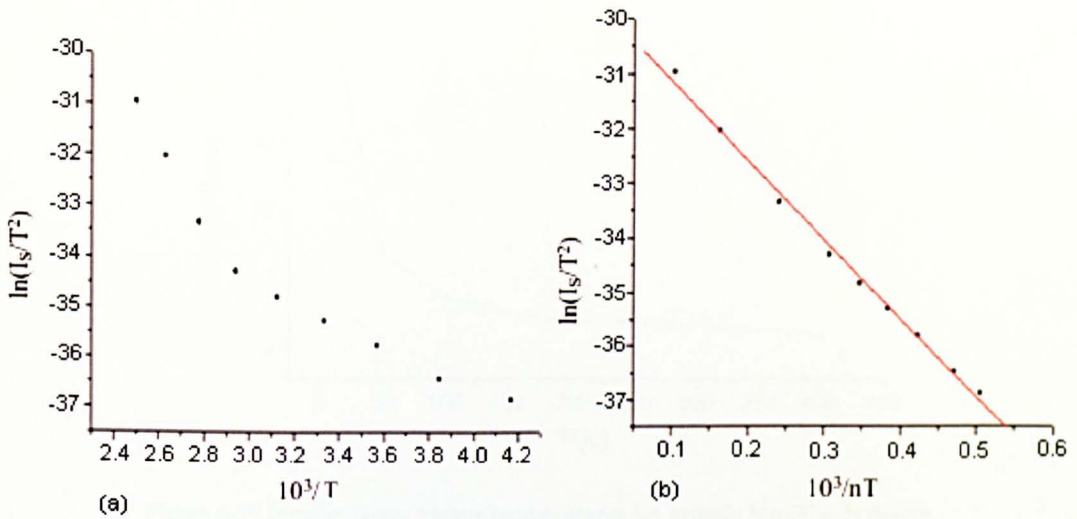


Figure 5.77 (a) The plot  $\ln(I_s/T^2)$  versus  $10^3/T$  and (b) The plot  $\ln(I_s/T^2)$  versus  $10^3/nT$  (with  $R=0.99883$ ) for Mn (376-1) device in the forward bias

The calculated values for the barrier height  $\Phi_b$  at various temperatures for Mn (376-1) device are shown in Figure 5.78. The temperature dependence is clearly seen for Mn (376-1) device.

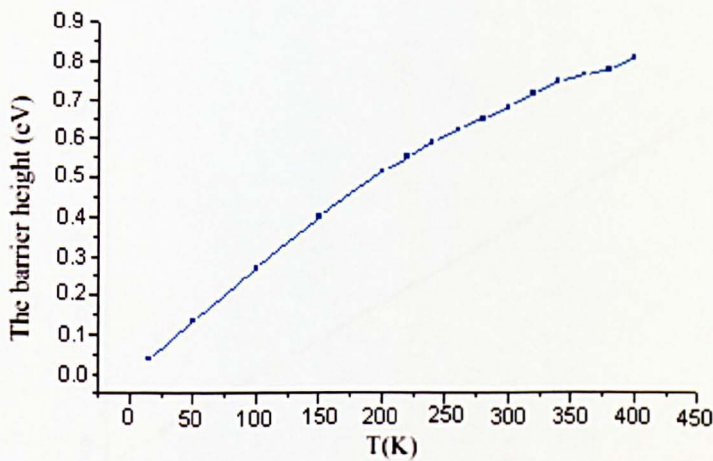


Figure 5.78 The temperature dependence of the barrier height in forward bias for GaMnAs (sample Mn (376-1)) in the temperature range 400-15 K

The ideality factor is determined from equation (2.15) for the full temperatures range. The ideality factor exhibits a tendency to increase with the decreasing temperature as shown in Figure 5.79. The ideality factor approaches  $2 \pm 0.005$  at 400 K.

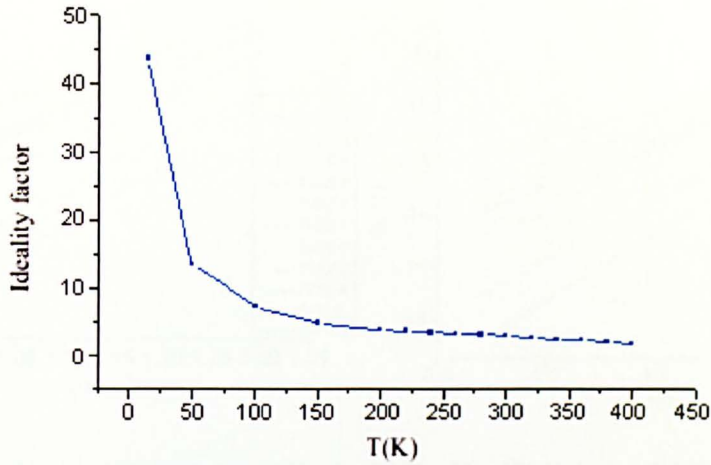


Figure 5.79 Ideality factor versus temperatures for sample Mn (376-1) device

The ideality factor is inversely proportional to temperature in forward bias as shown in Figure 5.80. This is similar to the behaviour of the ideality factors for other devices studied in this thesis Mn (374), Mn (375-1) and Mn (375-2). The temperature dependence of the ideality factor follows the  $T_0$  effect, which has also been observed in all devices studied. The value of  $T_0$  for Mn (376-1) device is equal to  $645.7 \pm 0.003$  K while the intercept gives a value of  $n_0$  equal to  $0.8 \pm 0.05$ .

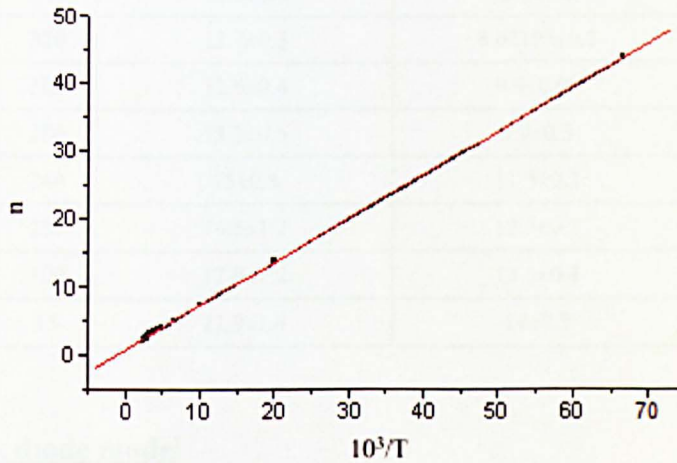


Figure 5.80 The plot of the ideality factor versus  $10^3/T$  in forward bias from temperature range 400-15 K in Mn (376-1) device

### c) GaAs:Mn-Insulator

The Schottky emission possibility is discussed by plotting  $\ln(I)$  versus  $V^{1/2}$ . This is shown in Figure 5.81 (a) and (b) for Mn (376-1) device.

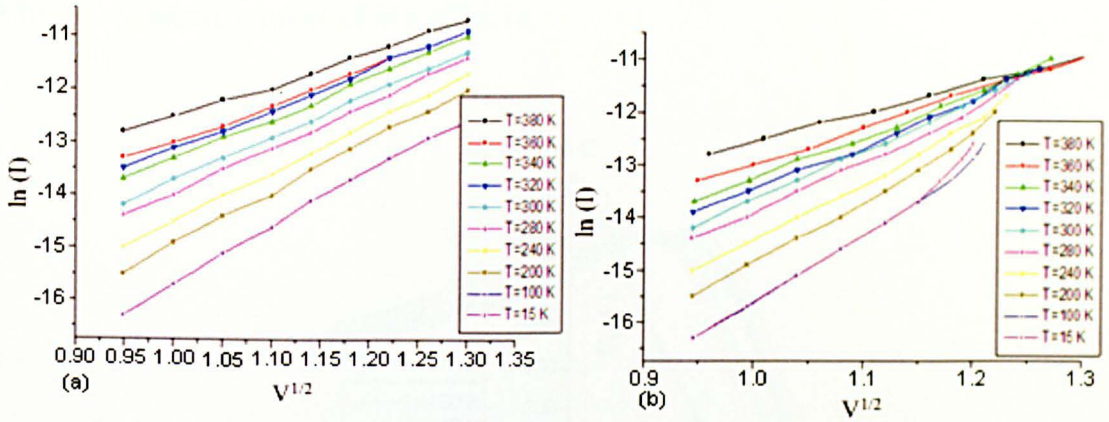


Figure 5.81 Reverse characteristic in the form of  $\ln(I) - V^{1/2}$  for Mn (376-1) device at different temperatures (a) before  $R_s$  corrections and (b) after  $R_s$  corrections

Table 5.10 shows the slope and the voltage range between  $\ln(I) - V^{1/2}$  plot for both polarities for Mn (376-1) device.

Table 5.10 The slope between  $\ln I$  versus  $V^{1/2}$  plot after  $R_s$  corrections in both polarities

| T   | $\beta_s$ ( $10^{-5}$ eV.m <sup>1/2</sup> .V <sup>-1/2</sup> )<br>(Forward bias)<br>voltage range =0.9-1.7 V | $\beta_s$ ( $10^{-5}$ eV.m <sup>1/2</sup> .V <sup>-1/2</sup> )<br>(reverse bias)<br>voltage range =0.7-1.3 V |
|-----|--|--|
| 380 | 11.4±0.2   | 5.26±0.08  |
| 360 | 11.86±0.2  | 6.7±0.1  |
| 340 | 12.3±0.3   | 8.2±0.2  |
| 320 | 12.7±0.3   | 8.62198±0.2  |
| 300 | 12.6±0.4   | 9.9±0.09   |
| 280 | 13.3±0.5   | 9.9±0.3  |
| 240 | 15±0.8   | 11.3±0.3   |
| 200 | 16.5±1.2   | 12.3±0.3   |
| 100 | 17.8±1.2   | 13.5±0.4   |
| 15  | 21.9±1.4   | 14±0.5   |

#### d) Back- to -back diode model

The I-V characteristics of the Mn (376) devices can be explained on the basis of a back-to-back model. Similar to Mn (375) where the top contact is Schottky and the bottom is a p n junction with GaAs:Mn as p-type and GaAs:Si as n-type. The energy band diagram of the structure is shown in Figure 5.24. As will be shown later, C-V measurement indicates that the depletion region is in the n-type side, which is GaAs:Si with doping concentration of  $2 \times 10^{17}$  cm<sup>-3</sup>.

## 5.10.1 C-V measurement of Mn (376-1)

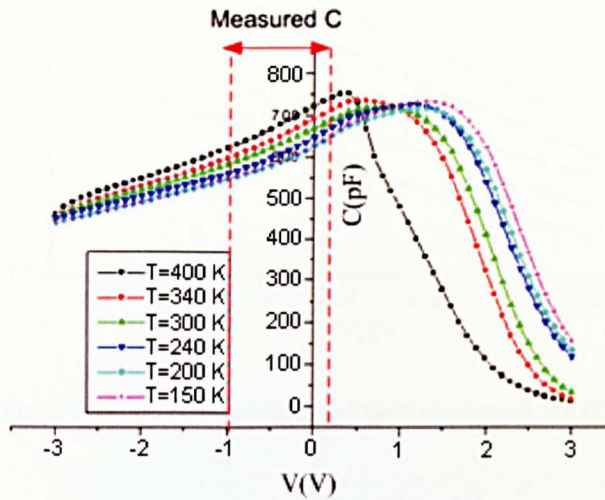


Figure 5.82 The capacitance versus bias voltage for GaMnAs sample Mn (376-1)

The temperature dependent C-V characteristic of Mn (376-1) device is shown in Figure 5.82. Over the measurement range of temperature and voltages, the capacitance exhibits a peak value. The peak shifts to higher voltages with decreasing temperature. The capacitance decreases in both bias directions. For sample Mn (376-1) however, the plot just begins to cross over at -3 V where the capacitance decreases with increasing temperature.

The measured capacitance is only valid at certain range (the red lines labelled). After certain range of the applied voltages, the current begins to be large for the capacitance to be measured due to the large conductance.

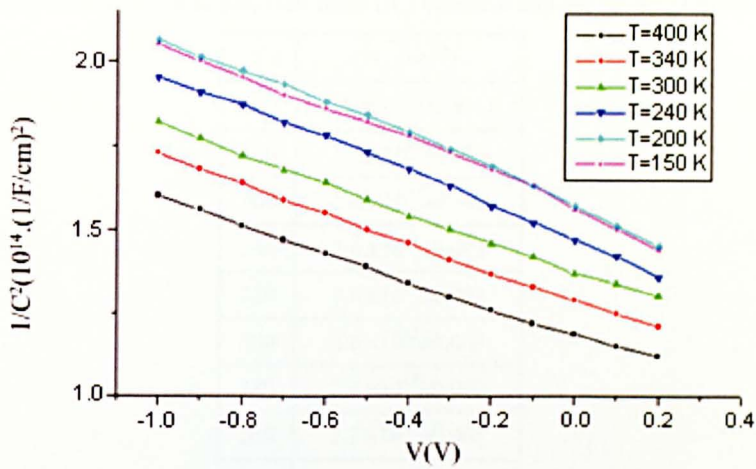


Figure 5.83 The  $1/C^2$  versus reverse voltage for GaMnAs sample Mn (376-1) device

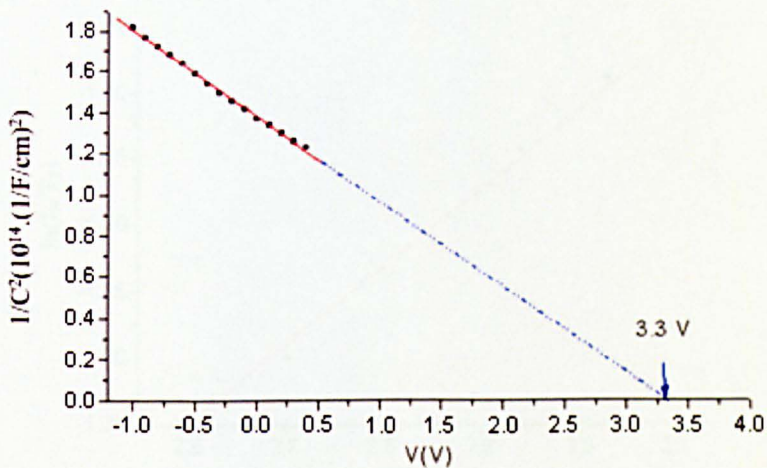
It should be observed that the plot of  $1/C^2$  versus reverse bias is a straight line as shown in Figure 5.83.

In the region limited by the two red lines in Figure 5.82 for Mn (376-1) device, the doping concentration has been measured. Table 5.11 shows the doping concentration  $N_A$  as obtained from  $1/C^2$  versus applied voltage ranges from -1 volt (in the reverse bias side) to the 0.3 volt (in the forward bias side). The doping concentration ranges from  $2.8 \times 10^{17} \pm 0.004 \text{ cm}^{-3}$  to the  $2.2 \times 10^{17} \pm 0.008 \text{ cm}^{-3}$  in the temperature ranges 400 K to 150 K respectively. This is equal to the doping concentration of the Si-GaAs. The simulation program (shown in Table 5.2) indicates that the majority of the depletion region extended to the n-type region and therefore, we get  $\sim 2 \times 10^{17} \text{ cm}^{-3}$  which is the right order of magnitude of the doping concentration of the Si-GaAs.

Table 5.11 The doping concentration as obtained from  $1/C^2$  versus  $V$  and the intercept of the x-axis of this plot

| T   | $N_A$ ( $\text{cm}^{-3}$ )      |
|-----|---------------------------------|
| 400 | $2. \times 10^{17} \pm 0.004$   |
| 380 | $2.72 \times 10^{17} \pm 0.004$ |
| 360 | $2.65 \times 10^{17} \pm 0.003$ |
| 340 | $2.6 \times 10^{17} \pm 0.003$  |
| 320 | $2.6 \times 10^{17} \pm 0.003$  |
| 300 | $2.6 \times 10^{17} \pm 0.003$  |
| 280 | $2.4 \times 10^{17} \pm 0.002$  |
| 260 | $2.3 \times 10^{17} \pm 0.001$  |
| 240 | $2.2 \times 10^{17} \pm 0.003$  |
| 220 | $2 \times 10^{17} \pm 0.001$    |
| 200 | $2.2 \times 10^{17} \pm 0.007$  |
| 150 | $2.2 \times 10^{17} \pm 0.008$  |

The  $1/C^2$  versus voltage plot at 360 K is shown in Figure 5.84. The intercept with x-axis gives the barrier height of a value 3.3 V which is unacceptably high. Similar result is obtained for Mn (376-2) device.

Figure 5.84 Plot  $1/C^2$  versus reverse bias voltage for GaMnAs film Mn (376-1) device at 360 K.

## 5.10.2 C-F-T for Mn (376-1)

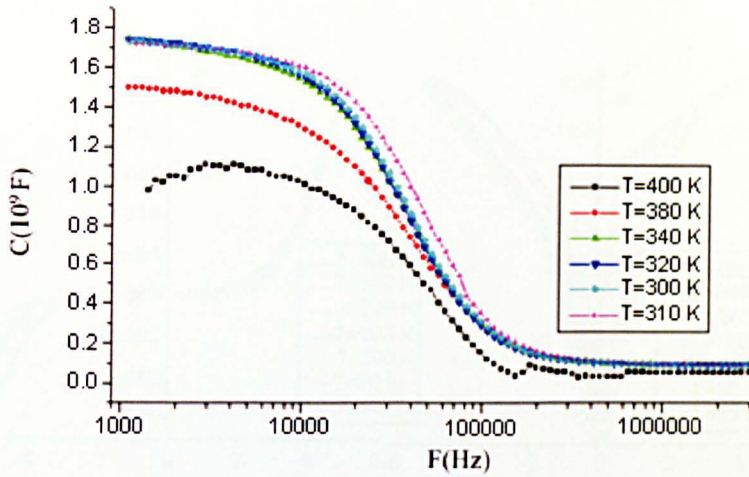


Figure 5.85 The capacitance versus the frequency voltage for GaMnAs sample Mn (376-1)

Figure 5.85 shows the capacitance spectra of the device at zero voltage bias with the temperatures range between 400 K and 300 K. The activation energy with a value of  $0.05 \pm 0.003$  eV is estimated from Figure 5.86.

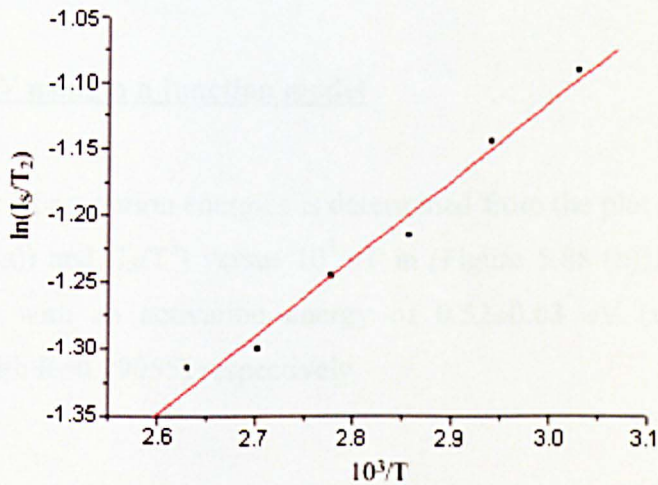


Figure 5.86 The Arrhenius plot for Mn (376-1)

### 5.11 (Mn376-2) Device

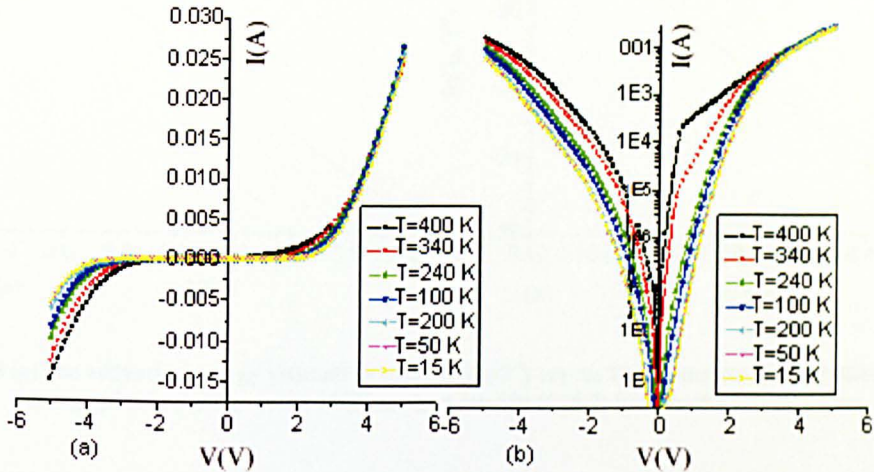


Figure 5.87 Current-voltage curve for GaMnAs (Mn376-2) device

The I-V characteristic of sample Mn (376-2) for GaMnAs diode at different selected temperatures, ranging from 400 to 15 K, is given in Figure 5.87 (a) and (b). The general shapes of the I-V curves in forward and reverse biases are similar. They do not show linear behaviour in either directions.

#### a) Analysis of I-V using p n junction model

The value of activation energies is determined from the plot  $(I_S/T^3)$  versus  $10^3/T$  in (Figure 5.88 (a)) and  $(I_S/T^3)$  versus  $10^3/nT$  in (Figure 5.88 (b)). Both plots show a linear behaviour with an activation energy of  $0.52 \pm 0.03$  eV (with  $R=0.988$ ) and  $1.73 \pm 0.03$  eV (with  $R=0.99055$ ) respectively.

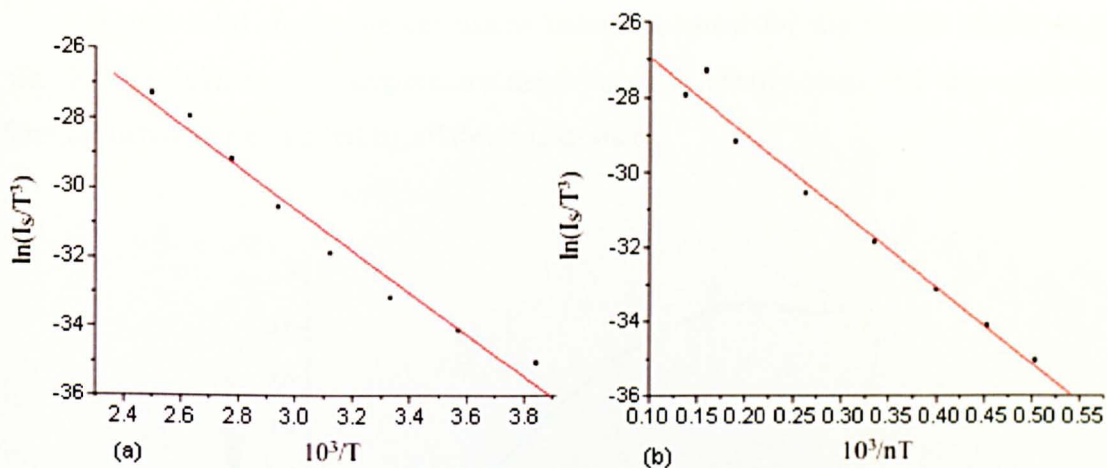


Figure 5.88 (a) The activation energy estimation using  $\ln(I_s/T^3)$  versus  $10^3/T$  and (b) The modified activation energy plot  $\ln(I_s/T^3)$  versus  $10^3/nT$  method for Mn (376-2) both in the forward bias

### b) Analysis of I-V using Schottky model

The activation energy in forward bias can be obtained from the plot  $\ln(I_s/T^2)$  versus  $10^3/T$  which fits to a straight line as shown in Figure 5.89 (a), with a value of  $0.55 \pm 0.03$  eV (with  $R=0.98875$ ). While the plot  $(I_s/T^2)$  versus  $10^3/nT$  shown in Figure 5.89 (b), also shows a straight line. The activation energy estimated from this plot is equal to  $1.7 \pm 0.1$  eV (with  $R=0.99059$ ).

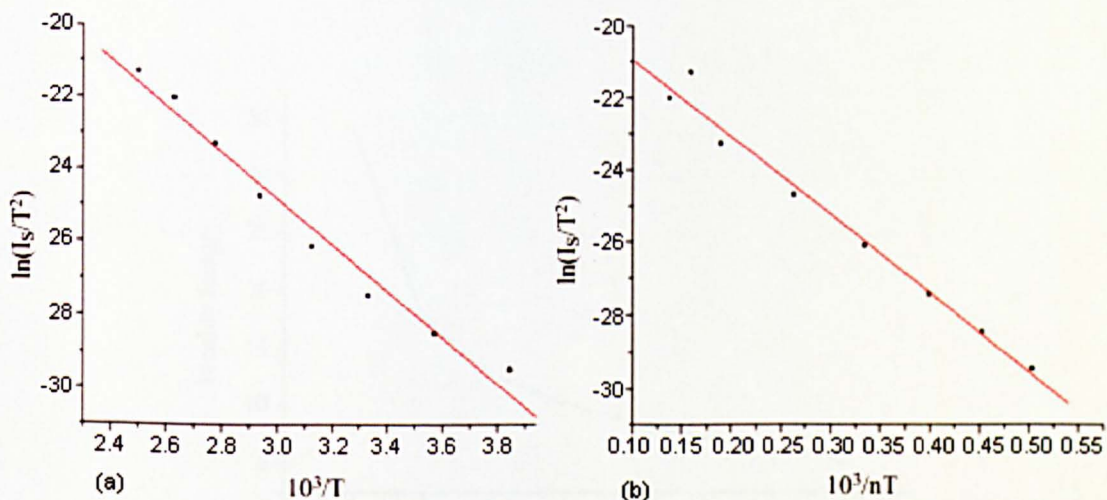


Figure 5.89 (a) The activation energy estimation using  $\ln(I_s/T^2)$  versus  $10^3/T$  and (b) The modified activation energy plot method for Mn (376-2) in forward bias

Figure 5.90 shows the calculated values obtained for the barrier height  $\Phi_b$  for Mn (376-2) device. The temperature dependence is clearly seen and this again is a familiar behaviour exhibited by all devices studied.

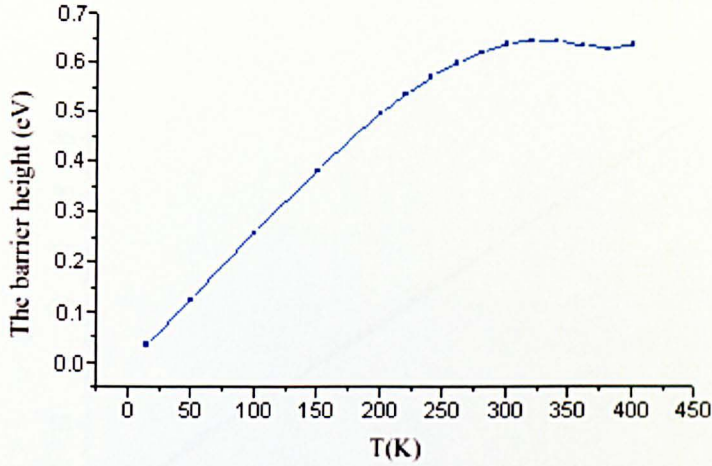


Figure 5.90 The temperature dependence of the barrier height in forward bias for GaMnAs (sample Mn (376-2) in the temperature range 400-15 K

The ideality factor ( $n$ ) calculated at various temperatures for forward bias is shown in Figure 5.91. The ideality factor  $n$  decreases with temperature. This device again has the same behaviour as the devices Mn (374) and Mn (375). The value of the ideality factor for Mn (376-2) approaches  $5 \pm 0.03$  at 400 K.

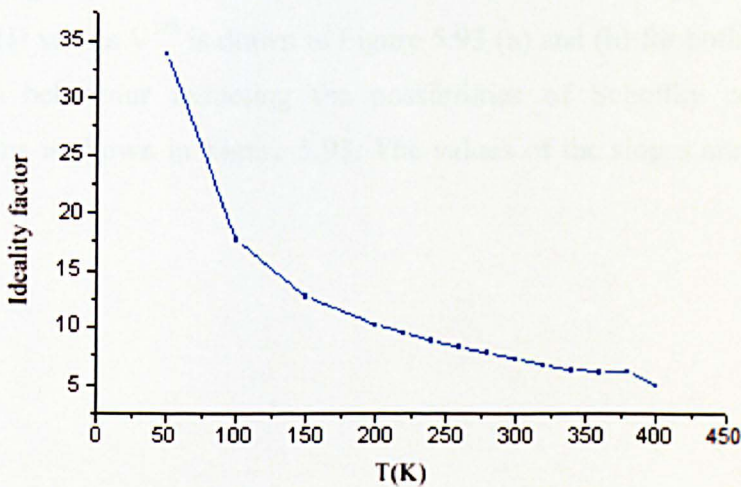


Figure 5.91 Ideality factor versus temperatures for Mn (376-2) device

Considering the  $T_0$  effect on the ideality factor, the ideality factor varies linearly with the inverse temperature for forward bias only as shown in Figure 5.92 from 400 K up to 15 K for Mn (376-2) device. The estimated  $T_0$  value is  $1661 \pm 0.007$  and the value of the intercept ( $n_0$ ) is equal to  $2 \pm 0.1$ . Furthermore,  $T_0$  and  $n_0$  values in reverse bias have similar values as Mn (375-2) device.

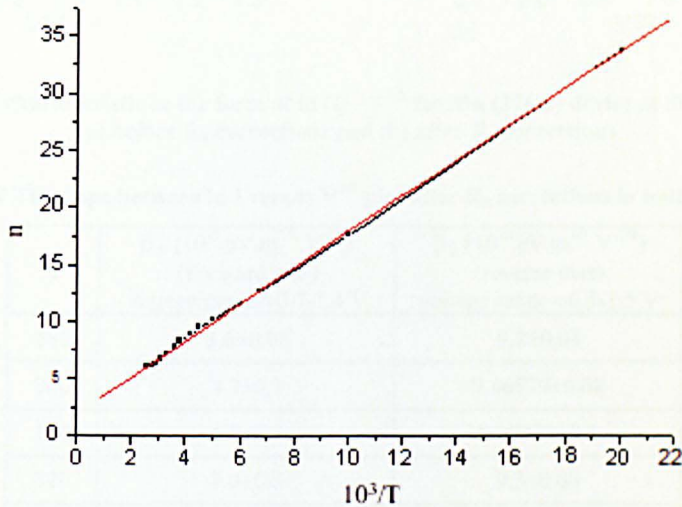


Figure 5.92 The plot of the ideality factor versus  $10^3/T$  in forward bias from temperature range 400-15 K for Mn (376-2) device

#### **d) GaAs: Mn-Insulator**

Processing the I-V-T data further to determine the possible conduction mechanism  $\ln(I)$  versus  $V^{1/2}$  is drawn in Figure 5.93 (a) and (b) for both polarities. This exhibits linear behaviour indicating the possibilities of Schottky conduction type mechanism. This is shown in Figure 5.93. The values of the slopes are given in Table 5.12.

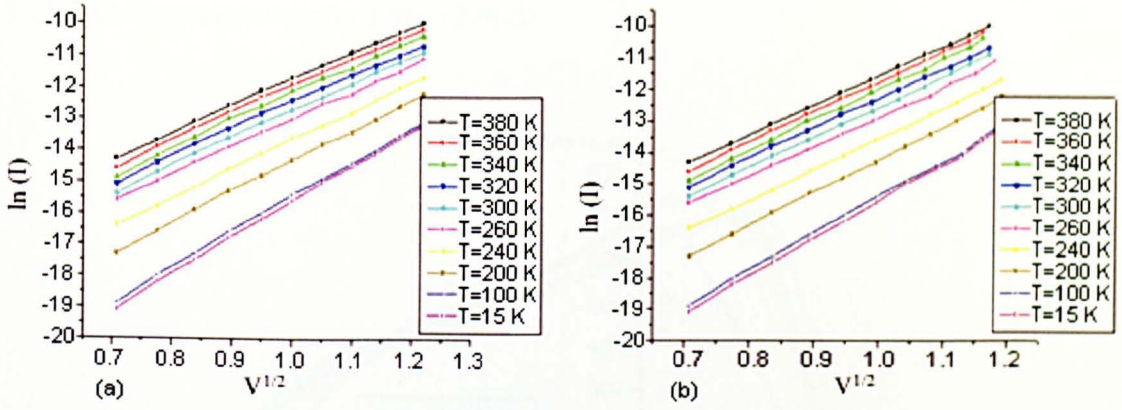


Figure 5.93 Reverse characteristic in the form of  $\ln(I) - V^{1/2}$  for Mn (376-2) device at different temperatures (a) before  $R_s$  corrections and (b) after  $R_s$  corrections

Table 5.12 The slope between  $\ln I$  versus  $V^{1/2}$  plot after  $R_s$  corrections in both polarities

| T   | $\beta_s$ ( $10^{-5}$ eV.m <sup>1/2</sup> .V <sup>-1/2</sup> )<br>(Forward bias)<br>voltage range =0.7-1.4 V | $\beta_s$ ( $10^{-5}$ eV.m <sup>1/2</sup> .V <sup>-1/2</sup> )<br>(reverse bias)<br>voltage range =0.5-1.5 V |
|-----|--|--|
| 380 | 3.6±0.05   | 9.2±0.04   |
| 360 | 4.7±0.1  | 9.46879±0.08   |
| 340 | 6.2±0.1  | 9.68922±0.1  |
| 320 | 7.9±0.3  | 9.3±0.08   |
| 300 | 9.5±0.3  | 9.6±0.06   |
| 280 | 11±0.2   | 9.3±0.09   |
| 240 | 12.8±0.1   | 9.7±0.04   |
| 200 | 14.3±0.1   | 10.4±0.07  |
| 100 | 16±0.09  | 11.7±0.1   |
| 15  | 17±0.1   | 12±0.1   |

#### d) Back to back diode model

Mn (376-2) with  $1 \times 10^{19}$  cm<sup>-3</sup> Mn doping concentration is also explained in terms of the back to back model which has already been discussed in details in section (5.7) (d).

## 5.11.1 C-V measurement of Mn (376-2)

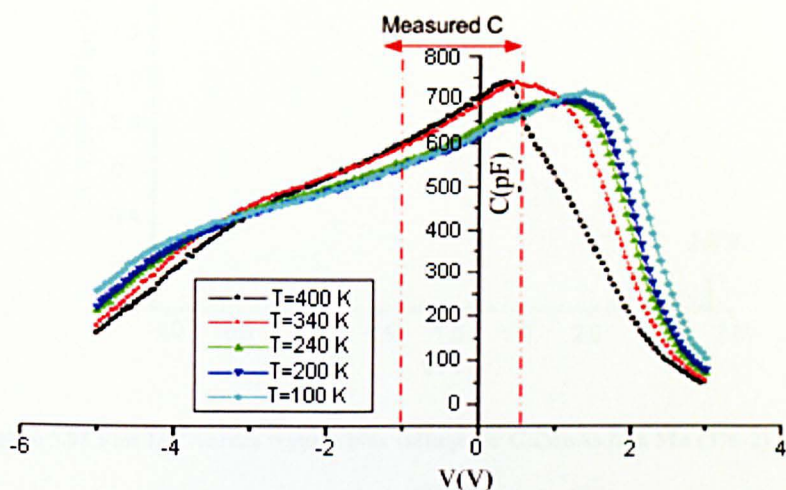


Figure 5.94 The capacitance versus bias voltage for GaMnAs sample Mn (376-2)

The behaviour is similar to that one observed in the Mn (376-1). The temperature dependence C-V characteristic of the Mn (376-2) is shown in Figure 5.94. For sample Mn (376-2), there appears to be a cross point at around -3 V reverse bias where the capacitance decreases with increasing temperature.

Table 5.13 The doping concentration as obtained from  $1/C^2$  versus V

| T   | $N_A$                           |
|-----|---------------------------------|
| 400 | $2.44 \times 10^{17} \pm 0.006$ |
| 380 | $2.43 \times 10^{17} \pm 0.006$ |
| 360 | $2.39 \times 10^{17} \pm 0.005$ |
| 340 | $2.41 \times 10^{17} \pm 0.004$ |
| 320 | $2.45 \times 10^{17} \pm 0.005$ |
| 300 | $2.4 \times 10^{17} \pm 0.005$  |
| 280 | $2.46 \times 10^{17} \pm 0.004$ |
| 260 | $2.4 \times 10^{17} \pm 0.005$  |
| 240 | $2.33 \times 10^{17} \pm 0.006$ |
| 220 | $2.4 \times 10^{17} \pm 0.006$  |
| 200 | $2.45 \times 10^{17} \pm 0.006$ |
| 150 | $2.5 \times 10^{17} \pm 0.005$  |
| 100 | $2.46 \times 10^{17} \pm 0.007$ |
| 50  | $2.23 \times 10^{17} \pm 0.01$  |

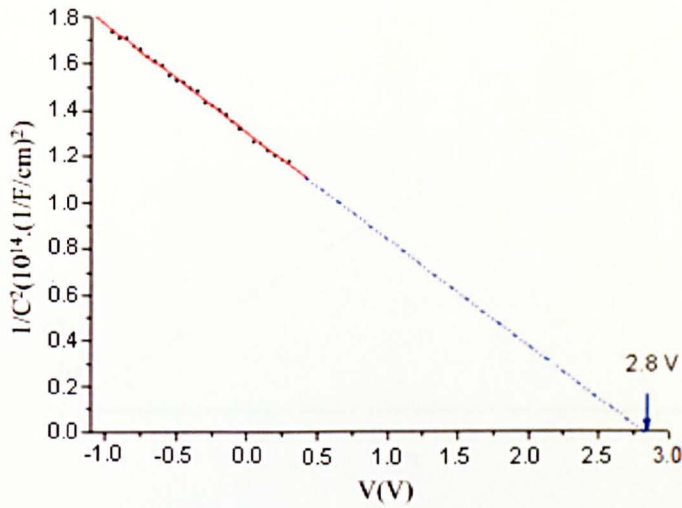


Figure 5.95 Plot  $1/C^2$  versus reverse bias voltage for GaMnAs film Mn (376-2) device

The room temperature measurement is shown in Figure 5.95. The measured value is  $2.4 \times 10^{17} \pm 0.006 \text{ cm}^{-3}$  and  $2.23 \times 10^{17} \pm 0.01 \text{ cm}^{-3}$  in the range 400 K to 50 K. This again gives the doping concentration of the Si-GaAs.

### 5.11.2 C-F-T behaviour of Mn (376-2)

Figure 5.96 shows the capacitance spectra of the device at zero voltage bias over the temperatures range 400 K and 150 K. Activation energy of  $0.06 \pm 0.004 \text{ eV}$  is estimated from Figure 5.97.

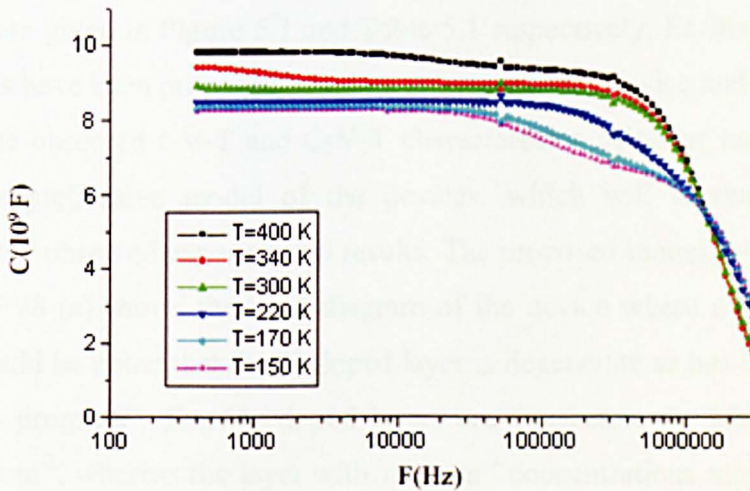


Figure 5.96 The capacitance versus the frequency voltage for GaMnAs sample Mn (376-2)

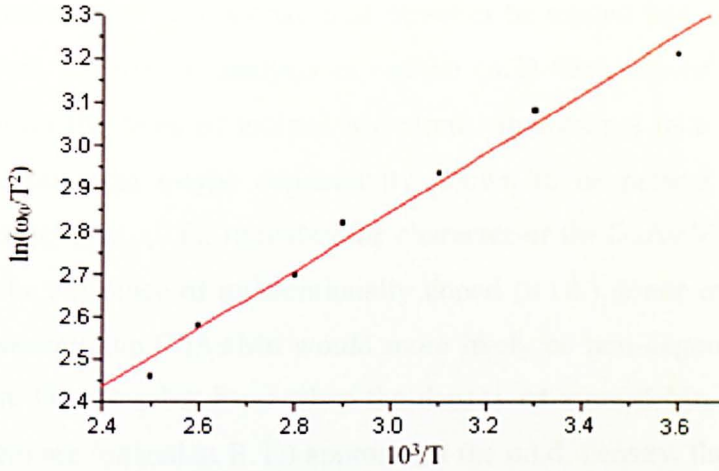


Figure 5.97 The Arrhenius plot for Mn (376-2)

## 5.12 Discussion of Results

Metal / GaAs: Mn /GaAs:Si structures have been studied by the I-V-T and C-V-T techniques. In all, five devices were used. All devices have the Si doped GaAs layer with the same concentrations ( $\sim 2 \times 10^{17} \text{ cm}^{-3}$ ) and a thickness of 700 nm. The Mn doped GaAs layer had three different concentrations varying from  $10^{21}$  down to  $10^{19} \text{ cm}^{-3}$ .

### 5.12.1 I-V-T measurements on GaAs: Mn /GaAs:Si Devices

The device structure, different doping concentrations and the growth temperatures are given in Figure 5.1 and Table 5.1 respectively. Earlier in this chapter, various models have been proposed based on structure of the device and the materials to account for the observed I-V-T and C-V-T characteristics. Attempt has been made to propose a comprehensive model of the devices, which will account for, at least qualitatively, the observed experimental results. The proposed model is shown in Figure 5.98. Figure 5.98 (a) shows the band diagram of the device where no external bias is applied. It should be noted that the Si-doped layer is degenerate as has been determined using “Matlab program”. The Mn doped layers are degenerate for Mn concentrations  $10^{21}$  and  $10^{20} \text{ cm}^{-3}$ , whereas the layer with  $10^{19} \text{ cm}^{-3}$  concentrations may or not may be degenerate.

The degeneracy of the material must however be treated with caution and some degree of reserve. Theoretical analysis in section (5.3) “determined” the material as degenerate only on the basis of ionized Mn-atoms. It does not take into account the presence of unintentional n-type conductivity known to be present in GaAs layers grown at low temperature (LT). In reality the character of the GaAs:Mn layer would be determined by the existence of unintentionally doped (u.i.d.) donor concentration. For higher u.i.d. concentration GaAs:Mn would more likely be non-degenerate p-type due to compensation. On the other hand when the density of ionized Mn-atoms (and only about 1% of them are ionized at R.T.) approaches the u.i.d. density, the material would be an insulator. However even if 1% Mn-atoms are ionized it would give an acceptor concentration of  $2.4 \times 10^{19}$ ,  $7.410^{18}$  and  $2 \times 10^{18} \text{ cm}^{-3}$  respectively. And in such cases the material may well behave like a degenerate material.

The proposed model has been drawn for the degenerate case. The structure is completed by a top Schottky contact.

**Table 5.14** The measured experimental values of the barrier height using  $\ln(I_s/T^3)-10^3/nT$  plot for pn junction analysis and  $\ln(I_s/T^2)-10^3/nT$  plot for Schottky analysis (except the last device analysed by additional method which is  $\ln(I_s/T^3)-10^3/T$  for p n junction and  $\ln(I_s/T^2)-10^3/T$  for Schottky)

| Device number | p n junction model            |                               | Schottky model                |                               |
|---------------|-------------------------------|-------------------------------|-------------------------------|-------------------------------|
|               | The activation (Forward bias) | The activation (Reverse bias) | The activation (Forward bias) | The activation (Reverse bias) |
| 374           | 1.1±0.07<br>(R=0.98756)       | Not fit                       | 1.4±0.05<br>(R=0.99631)       | 0.52±0.05<br>(R=0.996624)     |
| 375-1         | 0.98±0.1<br>(R=0.96627)       | Not fit                       | 1.4±0.2<br>(R=0.94188)        | 0.85±0.05<br>(R=0.99056)      |
| 375-2         | 0.85±0.05<br>(R=0.99951)      | 0.8±0.03<br>(R=0.99548)       | 0.93±0.01<br>(R=0.99943)      | 1±0.02<br>(R=0.99888)         |
| 376-1         | 1.25±0.03<br>(R=0.99764)      | Not fit                       | 1.36±0.03<br>(R=0.99883)      | Not fit                       |
| 376-2         | 1.73±0.1<br>(R=0.99055)       | Not fit                       | 1.7±0.1<br>(R=0.99059)        | Not fit                       |
| 376-2         | 0.52±0.03<br>(R=0.988)        | Not fit                       | 0.55±0.03<br>(R=0.98875)      | Not fit                       |

Table 5.14 gives the summary of the calculated barrier heights for forward and reverse directions for all devices studied. It can be seen that the experimentally determined values agree in general with the proposed model.

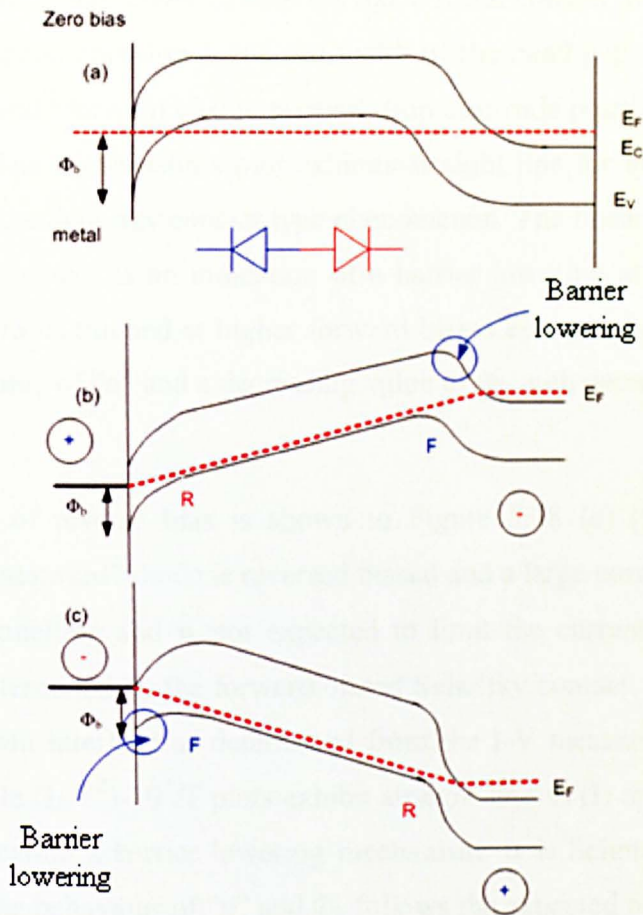


Figure 5.98 The proposed model for GaMnAs devices

The proposed energy band diagram the GaAs:Si /GaAs:Mn junction, and can be looked upon as a “backward” diode. According to calculations, the position of the Fermi level is only 30 meV below the valence band ( $E_V$ ) edge for  $10^{21} \text{ cm}^{-3}$  Mn doping at room temperature. It becomes non-degenerate just below 190 K. Whereas GaAs:Mn layer with  $10^{20} \text{ cm}^{-3}$  concentration is just non-degenerate at room temperature with the Fermi level moving marginally below the top of the valence band at higher temperature. Mn doped GaAs layer with  $10^{19} \text{ cm}^{-3}$  concentration of Mn is non-degenerate at all temperatures with the Fermi level very close to the top of the valence band ( $\sim 30 \text{ meV}$  at 300 K). The small potential difference ( $\leq 30 \text{ meV}$ ) would easily be overcome by the forward bias to drive the junction into “backward” diode mode.

The forward current for the case of the “backward” diode as shown in Figure 5.98 (b), would be the thermionic injection of carriers from the degenerate n-type into the conduction band of the p-type Mn doped layer, not unlike the thermionic emission

in a Schottky diode where GaAs:Si behaves like a metal contact. It should be noted that the barrier to electron emission is the full width of the band gap which is 1.42 eV for GaAs. The observed “forward characteristics” (top electrode positive) appear to support this hypothesis. The Richardson’s plot exhibits straight line for  $\ln(I_S/T^2) - 10^3/T$  and is an indication for the Schottky contact type phenomenon. The linear dependence of  $\ln(I) - V^{1/2}$  for higher voltages is an indication of a barrier lowering at the backward diode barrier. This barrier is thinned at higher forward biases encouraging TFE which results in an increased value of “n” and a decreasing value of  $\Phi_b$  with decreasing temperature.

The case of reverse bias is shown in Figure 5.98 (c) (top electrode biased negative). The “backward” diode is reversed biased and a large current can flow through the device by tunnelling and is not expected to limit the current. The current in the device will be determined by the forward biased Schottky contact. The barrier height at the metal/GaAs:Mn interface as determined from the I-V measurements is 0.5 eV. In this case too the  $\ln(I_S/T^2) - 10^3/T$  plots exhibit straight line  $\ln(I)$  and  $V^{1/2}$  also plot as a straight line indicating a barrier lowering mechanism. It is Schottky barrier, which is being lowered. The behaviour of “n” and  $\Phi_b$  follows the expected pattern.

The model suggesting the existence of a Schottky contacts has been proposed on the basis of experimental evidence, which is:

1. Si doped GaAs is degenerate and the Fermi level is located in the conduction band giving it metallic character.
2. The Richardson plots,  $\ln(I_S/T^2) - 10^3/T$  are straight lines which is indicative of a Schottky contacts.
3. The reverse and forward characteristics are straight lines for  $\ln(I) - V^{1/2}$  plots-indicative of a barrier lowering phenomenon.
4. The reverse current shows the existence of TFE which results in lower values of “n” with increasing temperature. This phenomenon is more likely to occur in Schottky contacts.

However, the value of the Schottky barrier height of 1.42 eV appears too high for the Schottky contacts. A more plausible explanation would be on the basis of a p n junction-which it is! This junction behaves like a backward diode and when the bottom electrode is biased negative, the “backward diode” is forward biased. The saturation current  $I_s$  in this case should be given by equation (2.3).

The Richardson plots  $\ln(I_s/T^3)-10^3/T$  should yield the bandgap for GaAs which is 1.42 eV. This would be an elegant conclusion had it not been for the experimental evidence mentioned above. It is possible that through some mathematical “reasoning” based on the complicated physical process of conduction  $(I_s/T^2)-10^3/T$  plots are linear and the bottom contact is indeed behaving like a p n<sup>+</sup> junction.

This general pattern is observed for all devices measured with some variation in the values of barrier height, which is not surprising considering the fact that all devices were made separately and at different temperatures so there must be a considerable variation not only in doping concentration but also on the character of the deposited films. The surfaces too are expected to be different. Only one device Mn (376-2) gives a high value of the barrier height (1.7 eV) which is unacceptably high.

### 5.12.2 Capacitance measurements on GaAs: Mn /GaAs: Si Devices

The analysis of the C-V-T measurements is more complicated. The behaviour of 374 device ( $10^{21} \text{ cm}^{-3}$ ) and the two 376 devices ( $10^{19} \text{ cm}^{-3}$ ) appear to be qualitatively similar in as much as the capacitance goes through a peak value with changing bias. This is characteristic of two back-to-back devices. Since the measured capacitance is the resultant of two capacitances in series, it is the lower capacitance which will ultimately dominate.

Measurements on the two 375 devices ( $10^{20} \text{ cm}^{-3}$ ) on the other hand, show a steady increase in capacitance from “far” reverse bias to increasing forward bias. The response is not that of two back-to-back junctions. It is the response of a single junction. This is a feature which both devices exhibit and which does not match with the response of the other three devices. This behaviour cannot be examined by the proposed model.

However, the model does satisfactorily account for the qualitative features of the I-V-T measurements for all devices and C-V-T measurements for three devices.

## CHAPTER 6 Measurement Results of GaMnN

### 6.1 Introduction

This chapter presents the results of a study of Schottky diodes made on Mn doped GaN. The Mn doped GaN was grown at Nottingham University by radio frequency plasma assisted MBE method.

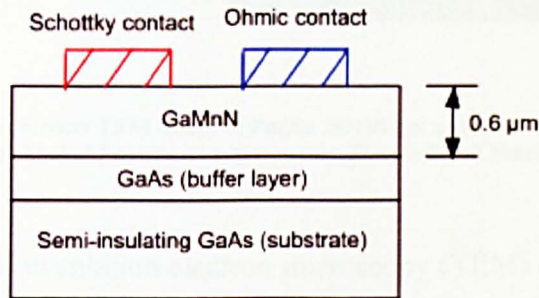
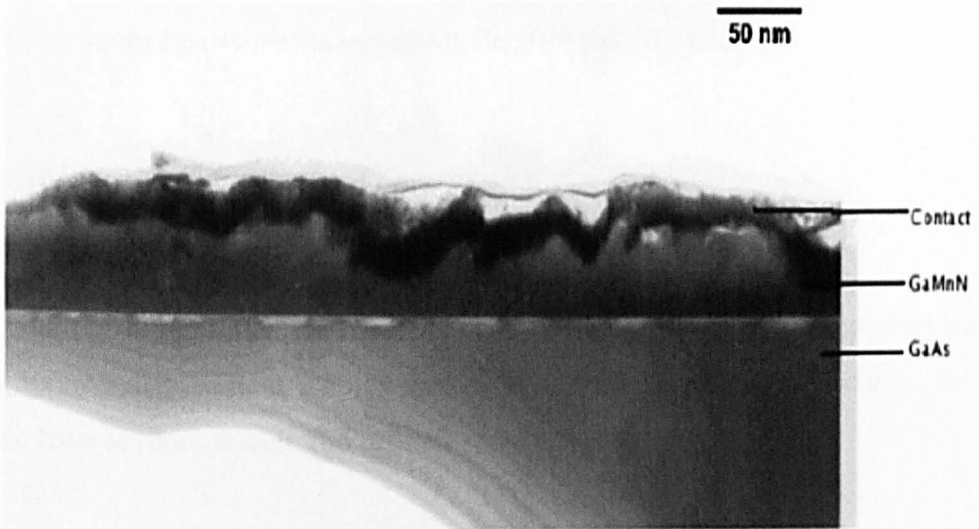


Figure 6.1 Schematic drawing of the device geometry of the GaMnN film

Mn is an acceptor and so the resulting material will have p-type conductivity [65]. Figure 6.1 shows a schematic diagram of the device geometry. The 0.6 μm thick Mn doped GaN was grown epitaxially on top of a nominally undoped GaAs buffer layer. The substrate was semi-insulating GaAs. Since the substrate is semi-insulating both the Ohmic and Schottky contacts were on the top of the semiconductor and the patterns were defined using standard photolithographical techniques. The samples used in the current study were fabricated by V. Sundaramoorthy [130] and full details of the device fabrication can be found in his thesis [130]. The sample consists of a number of circular Schottky contacts which were made from 100 nm thick Au layer. The outer Ohmic contact was made from Palladium/Gold layer (30nm/100nm). Devices of different areas have been tested. These had a diameter of 800 μm, 400 μm and 200 μm. The doping concentration for this sample was between  $7-8 \times 10^{17} \text{ cm}^{-3}$  (p-type

material). For a Schottky diode made on a p-type material, the diode is forward biased when a positive voltage is applied to the Ohmic contact relative to the Schottky contact.



**Figure 6.2** Bright field cross section TEM image of Pd/Au 25/160 nm annealed at 600 °C† Courtesy of Dr. Michael Fay, School of Physics and Astronomy, University of Nottingham [130]

Cross sectional transmission electron microscopy (TEM) on related samples has been performed after this sample was measured. A typical micrograph is shown in Figure 6.2. The diagram shows the high quality GaAs buffer layer but the surface appears slightly pitted. On top of this is the very rough Mn doped GaN, although the nominal thickness of the GaN epilayer was 600nm the actual thickness varies considerably. Although TEM provides no evidence, the rough surface is likely to affect the I-V performance in several ways:

1. The variation of thickness of the contact could effectively give rise to tunnelling "areas" across the plane of the contact.
2. The Mn rich layer observed on top of the GaMnN layer would cause a change in barrier height. For example, it could be "Gaussian in nature".
3. The layer could be over compensated to give an n-type region which will change the nature of the contact to metal/n-type semiconductor.

Current-Voltage-Temperature (I-V-T) characteristics, Capacitance-Voltage-Temperature (C-V-T) characteristics and Capacitance-frequency-Temperature (C-F-T) characteristics are the three methods that have been used to characterize Schottky contacts on GaMnN. Diode parameters like the ideality factor  $n$ , saturation current  $I_S$  and the diode series resistance  $R_S$  have been determined.

## 6.2 Possible models to analyse the results

Different possibilities for the behaviour of the carrier type and conductivity of GaMnN are investigated before going further in analysing the results in detail. For this device we have several models and refinements.

### Model one

The GaMnN layer is P-type and the diode exhibits the standard diode characteristics. The structure will look like p-type GaN: Mn / Schottky contact as shown in Figure 6.3.

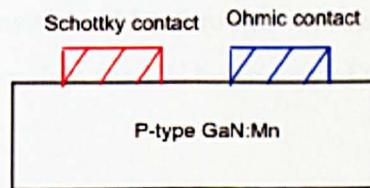


Figure 6.3 Schottky diode model for p-type GaMnN

Cubic GaN has a bandgap  $E_g$  of 3.2 eV [131] and an electron affinity  $\chi$  of 4.1 eV [132]. The Schottky contact was made from Au with work function of  $4.82 \pm 0.02$  eV [133]. In p-type material the Fermi level is located near the valence band, and the work function of p-type GaN will nearly be the sum of the electron affinity and the band gap which yields a value of  $\sim 7.3$  eV. Similar result was found by [134] for p-type GaN. In this case, the metal work function ( $\Phi_m$ ) is smaller than that of the GaN ( $\Phi_s$ ) and when the contact is made electrons from the metal will move into GaN. Consequently, a

rectifying contact will be formed. The possible energy band diagram is given in Figure 6.4. This however, is an ideal scenario. The behaviour of real contacts will be modified by the presence of inhomogeneities in the barrier height across the plane of the Schottky contact. Several workers have attempted to explain their “non-ideal” results on the basis of a Gaussian distribution of barrier heights not in GaN [19, 135] but also in other material like Pd/Zno [20] and n-InP [136].

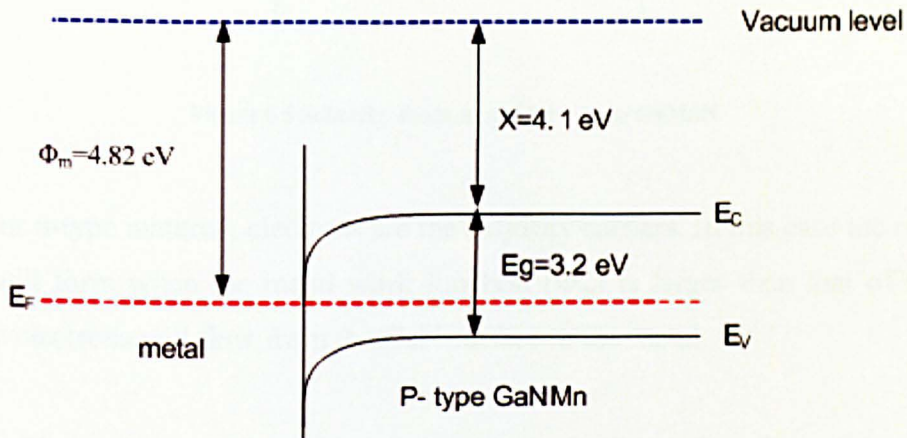


Figure 6.4 The band diagram for Schottky diode with p-type GaN: Mn

Another factor most likely to cause deviation from “ideal conduction” mechanism, thermionic emission over the Schottky barrier, is the thermionic field emission (TFE) and field emission (FE) through the barriers. These factors must be considered in any attempt to explain the I-V behaviour of these devices.

### Model Two

There is a great possibility of unintentional n-type doping of GaMnN due to the existence of nitrogen vacancies [137] which create an n-type conductivity. The possibility of compensation of p-type dopants by n-type vacancies cannot be ruled out. This appears even more likely since Mn-atoms tend to migrate to the surface leaving a lower p-type conductivity region just below the surface which might be easier to compensate.

If the sample is n-type, the diode characteristics will be reversed (with respect to the first model). In this case the standard Schottky analysis will apply to the reverse bias.

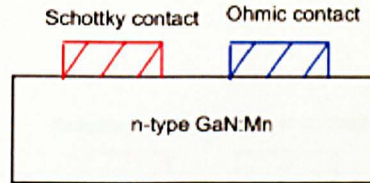


Figure 6.5 Schottky diode model for n-type GaMnN

For n-type material, electrons are the majority carriers. In this case the rectifying contact will form when the metal work function ( $\Phi_m$ ) is larger than that of the GaN ( $\Phi_s$ ). The electrons will flow from the GaN surface to the metal.

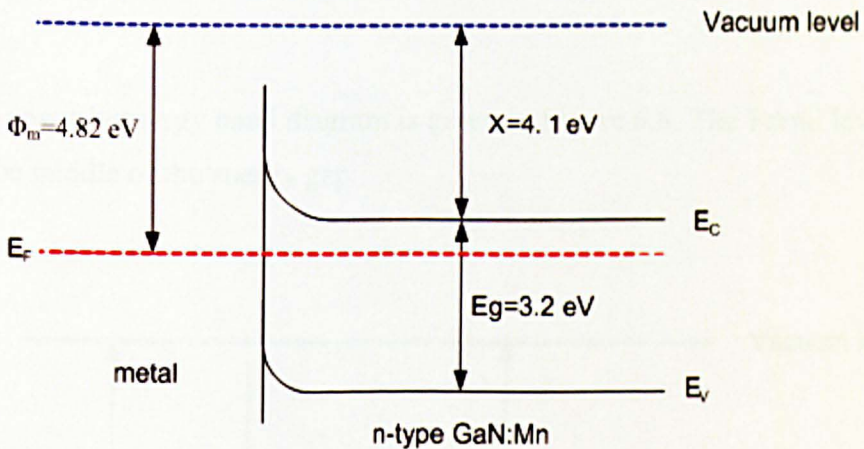


Figure 6.6 The band diagram for Schottky diode with n-type GaN: Mn

The suggested energy band diagram is given in Figure 6.6.

### Model Three

The material can become effectively insulating if the concentration of p-type dopants is approximately equal to the n-type vacancies or there is an insulating layer

between the contact and the semiconductor. In this case, the Poole-Frenkel mechanism limits the current flow through the diode. At low bias the current flow is dominated by the Schottky contact but as the bias increases, the current flow through the “insulating” GaMnN is via Poole-Frenkel mechanism. The electrical structure of the device will look more like an insulator with SI-GaN: Mn layer as shown in Figure 6.7.

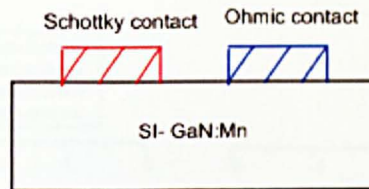


Figure 6.7 Insulator model for GaN: Mn

Since semi-insulating (SI) GaMnN is being considered, it can be safely assumed that the Fermi level lies in the middle of the band gap. The work function of the SI GaMnN will be  $(X+E_g/2=4.1+1.6=5.7$  eV). This is higher than the work function of the Schottky contact (gold) which is 4.82 eV.

The possible energy band diagram is given in Figure 6.8. The Fermi level ( $E_F$ ) is located in the middle of the energy gap.

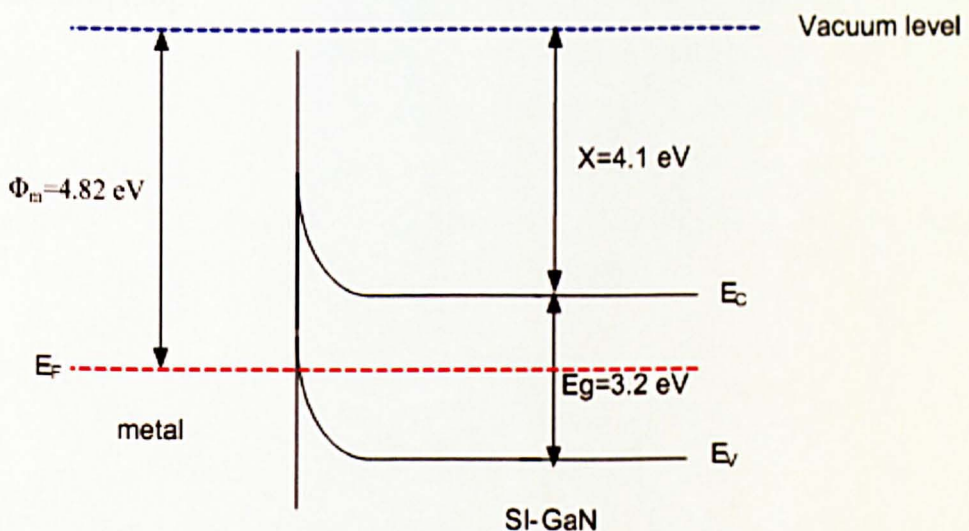


Figure 6.8 The band diagram for the insulator model, which shows the  $E_F$  in the middle

### 6.3 Comparison of the samples with different Mn concentrations

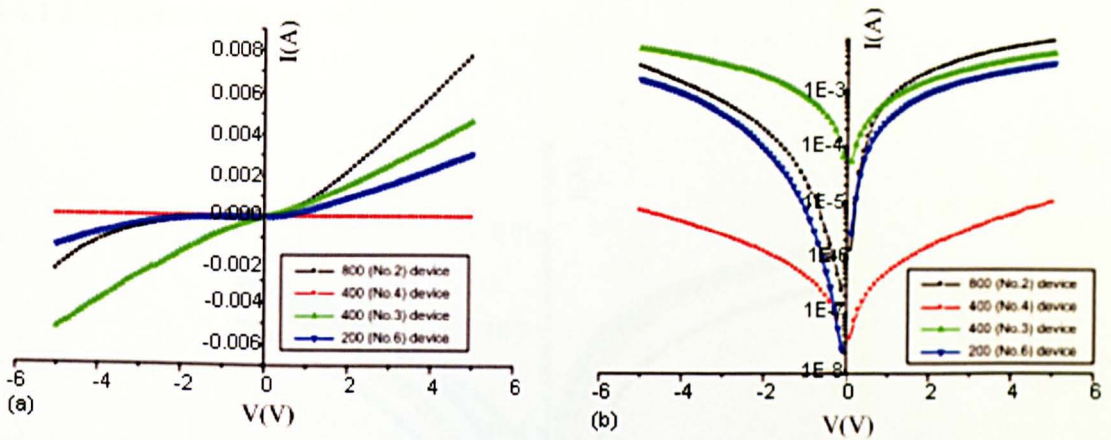


Figure 6.9 I-V comparison of different areas of GaMnN sample at 300 K

The I-V characteristics of devices of different sizes measured at room temperature are shown in Figure 6.9. The measured I-V characteristics are not what one would expect from a high quality diode. For example, the two 400  $\mu\text{m}$  devices exhibit completely different behaviour. One sample 400  $\mu\text{m}$  (no.3) is almost Ohmic whilst the other (no. 4) exhibits Schottky behaviour but with significant series resistance. The 200  $\mu\text{m}$  (no.6) and 800  $\mu\text{m}$  (no.2) devices appear to exhibit Schottky behaviour with soft breakdown. However, the currents do not seem to scale appropriately with device area. These results indicate that the electrical behaviour of the Mn-doped GaN depends strongly on lateral position of the sample. Similar effects have been observed by Sundarmoorthy [130].

## 6.4 800 diameter device (no.2)

### 6.4.1 I-V Behaviour

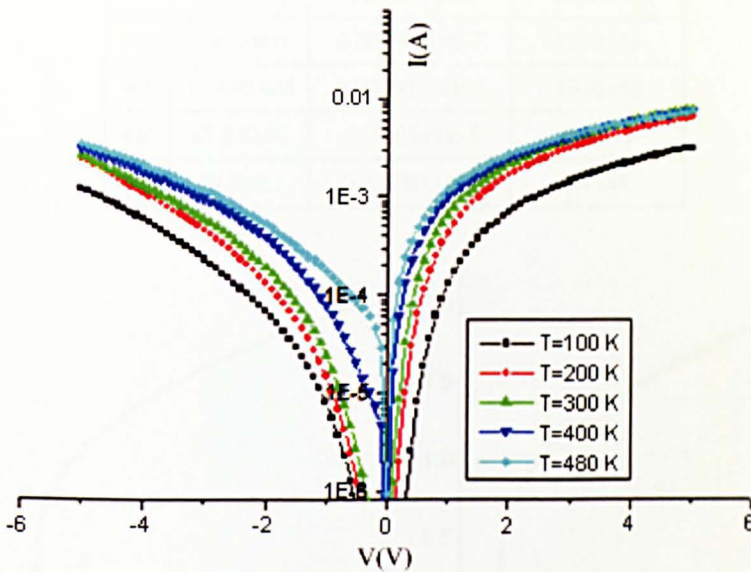


Figure 6.10 I-V characteristic of GaMnN device (2)

For the 800 $\mu\text{m}$  diameter device, which has the largest diameter of all the diodes studied, the current-voltage-temperature measurements were made for both the forward and the reverse directions and are shown in Figure 6.10. An artifact of plotting the logarithm of the current in figure 6.10 is that the reverse current is shown positive. The I-V curves show that at lower voltages the current exhibits stronger temperature dependence. The current is lower when the sample is the coldest. Between 100 K and 400 K the current at low diode biasing increases by approximately two orders of magnitude. However, at higher voltages the sensitivity of the current to the sample temperature becomes less and for all temperature ranges the current appears to approach the same value except for the lowest temperature (100K).

The ideality factor ( $n$ ), the saturation current ( $I_S$ ) and the series resistance ( $R_S$ ) were found by fitting equation (2.15) using least squares technique (see section 5.7). These quantities are listed in Table 6.1 and the fitting curves at 200 and 300 K are shown in Figure 6.11 (a) and (b) respectively.

**Table 6.1** Some parameters obtained experimentally from the forward I-V characteristic of the GaMnN (800 device) Schottky diode at some selected temperatures

| T   | n          | $I_s$ (A)       | R ( $\Omega$ ) |
|-----|------------|-----------------|----------------|
| 100 | 21±0.009   | 0.00000005±1E-7 | 10418.5±611.6  |
| 150 | 14±0.009   | 0.00000007±1E-7 | 6645.3±375     |
| 200 | 11±0.008   | 0.0000001±2E-7  | 5145 ±267      |
| 300 | 8.3±0.006  | 0.0000003±3E-7  | 3421±133       |
| 340 | 8.3±0.005  | 0.000002±9E-7   | 2230±50        |
| 400 | 11.4±0.008 | 0.000009±4E-6   | 1310±46        |
| 440 | 17.2±0.06  | 0.00004±4E-5    | 694±17         |
| 460 | 25.3±0.2   | 0.00008±1E-4    | 246±4          |

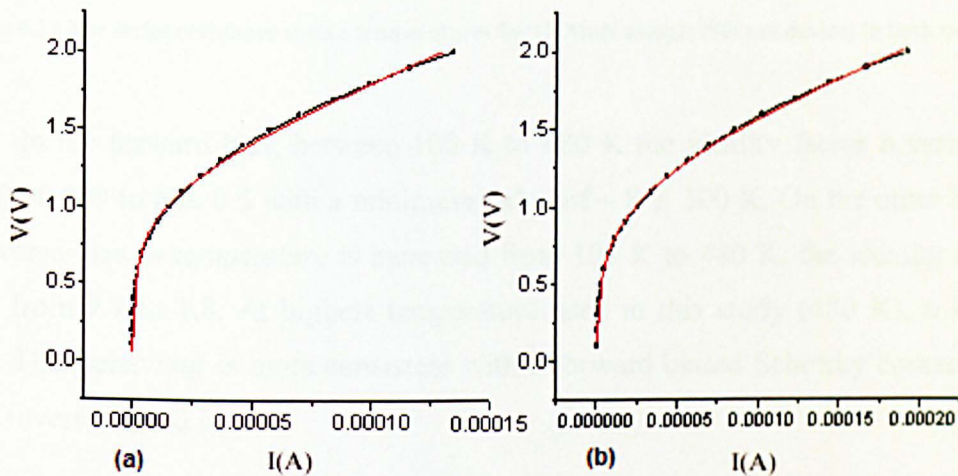


**Figure 6.11** The applied forward bias against current at (a) 200 K and (b) at room temperature. The graph shows the fitting applied to equation (2.15) (red lines) for 800 device

The series resistance of the device has been determined from the I-V-T measurements using equation (2.15) for both polarities as shown in Figure 6.12. In general, it was found that the series resistance was much higher in forward compared to the reverse direction.

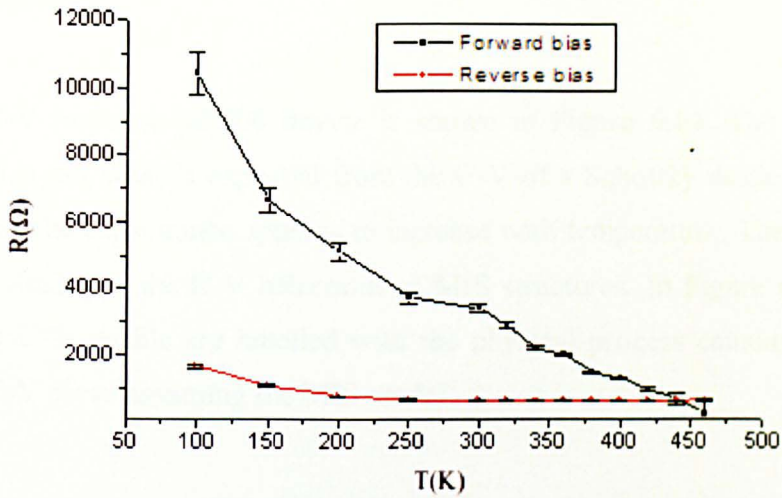


Figure 6.12 The series resistance versus temperatures for GaMnN sample (800 $\mu$ m device) in both polarities

In the forward bias, between 100 K to 480 K the ideality factor  $n$  varies from  $20.000 \pm 0.009$  to  $63 \pm 0.5$  with a minimum value of  $\sim 8$  at 300 K. On the other hand, in the reverse bias as temperature is increased from 100 K to 480 K, the ideality factor  $n$  varies from 9.7 to 1.8. At highest temperature used in this study (480 K),  $n$  is  $1.8 \pm 0.001$ . This behaviour is more consistent with a forward biased Schottky contact rather than a reverse biased one.

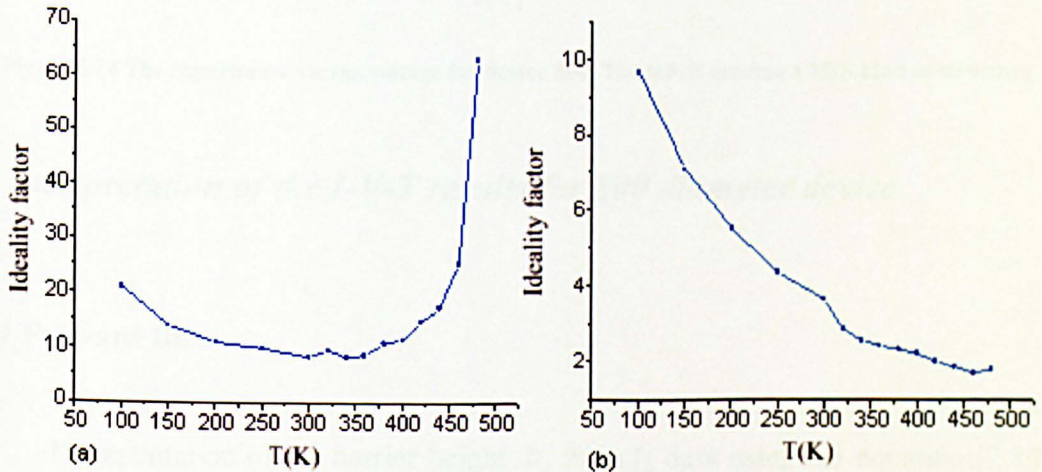


Figure 6.13 (a) Ideality factor as a function of temperature in case of forward and (b) In reverse biases for GaMnN material (800 device)

## 6.4.2 C-V Behaviour

The C-V response of 800 device is shown in Figure 6.14. The shape of the characteristics is not what is expected from the C-V of a Schottky diode. Namely, for the reverse bias the capacitance appears to increase with temperature. The shape of the C-V curve is similar to the C-V behaviour of MIS structures. In Figure 6.14 different regions of the C-V profile are labelled with the physical process causing the general shape of the C-V curve assuming the MIS model.

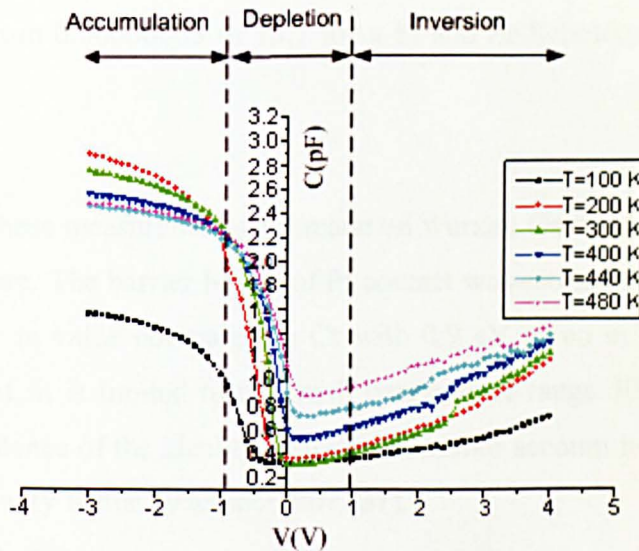


Figure 6.14 The capacitance versus voltage for device 800. The labels assume a MIS kind of structure

## 6.5 Interpretation of the I-V-T results for 800 diameter device

### 6.5.1 Forward Bias

The estimation of the barrier height  $\Phi_b$  from  $I_s$  data using the equation (2.14) is plotted in Figure 6.15 (a). The barrier height shows temperature dependence with the highest value being 0.43 eV at a temperature of 400 K in the forward bias. As the temperature increases the barrier height starts to fluctuate in the 420–480 K temperature range due to observed value of fluctuation of the saturation current.

The plot of the natural logarithm of  $(I_s/T^2)$  against  $10^3/T$  for forward bias is shown in Figure 6.15 (b). The slope of the plots gives the barrier height according to equation (2.14). The calculated value for the barrier height in the forward bias is  $0.37 \pm 0.03$  eV. The intercept of this plot on current axis gives the value of the Richardson's constant. From Figure 6.15 (b), its estimated value is  $0.009 \pm 0.9$  A.cm<sup>-2</sup>.K<sup>-2</sup> which is very small compared with other reports of 103.8 A.cm<sup>-2</sup>.K<sup>-2</sup> for p-GaN [138]. Tan et al. [138] attributed the error in the estimated value of  $A^*$  to the limitation of the data taken in y-axis, for example for this device the range is limited from 300 K to 480 K. However, there is a considerable degree of uncertainty in the reported values of the Richardson's constant for Mg doped p-GaN samples grown on sapphire which has been reported to vary from 0.00000003 to 13.7 for a Pt and Zr-Schottky contacts to p-GaN respectively.

However, these measurements are made on wurzite GaN rather than cubic GaN, which is studied here. The barrier height of Pt contact was estimated to be 0.5 eV [138] which was smaller in value compared to Cr with 0.9 eV given in the same reference [138]. The range of fit is limited to the small temperature range 300 K to 480 K. The temperature dependence of the ideality factor is taken into account in equation (2.35) by multiplying the ideality factor by temperature [31].

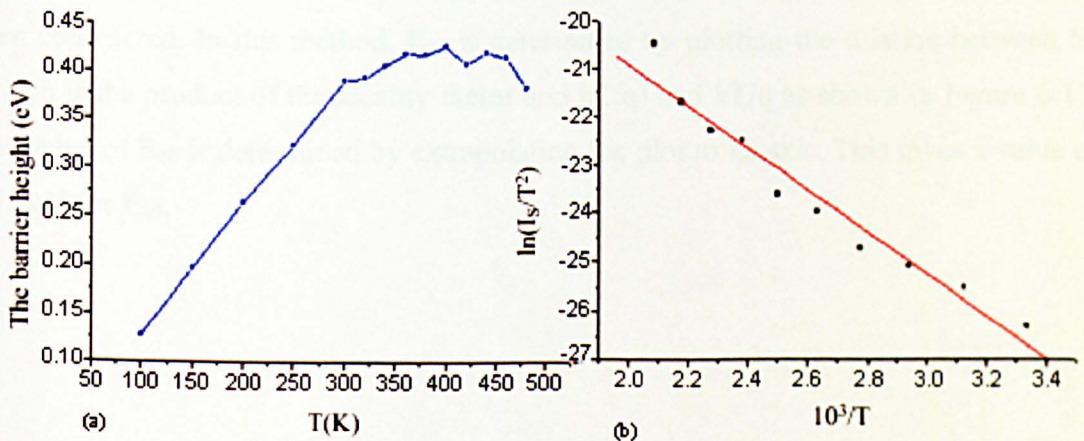


Figure 6.15 (a) The temperature dependence of the barrier height and (b) The plot of  $\ln(I_s/T^2)$  versus  $10^3/T$  in case of forward bias which gives barrier height  $\Phi_b = 0.37 \pm 0.03$  eV. The data for both is taken in the temperature range 300 K to 480 K

The conventional plot then becomes  $(I_s/T^2)$  versus  $10^3/nT$  whose slope gives the barrier height ( $\Phi_b$ ) of  $1.14 \pm 0.06$  eV as shown in Figure 6.16.

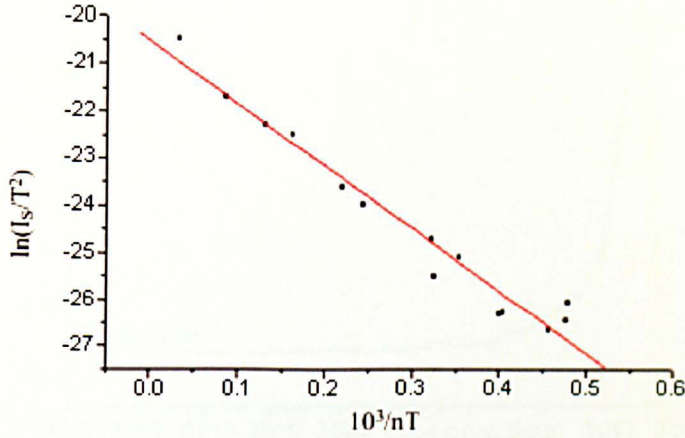


Figure 6.16 the plot  $\ln(I_s/T^2)$  versus  $10^3/nT$

### 6.5.1.1 Thermionic-field emission (TFE) Model

Using equation (2.22) where  $m^* = 0.2 m_0$  [129] and  $\epsilon_s = 9.5 \epsilon_0$  for p-type GaN, the values of  $E_{00}$  turn out to be 11.23 meV and 12 meV corresponding to acceptor concentrations of  $7 \times 10^{17} \text{ cm}^{-3}$  and  $8 \times 10^{17} \text{ cm}^{-3}$  respectively. The TFE becomes important when  $E_{00} \sim kT$  since  $E_{00}$  is comparable to  $kT$  at 130 K and 140 K ( $kT = 11.2$  meV and 12 meV respectively). There is good reason to believe that TFE is significant.

To analyse the conduction mechanism in the forward bias the technique developed by Padovani and Stratton [15] and used by several workers [14, 16, 33] has been considered. In this method,  $E_{00}$  is determined by plotting the relation between  $E_0$  (which is the product of the ideality factor and  $kT/q$ ) and  $kT/q$  as shown in Figure 6.17. The value of  $E_{00}$  is determined by extrapolating the plot to  $E_0$  axis. This gives a value of 0.18 eV for  $E_{00}$ .

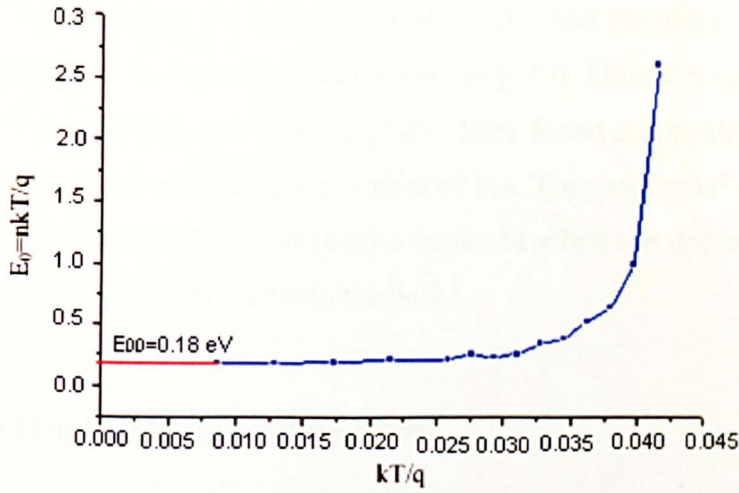


Figure 6.17 Experimental values of  $E_0$  as a function of temperature for 800  $\mu\text{m}$  diameter device

Barrier heights have been calculated based on TFE theory, by plotting equation (2.23). Results obtained from the I-V-T measurements of the forward bias for the 800  $\mu\text{m}$  device by plotting the logarithm of  $I_S \cosh(E_{00}/kT)/T$  versus  $1/E_0$  are shown in Figure 6.18. The slope of this plot gives the value of barrier height as  $0.36 \pm 0.033$  eV. This is in good agreement with the value of 0.37 eV of the barrier height obtained from the plot of the natural logarithm of  $(I_S/T^2)$  against  $10^3/T$  in the forward bias as shown in Figure 6.15 (b).

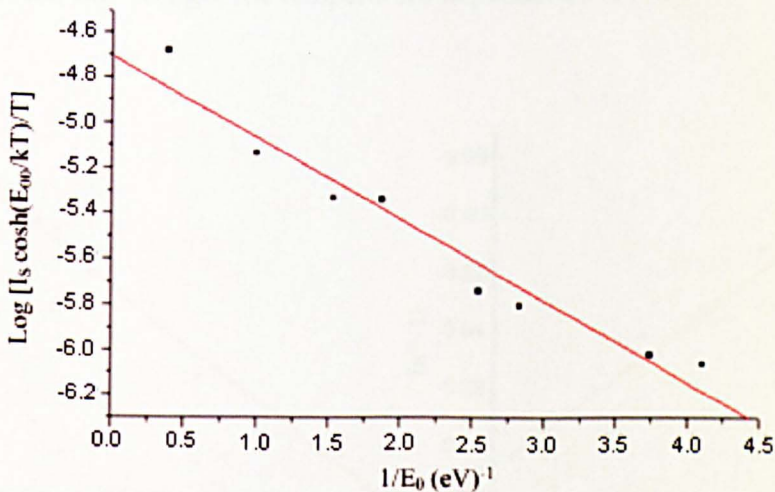


Figure 6.18 The saturation current versus  $1/E_0$  as given by equation (2.23)

The experimentally observed  $E_{00}$  value of 180 meV for forward bias is much higher than the theoretically calculated value of 11.23 meV and 12 meV. The high value of  $E_{00}$  can be related to two factors. One factor is the electric field on the surface which

determines the barrier shape and tunnelling probability, and the other is the density of states which play a role through the effective masses [139]. Similar result is obtained by Hasegawa and Oyama [129] and Morkoc [140]. They found a considerable difference between the experimental and theoretical values of  $E_{00}$ . They attributed this to the effect of surface and bulk defects. They obtained a better fit when the doping concentration near the surface is higher as compared to the bulk.

### 6.5.1.2 Barrier Height Inhomogeneities Model

The two main diode parameters such as ideality factor ( $n$ ) and the barrier height ( $\Phi_b$ ) were found to be strongly temperature dependent. The model Werner and Guttler [18] explains the dependence of these two parameters on temperature by considering of a Gaussian distribution characterized for the barrier height variations that consists of low and high barrier areas. Using equation (2.28), the barrier height  $\Phi_b$  has been plotted against  $q/(2kT)$  as shown in Figure 6.19 (a) in the case of “forward bias”. A mean barrier height of  $0.6 \pm 0.01$  eV is obtained as the intercept of this plot. The standard deviation ( $\sigma_{s0}$ ) relates to the slope of this plot by  $\sqrt{(\text{slope})}$  with a value of  $0.1 \pm 0.0005$  eV. This indicates that the standard deviation is 16% of the mean barrier height. The standard deviation is a measure of the barrier homogeneity [136]. The larger the standard deviation, the stronger the temperature dependence is [18].

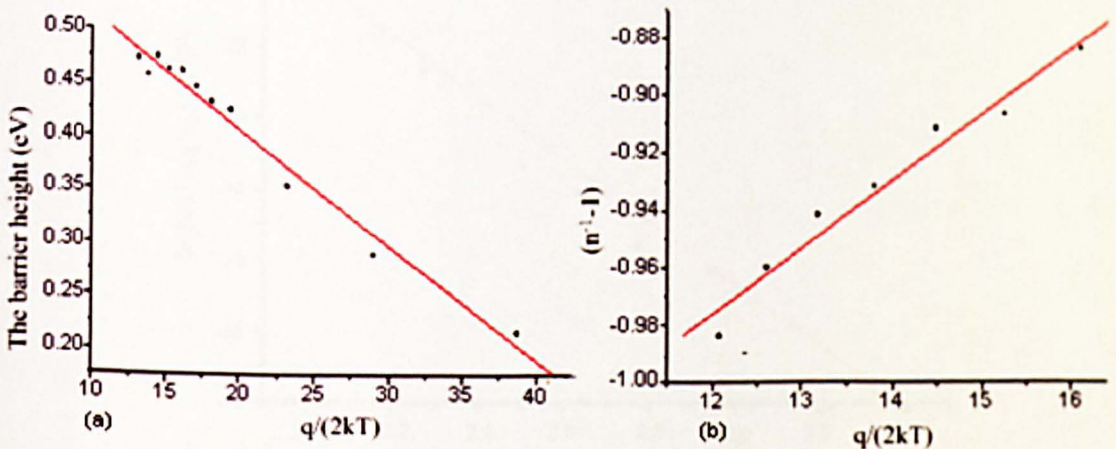


Figure 6.19 (a) The forward barrier height and (b) Ideality factor versus  $q/(2kT)$  plot of the GaMnN Schottky diode according to the Gaussian distribution model of the barrier heights. The modified Richardson plot as given by this model can be obtained by combining equation (2.14) and (2.28).

The conventional Richardson plot is modified according to the barrier inhomogeneities model given by equation (2.34). A plot of the modified  $[\ln(I_S/T^2) - (q^2\sigma_{so}^2/2k^2T^2)]$  versus  $10^3/T$  yields a straight line with the slope giving the mean barrier height and the intercept giving the modified Richardson constant as shown in Figure 6.20. Table 6.2 shows the parameters used to apply the modified Richardson plot in case of the forward bias. The modified Richardson plot for forward bias yields a value of  $0.38 \pm 0.02$  eV of the barrier height which is comparable to the value obtained (0.37 eV) from the conventional Richardson plot.

Table 6.2 The parameters used to apply the modified Richardson plot in case of the forward bias

| T   | $10^3/T$ | $I_S$   | $\ln I_S/T^2$ | $q/kT$ | $\ln(I_S/T^2) - (q^2\sigma_{so}^2/2k^2T^2)$ |
|-----|----------|---------|---------------|--------|---|
| 300 | 3.3      | 3.4E-07 | -26.3         | 38.7   | -26.4                                       |
| 320 | 3        | 8.5E-07 | -25.5         | 36     | -25.6                                       |
| 340 | 2.9      | 1.5E-06 | -25           | 34     | -25.2                                       |
| 360 | 2.8      | 2.4E-06 | -24.7         | 32     | -24.8                                       |
| 380 | 2.6      | 5.6E-06 | -24           | 30.5   | -24.  |
| 400 | 2.5      | 8.9E-06 | -23.6         | 29     | -23.7                                       |
| 420 | 2.4      | 0.00003 | -22.5         | 27.6   | -22.5                                       |
| 440 | 2.3      | 0.00004 | -22           | 26.4   | -22.3                                       |
| 460 | 2.2      | 0.00008 | -21.7         | 25     | -21.7                                       |
| 480 | 2.1      | 0.0003  | -20.5         | 24     | -20.5                                       |

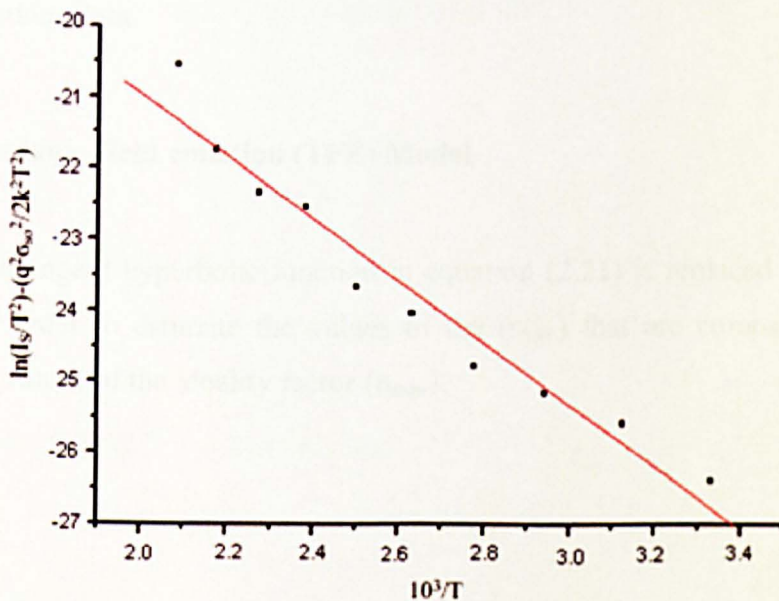


Figure 6.20 Modified Richardson plot as given by equation (2.34) for the GaMnN Schottky diode which gives barrier height  $\Phi_b = 0.38 \pm 0.03$  eV in forward bias

The current–voltage characteristics of GaMnN based Schottky diode has been interpreted based on assumption of a Gaussian distribution of barrier heights. It is seen that the value of 0.1 eV for the standard deviation ( $\sigma_{s0}$ ) is not small compared to the mean barrier height 0.6 eV and it indicates greater inhomogeneities of the barrier height.

The voltage coefficients are obtained as  $\rho_2 = -1.2 \pm 0.03$  V and  $\rho_3 = -0.02 \pm 0.002$  V from the intercept and the slope of the Figure 6.19 (b), respectively. The parameter  $T_0$  is related to  $\rho_3$  by  $[T_0 = \rho_3 / (2k/q)]$  which gives a value of 133.6 K for  $T_0$ . On the other hand, the value of  $T_0$  could not be determined from the  $n$  versus  $1/T$  plot as is usually done because in this case, the relationship between  $n$  versus  $1/T$  was not linear.

## 6.5.2 Reverse Bias

According to this model, the semiconductor just below the Schottky contact has an n-type characteristic as explained in model two earlier in this chapter. In such cases, the applied bias, which makes the Schottky contact positive with respect to the semiconductor, will be the “forward bias”. Consequently; what was considered as reverse bias for a p-type GaMnN, would be “forward bias” for over n-type GaMnN layer. This implies that the standard Schottky analysis can be considered for “reverse bias” observations/data.

### 6.5.2.1 Thermionic-field emission (TFE) Model

The cotangent hyperbolic function in equation (2.21) is replaced by the Taylor expansion in order to estimate the values of the ( $n_{\text{tun.}}$ ) that are compatible with the experimental values of the ideality factor ( $n_{\text{exp.}}$ ).

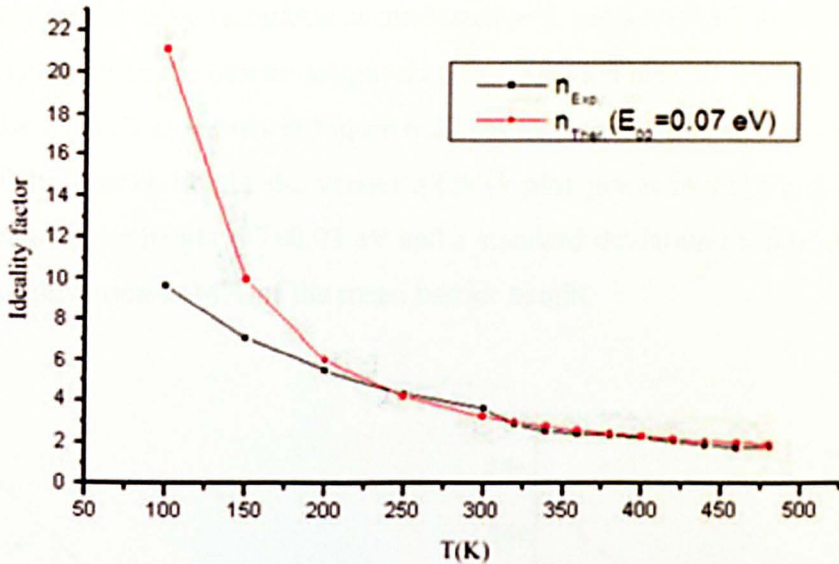


Figure 6.21 Theoretical temperature dependence of ideality factor obtained by the TFE model for tunnelling characteristic energy  $E_{00}=0.07$  eV (red line), and the experimental determined ideality factor (black line) as a function of temperature in the reverse bias

Using the method of iteration, it is found that a value of 70 meV for  $E_{00}$  gives a good fit above 200 K as shown in Figure 6.21. With increasing temperature the value of  $kT/q$  increases and becomes comparable to  $E_{00}$ . As the difference between  $E_{00}$  and  $kT/q$  narrows the thermionic component of current increases and the ideality factor approaches unity as is experimentally observed. Equation (2.21), which is the temperature dependence of the ideality factor for tunnelling ( $n_{\text{tun}}$ ), predicts a value of about 1.87 at 480 K for this sample. This value is compatible with the measured value of  $n$  at the same temperature (1.79).

The estimated tunnelling characteristic energy of 70 meV for  $E_{00}$  is used in equation (2.21). Both  $n_{\text{tun}}$  and  $n_{\text{exp}}$  parameters plots are shown as a function of the temperature in Figure 6.21.

### 6.5.2.2 Barrier Height Inhomogeneities Model:

The plot of the natural logarithm of  $(I_S/AT^2)$  against  $10^3/T$  for “reverse bias” is shown in Figure 6.22 (a). The slope of the plots gives the barrier height for the reverse bias as  $0.2 \pm 0.02 \text{ eV}$ .

Applying the same technique as used earlier in section (6.5.1.2), for determining the inhomogeneities in the barrier height, data for “forward bias” is plotted as the barrier height versus  $q/(2kT)$  as shown in Figure 6.22 (b) in the case of “reverse bias”, and the linearity of the barrier height  $\Phi_b$  versus  $q/(2kT)$  plot given in Figure 6.22 (b). This yields a mean barrier height  $0.7\pm 0.03$  eV and a standard deviation ( $\sigma_{s0}$ ) of  $0.1\pm 0.02$  eV. The standard deviation is 14% of the mean barrier height.

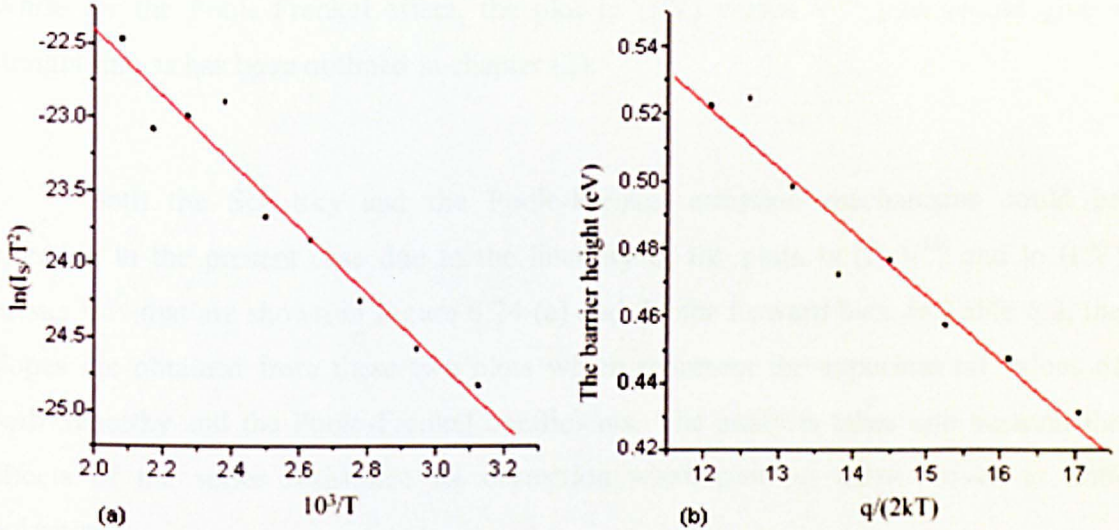


Figure 6.22 (a) The plot of  $\ln(I_s/T^2)$  versus  $10^3/T$  in case of reverse bias and (b) Zero-bias reverse apparent barrier height versus  $q/(2kT)$  plot of the GaMnN Schottky diode according to the Gaussian distribution model of the barrier heights

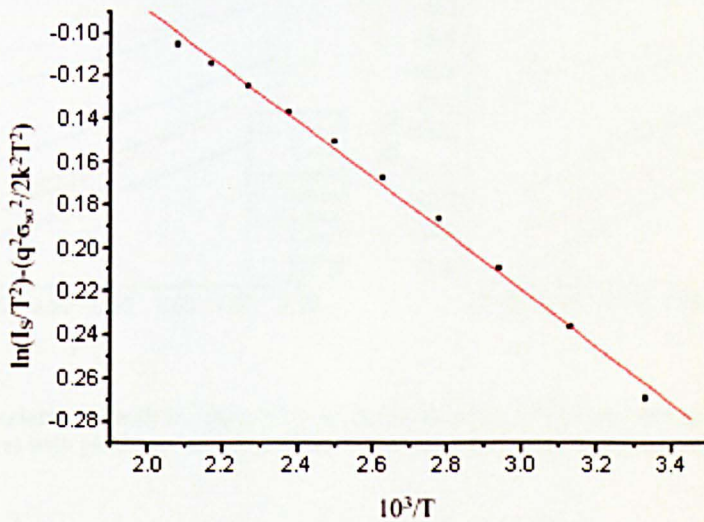


Figure 6.23 The plot of  $\ln[(I_s/T^2) - (q^2 \sigma_{s0}^2 / 2k^2 T^2)]$  versus  $10^3/T$  in case of reverse bias which gives barrier height  $\Phi_b = 0.2\pm 0.03$  eV. The data is taken in the temperature range 300 K to 480 K

A plot of the modified  $[\ln[(I_s/T^2) - (q^2 \sigma_{s0}^2 / 2k^2 T^2)]]$  versus  $10^3/T$  yields a straight line with the slope giving the mean barrier height and the intercept giving the modified

Richardson constant as shown in Figure 6.23 in the case of reverse bias. The modified Richardson plot yields a value of  $0.01 \pm 0.0002$  eV of the barrier height which is smaller than the value obtained from the conventional Richardson plot (0.2 eV).

### 6.5.3 The Insulator GaMnN layer in both polarities:

In case of the Schottky effect,  $\ln(I)$  versus  $V^{1/2}$  plot should give a straight line. While for the Poole-Frenkel effect, the plot  $\ln(I/V)$  versus  $V^{1/2}$  plot should give a straight line as has been outlined in chapter (2).

Both the Schottky and the Poole-Frenkel emission mechanisms could be effective in the present case due to the linearity of the plots  $\ln(I)-V^{1/2}$  and  $\ln(I/V)$  versus  $V^{1/2}$  that are shown in Figure 6.24 (a) and (b) for forward bias. In Table 6.3, the slopes are obtained from these two plots which represent the experimental values of both Schottky and the Poole-Frenkel coefficients. The analysis takes into account the effects of the series resistance  $R_S$  correction when plotting these curves in both polarities.

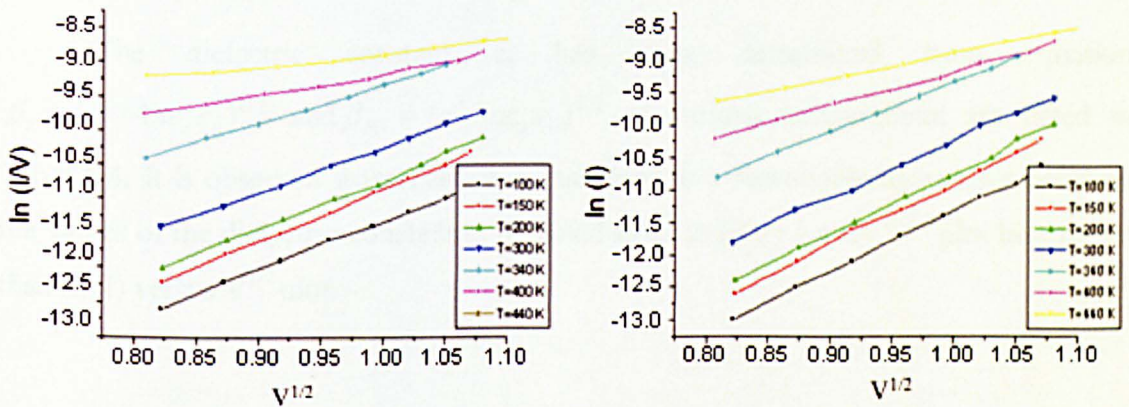


Figure 6.24 (a) Variation of  $\ln(I/V)$  versus  $V^{1/2}$  and (b)  $\ln(I)$  versus  $V^{1/2}$  in high forward voltage range at various temperatures with good correlation coefficient. In both cases, these two plots after the  $R_S$  correction.

The slope from  $\ln(I/V)$  versus  $V^{1/2}$  plot in forward bias ranges from  $7.2 \pm 0.1$  at 100 K to  $1.2 \pm 0.09$  at 480 K. This plot is shown in Figure 6.24 (a) and the values of the slope are listed in Table 6.3 after  $R_S$  correction. The slope from  $\ln(I)$  versus  $V^{1/2}$  plot in forward bias ranges from  $9.4 \pm 0.1$  at 100 K to  $3 \pm 0.03$  at 480 K. This plot is shown in Figure 6.24 (b) and the values of the slope are listed in Table 6.3 for both polarities. The

slope of these curves decreases with increases of temperature in the case of forward bias.

**Table 6.3 Coefficient of barrier lowering for 800 device**

| T   | $\beta_{PF}$ ( $10^{-5}$ eV.m <sup>1/2</sup> .V <sup>-1/2</sup> )<br>(Forward bias)<br>voltage range<br>0.7-1.4 V | $\beta_{PF}$ ( $10^{-5}$ eV.m <sup>1/2</sup> .V <sup>-1/2</sup> )<br>(Reverse bias)<br>voltage range<br>0.4-1.2 V | $\beta_S$ ( $10^{-5}$ eV.m <sup>1/2</sup> .V <sup>-1/2</sup> )<br>(Forward bias)<br>voltage range<br>0.7-1.4 V | $\beta_S$ ( $10^{-5}$ eV.m <sup>1/2</sup> .V <sup>-1/2</sup> )<br>(Reverse bias)<br>voltage range<br>0.4-1.2 V |
|-----|---|---|--|--|
| 100 | 7.2±0.1   | 12.5±0.2  | 9.4±0.1  | 15.1±0.2   |
| 150 | 7.6±0.08  | 10.85±0.2   | 9.6±0.1  | 13.6±0.1   |
| 200 | 7.3±0.1   | 10±0.1  | 9.41±0.1   | 12.8±0.1   |
| 300 | 6.6±0.07  | 9±0.1   | 8.7±0.2  | 12.2±0.1   |
| 340 | 5.5±0.07  | 13±0.2  | 7.6±0.07   | 14.6±0.07  |
| 400 | 3.24±0.1  | 9.9±0.03  | 5.4±0.1  | 14.2±0.09  |
| 440 | 1.9±0.09  | 10.8±0.09   | 4±0.05   | 14.6±0.06  |
| 460 | 1.2±0.09  | 11±0.2  | 3±0.03   | 15±0.2   |

Since  $\epsilon_s=9.5$  (for GaN) and  $\epsilon_0=8.85 \times 10^{-12}$  F/m, the estimated theoretical values of these two coefficients are  $\beta_S = 1.23 \times 10^{-5}$  eV m<sup>1/2</sup> V<sup>1/2</sup> and  $\beta_{PF} = 2.46 \times 10^{-5}$  eV m<sup>1/2</sup> V<sup>1/2</sup>.

The dielectric constant  $\epsilon_s$  has been determined from equation  $\beta_s = (q^3 / 4\pi\epsilon_s\epsilon_0)^{1/2}$  and  $\beta_{PF} = (q^3 / \pi\epsilon_s\epsilon_0)^{1/2}$  at various temperatures are listed in Table 6.4. It is observed from Table 6.4 that there is a reasonable agreement between the values of the dielectric constant  $\epsilon_s$  obtained from ln(I/V) versus V<sup>1/2</sup> plot bias rather than ln(I) versus V<sup>1/2</sup> plot.

Table 6.4 The estimated dielectric constant  $\epsilon$ , from both plots.

| T   | From the plot $\ln I$ vs. $V^{1/2}$ |         | From the plot $\ln I/V$ vs. $V^{1/2}$ |         |
|-----|-------------------------------------|---------|---------------------------------------|---------|
|     | Forward                             | Reverse | Forward                               | Reverse |
| 100 | 0.16                                | 0.17    | 1                                     | 1.6     |
| 150 | 0.3                                 | 0.13    | 3.26                                  | 1.17    |
| 200 | 1                                   | 0.16    | 22.5                                  | 1.84    |
| 300 | 0.4                                 | 0.15    | 4                                     | 1.65    |
| 340 | 0.4                                 | 0.11    | 3                                     | 1       |
| 400 | 0.3                                 | 0.16    | 4.4                                   | 1.71    |
| 440 | 0.4                                 | 0.07    | 5.3                                   | 1.4     |
| 480 | 0.16                                | 0.17    | 1                                     | 1.6     |

### 6.6 400 diameter device (no.3)

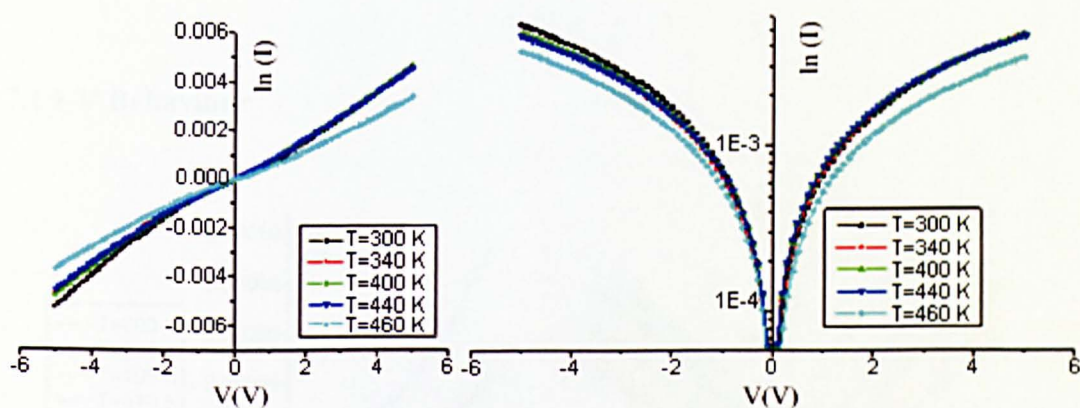


Figure 6.25 I-V characteristic of GaMnN device (3)

This device exhibits characteristic of an extremely soft diode, as shown in Figure 6.25. The current actually decreases with increasing temperature, and the series resistance exhibits a metallic behaviour. This may be due to a Mn layer that tends to migrate to the surface and may provide a conducting metallic path between the two contacts as shown in Figure 6.26. Such a resistance would imply that the parallel resistance of the semiconductor is extremely high (the two resistances would add in parallel and if the metallic character is dominant, it must be lower). There is indeed a possibility for this as Mn migrates to the surface it leaves behind a near intrinsic GaN and with this high bandgap, it acts as an insulator. Unintentionally doped (u.i.d.) behaviour is not withstanding.

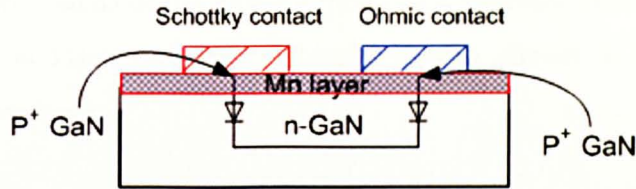


Figure 6.26 The Mn layer short circuits the two contacts

However, the device is almost Ohmic and there are clearly strong conduction paths between the Ohmic and the Schottky contact

## 6.7 400 diameter device (no.4)

### 6.7.1 I-V Behaviour

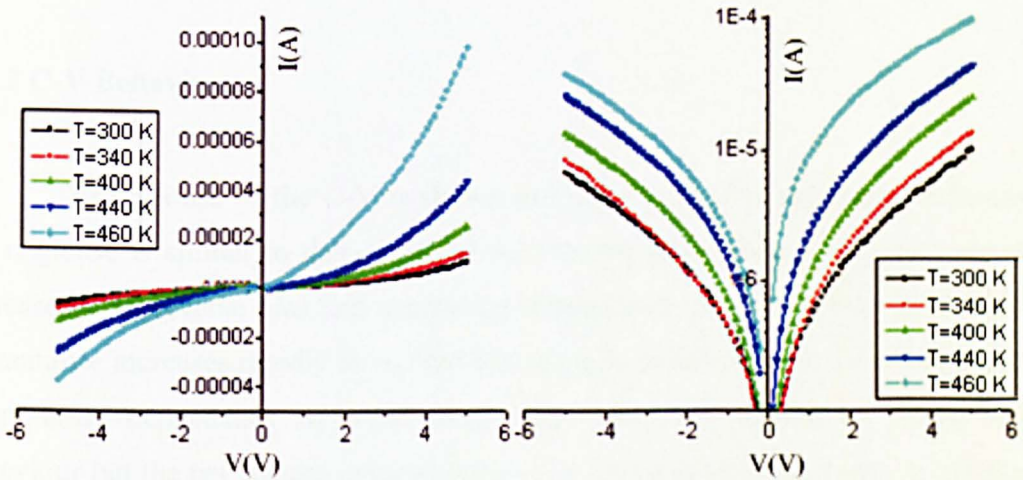


Figure 6.27 I-V characteristic of GaMnN for 400 device (no.4)

The I-V characteristic of the measured Schottky diode at different temperature is shown in Figure 6.27. The general shapes of the characteristics of this device in the forward and reverse directions are nearly similar but the current in the forward direction is generally larger than the current in the reverse direction.

The measured values of the ideality factor as a function of temperature is shown in Figure 6.28. In addition, the barrier height is also shown in Figure 6.28 and it increases with temperature.

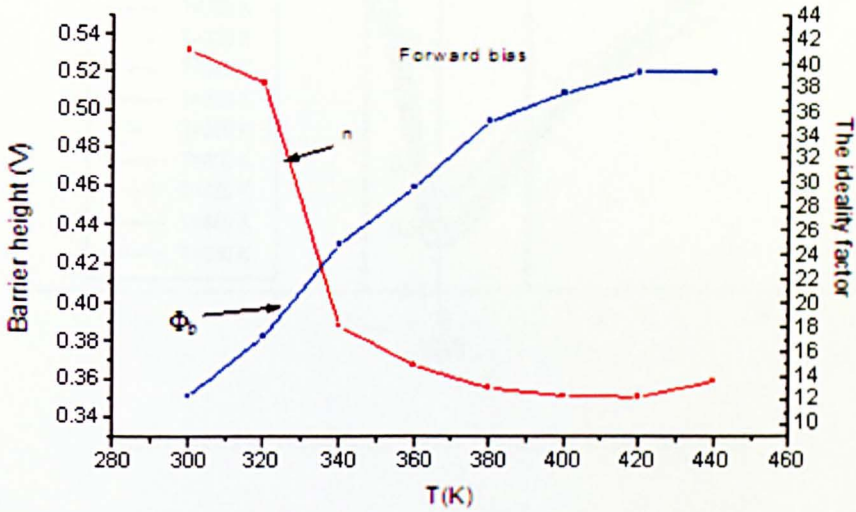


Figure 6.28 The temperature dependence of the barrier height and ideality factor of 400 device

### 6.7.2 C-V Behaviour

The response of the C-V is shown in Figure 6.29. The qualitative behaviour of the response is similar to that observed for the 800  $\mu\text{m}$  device where the capacitance increases with reverse bias and increasing temperature. For the forward direction, the capacitance increases rapidly from zero bias initially followed by a slower increase. The temperature dependence of capacitance again does not appear to follow a fixed behaviour but the net change in capacitance as a function of temperature is less than the 800  $\mu\text{m}$  device. An interpretation of the results for all the C-V measurements is presented in section (6.11) later.

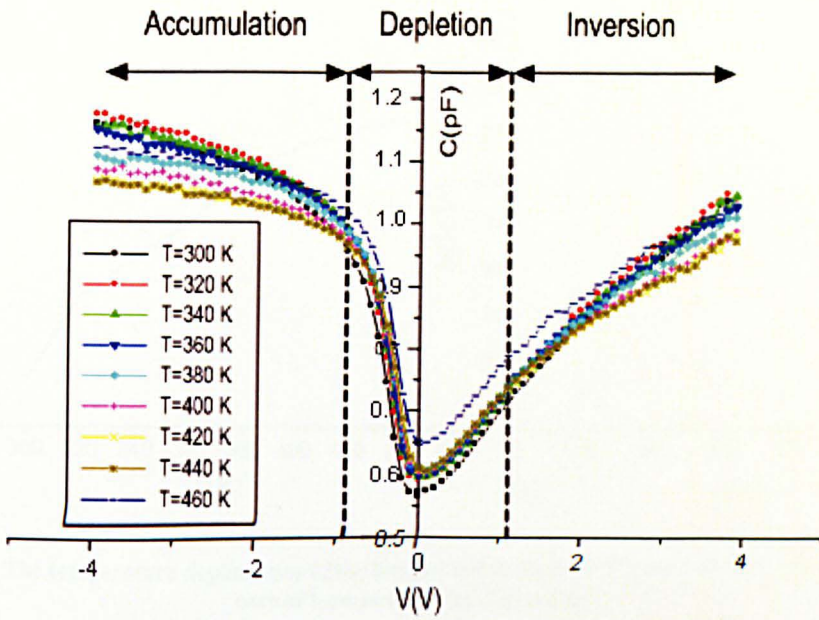


Figure 6.29 The capacitance versus voltage for device 400 (no.4)

## 6.8 Interpretation of the $I$ - $V$ - $T$ results for 400 diameter device (no.4)

### 6.8.1 Forward Bias

The variation of the barrier height over the temperature range 300-480 K for the 400  $\mu\text{m}$  device is shown in Figure 6.30 (a). It is observed that the barrier height increases with increasing temperature. The plot of  $(I_s/T^2)$  against  $10^3/T$  for forward bias is shown in Figure 6.30 (b) which is expected to be a straight line from which the barrier height can be estimated.

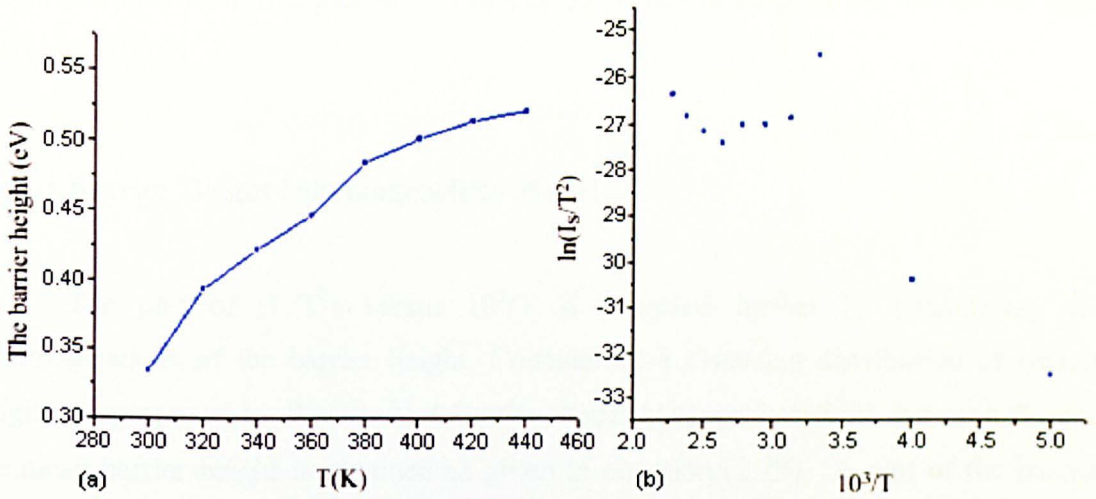


Figure 6.30 (a) The temperature dependence of the barrier height and (b) The plot of  $\ln(I_s/T^2)$  versus  $10^3/T$  in case of forward bias for 400 (no.4)

There appears to be a considerable scatter of points on this plot, which is attributed to the lateral variation of barrier heights on the surface of the Schottky contact. The area under each patch of different barrier height is not known and their collective behaviour would be difficult to speculate. This however, can be taken into account by considering the barrier inhomogeneities model, which is done in the following section.

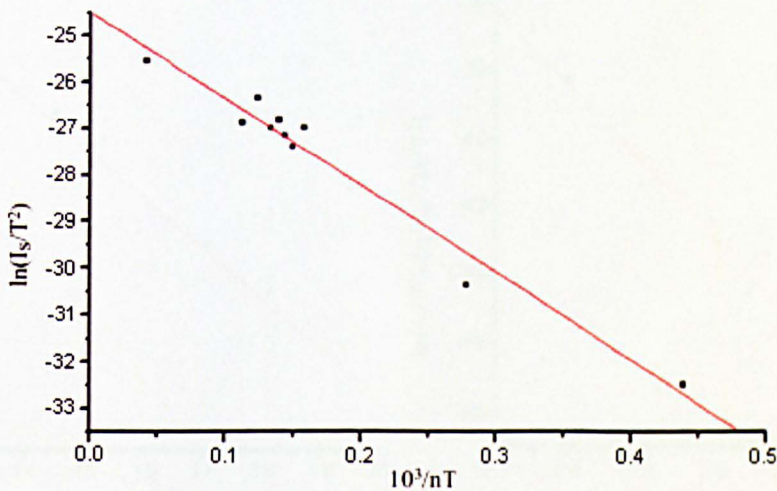


Figure 6.31 The plot of  $\ln(I_s/T^2)$  versus  $10^3/nT$  the barrier height yields a value of  $1.61 \pm 0.098$  eV in case of forward bias for (400d no.4)

Better linearity is found when a modified Richardson plot ( $(I_s/T^2)$  vs.  $10^3/nT$ ) is used since this takes into account  $n$ . This plot is shown in Figure 6.31. The barrier

height obtained from this plot is  $1.61 \pm 0.098$  eV which is close to the half of the band gap ( $\sim 1.6$  eV).

### 6.8.1.1 Barrier Height Inhomogeneities Model

The plot of  $(I_s/T^2)$  versus  $10^3/T$  is analysed further by considering the inhomogeneities of the barrier height. Considering a Gaussian distribution of barrier heights as proposed by Werner and Guttler model [18] a relationship between  $\Phi_b$  and the mean barrier height is obtained as given in equation (2.28). A plot of the barrier height versus  $q/(2kT)$  is shown plotted in Figure 6.32 (a). The intercept gives value of  $1 \pm 0.03$  eV for the mean barrier height and a standard deviation of  $0.17 \pm 0.01$  eV in forward bias. This represents a 12% of the mean barrier height.

A modified Richardson plot which relates the term  $[\ln [(I_s/T^2)] - q \sigma_{so}^2/2k^2T^2]$  to  $10^3/T$  [equation (2.34)] is shown plotted in Figure 6.32 (b). The estimated barrier height which is the slope of this plot is  $0.96 \pm 0.05$  eV. This compares favourably with the value of  $1 \pm 0.03$  eV obtained from Figure 6.32 (a).

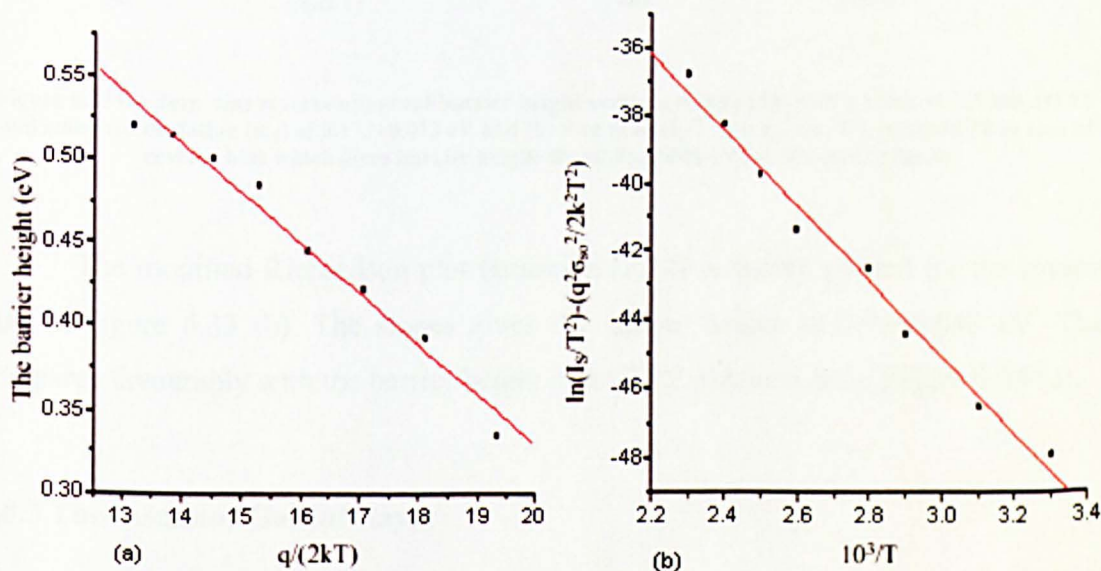


Figure 6.32 (a) Zero-bias forward apparent barrier height versus  $q/(2kT)$  plot with a value of  $1 \pm 0.03$  eV and standard deviation of  $0.17 \pm 0.01$  eV and (b) Plot of  $\ln[(I_s/T^2)] - q \sigma_{so}^2/2k^2T^2$  versus  $10^3/T$  which gives barrier height  $\Phi_b = 0.96 \pm 0.05$  eV in case of forward bias for 400 (no.4) device

## 6.8.2 Reverse Bias

### 6.8.2.1 Barrier Height Inhomogeneities Model

The barrier height inhomogeneities is also investigated in the reverse bias using the same technique as for the forward bias by plotting the barrier height versus  $q/(2kT)$  as shown Figure 6.33 (a). The obtained value for the mean barrier height yields a value of  $0.93 \pm 0.035$  eV and the standard deviation which is  $\sqrt{\text{slope}}$  of this plot, with a value of  $0.173 \pm 0.013$  eV. This means that the standard deviation is 18% of the mean barrier height is the same as for the forward bias.

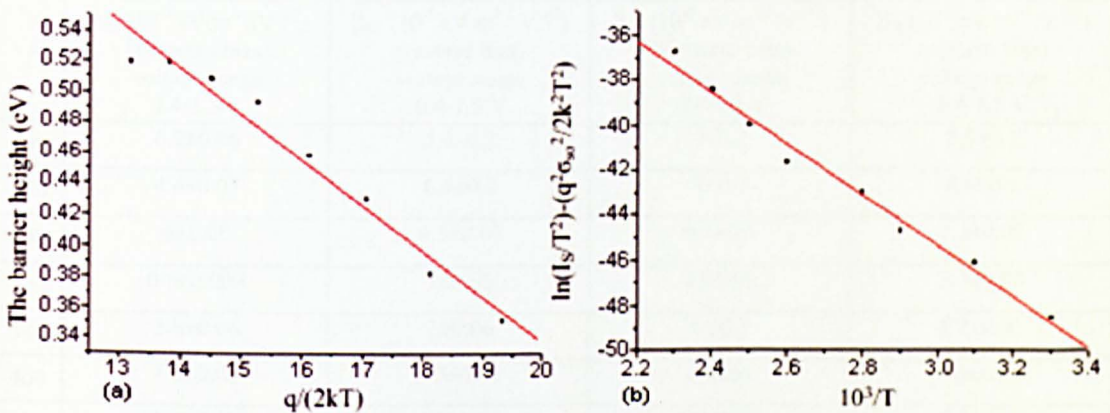


Figure 6.33 (a) Zero-bias reverse apparent barrier height versus  $q/(2kT)$  plot with a value of  $0.93 \pm 0.035$  eV and standard deviation ( $\sigma_0$ ) of  $0.173 \pm 0.013$  eV and (b) Plot of  $\ln[(I_s/T^2) - q^2 \sigma_0^2 / 2k^2 T^2]$  versus  $10^3/T$  in case of reverse bias which gives barrier height  $\Phi_b = 0.98 \pm 0.048$  eV for 400 device (no.4)

The modified Richardson plot (equation (2.34)) is shown plotted for the reverse bias in Figure 6.33 (b). The slopes gives the barrier height as  $0.98 \pm 0.048$  eV. This compares favourably with the barrier height of 0.93 eV obtained from Figure 6.33 (a).

## 6.8.3 The Insulator GaMnN layer

Both the Schottky and the Poole-Frenkel emission mechanisms could be effective in the present case as indicated by the linearity of the plots  $\ln(I) - V^{1/2}$  and  $\ln(I/V)$  versus  $V^{1/2}$ , which are shown in Figure 6.34 (a-b), after  $R_S$  corrections.

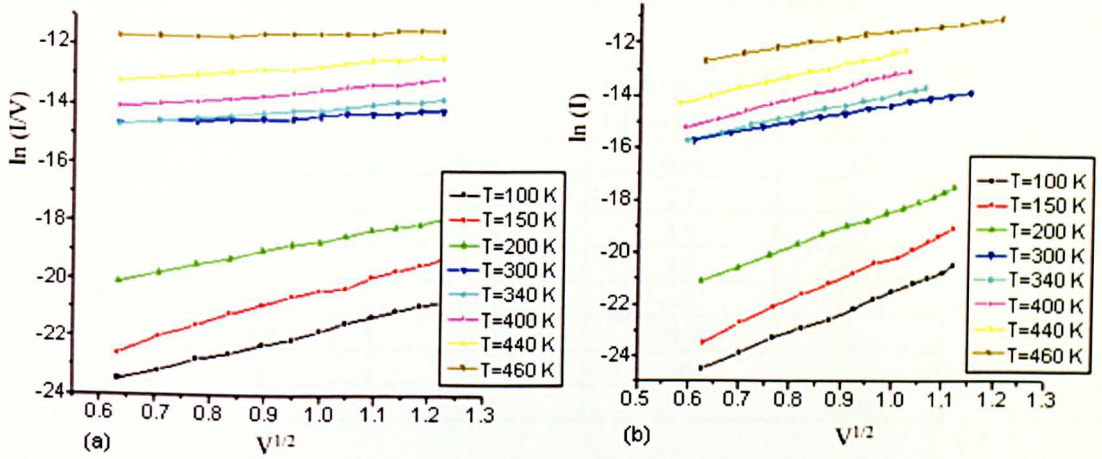


Figure 6.34 Shows (a) plot of  $\ln(I/V)$  versus  $V^{1/2}$  in high reverse voltage range and (b)  $\ln(I)$  versus  $V^{1/2}$  at various temperatures. A straight line is an indication of Poole-Frenkel emission in (a) and the Schottky effect in (b)

Table 6.5 Coefficient of barrier lowering for 400 device (no.4)

| T   | $\beta_{PF}$ ( $10^{-5}$ eV.m <sup>1/2</sup> .V <sup>-1/2</sup> )<br>(Forward bias)<br>voltage range<br>0.4-1.3 V | $\beta_{PF}$ ( $10^{-5}$ eV.m <sup>1/2</sup> .V <sup>-1/2</sup> )<br>(reverse bias)<br>voltage range<br>0.4-1.5 V | $\beta_S$ ( $10^{-5}$ eV.m <sup>1/2</sup> .V <sup>-1/2</sup> )<br>(Forward bias)<br>voltage range<br>0.4-1.3 V | $\beta_S$ ( $10^{-5}$ eV.m <sup>1/2</sup> .V <sup>-1/2</sup> )<br>(reverse bias)<br>voltage range<br>0.4-1.5 V |
|-----|---|---|--|--|
| 100 | 6.2±0.06  | 5.6±0.2   | 9±0.2  | 7.9±0.1  |
| 150 | 4.6±0.07  | 6.4±0.2   | 7±0.3  | 8.6±0.1  |
| 200 | 6±0.06  | 4.5±0.07  | 9.3±0.5  | 7.1±0.08   |
| 300 | 0.5±0.009   | 1±0.06  | 2.9±0.1  | 3.3±0.05   |
| 340 | 3.8±0.06  | 2±0.06  | 8 ±0.3   | 4.2±0.05   |
| 400 | 1.6±0.02  | 2.3±0.07  | 4±0.08   | 4.8±0.08   |
| 440 | 1.2±0.01  | 1.9±0.06  | 3.7±0.07   | 4.4±0.06   |
| 460 | 1.3±0.01  | 0.4±0.05  | 3.9±0.06   | 2.6±0.08   |

It is difficult to distinguish Schottky and the Poole-Frenkel emission mechanisms. Table 6.5 shows the coefficient of barrier lowering at different temperatures.

The dielectric constant  $\epsilon_s$  have been determined and listed in Table 6.6

Table 6.6 The estimated dielectric constant  $\epsilon_s$  from both plots.

| T   | From the plot $\ln I$ vs. $V^{1/2}$ |         | From the plot $\ln I/V$ vs. $V^{1/2}$ |         |
|-----|-------------------------------------|---------|---------------------------------------|---------|
|     | Forward                             | Reverse | Forward                               | Reverse |
| 100 | 0.28                                | 0.09    | 1.50                                  | 1.8     |
| 150 | 0.25                                | 0.12    | 2.7                                   | 1.4     |
| 200 | 0.27                                | 0.14    | 1.6                                   | 2.8     |
| 300 | 0.33                                | 0.18    | 2.3                                   | 57.5    |
| 340 | 0.48                                | 0.09    | 4                                     | 14.4    |
| 400 | 1.4                                 | 0.15    | 21.9                                  | 10.9    |
| 440 | 4                                   | 0.12    | 40                                    | 15.9    |
| 460 | 10                                  | 0.12    | 34                                    | 0.004   |

## 6.9 200 diameter device (no.6)

### 6.9.1 I-V Behaviour

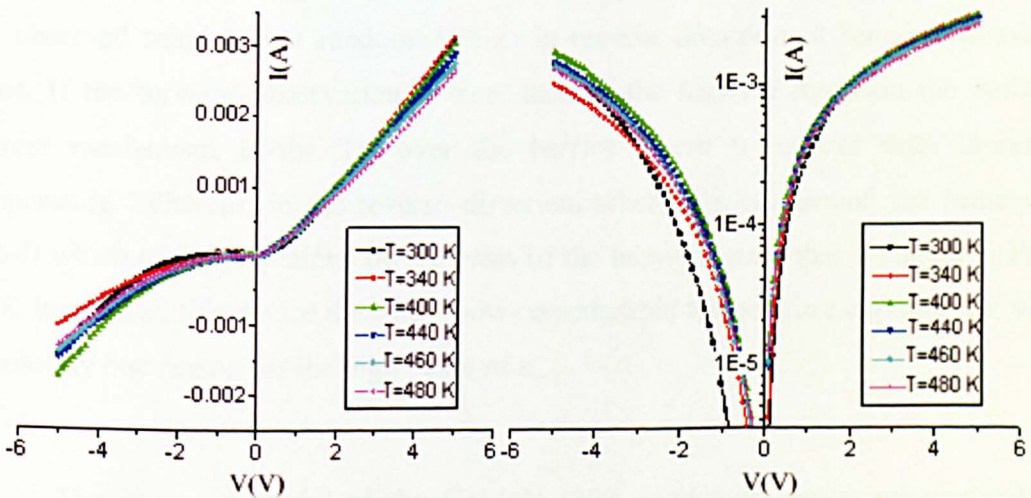


Figure 6.35 I-V characteristic of GaMnN device 200

For this device, the temperature does not have much effect on the current as shown in Figure 6.35.

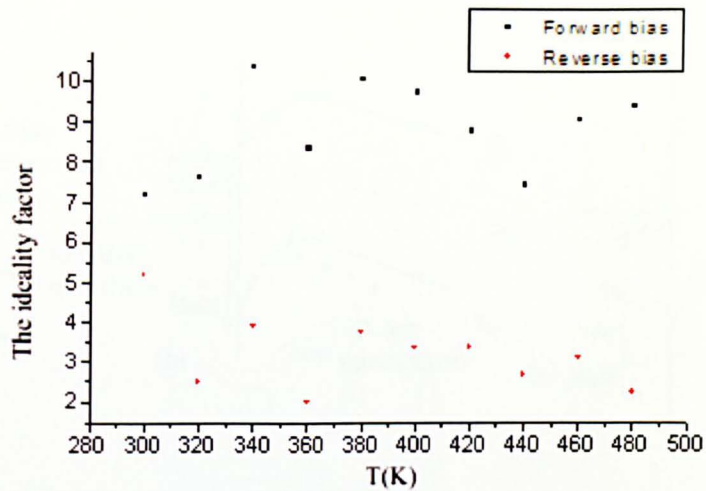


Figure 6.36 Variation of the ideality factor as a function of the temperature

The ideality factor ( $n$ ) which is the measure of the deviation from pure TE theory is shown in Figure 6.36. There appears to be a trend for the forward bias of  $n$  decreasing with increasing temperature but the experimental scatter of the data means the observed trend is just random. Whilst in reverse direction, it remains almost the same. If the forward observation is true, then in the forward direction the dominant current mechanism is the TE over the barrier where  $n$  reduces with increasing temperature. Whereas, in the reverse direction, where  $n$  stays around the same value ( $\sim 2-4$ ) which can be explained on the basis of the band diagram that is shown in Figure 6.38. In general, this device does not show considerable temperature dependence, which is possibly one reason for the high value of  $n$ .

The proposed model of the GaMnN (200 device) is shown schematically in Figure 6.37 along with the corresponding energy band diagram of a metal p-type semiconductor junction where the  $\Phi_m < \Phi_s$ . This gives an accumulation layer in the semiconductor and a positively charged metallic surface as is shown in Figure 6.37 (a). In forward direction Figure 6.37 (b), the holes will go either over the barrier or tunnel through the junction; at higher temperature at least, a significant TE will be observed from the semiconductor into the metal which will give a temperature dependent ideality factor. On the other hand, in reverse bias Figure 6.37 (c), the TFE mechanism will be dominant. The electrons tunnelling from semiconductor to the metal would correspond to a hole tunnelling from metal to semiconductor. This is largely a non-TE process and the value of the ideality factor would remain high.

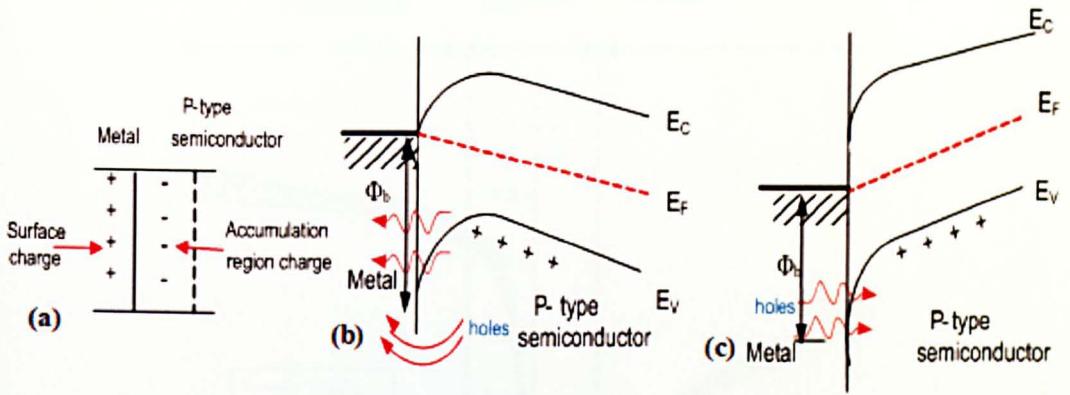


Figure 6.37 Energy band profile of the proposed model for the p-GaMnN; (a) schematic diagram for the depletion region (b) under applying “forward bias” on the semiconductor and (c) under applying “reverse bias” on the semiconductor

### 6.9.2 C-V Behaviour

The C-V pattern is shown in Figure 6.38. Although the qualitative features of the device are similar to those observed for the 800  $\mu\text{m}$  and 400  $\mu\text{m}$  device the temperature variation is considerably less than the other devices. This is one important general pattern which can be discerned from the three devices. The other is that the sharpness of the transition from the depletion to the accumulation region increases with reducing area of the devices. It will be later shown in the discussion that this is an important observation and may support the idea of the model of inhomogeneous Schottky contacts.

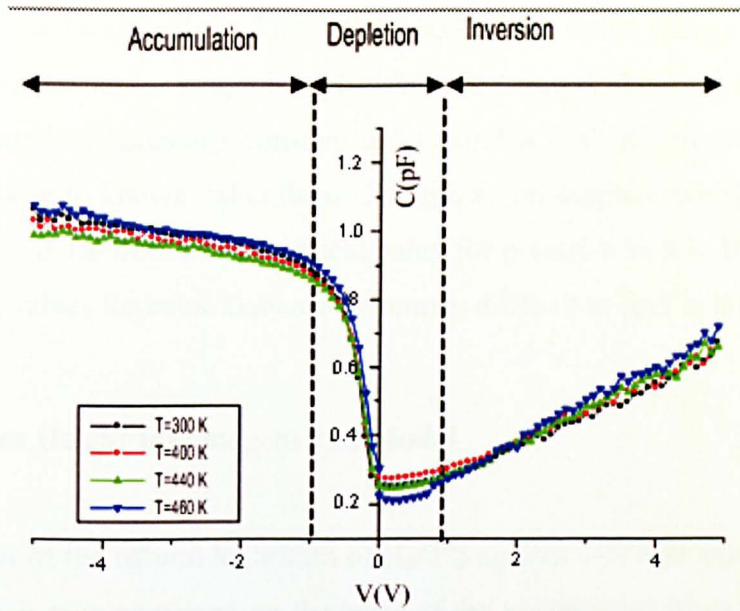


Figure 6.38 The capacitance versus voltage for 200 device

## 6.10 Interpretation of the $I$ - $V$ - $T$ results for 200 diameter device

### 6.10.1 Forward Bias

The data in the plot of  $\ln(I_S/T^2)$  against  $10^3/T$  in Figure 6.39 (a), was found to be non-linear. Like the other devices, the plot  $\ln(I_S/T^2)$  against  $10^3/nT$  does result in a straight line as shown in Figure 6.39 (b).

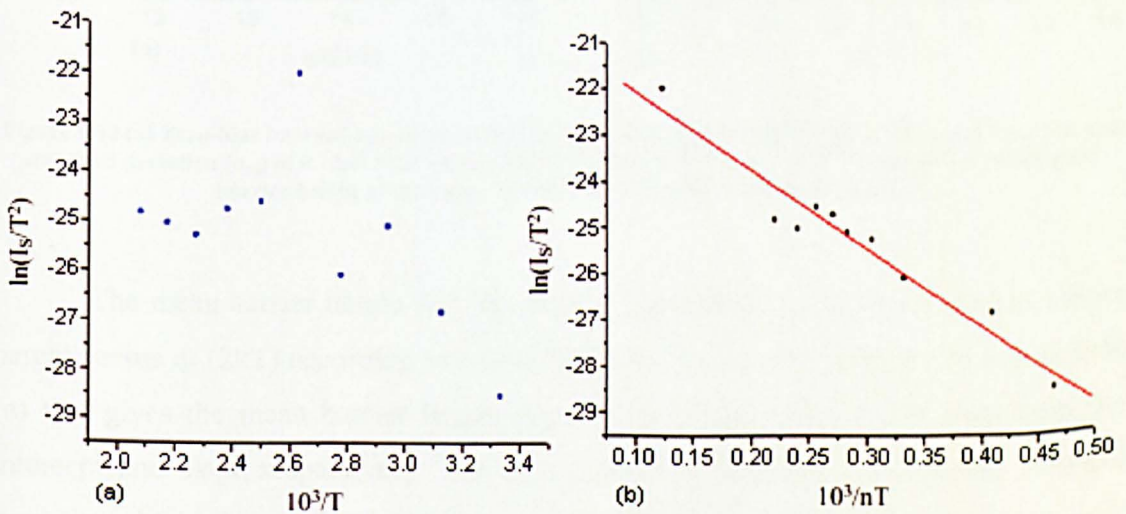


Figure 6.39 The activation energy plot: (a) Richardson plot  $\ln(I_S/T^2)$  and (b) Modified Richardson plot  $\ln(I_S/nT^2)$  in forward bias for 200 devices

The barrier height obtained from the modified activation energy plot is  $1.46 \pm 0.1$  eV. The value of the barrier height is higher than the theoretical barrier height value of 1 eV. The estimated Richardson's constant is  $20.4 \pm 0.4$  A cm<sup>-2</sup> K<sup>-2</sup> from Figure 6.39 (b). This value is close to known value for n-GaN grown on sapphire which is 26.4 A cm<sup>-2</sup> K<sup>-2</sup>. However, it is far from the theoretical value for p-GaN which is 103.8 A cm<sup>-2</sup> K<sup>-2</sup>. Corresponding values for cubic GaN are extremely difficult to find in literature.

### 6.10.1.1 Barrier Height Inhomogeneities Model

The plot of the natural logarithm of  $(I_S/T^2)$  against  $10^3/T$  do not show linearity. This behaviour is now examined on the basis of the assumption of inhomogeneities of the barrier height by using equation (2.28) to obtain the mean barrier height  $\Phi_{b0} \text{ (mean)}$  and the standard deviation of the barrier distribution  $\sigma_{s0}$ .

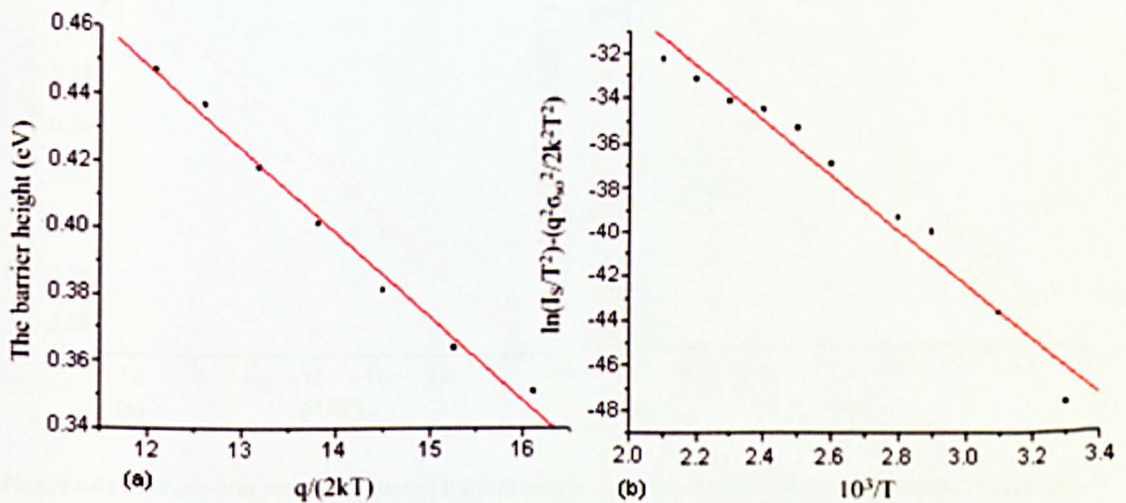


Figure 6.40 (a) Zero-bias forward apparent barrier height versus  $q/(2kT)$  plot with a value of  $0.75 \pm 0.016$  eV and standard deviation ( $\sigma_{s0}$ ) of  $0.16 \pm 0.0064$  eV and (b) Plot of  $\ln(I_S/T^2) - q^2 \sigma_{s0}^2 / 2k^2 T^2$  versus  $10^3/T$  which gives barrier height of the value  $1.06 \pm 0.067$  eV in case of the forward bias

The mean barrier height and the standard deviation  $\sigma_{s0}$  can be plotted as barrier height versus  $q/(2kT)$  according to equation (2.28). Such a plot is shown in Figure 6.40 (a) that gives the mean barrier height  $\Phi_{b0} \text{ (mean)}$  and the standard deviation from the intercept and slope respectively. The mean barrier height  $\Phi_{b0} \text{ (mean)}$  and the standard deviation obtained are  $0.75 \pm 0.016$  eV and  $0.16 \pm 0.0064$  eV respectively. This represents a 16% of the mean barrier height.

The modified Richardson plot relates the term  $[\ln [(I_S/T^2)] - q \sigma_{so}^2/2k^2T^2]$  to  $10^3/T$  [equation (2.34)]. The estimated barrier height which is the slope of Figure 6.40 (b) is  $1.06 \pm 0.067$  eV.

### 6.10.2 Reverse Bias:

The barrier height inhomogeneities model is also investigated in the reverse bias by plotting the barrier height versus  $q/(2kT)$  as shown in Figure 6.41 (a) which gives an indication of Gaussian distribution barrier height. The value of barrier height  $0.66 \pm 0.026$  eV by using equation (2.28) and the standard deviation with a value of  $0.15 \pm 0.012$  eV are shown plotted below.

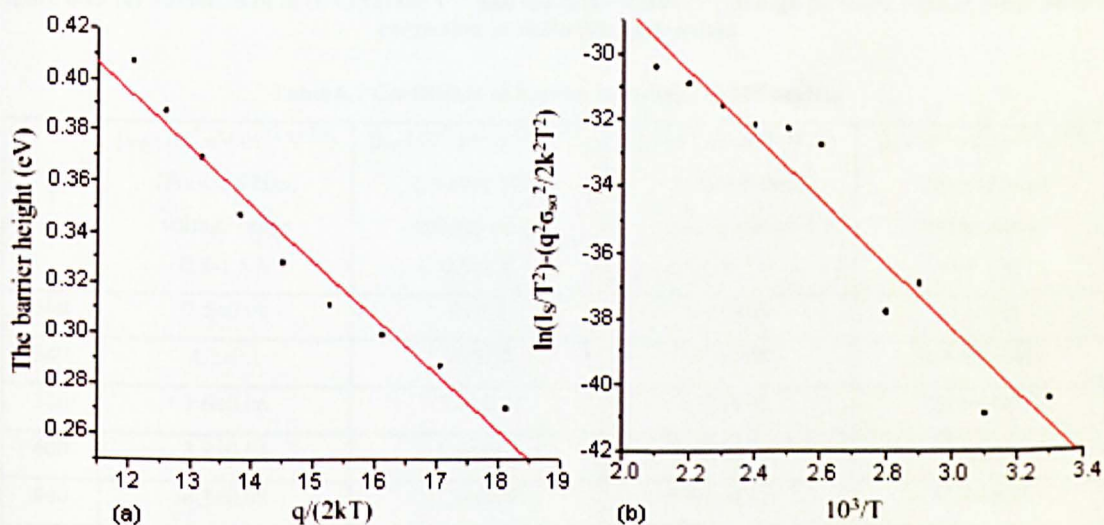


Figure 6.41 (a) Zero-bias reverse apparent barrier height versus  $q / (2kT)$  plot gives a value of  $0.66 \pm 0.026$  eV and standard deviation ( $\sigma_{s0}$ ) of  $0.15 \pm 0.012$  eV and (b) The barrier height  $\Phi_b = 0.79 \pm 0.067$  eV as obtained from equation (2.34) in case of reverse bias or 200 device

The modified plot of  $[\ln [(I_S/T^2)] - q \sigma_{so}^2/2k^2T^2]$  versus  $10^3/T$  (Figure 6.41 (b)) according to equation (2.34) should give a straight line and the slope yields the mean barrier height  $0.79 \pm 0.067$  eV with 17% of the mean barrier height.

### 6.10.3 The Insulator GaMnN layer

In the 200  $\mu\text{m}$  device,  $\ln(I)$  versus  $V^{1/2}$  (Schottky effect) and  $\ln(I/V)$  versus  $V^{1/2}$  (Poole-Frenkel) plots are found to be straight line with good correlation coefficient after

the  $R_s$  correction. These are shown in Figure 6.42 and the values of the slopes are listed in Table 6.7 for both polarities in the case of Poole-Frenkel emission mechanism and Schottky effect.

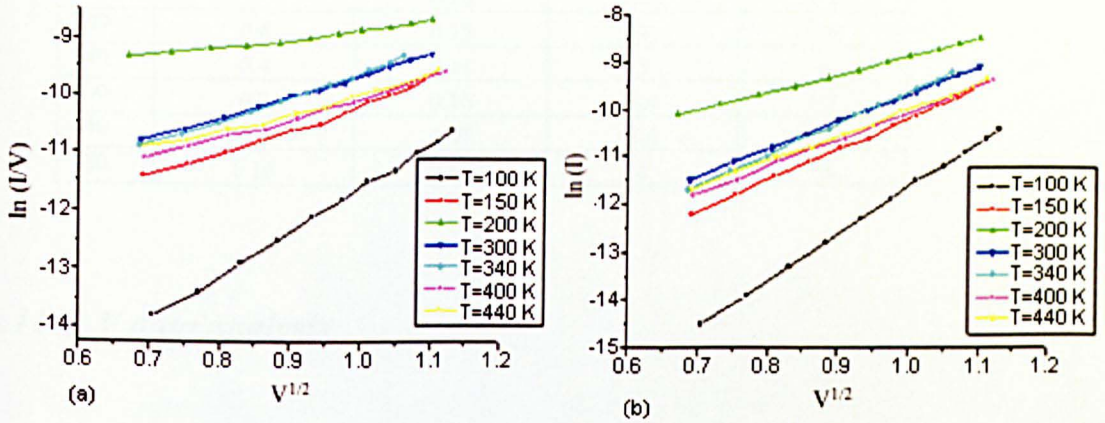


Figure 6.42 (a) Variation of  $\ln(I/V)$  versus  $V^{1/2}$  and (b)  $\ln(I)$  versus  $V^{1/2}$  in high forward voltage range after  $R_s$  correction at various temperatures

Table 6.7 Coefficient of barrier lowering for 200 devices

| T   | $\beta_{PF}$ ( $10^{-5}$ eV.m <sup>1/2</sup> .V <sup>-1/2</sup> ) | $\beta_{PF}$ ( $10^{-5}$ eV.m <sup>1/2</sup> .V <sup>-1/2</sup> ) | $\beta_S$ ( $10^{-5}$ eV.m <sup>1/2</sup> .V <sup>-1/2</sup> ) | $\beta_S$ ( $10^{-5}$ eV.m <sup>1/2</sup> .V <sup>-1/2</sup> ) |
|-----|---|---|--|--|
|     | (Forward bias)<br>voltage range<br>0.5-1.5 V                      | (reverse bias)<br>voltage range<br>0.3-1 V                        | (Forward bias)<br>voltage range<br>0.5-1.5 V                   | (reverse bias)<br>voltage range<br>0.3-1 V                     |
| 300 | 7.5±0.08  | 6±0.2   | 9.6±0.05   | 9.2±0.3  |
| 340 | 4.2±0.1   | 7±0.09  | 6.6±0.06   | 10.5±0.11491   |
| 380 | 1.6±0.06  | 5.6±0.1   | 3.8±0.03   | 9.6±0.07   |
| 400 | 3.8±0.04  | 5.9±0.07  | 5.9±0.04   | 9.8±0.04   |
| 440 | 4.3±0.08  | 7.6±0.09  | 6.7±0.07   | 11.4±0.08  |
| 460 | 3.6±0.09  | 5.8±0.09  | 5.8±0.06   | 9.5±0.1  |
| 480 | 3.3±0.1   | 6.3±0.1   | 5.5±0.09   | 14±0.2   |

The dielectric constant  $\epsilon_s$  have been determined and listed in Table 6.8 at various temperatures. It is observed from Table 6.8 that there is a reasonable agreement between the values of the dielectric constant  $\epsilon_s$  obtained from  $\ln(I/V)$  versus  $V^{1/2}$  plot rather than  $\ln(I)$  versus  $V^{1/2}$  plot.

Table 6.8: The estimated dielectric constant  $\epsilon$ , from both plots.

| T   | From the plot $\ln I$ vs. $V^{1/2}$ |         | From the plot $\ln I/V$ vs. $V^{1/2}$ |         |
|-----|-------------------------------------|---------|---------------------------------------|---------|
|     | Forward                             | Reverse | Forward                               | Reverse |
| 100 | 0.16                                | 0.17    | 1.02                                  | 1.6     |
| 150 | 0.33                                | 0.13    | 3.2                                   | 1.17    |
| 200 | 1                                   | 0.16    | 22.5                                  | 1.8     |
| 300 | 0.4                                 | 0.15    | 4                                     | 1.6     |
| 340 | 0.4                                 | 0.11    | 3                                     | 1       |
| 400 | 0.3                                 | 0.16    | 4.4                                   | 1.7     |
| 440 | 0.4                                 | 0.07    | 5.3                                   | 1.45    |
| 480 | 0.16                                | 0.17    | 1                                     | 1.6     |

### 6.11 C-V data analysis

The observed C-V behaviour of GaMnN for 800 devices (no.2) (Figure 6.14), 400 device (no.4) (Figure 6.29) and 200 device (no.6) (Figure 6.38) could be explained on the basis of the metal-insulator-semiconductor or a metal-oxide-semiconductor (MIS/ MOS) structure (Figure 6.43). As the gate of the MIS/ MOS structure is varied from negative through zero to a positive voltage, the charge in the semiconductor layer below oxide is strongly affected. Not only does the density of charge change but there is also a reversal in sign. Assuming there is an insulating layer between the considering p-type semiconductor and the metal Schottky contact, the Schottky contact will then be similar to the Gate of a MIS structure. When the Schottky contact (Gate) is forward biased, the voltage on the contact is negative with respect to the semiconductor and this will attract hole towards the insulator/semiconductor interface and accumulation will occur as shown in Figure 6.43 (a). The holes are separated from the metal contact by a fixed distance and so the capacitance should be approximately constant.

As the gate voltage is reduced, and there is no accumulation of holes, the depletion region will extend and the capacitance will decrease. On the other hand, as the gate potential is made positive a negatively charged layer is formed beneath the oxide- this is the inversion layer- and the capacitance increases as the gate is made more positive (under reverse bias condition as shown in Figure 6.43 (b)).

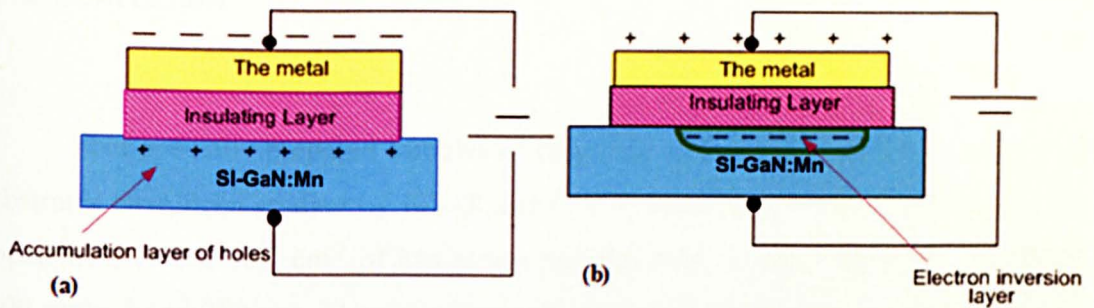


Figure 6.43 The explanation of the behaviour of GaMnN samples on the basis of MOS capacitor under (a) forward bias and (b) reverse bias.

A similar  $C-V$  behaviour can also be explained by the existence of the interfacial surface states as shown in Figure 6.44. According to Monch [141] the surface states play a dominant role. These states are characterized by a charge neutrality level (CNL). Interfacial states are considered acceptor type above Fermi level  $E_F$  and donor type below  $E_F$ . As  $E_F$  moves upward towards the conduction band, these states trap electrons which make the surface negative Figure 6.44 (a), whereas a downward movement of the  $E_F$  causes the donor type states to lose electrons and acquire a positive charge Figure 6.44 (b). Consequently, the charge density on the surface will increase either way as the  $E_F$  moves towards the band edges causing the capacitance to increase. The density of trapped charge and the resultant capacitance will depend upon the distribution of these interfacial states in the bandgap.

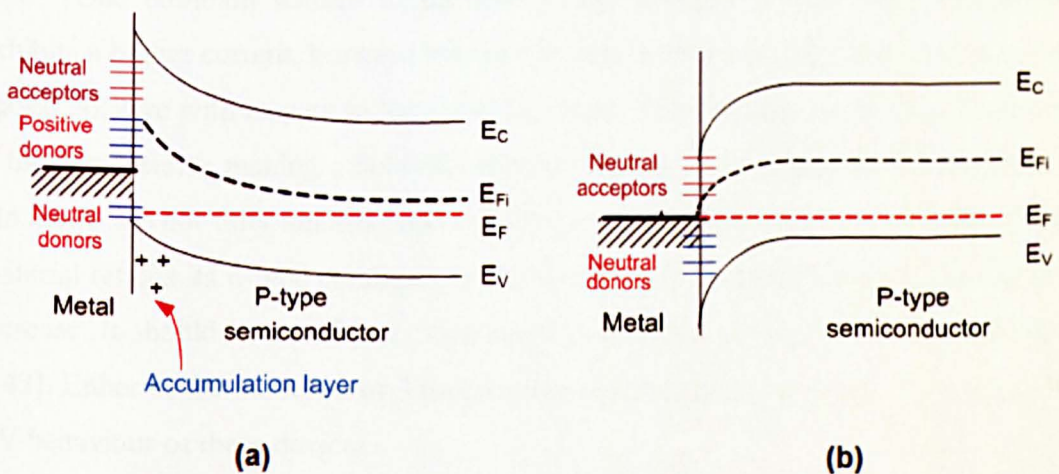


Figure 6.44 The energy band diagram of the metal- semiconductor in case of existing interfaces state under (a) in accumulation, and (b) at mid- gap [7]

## 6.12 Conclusion

Four specially prepared samples of epitaxially grown cubic GaMnN on SI-GaAs substrates have been studied by I–V–T and C–V–T techniques. Cubic GaN layers were doped with  $7\text{--}8 \times 10^{17} \text{ cm}^{-3}$  of Mn atoms and the devices had a diameter of 800  $\mu\text{m}$ , (400  $\mu\text{m}$ ) $\times$  2 and 200  $\mu\text{m}$ . The geometry and details of the samples are given in section (6.1). In these devices GaN: Mn was the active layer with Schottky and Ohmic contacts on the top.

The I–V performance of the device is determined by the GaN: Mn layer and such layers are expected to be p-type. However, it has been suggested that only a fraction of the Mn atoms may be electrically active and may compensate the u.i.d. n-type behaviour of GaN [142]. The nature of the Schottky contact is determined by the “conductivity type” of GaN layer near the surface and there is a considerable degree of uncertainty here since Mn atoms tend to migrate to the surface. Under such uncertain conditions, any interpretation of electrical behaviour would be based on “informed speculations” obtained from experimental evidence.

### 6.12.1 Model to explain I–V behaviour of GaN: Mn

One common feature of the I–V–T characteristic is that the “forward bias” exhibits a higher current. Forward bias in this case is defined as the top Schottky contact biased positive with respect to the GaN: Mn layer. One obvious conclusion to be drawn is that the metal is making a Schottky contact with an n-type material. This implies that Mn atoms are not fully ionized and even after compensation of the u.i.d. n-type GaN the material retains its n-type conductivity, although it is expected that its resistivity would increase. It should be noted that “nominally undoped” GaN layers are strongly n-type [142]. Either of the models 2 or 3 proposed in section (6.2) can possibly account for the I–V behaviour of these devices.

All I–V–T characteristics exhibit a straight line for  $\ln(I/V) - V^{1/2}$  plots for voltage range above 2–3 V for both directions of biases. On the basis of models 2 or 3 the

observed behaviour can be explained on the basis of the barrier “lowering mechanism” or on a P.F. mechanism.

### 6.12.1.1 Forward bias

In forward bias, the current is the thermionic, and carriers are injected over the barrier from the semiconductor into the metal. The transport of carriers in the semiconductor is determined by the Poole-Frenkel type centres in the compensated region (the near insulating region). The logarithm of current will be proportional to temperature and to  $V^{1/2}$  that is observed in all samples except (400 device no.3) which shows an Ohmic character. Using the forward characteristic the ideality factor and the barrier height has been determined at various temperatures. It has been found that the ideality factor decreases with temperature and the barrier height increases with temperature.

Plotting the Richardson’s relation  $\ln(I_s/T^2)-10^3/T$  the barrier height can be determined. However, such plots do not give a straight line indicating that the barrier height is changing with temperature. There is another way of looking at the barrier height which is reduced due to TFE modified Richardson’s relation  $\ln(I_s/T^2)-10^3/nT$  when plotted gives straight line and from the slope the barrier height is obtained. The barrier height determined from the forward I–V–T characteristics for 800  $\mu\text{m}$ , (400  $\mu\text{m}$ ) and 200  $\mu\text{m}$  samples are  $1.14\pm 0.065$  eV,  $1.6\pm 0.098$  eV and  $1.46\pm 0.1$  eV respectively, and are shown in Table 6.9. The homogeneity of the barrier heights across the surface of the contact has been calculated using equation (2.34). This relationship has already been explained in detail in chapter (3). The mean values of the barrier heights are determined and the standard deviations are given in Table 6.9. All samples give a standard deviation of nearly 0.1 eV over the mean value. This has been calculated as around 16% the mean value. It should be noted that a lower value of standard deviation gives a more homogenous contact. A large variation is an indication of a poor material surface and/or material’s quality. It is not only due to the fact that Mn migration to the surface [143] modifying its character but also to the non uniformity (thickness) of the GaN:Mn layer which may contribute to this lateral inhomogeneity as can be seen from the TEM image in Figure (6.2).

Table 6.9 The size, barrier height and the standard deviation of the devices under study

| Size                | The barrier height $[(I_s/T^2)]$ vs. $10^3/T$ | The barrier height $[(I_s/AT^2)]$ vs. $10^3/nT$ | The barrier height $[\ln[(I_s/T^2)] - q\sigma_{so}^2 / 2k^2T^2]$ vs. $10^3/T$ | The mean barrier height $[\Phi_{bo(mean)}]$<br>$\Phi_b = \Phi_{b0(mean)} - \frac{q\sigma_{s0}^2}{2kT}$ | The standard deviation ( $\sigma_{s0}$ ) |
|---------------------|---|---|---|--|--|
| 800 (Forward)       | 0.37 ± 0.03 eV                                | 1.14 ± 0.06 eV                                  | 0.38 ± 0.02 eV  | 0.6 ± 0.01 eV  | 0.1 ± 0.0005 eV                          |
| 400(no.3)           | Ohmic   |   |   |  |  |
| 400(no.4) (forward) | Not linear                                    | 1.61 ± 0.09 eV                                  | 0.96 ± 0.05 eV  | 1 ± 0.03 eV  | 0.17 ± 0.01 eV                           |
| 200 (Forward)       | Not linear                                    | 1.46 ± 0.1 eV                                   | 1.06 ± 0.06 eV  | 0.75 ± 0.016 eV  | 0.16 ± 0.006 eV                          |

### 6.12.1.2 Reverse bias

All the devices studied exhibit a soft reverse characteristic over the full temperature range. The  $\ln(I)-V^{1/2}$  plots for these devices are linear giving a strong indication of a barrier lowering type mechanism. This can be either the Schottky lowering of the barrier at the metal-semiconductor interface or a Poole-Frenkel type mechanism in the bulk as shown in Figure 6.45. The process can be understood with reference to the proposed model.

At low applied biases and at higher temperatures electrons are injected from the reversed biased Schottky contact by thermionic emission over the barrier into the semiconductor. Their transport is limited by a Poole-Frenkel type process. It should be noted that the thermionic-field emission probability from the Poole-Frenkel centres increases with applied field (Figure 6.46).

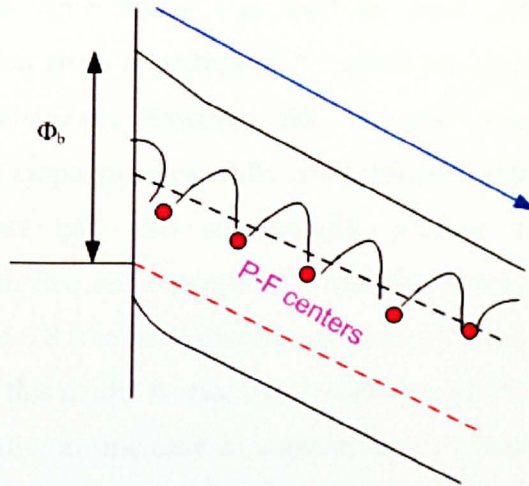


Figure 6.45 The P-F centres in the compensated layer below the Schottky contact

The possibility of direct tunnelling from either the Schottky contact or the Poole-Frenkel centres to the conduction band of the semiconductor appears unlikely when it is noted that the maximum field at the highest of voltages (5 V) is ( $5/0.6 \times 10^{-6} \sim 0.8 \times 10^6 \text{ Vcm}^{-1}$ ) which is given below the threshold of the direct tunnelling.

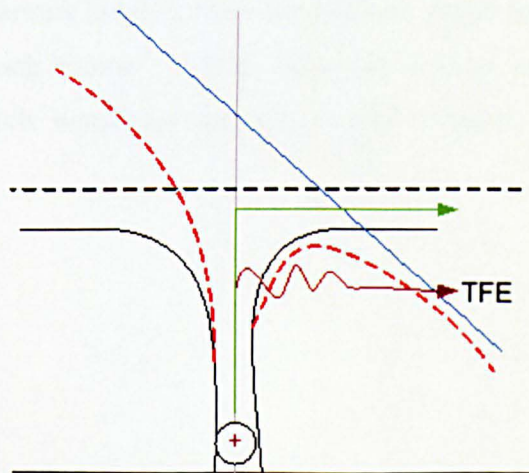


Figure 6.46 The lowering of the barrier height due to high field for a P-F centre

### 6.12.2 Model to explain C-V response of GaN: Mn

The C-V measurements on all GaN: Mn doped samples exhibit a behaviour which is qualitatively similar. The important points have been discussed in section (6.11). It is imperative that the same model be used to explain the I-V-T and C-V-T

behaviour. Since the same device was used for both measurements. A number of explanations have been given in section (6.11) which could account at least qualitatively for the observed behaviour. However, the “chosen” model to explain the I-V-T measurements which employs a near fully compensated (almost insulating) layer below the Schottky contact can also successfully account for the observed C-V-T characteristics. The device corresponds to a MIS/MOS structure and this is shown in Figure 6.6 and Figure 6.8 (the band diagram of model (2) and model (3)). It can be seen in section (6.11) that this model is successful in explaining the salient features of C-V-T performance. Generally, an increase in capacitance is observed with temperature and voltage. Such an increase has been attributed to an increased charge. It is postulated that the Poole-Frenkel centres in the near insulating region become progressively more ionized with temperature and increasing field (voltage) due to an increased thermal emission probability and a reduced potential barrier.

The inhomogeneous barrier height model may also be able to account for the “apparent random variation” in capacitance as a function of temperature as observed in these samples. Since the net capacitance will be a sum of all parallel capacitances under Schottky contacts of various heights, their temperature dependence would depend upon the relative areas of each “patch”. Additionally, the density and nature of the surface states under each patch would govern the overall temperature dependence which remains unpredictable.

## CHAPTER 7 General Conclusions

### *7.1 Introduction*

Electrical properties of devices fabricated using cubic GaAs and cubic GaN have been studied by the I-V-T, C-V-T and C-F-T methods over a wide temperature range.

### *7.2 GaMnAs devices*

For the case of p n junction devices fabricated on cubic GaAs substrate and employing a Mn doped epi-layer a detailed interpretation of current transport is given in chapter 5. This is based on the existence of two junctions one at the back between Si doped n-type and the Mn doped p-type cubic GaAs and the other on top between Mn doped GaAs and the metal contact.

The I-V-T behaviour has been interpreted on the basis of a band diagram which has been calculated from a simulation program. This however, has been done on the assumption that GaAs: Mn doped epi-layer is crystalline. This is an over simplification since the epi-layers were grown at low temperature. Additionally, the Mn doped layers with three different concentrations were all grown at different temperatures making the comparison between layers difficult. It is necessary to grow these films at low temperature to avoid the formation of “additional” phases such as MnAs which are thermodynamically more stable. These phases create defects which tend to compensate Mn acceptors and reduce p-type conductivity.

The growth at low temperature however, has other advantages: the solubility limit of Mn in GaAs increases making it possible to dope higher concentration of Mn and there is a reduction in the segregation of Mn to the surface [49].

On the other hand, films grown at low temperatures contain a large number of defects e.g. As antisites and Mn interstitials; both of which act as deep donors and can compensate p-type conductivity of GaAs: Mn films. It is desirable to have a low density of defects and high crystalline quality [123].

Since Mn is a deep acceptors in GaAs (112 meV [121]), the carrier concentrations in the Mn doped GaAs epi-layers are a function of temperature. This will affect the nature of the GaAs: Mn interfaces with both the Si doped layer and metal contact. Keeping in view the “poor” structural quality of the films, the I-V-T behaviour is difficult to explain on the basis of any single mechanism in one specimen and even more uncertain between the samples grown at different temperatures. It appears, however, that the p n junction between Si doped GaAs and Mn doped GaAs behaves like a backward diode whereas the top contact behaves like a Schottky contact.

The Schottky contact was analysed using the modified Richardson plots. It was found that the plots became straight lines when  $\ln(I_s/T^2)$  was plotted against  $10^3/nT$ . indicating an increase in the TFE component as the temperature is reduced. It should be noted that  $n$  increases and  $\Phi_b$  decreases with decreasing temperature. On the other hand, the p n junction is between a degenerate n-type GaAs and a near degenerate p-type GaAs. It is postulated that this junction behaves like a backward diode and gives a high value of  $\Phi_b$  which is nearly equal to the band gap of GaAs (1.42 eV). However, the behaviour of this junction can be explained on the basis of either a Schottky contact or a  $p n^+$  junction. All experimental evidence indicates the presences of a Schottky contact. However, the same value of 1.4 eV can also be obtained from the forward diode I-V characteristics of this contact. No definite conclusion can be made. At least the major parameters obtained from the I-V-T of the characteristics can be adequately accounted for on this basis.

Following the same model, the C-V-T behaviour would be that of two back-to-back contacts. The net measured capacitance would be the series addition of the capacitances of the two contacts. This is the qualitatively observed response of all samples.

The admittance spectroscopy measurements gave the activation energy of  $0.117 \pm 0.005$  eV for the sample with the highest dopant concentration ( $10^{21}/\text{cm}^3$ ) which was similar to the activation energy of Mn in GaAs. The samples with lower concentration gave a value nearly half this value. The reason for the difference can not be explained.

### 7.3 GaMnN devices

Low temperature (LT) epitaxially grown cubic GaN layers doped with Mn were studied by making Schottky contacts. The layer had a Mn concentration of  $7-8 \times 10^{17}/\text{cm}^3$ . Both, the Ohmic and the Schottky contacts were deposited on the surface. The layers were grown on a cubic GaAs substrate.

In this case, the material's quality was also highly suspect. LT grown GaN layers had been studied for the structural quality by a number of workers [64, 144-146]. The general observation is that LT grown films have a "large number of structural faults, a rough surface morphology, voids in the buffer layer and pyramidal inclusions having dimension of  $\sim 100$  nm extending into the buffer layer" [64].

Since Mn has a limited solubility in GaN, Mn diffuses towards GaAs substrate forming a MnAs phase. Mn also diffuses/segregates toward the surface and builds up as a layer of Mn on top [64]. It is this layer that has an important bearing on the contacts to the surface.

At least one device studied for I-V-T characteristics exhibits the Ohmic behaviour which is possibly due to a conducting sheet on the surface. The other three devices exhibit Schottky type behaviour. On the basis of the proposed model the other parameters calculated from the I-V-T measurements indicate that a TFE mechanism dominates. This is borne out by the modified Richardson plots.

The current is limited by  $\ln(I)-V^{1/2}$  law. This can be due either to Schotky or Poole-Frenkel (P.F.) type mechanism. It has always been difficult to distinguish between these mechanisms. However, in the present case it is postulated that P.F.

centres dominate the current transport since it is expected to occur in insulating materials. A region of high resistance is likely to exist just beneath the surface due to the out migration of Mn atoms leaving a “compensated” region of high resistivity behind.

For the case of capacitance measurements, the C-V-T behaviour is similar to that of the MIS structure. The insulating layer results from the compensation/or out migration of Mn atoms. Such a model appears to be compatible with the P.F. type conduction observed in the I-V-T response.

The increase in capacitance is attributed to an increase in charge. The existence of P.F. centres in the insulating region and their subsequent ionization with temperature and increasing voltage (field) would create additional charge responsible for the increase in capacitance.

However, a similar C-V-T behaviour will also be observed if the existence of interfacial states is taken into account. A high density of surface states is expected to be present in a highly defective material. The situation will be compounded by the fact that Mn atoms migrate to the surface as well [143].

The density of interfacial states will not be uniform on the surface due to the presence of localized defects. This will lead to a non uniform Schottky contact. The situation is described by the “inhomogeneous barrier height model”. It has been observed in some devices that the capacitance varies randomly with temperature. This may be due to different “patches” of the Schottky contact contributing their capacitances separately-which will eventually add up in parallel. Their temperature dependence however, remains unpredictable.

The C-F-T measurements for GaMnN samples show that there is no change of capacitance with frequency. Consequently, no information can be obtained from these measurements.

### ***7.4 General conclusion***

It is therefore, concluded that I-V-T and C-V-T measurements on LT grown Mn doped epi-layers give some general trends. Any precise conclusion is difficult to make. This is due to the poor quality of the epi-layers which had a large number of defects, dislocation and voids. In case of GaAs films, it is difficult to make any direct comparison between films as they were all grown at different temperatures. Only one GaN layer was used for making Schottky contacts of different diameters. Here again the lateral homogeneity of the film was questionable.

Better quality of films and more controlled growth techniques are required if LT grown films of GaAs and GaN are to yield more reproducible results.

## REFERENCES

1. T. Dietl, H. Ohno, F. Matsukura, J. Cibert, and D. Ferrand, *Zener Model Description of Ferromagnetism in Zinc-Blende Magnetic Semiconductors*. Science, 2000. **287**: p. 1019.
2. T. Dietl, H. Ohno, and F. Matsukura, *Hole-mediated ferromagnetism in tetrahedrally coordinated semiconductors*. Phys. Rev. B 2001. **63**: p. 195295.
3. H. Ohno, A. Shen, F. Matsukura, A. Oiwa, A. Endo, S. Katsumoto, and Y. Iye, *(Ga,Mn)As: A new diluted magnetic semiconductor based on GaAs*. Applied Physics Letters, 1996. **69**: p. 363.
4. K.W. Edmonds, S.V. Novikov, M. Sawicki, R.P. Campion, C.R. Staddon, A.D. Giddings, L.X. Zhao, K.Y. Wang, T. Dietl, C.T. Foxon, and B.L. Gallagher, *P-type conductivity in cubic (Ga,Mn)N thin films*. Applied Physics Letters 2005. **86**: p. 152114.
5. Zaja,c, R.Doradzinki, J.Gosk, J.Szczytko, M.Lefeld-Sosnowska, M.Kaminska, A.Twardowski, M.Palczewska, E.Grzanka, and W.Gebicki, *Magnetic and optical properties of GaMnN magnetic semiconductor*, Applied Physics Letters, 2001. **78**(9): p. 1276-1278.
6. S.M. Sze, *Physics of semiconductor devices*. 1981, New York: Wiley sons.
7. D. Neamen, *Semiconductor Physics and Devices*. Third ed. 2003, New York: Mc Graw Hill.
8. E.H. Rhoderick, *Transport processes in Schottky diodes*. Institute of physics conf., 1974. Ser.No.22: p. 3-19.
9. W. Monch, *Semiconductor surface and interfaces*. 3 ed. Springer Series in Surface Sciences, ed. G. Ertl, Lüth, Hans, Mills, Douglas L. Vol. 26. 2001: Springer.
10. S.M. Sze, *Physics of semiconductor devices*. 1969, New York: A Division of John Wiley & sons.
11. S. Aydogan, M.Saglam, and A.Turut, *The effects of the temperature on the some parameters obtained from current-voltage and capacitance-voltage Characteristics of polypyrrole/n-Si structure* Polymer, 2005. **46**: p. 563-568.
12. J.F. Bobo, S. Couderc, A. Arnoult, C. Fontaine, and R. Mamy, *Comparative I(V) study of pure Schottky contacts used in spin-LEDs*. Solid-State Electronics, 2004. **48**(5): p. 845-849.
13. E.H. Rhoderick, *Metal-semiconductor contacts*. 1978, Oxford: Oxford University press.
14. A.M. Rodrigues, *Analysis of the current-transport mechanism across a CVD diamond/silicon interface*. Applied Surface Science 2007. **253**: p. 5992-5999.
15. F.A. Padovani and R.Stratton, *Field and thermionic-field emission in Schottky barriers*. Solid State Electronics, 1966. **9**: p. 695-707.
16. Y. Kribes, I. Harrison, B. Tuck, T.S. Cheng, and C.T. Foxon, *Investigation of Au Schottky contacts on GaN grown by molecular beam epitaxy*. Semicond. Sci. Technol., 1997. **12**: p. 913-916.
17. R.T. Tung, *Recent advances in Schottky barrier concepts*. Materials Science and Engineering, 2001. **R 35**: p. 1-138.
18. J.H. Werner and H.H. Gijttler, *Barrier inhomogeneities at Schottky contacts*. J. Appl. Phys., 1991. **69**(3): p. 1522-1533.

19. Y. Kribes, *Electrical and Optical Characterisation of GaN Grown by MBE*, in *Electrical and Electronic Engineering*. 1998, University of Nottingham.
20. W. Mtangi, F.D. Auret, C. Nyamhere, P.J. Janse van Rensburg, and C.M.D. A., *Analysis of temperature dependent I-V measurements on Pd/ZnO Schottky barrier diodes and the determination of the Richardson constant*. *Physica B: Condensed Matter*, 2009. **404**(8-11): p. 1092-1096.
21. L.J. Brillson, *Contacts to semiconductors fundamentals and technology*. 2007, New Jersey,USA: Noyes.
22. N.P. Harde, P.P. Altermatt, and D.H. Neuhaus. *Discussion of recombination current mechanisms at grain boundaries in the bulk: a simplified model*. in *Photovoltaic Specialists Conference. Conference Record of the Thirty-first IEEE* 2005.
23. Y. Kribes, I. Harrison, B. Tuck, T.S. Cheng, and C.T. Foxon, *Electrical properties of n-GaN/n<sup>+</sup>-GaAs interfaces*. *Journal of Crystal Growth*, 1998. **189-190**: p. 773-777.
24. L.J. Brillson, *Contacts to Semiconductors: Fundamentals and Technology*. 1993, New Jersey: William Andrew Inc.
25. K. Maeda, *Defect causing nonideality in nearly ideal Au/Si Schottky barrier*. *Applied Surface Science*, 2000. **159-160**: p. 154-160.
26. N.Jensen, U.Rau, M.Hausner, S.Uppal, L.Oberbeck, and R.B.Bergmann, *Recombination mechanisms in amorphous silicon/crystalline silicon hetero junction solar cells* 2000. **87**(5): p. 2639-2645.
27. M. Biber, *Low-temperature current-voltage characteristic of MIS Cu/n-GaAs and inhomogeneous Cu/n-GaAs Schottky diodes*. *Physica B*, 2003. **325**: p. 138-148.
28. S. Karatas and S. Altındal, *Analysis of I-V characteristics on Au/n-type GaAs Schottky structures in wide temperature range*. *Materials Science and Engineering B* 2005. **122**: p. 133-139.
29. E.H. Rhoerick and R.H. Williams, *Metal-Semiconductor contacts*. second ed. 1988, Oxford: Oxford Science publications.
30. H. Korkut, N.Yildirim, and A.Turut, *Temperature-dependent current-voltage characteristic of Cr/n-GaAs Schottky diodes*. *Microelectronic Engineering*, 2009. **86**: p. 111-116.
31. A. Gumus, A.Turut, and N.Yalcin, *Temperature dependent barrier characteristic of CrNiCo alloy Schottky contacts on n-type molecular- beam epitaxy GaAs*. *Journal of applied physics*, 2002. **91**(1): p. 245-249.
32. H. Korkut, N.Yildirim, and A.Turut, *Thermal annealing effects on I-V-T characteristic of sputtered Cr/n-GaAs diodes*. *Physica B*, 2009. doi:10.1016/j.physb.2009.07.156.
33. A. Bengi, S. Altındal, S. Özçelik, S.T. Agaliyeva, and T.S. Mammadov, *Analysis of temperature dependent electrical characteristics of Au/n-GaAs/GaAs structures in a wide temperature range*. *Vacuum*, 2009. **83**(2): p. 276-281.
34. J. Singh, *Semiconductor devices an introduction*. 1990, New York: McGraw-Hall, Inc.
35. P. Blood and J.W. Orton, *The Electrical Characterization of Semiconductors :Majority Carriers and Electron States*. 1992: Academic Press.
36. D.L. Losee, *Admittance spectroscopy of deep impurity levels: ZnTe Schottky barriers*. *Applied Physics Letters*, 1972. **21**.
37. H.G. Svavarsson, J.T.Gudmundsson, and H.P.Gislason, *Lithium-diffused and annealed GaAs: An Admittance spectroscopy study*. *Physical Review B*, 2004. **69**: p. 155209.

38. D.L. Polla and C.E.Jones, *Admittance spectroscopy of deep levels in  $Hg_{1-x}Cd_xTe$* . J. Appl. Phys, 1980. **51**(12): p. 6233-6237.
39. Y. Tokuda and A. Usami, *Admittance studies of neutron-irradiated Silicon  $P^+-n$* . J. Appl. Phys, 1977. **84**(4): p. 1668-1672.
40. Y.M. Hounq and G.L.Pearson, *Deep trapping effects at the GaAs-GaAs : Cr interface in GaAs FET structure* J. Appl. Phys, 1978. **49**(6): p. 3348-3352.
41. N.H. Hong, *Ferromagnetism in transition-metal-doped semiconducting oxide thin films*. Journal of Magnetism and Magnetic Materials 2006. **303**: p. 338-343.
42. H. Katayama-Yoshida and K. Sato, *Spin and charge control method of ternary II-VI and III-V magnetic semiconductors for spintronics: theory vs. experiment*. Journal of Physics and Chemistry of Solids, 2003. **64**(9-10): p. 1447-1452.
43. H. Ohno, *Making Nonmagnetic Semiconductors Ferromagnetic*. Science, 1998. **281**: p. 951.
44. I. Zutic, J. Fabian, and S.D. Sarma, *Spintronics: Fundamental and applications* Review of Modern Physics 2004. **76**: p. 323-410.
45. T. Jungwirth, J. Mašek, K.Y. Wang, K.W. Edmonds, M. Sawicki, M. Polini, J. Sinova, A.H. MacDonald, R.P. Campion, L.X. Zhao, N.R.S. Farley, T.K. Johal, G.v.d. Laan, C.T. Foxon, and B.L. Gallagher, *Low-temperature magnetization of (Ga,Mn)As semiconductors*. Phys Rev B, 2006. **73**: p. 165205.
46. J.F. Xu, P.M. Thibado, C. Awo-Affouda, R. Moore, and V.P. LaBella, *Atmospheric oxygen in Mn doped GaAs/GaAs(0 0 1) thin films grown by molecular beam epitaxy*. Journal of Crystal Growth 2007. **301-302**: p. 54-57.
47. S. Lee, S.J. Chung, X. Liu, and J.K. Furdyna, *Doping Effect on the Properties of III-V Ferromagnetic Semiconductor GaMnAs Epilayers and Their Superlattices*. Journal of the Korean Physical Society, 2005. **47**(3): p. 444-447.
48. K. Yanagisawa, S. Takeuchi, H. Yoshitake, K. Onomitsu, and Y. Horikoshi, *Enhanced magnetization by modulated Mn delta doping in GaAs*. Journal of Crystal Growth 2007. **301-302**: p. 634-637
49. R.P. Campion, V.A. Grant, K.W. Edmonds, B.L. Gallagher, and C.T. Foxon, *The growth of high quality GaMnAs layers and heterostructures by molecular beam epitaxy*. phys. stat. sol. (b) 2007. **244**(8): p. 2944-2949.
50. J. Sadowski, *GaMnAs: Layers, Wires and Dots*. Acta Physica Polonica A, 2008. **5**: p. 1001-1011.
51. F. Tuomisto, J.Slotte, K.Saarinen, and J.Sadowski, *Observation of Vacancies in  $Ga_{1-x}Mn_xAs$  with positron Annihilation Spectroscopy*. Acta Physica Polonica A, 2003. **103**(6): p. 601-606.
52. C.T. Foxon, T.S. Cheng, S.V. Novikov, D.E. Lacklison, L.C. Jenkins, D. Johnston, J.W. Orton, S.E. Hooper, N. Baba-Ali, T.L. Tansley, and V.V. Tret'yakov, *The growth and properties of group III nitrides*. Journal of Crystal Growth, 1995. **150**: p. 892-896.
53. H. Morkoç, *Nitride semiconductors and devices*. 1999, Berlin: Springer-Verlag.
54. G. Biasiol and L.Sorba, *Molecular Beam Epitaxy : Principles and Applications*. Crystal growth of materials for energy production and energy-saving applications, 2001: p. 66-83.
55. J.-K. Tsai, *Growth and characterization of wide bandgap GaN semiconductor*. 2002.
56. S. Einfeldt, U. Birkle, C. Thomas, M. Fehrer, H. Heinke, and D. Hommel, *Plasma assisted molecular beam epitaxy growth of GaN*. Materials Science and Engineering B, 1997. **50**(1-3): p. 12-15.
57. M.C. Yoo, M.Y. Park, S.K. Kang, H.D. Cho, and J.W. Lee, *Growth and p-type doping of GaN on c-plane sapphire by nitrogen plasma-assisted molecular beam epitaxy*. Journal of Crystal Growth, 1997. **175-176**(Part 1): p. 100-106.

58. T. Jungwirth, J. Sinova, A.H. MacDonald, B.L. Gallagher, V. Novák, K.W. Edmonds, A.W. Rushforth, R.P. Campion, C.T. Foxon, L. Eaves, E. Olejník, J. Mašek, S.-R.E. Yang, Wunderlich, C. Gould, L.W. Molenkamp, T. Dietl, and H. Ohno, *Character of states near the Fermi level in (Ga,Mn)As: Impurity to valence band crossover*. Physical Review B 2007. **76**: p. 125206.
59. K.W. Edmonds, K.Y. Wang, R.P. Campion, A.C. Neumann, C.T. Foxon, B.L. Gallagher, and P.C. Main, *Hall effect and hole densities in Ga<sub>1-x</sub>Mn<sub>x</sub>As*. Appl. Phys. Lett., 2002. **81**(16): p. 3010-3012.
60. R.P. Campion, K.W. Edmonds, L.X. Zhao, K.Y. Wang, C.T. Foxon, B.L. Gallagher, and C.R. Staddon, *The growth of GaMnAs films by molecular beam epitaxy using arsenic dimers*. Journal of Crystal Growth 2003. **251**: p. 311–316.
61. I.T. Yoon, T.W. Kang, K.H. Kim, and D.J. Kim, *A Hall coefficient investigation of ferromagnetic Ga<sub>1-x</sub>Mn<sub>x</sub>As layers on (100) GaAs substrates*. Solid State Communications, 2004. **130**: p. 627-630.
62. F. Matsukura, H. Ohno, and T. Dietl, *III-V Ferromagnetic Semiconductors*. Submitted to Handbook of Magnetic Materials ed. K.H.J. Buschow. 2003: Elsevier Science.
63. S. Das Sarma, E.H. Hwang, and A. Kaminski, *How to make semiconductors ferromagnetic: a first course on spintronics*. Solid State Communications, 2003. **127**(2): p. 99-107.
64. Y. Han, M.W. Fay, P.D. Brown, S.V. Novikov, K.W. Edmonds, B.L. Gallagher, R.P. Campion, C.R. Staddon, and C.T. Foxon, *Structural characterisation of zinc-blende Ga<sub>1-x</sub>Mn<sub>x</sub>N epilayers grown by MBE as a function of Ga flux*. Journal of Crystal Growth 2005. **284**: p. 324–334.
65. S.V. Novikov, K.W. Edmonds, A.D. Giddings, K.Y. Wang, C.R. Staddon, R.P. Campion, B.L. Gallagher, and C.T. Foxon, *P-type conductivity in cubic GaMnN layers grown by molecular beam epitaxy*. Semicond. Sci. Technol., 2004. **19**: p. L13–L16
66. D.C. Look, Z. Fang, and L. Polenta. *Electrical Measurements in GaN: Point Defects and Dislocations*. in *Online Proceedings Library*. 1999: MRS.
67. G. Chris, V.d. Walle, and J. Neugebauer, *Defects, Impurities and Doping levels on wide-Band Gap Semiconductors* Brazilian Journal of Physics, 1996 **26**(1).
68. S.L. Sheng, *Semiconductor Physical Electronics*. Second ed. 2006: Spinger
69. H. Harima, *Properties of GaN and related compounds studied by means of Raman scattering*. Journal of Physics: Condensed Matter, 2002. **14**: p. R967-R993.
70. X.M. Shen, Y.T. Wang, X.H. Zheng, B.S. Zhang, J. Chen, G. Feng, and H. Yang, *X-ray diffraction analysis of MOCVD grown GaN buffer layers on GaAs(0 0 1) substrates*. Journal of Crystal Growth, 2003. **254**(1-2): p. 23-27.
71. R. Kimura, T. Suzuki, M. Ouchi, K. Ishida, and K. Takahashi, *Thick cubic GaN film growth using ultra-thin low-temperature buffer layer by RF-MBE*. Journal of Crystal Growth 2005. **278**: p. 411-414.
72. V.K. Lazarov, S.H. Cheung, L.L. Y. Cui, and M. Gajdardziska-Josifovska, *Role of Mn and H in formation of cubic and hexagonal GaMnN*. Applied Physics Letter 2008. **92**: p. 101914.
73. Z.Q. Li, H.Chen, H.F.Liu, J.H.Li, L.Wan, S.Liu, qQ.Huang, and J.M.Zhou, *MBE growth and X-ray study of high-quality cubic-GaN on GaAs (001)*. Journal of crystal growth, 2000. **208**: p. 786-790.
74. O. Maksimov, Y. Gong, H. Du, P. Fisher, M. Skowronski, I.L. Kuskovsky, and V.D. Heydemann, *Structural and optical properties of GaN films grown on GaAs substrates by molecular beam epitaxy*. Vacuum, 2006. **80**(9): p. 1042-1045.

75. Z. Benamara, B. Akkal, A. Talbi, and B. Gruzza, *Electrical transport characteristics of Au/n-GaN Schottky diodes*. Materials Science and Engineering: C, 2006. **26**(2-3): p. 519-522.
76. J. Osvald, J. Kuzmik, G. Konstantinidis, P. Lobotka, and A. Georgakilas, *Temperature dependence of GaN Schottky diodes I-V characteristics*. Microelectronic Engineering, 2005. **81**(2): p. 181-187.
77. E.J. Miller, E.T. Yu, P. Waltereit, and J.S. Speck, *Analysis of reverse-bias leakage current mechanism in GaN grown by molecular beam epitaxy* Applied Physics Letter, 2004. **84**(4): p. 535-537.
78. D.J. Kim, D.Y. Ryu, N.A. Bojarczuk, J. Karasinski, S. Guha, S.H. Lee, and J.H. Lee, *Thermal activation energies of Mg in GaN:Mg measured by the Hall effect and admittance spectroscopy*. Journal of Applied Physics 2000. **88**(5): p. 2564-2569.
79. J.W. Kim and J.W. Lee, *Ti/Al p-GaN Schottky barrier height determined by C-V measurements*. Applied Surface Science, 2005. **250**(1-4): p. 247-251.
80. J.W. Huang, T.F. Kuech, H. Lu, and I. Bhat, *Electrical characterization of Mg-doped GaN grown by metal organic vapour phase epitaxy* Applied Physics Letter 1996. **68**(17): p. 2392-2394.
81. M.A. Reshchikov and H. Morkoc, *Luminescence from defects in GaN*. Physica B: Condensed Matter, 2006. **376-377**: p. 428-431.
82. X. Jian-jun, Z. Kai-ming, and X. Xi-de, *Formation Energies and Electronic Structures of Native Defects in GaN*. Chinese Phys. Lett., 1996. **13**(11): p. 867-869.
83. M. Lisker, A. Krtschil, H. Witte, and J. Christen, *Electrical and Photoelectrical Characterization of Deep Defects in Cubic GaN on GaAs in Symposium G "Gallium Nitride and Related Alloys" 1998*, The Materials Research Society: Boston, Massachusetts.
84. D.J. As, A. Richter, J. Busch, B. Schöttker, M. Lübbers, J. Mimkes, D. Schikora, K. Lischka, W. Kriegseis, W. Burkhardt, and B.K. Meyer, *Optical and Electrical Properties of MBE Grown Cubic GaN/GaAs Epilayers Doped by Si* MRS Internet J. Nitride Semicond. Res 2000. **5S1**: p. W3.81.
85. D.J. As, T. Simonsmeier, J. Busch, B. Schöttker, M. Lübbers, J. Mimkes, D. Schikora, K. Lischka, W. Kriegseis, W. Burkhardt, and B.K. Meyer, *P- and N-type doping of MBE grown cubic GaN/GaAs epilayers*. MRS Internet J. Nitride Semicond. Res., 1999. **4S1**, **G 3.24**
86. K.W. Edmonds, P.B. lawski, K.Y. Wang, R.P. Campion, S.N. Novikov, N.R.S. Farley, B.L. Gallagher, C.T. Foxon, M. Sawicki, T. Dietl, M.B. Nardelli, and J. Bernholc, *Mn Interstitial Diffusion in (Ga,Mn)As*. , Phys. Rev. Lett. , 2004. **92**: p. 037201.
87. R.H. Haisy and G.R. Cronin, *A Comparison Of Doping Of Transition Elements In Gallium Arsenide*. Physics of Semiconductors 1964: p. 1161.
88. K.W. Edmonds, K.Y. Wang, R.P. Campion, A.C. Neumann, N.R.S. Farley, B.L. Gallagher, and C.T. Foxon, *High Curie temperature Ga<sub>1-x</sub>Mn<sub>x</sub>As obtained by resistance-monitored annealing* Applied Physics Letters, 2002. **81**(26): p. 4991-4993.
89. F. Matsukura, H. Ohno, and T. Dietl, *III-V Ferromagnetic Semiconductors* in *Submitted to Handbook of Magnetic Materials*, K.H.J. Buschow, Editor, Elsevier Science. p. 1-42.
90. R. Jakiela, A. Barcz, E. Wegner, and A. Zagojski, *Diffusion of Mn in gallium arsenide*. Journal of Alloys and Compounds 2006. **423**: p. 132-135

91. A. Bengi, S. Altindal, S. Özçelik, S.T. Agaliyeva, and T.S. Mammadov, *Analysis of temperature dependent electrical characteristics of Au/n-GaAs/GaAs structures in a wide temperature range*. Vacuum, 2008. **83**(2): p. 276-281.
92. S. Hardikar, M.K.Hudait, P.Modak, S.B.Krupanidhi, and N. Padha, *Anomalous current transport in Au/low-doped n-GaAs Schottky barrier diodes at low temperatures*. Applied Physics A: Materials Science & Processing, 1999. **68**(1): p. 49-55.
93. S. Karatas and A. Türüt, *The determination of electronic and interface state density distributions of Au/n-type GaAs Schottky barrier diodes*. Physica B: Condensed Matter, 2006. **381**(1-2): p. 199-203.
94. Deepak and N. Lakshminarayana, *A detailed model for defect concentration and dopant activation in GaAs*. Bull. Mater. Sci., 2001. **24**(2): p. 225-229.
95. B. Nabet, A.E. Youtz, and P. Cooke, *Deep Defects in Intermediate Temperature Molecular Beam Epitaxy Grown GaAs and Their Role in Current Transport*. IEEE Conference Proceeding, 1997. **2**: p. 643 - 648.
96. R.M. Rubinger, H.A.Albuquerque, R.L.d. Silva, A.G.d. Oliveira, G.M.Ribeiro, W.N. Rodrigues, C.P.L. Rubinger, and M.V.b.Moreira, *Variable range hopping conduction in low-temperature molecular beam epitaxy GaAs* Brazilian Journal of Physics, 2006. **36**(2): p. 252-254.
97. K. Krambrock, M. Lindet, J.-M. Spaethi, D.C. Look, D. Bliss, and W. Walukiewicz, *Arsenic antisite-related defects in low temperature MBE grown GaAs*. Semicond. Sci. Technol. , 1992. **7**: p. 1037-1041.
98. D.C. Look, D.C. Walters, M.O. Manasreh, J.R. Sizelove, C.E. Stutz, and K.R. Evans, *Anomalous Hall-effect results in low-temperature molecular-beam-epitaxial GaAs: Hopping in a dense EL2-like band*. Phys Rev B, 1990. **42**: p. 3581-3581.
99. E. Weber, *Electronic properties of low-temperature grown III/V thin films*, in AFOSR, Regents, Editor. 1995, University of California Berkeley, CA. p. 1-17.
100. H. Thomas, J.K. Luo, D.V. Morgan, D. Westwood, K. Lipka, E. Splingart, and E. Kohn. *Improvement of the breakdown voltage of GaAs-FETs using low-temperature-grown GaAs insulator*. in Power Semiconductor Devices and ICs, 1994. ISPSD '94. Proceedings of the 6th International Symposium on. 1994.
101. U. Keller and A.C. Tropper, *Passively modelocked surface-emitting semiconductor lasers*. Physics Reports, 2006. **429**(2): p. 67-120.
102. P. Specht, M.J. Cich, R. Zhao, N.D. Jager, J. Gebauer, F. Borner, R. Krause-Rehberg, M. Luysberg, and E.R. Weber, *Defect engineering in MBE grown GaAs based materials*, in Semiconducting and Insulating Materials Conference, IEEE, Editor. 2000. p. 73-76.
103. M. Tanaka, *Spintronics: recent progress and tomorrow's challenges*. Journal of Crystal Growth, 2005. **278**: p. 25-37
104. J. Gebauer, F. Borner, R. Krause-Rehberg, P. Specht, and E.R. Weber. *Vacancies in low-temperature-grown GaAs: observations by positron annihilation*. in Semiconducting and Insulating Materials, 1998. (SIMC-X) Proceedings of the 10th Conference on. 1998.
105. B.G. Salamov, K.Colakoglu, and S.Altindal, *Recording the resistance inhomogeneity in high-resistivity semiconductor plates*. Infrared Phys. Technol., 1995 **36**(3): p. 661-668.
106. S. Lee and D.Y. Kim, *Correlation of electrical properties with magnetic properties for ferromagnetic (Ga<sub>1-x</sub>Mn<sub>x</sub>)As epilayer* Current Applied Physics, 2007. **7**: p. 156-159.

107. F. Tuomisto, K. Pennanen, K. Saarinen, and J. Sadowski, *Ga sublattice defects in (Ga,Mn)As : Thermodynamical and kinetic trends*. Physical Review Letters 2004. **93**(5): p. 055505.
108. J.R. Company, *Closed Cycle Refrigerator System manual*. 2004, Janis Research Company ,INC.: Wilmington, MA, USA.
109. O. Engstrom and H.G. Grimmesis, *Thermal activation energy of the gold-acceptor level in silicon* Journal of applied physics, 1975. **46**(2): p. 831-837.
110. S.J. Moloi and M. McPherson, *Current-voltage behaviour of Schottky diodes fabricated on p-type silicon for radiation hard detectors*. Physica B: Condensed Matter, 2009. **In Press, Accepted Manuscript**.
111. M.L. Lucia, J. L. Hernandez-Rojas, C. Leon, and I. Martil, *Capacitance measurements of p-n junctions: depletion layer and diffusion capacitance contributions* Eur.J.Phys., 1993. **14**: p. 86-89.
112. V.K. Peddinti. *Light Emitting Diodes (LEDs)*. 2008 [cited; Available from: <http://www.ele.uri.edu/courses/ele432/spring08/LEDs.pdf>
113. P. Shah, V. Mitin, M. Grupen, G.H. Song, and K. Hess, *Numerical simulation of wide band-gap AlGaIn/InGaIn light-emitting diodes for output power characteristics and emission spectra*. J. Appl. Phys., 1996. **79**( 5): p. 2755-2761.
114. J.M. Shah, Y.-L. Li, T. Gessmann, and E.F. Schubert, *Experimental analysis and theoretical model for anomalously high ideality factors ( $n \gg 2.0$ ) in AlGaIn/GaIn p-n junction diodes*. Journal of applied physics, 2003. **94**(4).
115. D. Zhu, J. Xu, A. N. Noemaun, J.K. Kim, E.F. Schubert, M.H. Crawford, and D.D. Koleske, *The origin of the high diode-ideality factors in GaInN/GaIn multiple quantum well light-emitting diodes*. Appl. Phys. Lett. , 2009. **94**: p. 081113.
116. Y. Yang, X.A. Cao, and C.H. Yan, *Rapid efficiency roll-off in high-quality green light-emitting diodes on freestanding GaN substrates*. Applied Physics Letter, 2009. **94**: p. 041117.
117. C.-L. Wang, M.-C. Tsai, J.-R. Gongc, W.-T. Liao, P.-Y. Lin, K.-Y. Yen, C.-C. Chang, H.-Y. Lin, and S.-K. Hwang, *Influence of AlGaIn/GaIn superlattice inserted structure on the performance of InGaIn/GaIn multiple quantum well light emitting diodes*. Materials Science and Engineering B, 2007. **138**: p. 180-183.
118. Y. Zohta, *Frequency dependence of the reverse-biased capacitance of blue and green light-emitting diodes*. Journal of Crystal Growth, 1998. **189/190**: p. 816-819.
119. N.D. Nguyen, M. Germain, M. Schmeits, R. Evrard, B. Schineller, and M. Heuken, *Experimental and theoretical investigations of the electrical properties of undoped and magnesium-doped GaN layers*. Journal of Crystal Growth, 2001. **230**(3-4): p. 596-601.
120. S. Wang, *Fundamentals of semiconductor theory and device physics*. 1989: Prentice-hall International, Inc.
121. I.T. Yoon, T.W. Kang, and D.J. Kim, *Analysis of magnetic field dependent mobility in ferromagnetic  $Ga_{1-x}Mn_xAs$  layers* Solid State Communications, 2006. **340-342**: p. 870-873.
122. T.W. Hickmott, *Admittance measurements of acceptor freezeout and impurity conduction in Be-doped GaAs*. Physical Review B, 1991. **44**(24): p. 13487.
123. L.X. Zhao, R.P. Champion, P.F. Fewster, R.W. Martin, Y. Ber, A.P. Kovarsky, C.R. Staddon, K.Y. Wang, K.W. Edmonds, C.T. Foxon, and B.L. Gallagher, *Determination of the Mn concentration in GaMnAs*. Semicond. Sci. Technol., 2005. **20**: p. 369-373.

124. *Online Simulation and more for nanotechnology* 2009 [cited; Available from: <http://nanohub.org/resources/tools/?with=ncnsupported>.
125. *The semiconductor Applet service* 2000 [cited; Available from: <http://jas.eng.buffalo.edu/education/pn/pnformation2/pnformation2.html>.
126. A.H. MacDonald, P.Schiffer, and N.Samarth, *Ferromagnetic Semiconductors: Moving Beyond (Ga,Mn)As*. Nature Materials, 2005. 4: p. 195-202.
127. [cited; Available from: [www.OriginLab.com](http://www.OriginLab.com).
128. R.K. Gupta and R.A.Singh, *Schottky diode based on composite organic semiconductors*. Materials Science in Semiconductor Processing. , 2004. 7: p. 83-87.
129. H. Hasegawa and S.Oyama, *Mechanism of anomalous current transport in n-type GaN Schottky contacts* J.Vac.Sci. Technol. B, 2002. 20(4).
130. V. Sundaramoorthy, *Design and characterization of group III-V heterojunction bipolar transistors.*, in *Department of Electrical and Electronic Engineering* 2008, University of Nottingham: Nottingham.
131. *Gallium Nitride (GaN)* [cited; Available from: <http://www.ioffe.ru/SVA/NSM/Semicond/GaAs/bandstr.htm#Basic>.
132. H.W. Choi, C.W.Jeon, and M.D.Dawson, *Low resistance contacts to p-type GaN by plasma treatment* Phys Stat.Sol. (C), 2003. 7: p. 2210-2213.
133. P.A. Anderson, *Work function of Gold*. Surface Science, 1966. 5(2): p. 221-229.
134. A.G. Baca, F. Ren, C. Zolper, R.D. Briggs, and S.J. Pearton, *A survey of ohmic contacts to III-V compound semiconductors*. Thin Solid Films 1997. 308–309: p. 599–606.
135. S. Dogan, S.Duman, B.Gurbulak, S.Tuzemen, and H.Morkoc, *Temperature variation of current-voltage characteristics of Au/Ni/n-GaN Schottky diodes*. Physica E, 2009. 41: p. 646-651
136. M. Soyulu and B. Abay, *Barrier characteristics of gold Schottky contacts on moderately doped n-InP based on temperature dependent I–V and C–V measurements*. Micro electronic Engineering, 2009. 86: p. 88-95.
137. S.J. Pearton, C.R. Abernathy, D.P. Norton, A.F. Hebard, Y.D. Park, L.A. Boatner, and J.D. Budai, *Advances in wide bandgap materials for semiconductor spintronics*. Materials Science and Engineering 2003. R 40 p. 137–168
138. C.K. Tan, A. Abdul Aziz, and F.K. Yam, *Schottky barrier properties of various metal (Zr, Ti, Cr, Pt) contact on p-GaN revealed from I-V-T measurement*. Applied Surface Science, 2006. 252(16): p. 5930-5935.
139. M.K. Hudait, P. Venkateswarlu, and S.B. Krupanidhi, *Electrical transport characteristics of Au/n-GaAs Schottky diodes on n-Ge at low temperatures*. Solid-State Electronics, 2001. 45(1): p. 133-141.
140. M.A. Reshchikov and H. Morkoç, *Luminescence properties of defects in GaN*. Journal of Applied Physics, 2005. 97: p. 061301
141. W. Monch, *Electronic characterization of compound semiconductor surfaces and interfaces*. Thin Solid Films, 1983. 104(3-4): p. 285-299.
142. S.V. Novikov, K.W. Edmonds, L.X. Zhao, A.D. Giddings, K.Y. Wang, R.P. Champion, C.R. Staddon, M.W. Fay, Y. Han, P.D. Brown, M. Sawick, B.L. Gallagher, and C.T. Foxon, *Mn doping and p-type conductivity in zinc-blende GaMnN layers grown by molecular beam epitaxy*. J. Vac. Sci. Technol. B, 2005. 23(3): p. 1294-1298.
143. V.K. Lazarov, S.H. Cheung, L.L. Y. Cui, and M. Gajdardziska-Josifovska, *Role of Mn and H in formation of cubic and hexagonal GaMnN*. Applied Physics Letter, 2008. 92: p. 101914.

144. C.T. Foxon, S.V. Novikov, L.X. Zhao, K.W. Edmonds, A.D. Giddings, K.Y. Wang, R.P. Champion, C.R. Staddon, M.W. Fay, Y. Han, P.D. Brown, M. Sawicki, and B.L. Gallagher, *Molecular beam epitaxy of p-type cubic GaMnN layers*. Journal of crystal growth 2005. **278**: p. 685–689.
145. M.W. Fay, Y. Han, P.D. Brown, S.V. Novikov, K.W. Edmonds, R.P. Champion, B.L. Gallagher, and C.T. Foxon, *Structural characterization of zincblende Ga<sub>1-x</sub>Mn<sub>x</sub>N epilayers grown by molecular beam epitaxy on (001) GaAs substrates*. Applied physics letters, 2005. **87**: p. 031902
146. Y. Han, M.W. Fay, P.D. Brown, S.V. Novikov, K.W. Edmonds, B.L. Gallagher, R.P. Champion, and C.T. Foxon, *Microstructural characterization of low-temperature grown GaMnN on GaAs(0 0 1) substrates by plasma-assisted MBE*. Semicond. Sci. Technol. , 2007. **22**: p. 1131–1139.
147. R.F. Pierret, *Semiconductor Device Fundamentals*. 1996: Addison-Wesley.

## APPENDIX A: Equations used in Matlab Program

The equations used in the Matlab program are presented in this appendix (the full details are given in [147]). The built-in potential was calculated using this equation

$$V_{bi} = \frac{kT}{q} \ln\left(\frac{N_A N_D}{n_i^2}\right) \quad (\text{A-1})$$

The potential at the edge of the depletion region at  $x_p$  on the p-side is given by

$$V(x) = \frac{qN_A}{2\epsilon_S\epsilon_0} (x_p + x)^2 \quad -x_p \leq x \leq 0 \quad (\text{A-2})$$

The potential at the edge of the depletion region at  $x_n$  on the n-side is given by

$$V(x) = V_{bi} - \frac{qN_D}{2\epsilon_S\epsilon_0} (x_n - x)^2 \quad 0 \leq x \leq x_n \quad (\text{A-3})$$

The depletion widths  $x_p$  and  $x_n$  are given by

$$x_n = \left[ \frac{2\epsilon_S\epsilon_0}{q} \frac{N_A}{N_D(N_A + N_D)} V_{bi} \right]^{1/2} \quad (\text{A-4})$$

$$x_p = \left[ \frac{2\epsilon_S\epsilon_0}{q} \frac{N_D}{N_A(N_A + N_D)} V_{bi} \right]^{1/2} \quad (\text{A-5})$$

The total width of the depletion region is

$$W = x_n + x_p = \left[ \frac{2\epsilon_S\epsilon_0}{q} \left( \frac{N_A + N_D}{N_A N_D} \right) V_{bi} \right]^{1/2} \quad (\text{A-6})$$

The Fermi level is given by

$$E_F = \frac{kT}{q} \ln\left(\frac{N_A}{n_i}\right) \quad (\text{A-7})$$

The written program [147]:

```
%Equilibrium Energy band diagram
%(GaAs,300K,nondegenerately doped step junction
%Contacts
T=300;      % Temperature in Kelvin
K=8.617e-5 % Boltzmann constant (eV/K)
ε₀=8.85e-14 % permittivity of free space (F/cm)
q=1.6e-19  % charge on electron (coul)
εₛ=12.8    % dielectric constant of GaAs
ni=1.8e6   % intrinsic carrier concentration in GaAs at 300 K (cm⁻³)
Eg=1.42    %GaAs band gap (eV)
%Control constant
xleft=-3.5e-4 % Leftmost x position
xright=-xleft; % Rightmost x position
NA=input('p-side doping (cm⁻³) ,N_A= 1e21');
ND=input('n-side doping (cm⁻³) ,N_D= 2e17');
```

```

%Computations
Vbi=k*T*log(NA*ND)/ni^2);
xN=sqrt(2* εs*e0/q*NA*Vbi/(ND*(NA+ND)));      % Depletion width n-side
xN=sqrt(2* εs*e0/q*ND*Vbi/(NA*(NA+ND)));      % Depletion width p-side
x=linspace (xleft,xright,200);
Vx1=(Vbi-q*ND.*(xN-x).^2/(2* εs*e0).*(x<=xN)).*(x>=0);
Vx2=(0.5*q*NA.*(xP+x).^2/(2* εs*e0).*(x>=xP))& x<0);
Vx=Vx1+Vx2;                                  % V as a function of x
VMAX=3;                                       % Maximum Plot Voltage
EF= Vx(1)+ VMAX/2-k*T*log(NA/ni);           % Fermi level
%Plot diagram
Close
Plot (x,-Vx+Eg/2+ VMAX/2);
axis ([xleft xright 0 VMAX]);
Axis ('off');hold on
Plot (x,-Vx-Eg/2+ VMAX/2);
Plot (x,-Vx+ VMAX/2), 'w');
Plot ([xleft xright],[EF EF ], 'w');
Plot ([0 0 ], 0.15 VMAX-0.5), 'w--');
Text(xleft*1.08,(-Vx(1)+Eg/2+ VMAX/2-.05), 'Ec');
Text(xright*1.02,(-Vx(200)+Eg/2+ VMAX/2-.05), 'Ec');
Text(xleft*1.08,(-Vx(1)-Eg/2+ VMAX/2-.05),Ev);
Text(xright*1.02,(-Vx(200)-Eg/2+ VMAX/2-.05), 'Ev');
Text(xleft*1.08,(-Vx(1)+ VMAX/2-.05), 'Ei');
Text(xright*1.02EF-.05), 'EF');
Set(gca, 'Default Text Units','normalized')
Text(.18,0, 'p-side');
Text(.47,0, 'x=0');
Text(.75,0, 'n-side');
Set(gca, 'Default Text Units','data')
Hold off

```

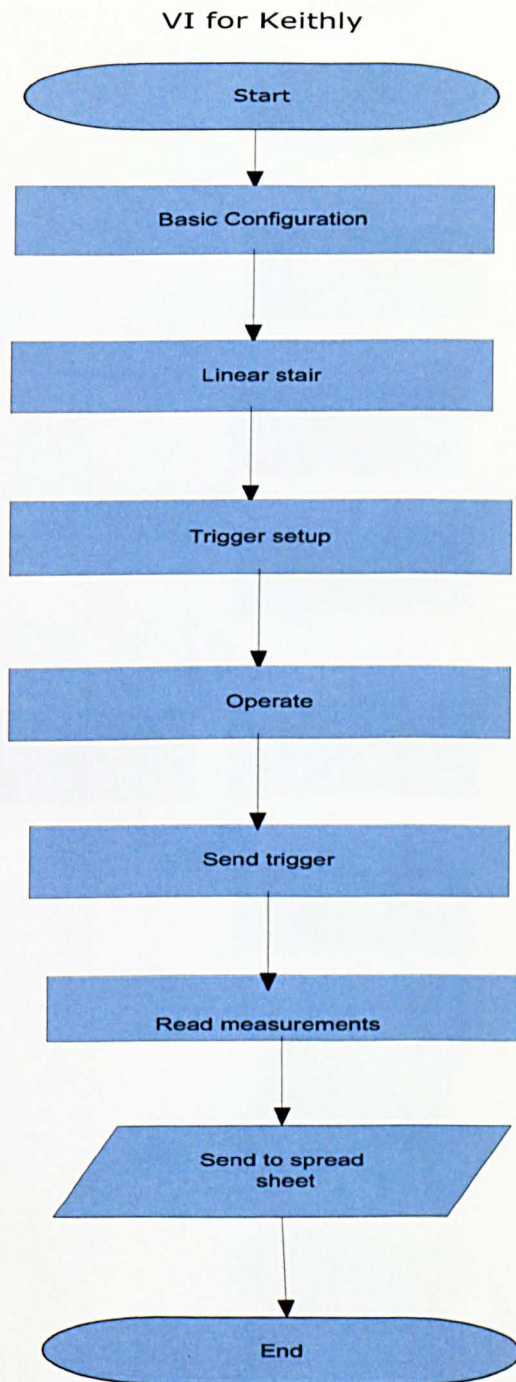
**APPENDIX B: LabView flow chart for I-V measurement**

Figure B.1: The flow chart of the I-V measurement using Keithley.

## Appendix C: LabView flow chart for C-V measurement

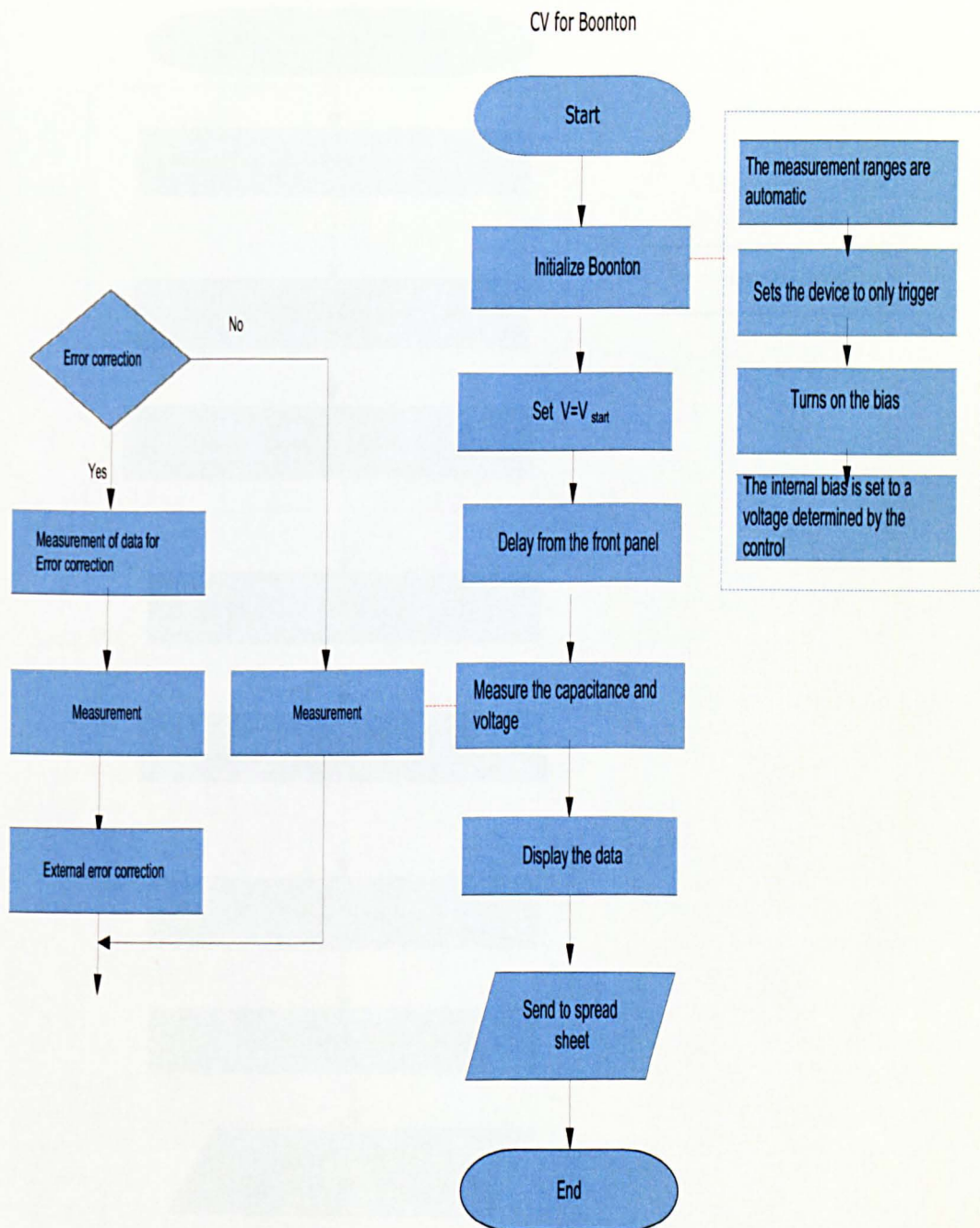


Figure C.2: The flow chart of the C-V measurement using Boonton.

## APPENDIX D: LabView flow chart for C-F measurement

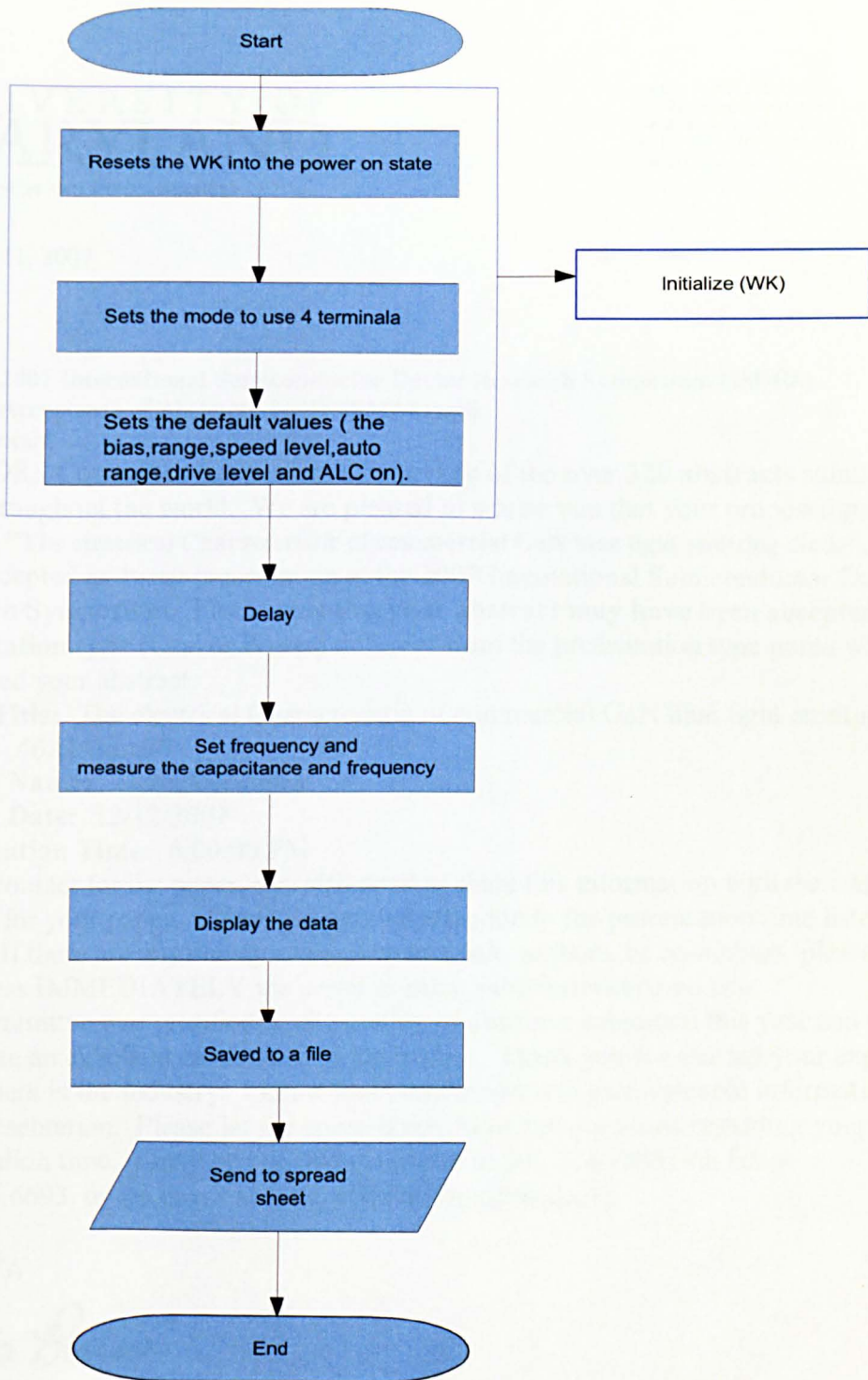


Figure D.3: The flow chart of the C-F measurement using Wayne Kerr.

## APPENDIX E: Published Paper

UNIVERSITY OF  
MARYLAND

CONFERENCES AND VISITOR SERVICES

Mailbox Turner Hall 1201  
8400 Baltimore Avenue, Suite 100  
College Park, Maryland 20742-5415  
301.314.7884 TEL 301.314.6693 FAX  
www.cvs.umd.edu

October 11, 2007

**Re: 2007 International Semiconductor Device Research Symposium (ISDRS)**  
Acceptance of Abstract Log ID 46AIAhmadi

Dear Noorah,

The ISDRS Committee has performed a review of the over **320 abstracts** submitted from throughout the world. We are pleased to advise you that your proposed paper entitled "**The electrical Characteristic of commercial GaN blue light emitting diode**", has been accepted as *Poster* presentation at the 2007 International Semiconductor Device Research Symposium. Please note that **your abstract may have been accepted for a presentation type** (Oral or Poster) different from the presentation type noted when you submitted your abstract.

**Paper Title:** The electrical Characteristic of commercial GaN blue light emitting diode

**LogID:** 46AIAhmadi

**Session Name:** Optoelectronics

**Session Date:** 12/12/2007

**Presentation Time:** 6:00:00 PM

As the contact for the paper, you will need to share this information with the additional authors for your paper. Please pay special attention to the presentation time listed above. If there are any changes in your paper title, authors, or co-authors, please advise Lisa Press IMMEDIATELY via email to [isdrs\\_submissions@umd.edu](mailto:isdrs_submissions@umd.edu).

The Committee was gratified by the quality of abstracts submitted this year and we anticipate an excellent conference in December. Thank you for sharing your expertise with others in the industry. I know that participants will gain valuable information from your presentation. Please let me know if you have any questions regarding your presentation time. I may be reached via phone at 301.314.7885, via fax at 301.314.6693, or via email at [isdrs\\_submissions@umd.edu](mailto:isdrs_submissions@umd.edu).

Sincerely,



**Lisa Press**  
**ISDRS '07 Conference Coordinator**  
**University of Maryland**